

AD-A113 892

PRINCETON UNIV NJ DEPT OF MECHANICAL AND AEROSPACE --ETC F/6 21/7  
HIGH PRESSURE ATOMIZATION.(U)  
MAR 82 F V BRACCO

DAAG29-76-G-0264

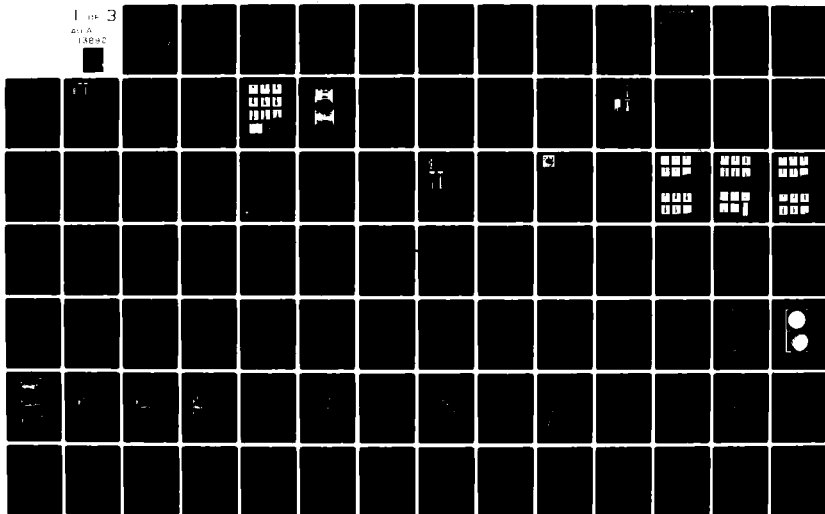
UNCLASSIFIED

ARO-13935.3-EX

NL

1 11-3

411 A  
13890



UNCLASSIFIED

SECURITY CLASSIFICATION OF THIS PAGE (When Data Entered)

(12)

REPORT DOCUMENTATION PAGE		READ INSTRUCTIONS BEFORE COMPLETING FORM
1. REPORT NUMBER 13935.3-EX	2. GOVT ACCESSION NO. AD A113892	3. RECIPIENT'S CATALOG NUMBER
4. TITLE (and Subtitle) High Pressure Atomization	5. TYPE OF REPORT & PERIOD COVERED Final: 1 Jun 76 - 31 May 81	
7. AUTHOR(s) F. V. Bracco	6. PERFORMING ORG. REPORT NUMBER	
9. PERFORMING ORGANIZATION NAME AND ADDRESS Princeton University Princeton, NJ 08540	8. CONTRACT OR GRANT NUMBER(s) DAAG29 76 G 0264; DAAG29 77 G 0146; DAAG29 78 G 0132	
11. CONTROLLING OFFICE NAME AND ADDRESS U. S. Army Research Office Post Office Box 12211 Research Triangle Park, NC 27709	10. PROGRAM ELEMENT, PROJECT, TASK AREA & WORK UNIT NUMBERS	
14. MONITORING AGENCY NAME & ADDRESS (if different from Controlling Office)	12. REPORT DATE Mar 82	
	13. NUMBER OF PAGES 264	
	15. SECURITY CLASS. (of this report) Unclassified	
	15a. DECLASSIFICATION/DOWNGRADING SCHEDULE	
16. DISTRIBUTION STATEMENT (of this Report) Approved for public release; distribution unlimited.		
17. DISTRIBUTION STATEMENT (of the abstract entered in Block 20, if different from Report) NA		
18. SUPPLEMENTARY NOTES The view, opinions, and/or findings contained in this report are those of the author(s) and should not be construed as an official Department of the Army position, policy, or decision, unless so designated by other documentation.		
19. KEY WORDS (Continue on reverse side if necessary and identify by block number) high pressure atomization atomization processes high pressure jets nozzles diesel engines fuel injection systems technical grants		
20. ABSTRACT (Continue on reverse side if necessary and identify by block number) The main objective has been to study the fundamental processes which lead to the atomization of high pressure jets injected into compressed gases through single hole nozzles. Appendices A-H are copies of technical publications and are included to give details of the findings.		

DTIC  
SELECTED  
APR 26 1982  
S H D

FILE COPY

DD FORM 1 JAN 73 1473

EDITION OF 1 NOV 65 IS OBSOLETE

UNCLASSIFIED

SECURITY CLASSIFICATION OF THIS PAGE (When Data Entered)

82

04

26

U57

**FINAL TECHNICAL REPORT**

**TO**

**U.S. ARMY RESEARCH OFFICE**

**ON**

**GRANT DAAG 29-78-G-0132**

**JUNE -1-1978 - May -31- 1981**

**HIGH PRESSURE ATOMIZATION**

**PRINCIPAL INVESTIGATOR**

**F. V. BRACCO**

**PRINCETON UNIVERSITY**

**MECHANICAL AND AEROSPACE ENGINEERING DEPARTMENT**

**MARCH 1982**

## OBJECTIVE AND SUMMARY OF RESULTS

This ARO grant lasted 36 months and provided support at the level of \$50,000/year. The main objective has been to study the fundamental processes which lead to the atomization of high pressure jets injected into compressed gases through single hole nozzles. We think we have identified the mechanism even though some elements remain unclear. Appendices A-H are copies of technical publications and are included here to give details of our findings. The following paragraphs give a general overview of the work. For a more detailed discussion the reader is invited to consult the above-mentioned appendices.

The range of conditions selected for our experimental study has been extensive and has included those operating conditions which are typical of fuel injection systems in Diesel and stratified charge engines. The test conditions have included:

Constant liquid injection pressures in the ranges of 500-2500 psi (APP. A, B) and 1600-13,300 psi (APP. D).

Constant gas pressures in the range of 1 atm to 600 psi with air, nitrogen, helium and xenon (different molecular weights to isolate effects of gas density and pressure). (APP. A, B, D, E).

Water and water + glycerol injections ( $10^3$  range in liquid viscosity - APP. A); Hexane, water and tetradecane (factor of 10 in viscosity, 4 in surface tension, 1.5 in liquid density); Pentane, hexane, and ethanol (factor of 3 surface tension, 1.5 liquid density). (APP. A, B, D, E).

21 different nozzles: sharp edge inlet tube nozzles (length to diameter ratio 0.5 - 85); rounded exit nozzles and cavitation free nozzles (APP. A, B, D, E).

Liquid temperature: room temperature and 100-200°C (APP. C).

The experimental data consists of some 500 short exposure (30 ns) photographs showing details of the steady state jet behavior up to 20 nozzle exit diameters downstream of the nozzle, and of about 60 ultra high speed films (each with 60 frames at about  $10^6$  frame/s) which show closeup details of the initial penetration and breakup of high velocity jets in compressed gases.

The experimental results were used to assess jet atomization theories for high velocity jet breakup, and for breakup due to thermodynamic instabilities (flash atomization). In addition, the experimental results have proved useful in deriving correlations (APP. A) for the initial spray parameters (such as the jet spreading angle) which are already being used in engine and spray modeling computations. (APP. G)

Over the years (mainly since the 1930's) many causes of high velocity jet atomization have been proposed. These include: jet turbulence - Refs. 1 and 2; jet velocity profile rearrangement effects - Ref. 3; instability of nozzle wall boundary layers - Ref. 4; aerodynamic gas-liquid surface interaction - Refs. 5, 6, and 7; upstream supply pressure oscillations - Ref. 8 and cavitation - Ref. 9.



Progress has been made in the assessment of these and other potential atomization mechanisms by comparison with our experiments. In APP. A we demonstrated that none of the previously proposed mechanisms, alone, explains the experiments, with the possible exception of cavitation. In APP. D we have shown that even cavitation by itself is inadequate to explain our measurements. More importantly, however, we have been able to conclude from the experiments that the most likely mechanism of high velocity jet atomization is the rapid growth of unstable surface waves (due to aerodynamics interactions with the gas) which are initially triggered by either cavitation or by unstable nozzle wall boundary layers, or by both. (APP. E).

This supplemented aerodynamic interactions theory contains an undetermined constant whose value at present must be found from experiments. In APP. A it is argued that the magnitude of the constant is determined by the cavitation and/or wall boundary layer effects. The results of APP. D further indicate that if the wall boundary layer effects are important - they are generated at the entrance and/or within the nozzle. The disruption of the wall boundary layer at the exit of the nozzle does not seem to be important. The proposed atomization mechanism has been able to match the experimental trends over the entire range of operating conditions explored provided that the undetermined constant is allowed to vary with nozzle design. However, there are still some small discrepancies at both very low and very high gas densities (APP. D). The theoretical dependence is derived from a first order perturbation solution of the coupled liquid and gas conservation equations for an infinite jet (APP. A). The theory does not account for the flow field within the nozzle, and it is therefore not surprising that effects due to changes in the nozzle internal design are not predicted. It is possible, however, that the discrepancies with regard to the high and low gas density limits, for a given nozzle, may be resolved by retaining some of the neglected effects in the perturbation solution or by considering a higher order analysis.

The supplemented aerodynamic theory predicts the jet spreading angle and the initial droplet sizes as the operating conditions are changed. The predictions of drop size at the nozzle have been matched with experimentally measured droplet sizes (from Ref. 10), some 300 nozzle exit diameters downstream by our spray modeling computations (Ref. 11).

Progress was also made toward an understanding of the jet breakup process due to thermodynamic instabilities (APP. C). The experimental results point to the importance of the details of heterogeneous nucleation in initiating the breakup process. Mathematical modeling of nucleation appears to be very complex (Ref. 12) and our results show that the available correlations are inadequate. However, for the later process of bubble growth experiments appear to confirm earlier theories (Ref. 13) that bubble growth is controlled by heat conduction. In this case agreement with the experimental results has been achieved with a modification of the theory which includes the bubble temperature at the moment of jet breakup. Even though flash atomization may be a very attractive technique for intake manifold fuel injection we have concluded that it is not likely to be practical for in-cylinder injection and significant in the commonly used high pressure in-cylinder injection systems.



Dist	Availability Codes	By	Distribution/	Accession for
	Avail and/or Special			
				HTS GRAI DTIC TAB <input type="checkbox"/> Unannounced <input type="checkbox"/> Justification

The experimental data and correlations obtained from our measurements of the atomization process were then used as initial conditions for studies of the scaling of sprays, of the similarities between gas and spray jets, and of the effects of injection pulsations in engine type environments (APP. F. G. H).

Through numerical solutions of appropriate two-dimensional unsteady conservation equations, it is found that transient laminar incompressible jets, turbulent incompressible jets and nonvaporizing and vaporizing sprays reach steady state around the back of their head vortices. Thus, for many applications, the stems of such transient jets can be considered in steady state and steady state information can be applied to large fractions of transient jets. Equations are given for the penetration rate of such jets. In particular, an equation is obtained for the penetration rate of the tip of sprays that compares favorably with measured ones. Also, scaling laws were obtained that are obeyed by each of the three families of jets. Since the laws are somewhat different, no precise similarity exists among the three types of jet. However, one type of jet can still be approximately simulated by another but only with respect to certain parameters and within definite time and space ranges, given the acceptable error (APP. F, H).

Computations were also made of transient axisymmetric pulsating and evaporation sprays that account also for drop collisions and coalescence. It is found that, for the same upstream and gas conditions, pulsating injections result in smaller drops than continuous injections. The difference is particularly marked at high gas densities and is due to the inhibition of collisions and coalescence of drops generated by the gas gap in between the pulses. However, the tip penetration rates are not markedly different for continuous and pulsating injections. For transient evaporating sprays it is found that all drops except the largest evaporate within a well defined distance from the injector. Beyond this distance only vaporized liquid and entrained gas continue the penetration. For engine applications the length of the liquid core is found to be of the order of centimeters and sensitive to conditions. In particular it decreases with increasing injection pressure, gas temperature, and gas density. The sensitivity of the liquid core length to conditions may explain the different importance attached by different authors to the liquid phase in direct injection stratified-charge and Diesel engines (APP. G).

# LIST OF PUBLICATIONS

- APPENDIX A: R. D. Reitz and F. V. Bracco, "On the Dependence of Spray Angle and Other Spray Parameters on Nozzle Design and Operating Conditions"; Society of Automotive Engineers, Paper 790494, February 1979
- APPENDIX B: R. D. Reitz and F. V. Bracco, "Ultra High Speed Filming of Atomizing Jets"; The Physics of Fluids, Vol. 22, No. 6, pp. 1054-1064, June 1979.
- APPENDIX C: K. J. Wu, R. L. Steinberger, and F. V. Bracco, "On the Mechanism of Breakup of Highly Super Heated Liquid Jets"; The Combustion Institute, Central States Section Spring Meeting Paper CSS/CI 81-17, March 1981.
- APPENDIX D: C. C. Su, K. J. Wu, R. L. Steinberger, D. A. Santavicca, and F. V. Bracco, "Measurements of the Spray Angle of Atomizing Jets"; Submitted for publication to the Journal of Fluids Engineering.
- APPENDIX E: R. D. Reitz and F. V. Bracco, "On the Mechanism of Atomization of a Liquid Jet"; Submitted for publication to The Physics of Fluids.
- \*APPENDIX F: T.-W. Kuo and F. V. Bracco, "On the Scaling of Transient Laminar, Turbulent, and Spray Jets"; Society of Automotive Engineers, Paper 820038, February 1982.
- \*APPENDIX G: T.-W. Kuo and F. V. Bracco, "Computations of Drop Sizes in Pulsating Sprays and of Liquid Core Length in Vaporizing Sprays"; Society of Automotive Engineers, Paper 820133, February 1982.
- \*APPENDIX H: T. -W. Kuo and F. V. Bracco, "On the Scaling of Impulsively Started Sprays"; Submitted to the Journal of Fluids Engineering.

---

\* Completed under the new ARO Grant  
DAAG 29-81-K-0135

PARTICIPATING SCIENTIFIC PERSONNEL

Professor F. V. Bracco, Principal Investigator  
Drs. C. Bruno, R. Steinberger, D. Santavicca, Research Staff

Messrs. J. Semler and T. Griffith, Technical Staff

Degrees Awarded:

Mr. R. D. Reitz, Ph.D., Thesis #1375, May 1978

Mr. C. C. Su, MS, Thesis #1502, December 1980

Mr. K.-W. Kuo, Ph.D. Thesis, #1538, May 1982

Current Student:

Mr. K. J. Wu, Ph.D. Candidate

#### REFERENCES

- 1) DEJUHASZ, K.J. TRANS. ASME(OGP), 53, 65, 1931.
- 2) SCHWEITZER, P.H., J. APPL. PHYS., 8, 513, 1937.
- 3) RUPE, JPL Tech. Report 32, 207, 1962.
- 4) SHKADOV, V. YA., FLUID DYNAMICS 5, 473, 1970.
- 5) CASTLEMAN, R.A., U.S. NATL Bureau STD. J. RES., 6, 281, 1931.
- 6) CASTLEMEN, R.A., NACA Report 440, 1932.
- 7) RANZ, W.E., CANAD. J. CHEM. ENGG., 36, 175, 1958.
- 8) GIFFEN, E. and MURASZEW, A., The Atomization of Liquid Fuels, JOHN WILEY and SONS, 1953.
- 9) BERGWERK, W., PROC. INST. MECH. ENGRS., 173, 655, 1959.
- 10) HIROYASU, H. and KADOTA, T., SAE Paper 740715, 1974.
- 11) O'ROURKE, P.J. AND BRACCO, F.V., INST. MECH. ENGRS., PUBL. 085298-469, 1980.
- 12) AVEDISIAN, T., PH.D. Thesis, Dept. Mechanical and Aerospace Engineering, Princeton University, 1979.
- 13) FOSTER, H.K. and ZUBER, N., J. APPL. PHYS., 25, 493, 1954.

APPENDIX A

ON THE DEPENDENCE OF SPRAY ANGLE  
AND OTHER SPRAY PARAMETERS ON NOZZLE  
DESIGN AND OPERATING CONDITIONS

R.D. Reitz and F.V. Bracco



# SAE Technical Paper Series

790494

## On the Dependence of Spray Angle and Other Spray Parameters on Nozzle Design and Operating Conditions

**R. D. Reitz and F. B. Bracco**  
Dept. of Mechanical and Aerospace Engrg.,  
Princeton Univ.  
Princeton, NJ

Congress and Exposition  
Cobo Hall, Detroit  
February 26-March 2, 1979

**SOCIETY OF AUTOMOTIVE ENGINEERS, INC.**  
400 COMMONWEALTH DRIVE  
WARRENDALE, PENNSYLVANIA 15096

The appearance of the code at the bottom of the first page of this paper indicates SAE's consent that copies of the paper may be made for personal or internal use, or for the personal or internal use of specific clients. This consent is given on the condition, however, that the copier pay the stated per article copy fee through the Copyright Clearance Center, Inc., Operations Center, P.O. Box 765, Schenectady, N.Y. 12301, for copying beyond that permitted by Sections 107 or 108 of the U.S. Copyright Law. This consent does not extend to other kinds of copying such as copying for general distribution, for advertising or promotional purposes, for creating new collective works, or for resale.

Papers published prior to 1978 may also be copied at a per paper fee of \$2.50 under the above stated conditions.

SAE routinely stocks printed papers for a period of three years following date of publication. Direct your orders to SAE Order Department.

To obtain quantity reprint rates, permission to reprint a technical paper or permission to use copyrighted SAE publications in other works, contact the SAE Publications Division.



# On the Dependence of Spray Angle and Other Spray Parameters on Nozzle Design and Operating Conditions

R. D. Reitz and F. B. Bracco

Dept. of Mechanical and Aerospace Engrg.,  
Princeton Univ.  
Princeton, NJ

IN DIESEL AND OPEN CHAMBER STRATIFIED CHARGE ENGINES, liquid atomization is often achieved by discharging pressurized liquid fuel through a small orifice, or set of orifices, into the compressed combustion chamber gases. The atomization phenomenon then serves to increase drastically the surface area of the sprayed fuel and leads to increased rates of mass, momentum and energy transfer between

the liquid and gas phases. The details of the combustion process are intimately affected by the spatial and temporal distributions of liquid and/or vaporized fuel within the combustion chamber, which, in turn, are dependent on the details of the initial atomization process itself.

The need for a better understanding of the atomization phenomenon to aid engine design

## ABSTRACT

In the Atomization regime, liquid jets breakup either within the nozzle or immediately upon entering the chamber gas and drops much smaller than the jet diameter are formed. The mechanism of Atomization, which is presently unknown, was investigated by the simultaneous use of two photographic techniques. The initial transient was observed with a  $10^6$  frames/s camera and the steady state by a technique similar to spark photography. The experiment range was: liquid pressure 500 to 2500 psia; five mixtures of water and glycerol to vary the liquid viscosity; air, nitrogen, helium, and xenon at up to 600 psia as chamber gases to separate gas pressure from gas density effects; and 14 nozzle designs. Not changed were the temperature (room value), the nozzle diameter (340  $\mu$ ), and the surface tension (70 dyne/cm). It was found that: jet divergence begins progressively closer to the nozzle exit as the gas density increases until

it reaches the exit with no evidence of abrupt change; the divergence angle (spray angle) increases with increasing gas density, and sharpness of nozzle inlet and with decreasing liquid viscosity and nozzle length; divergence angle and jet intact length are quasi-steady with respect to upstream pressure changes which occur on time scales greater than 10 to 30  $\mu$ s; aerodynamic effects, liquid turbulence, jet velocity profile rearrangements, and liquid pressure oscillations, each could not alone be the mechanism of atomization; cavitation or aerodynamic effects, supplemented by cavitation and/or wall boundary layer relaxation processes, could each be the mechanism of atomization; and the criterion  $We_g > 40.3$  for the onset of atomization and a commonly used gas jet expression to predict the spray divergence angle are inadequate. Equations are given for the divergence angle and the onset of atomization which are valid within the tested range.

is known and recently it was emphasized again in a paper by Reitz and Bracco (1)\* in which it is demonstrated that, for the achievement of satisfactory open chamber, direct injection charge stratification, accurate control of the atomization process is necessary. However, a survey of the jet atomization literature (2, 3) revealed that, in spite of the work already done, there is great uncertainty even about the mechanisms of high velocity liquid jet disruption.

For this reason, experiments were performed to help in the identification of the mechanisms by which liquid jets break up into droplets. The constant pressure injection of a liquid jet through a single hole nozzle into an initially stagnant, constant pressure gas was studied. It is felt that an understanding of the mechanism of atomization ultimately would be helpful to the engine designer.

In order to distinguish Atomization, which is the mode of breakup of interest in engine applications, from other types of jet breakup, the four main breakup regimes, each of which reflects the action of different forces on the jet, are briefly reviewed here. Further details may be found in a review by Reitz and Bracco (4). Photographs showing examples of jets operating in each of these four regimes from Lee and Spencer (5) and Reitz (3) are shown in Figure 1.

Figure 1a shows low velocity jet breakup in the Rayleigh regime. The breakup results in droplets with sizes larger than the jet diameter and is due to the unstable growth of axisymmetric surface waves caused by surface tension. As the jet velocity is increased, forces, due to the relative motion of the jet and the surrounding gas, augment the surface tension force and lead to droplets with sizes of the order of the jet diameter. This class of breakup is termed the First Wind-Induced breakup regime and is shown in Figure 1b.

A further increase in the jet velocity results in breakup in the Second Wind-Induced regime which is shown in Figure 1c. Here jet breakup is characterized by divergence of the jet-spray after an intact or undisturbed length downstream of the nozzle. The unstable growth of short wavelength waves on the jet surface produces droplets whose average size is very much less than the jet diameter. This wave growth is induced by the relative motion between the liquid and the ambient gas and is opposed by surface tension.

When the jet velocity is further increased, or the operating conditions appropriately changed, the jet forms a cone-shaped spray commencing at the nozzle exit. This corresponds to breakup in the Atomization regime and is shown in Figure 1d. This is the regime of interest in practical engine applications. Droplets are produced with sizes very much

less than the nozzle exit diameter and the breakup mechanism is unknown.

Various authors have proposed possible jet atomization mechanisms. Castleman (6) and Ranz (7) proposed that aerodynamic interaction between the gas and liquid was responsible for jet breakup in this case. However, since no evidence of an intact length was found for jets in this regime, DeJuhasz (8) reasoned that the jet breakup process occurs within the nozzle itself. He argued that liquid turbulence could play an important role in this process. Schweitzer (9) proposed that the radial turbulent velocity components would disrupt the jet-gas interface, leading to the formation of droplets, as soon as the restraint imposed on the flowing liquid by the orifice wall ceases at the nozzle exit.

Bergwerk (10) noted that a cavitation region may occur within the nozzles. He suggested that large turbulent disturbances may be created in these cavitation regions and play a role in the jet disruption process. Rupe (11) postulated that the abrupt change in boundary condition experienced by the liquid flow at the nozzle exit could destabilize the jet, leading to its breakup. Liquid supply pressure oscillations have also been thought to contribute to the breakup process (12).

In spite of these and other attempts to explain the process of atomization, no firm evidence has so far been provided in support of the various hypotheses and no complete theory of atomization exists. Moreover, it has been shown (3) that there is no valid criterion currently available to predict the locations of the boundary between the Second Wind-Induced regime and Atomization regime in terms of the operating conditions.

#### EXPERIMENTAL DETAILS

The experimental apparatus used to study the jet atomization phenomenon is shown in Figure 2. The spray chamber enabled jet breakup studies to be performed in a variety of controlled, constant pressure, gaseous environments, and allowed the breakup process to be photographically observed through 10 cm diameter transparent windows. The spray chamber was designed for gas pressures up to 1000 psia (70 atm) and gas temperatures up to 750°K. In addition, to ensure minimal effects due to the confinement of the spray, the chamber inside diameter to nozzle exit diameter ratio (for the nozzles explored in the experiments) was chosen to be about 500.

Two experimental techniques were employed. In the first, the behavior of a constant injection pressure high velocity liquid jet upon

(\*)Numbers in parenthesis designate references at end of the paper.

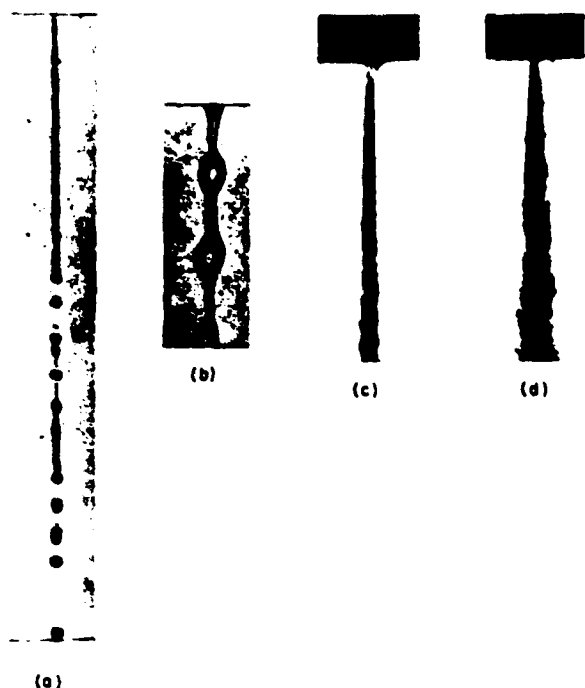


Fig. 1 - Examples of four jet breakup regimes (a) Rayleigh regime, (b) First Wind-Induced regime, (c) Second Wind-Induced regime, (d) Atomization regime - References (3) and (5)

its initial emergence into the chamber gas, was recorded using an ultra high speed Cordin Model 117 framing camera. These "Transient" studies, applied here for the first time to the authors' knowledge to the study of jet atomization, allowed 60 frames of film showing the developing jet breakup transient to be obtained at framing rates up to 1.25 million frames per second. In the second or "Steady State" studies, a single short exposure photograph of the jet taken long after its initial emergence into the chamber gas, was obtained using standard techniques. The two techniques were often applied simultaneously to the study of the same jet.

The liquid injection system consisted of a liquid reservoir section which housed up to 40 cm of a test liquid and a piston. The piston served to compress the test liquid to high pressures and was in turn driven by high pressure gas from a pressure amplifier system which was designed for pressures from 200 psia (13.3 atm) to as high as 20,000 psia (1300 atm). Fourteen individual single hole nozzles of differing internal geometry but fixed exit diameter ( $\sim 0.34$  mm) served to accelerate the test liquid from the almost stagnant reservoir into the chamber gas. Most of the nozzles

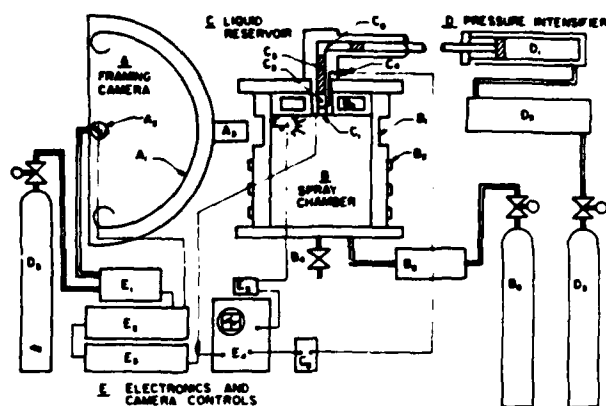


Fig. 2 - Schematic Diagram of Apparatus -  
A. Cordin Model 117 Camera (A<sub>1</sub> lens bank and stationary film strip; A<sub>2</sub> Rotating mirror; A<sub>3</sub> Camera lens)  
B. Spray Chamber (B<sub>1</sub> Quartz windows; B<sub>2</sub> Electrical heaters; B<sub>3</sub> Water cooling jacket; B<sub>4</sub> Drain and safety valves; B<sub>5</sub> Electrical gas heater; B<sub>6</sub> Bottled gas)  
C. Liquid Reservoir (C<sub>1</sub> Nozzle holder; C<sub>2</sub> Test liquid; C<sub>3</sub> Piston; C<sub>4</sub> Pressure transducer; C<sub>5</sub> Charge amplifier; C<sub>6</sub> Driver gas).  
D. Pressure Intensifier (D<sub>1</sub> Pressure amplifier; D<sub>2</sub> Accumulator; D<sub>3</sub> Bottled nitrogen)  
E. Electronics and Camera Controls (E<sub>1</sub> Camera gas control unit; E<sub>2</sub> Camera speed control unit; E<sub>3</sub> High energy pulse unit; E<sub>4</sub> Oscilloscope; E<sub>5</sub> Flash control units; E<sub>6</sub> Xenon flash tubes)

were designed in such a way that they could be interchangeably mounted in two specially constructed nozzle holders which could be screwed into the lower end of the reservoir section. Details of the design of a nozzle holder are shown in Figure 3. The nozzle geometry was varied by using different nozzle inserts whose lower face (nozzle exit plane) protruded into the chamber gas (see Fig. 3). The inserts were held in position by sealing and retaining rings and the liquid delivered from the reservoir through a 5/16" diameter passage.

The internal design details of the nozzles inserts employed in the tests are shown in Figure 4. The nozzles used fell into two categories: the converging nozzles, nozzles IV, XI, XII, XIII and XIV (Figure 4a) and the constant diameter tube nozzles, nozzles I, II, III, VI-X (Figure 4b). In Figure 4a the nozzle passage for nozzle IV was made from thin walled shaped glass tubing and the nozzle passage for nozzles XI and XII was made from short lengths of stainless steel hypodermic tubing which were flared at their inlet and glued in the insert to allow the effect of a rounded inlet on the jet breakup process to be explored. For nozzles XIII and XIV the 90° included angle taper within the insert

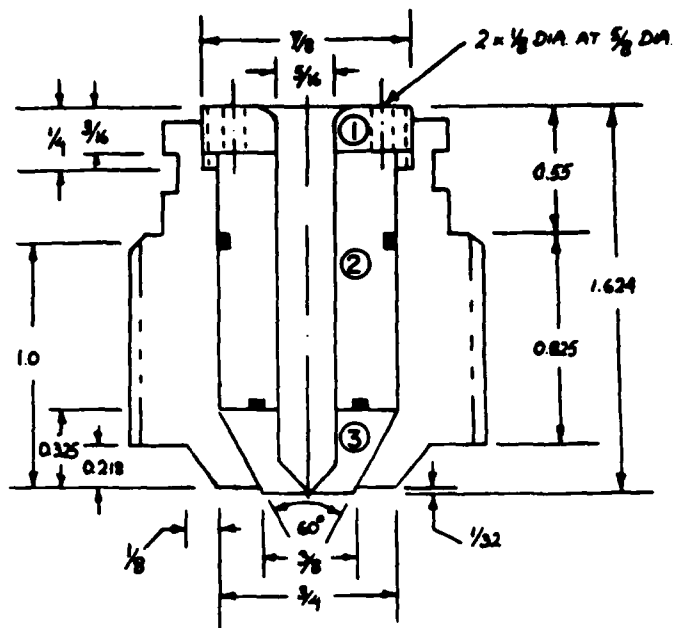


Fig. 3 - Details of nozzle holder: 1. retaining ring; 2. sealing ring; 3. nozzle insert - dimensions in inches

terminated at its apex and in a 0.34 mm diameter hole with  $L/d_0 \approx 0.5$ . The insert was made from plexiglass for nozzle XIII and from brass for nozzle XIV. The nozzle passages of nozzles VI to X are shown in Figure 4b all had the same internal design, that of a sharp edge inlet constant diameter tube with  $L/d_0 \approx 4$ , but differed in materials and method of construction. The nozzle passages VI, VII and VIII were made from plexiglass and teflon, while for nozzle IX the passage was made from stainless steel hypodermic tubing which was glued into a plastic insert. The entire insert was made from brass in the case of nozzles  $X_0$  and  $X_N$ .

For nozzle II, the lower face of the insert was attached to an extension section which contained a length of the hypodermic tubing with  $L/d_0 = 49.3$ . The nozzle passages for nozzles I and III were also made from hypodermic tubing with  $L/d_0 = 85$  and 10.1 respectively. However, for these nozzles, the nozzle holders were machined from brass plugs and the 5/16" diameter delivery passage (compare Figure 3) ended in a radius.

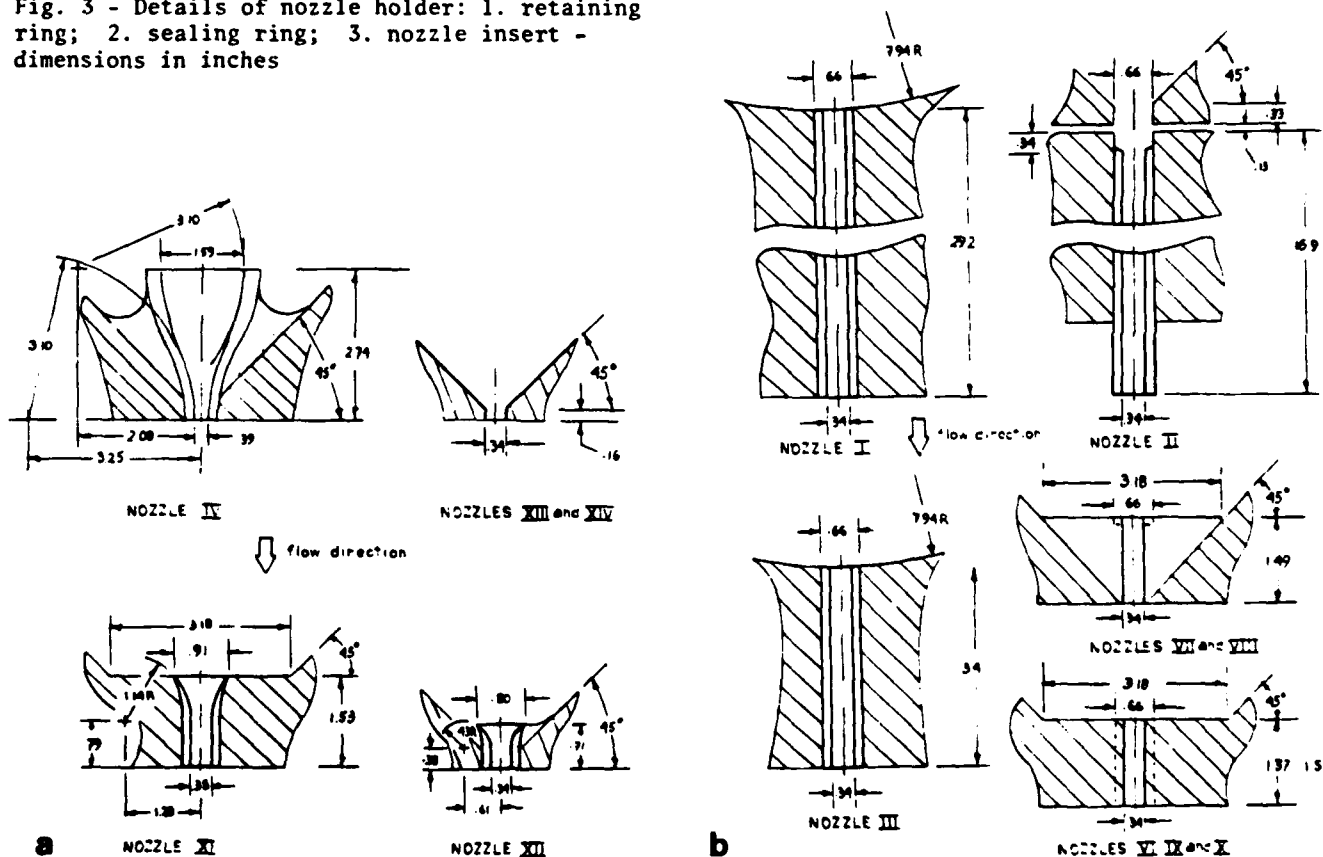


Fig. 4 - Schematic diagram of nozzle passage designs a) Converging nozzles; b) Constant diameter tube nozzles - dimensions in mm

Two methods of initiation of injection were used in the tests. In the first, the nozzle exit hole (nozzle inlet for nozzle II) was blocked by gluing a 0.013 cm thick length of tin fuse ribbon over the hole. The liquid in the liquid reservoir was pressurized to a steady pressure and the fuse metal was then removed in the vicinity of the exit hole by the application of a  $\sim 10 \mu\text{s}$  duration high energy electrical discharge pulse to the fuse. This allowed the constant injection pressure jet to emerge unobstructed into the chamber gas. One such jet is shown in Figure 5 in which a photograph of the fuse hole is also included. It can be seen that the boundary of the hole is clear and sharp.

The second method of injection initiation was used only for tests where the initial transient was not recorded. In this case, the piston above the reservoir liquid was held in place by a retractable trigger pin arrangement. With the driver gas above the piston pressurized to a steady value, removal of the pin caused the piston to compress rapidly the test liquid and, after a short unsteady transient, resulted in a constant pressure injection.

In Figure 6a, the oscilloscope trace shows the liquid pressure during the injection which was monitored using a fast response pressure transducer. It is seen that the injection pressure remained approximately constant at about 1700 psia (113 atm) and the injection duration  $\tau$  was about 3.2 sec. After the injection, the reservoir pressure dropped to the chamber gas pressure of 300 psia (20 atm).

In these tests, a single photograph of the jet was taken long after the initial emergence of the jet, i.e., during the constant pressure portion of the injection. The jet was illuminated by a  $\sim 1 \mu\text{s}$  duration strobe flash and the breakup details recorded on Polaroid film. A fast response photocell was used to monitor the light output as is also shown in Figure 6a.

An oscilloscope trace showing event sequencing and liquid pressure details for the fuse technique of injection initiation is shown in Figure 6b. In this case, the high speed framing camera was used to record the initial emergence of the jet. The Cordin camera consisted of a nitrogen driven turbine with a highly polished rotating mirror and a bank of sixty stationary lenses. The image was reflected from the mirror through each lens, in turn, onto a stationary film strip. The mirror period of rotation,  $M$  (framing rate) was indicated by reference spikes and the film occupied a writing window of 0.24  $M$  as shown in Figure 6b.

The high energy electrical discharge pulse supplied to the fuse ribbon triggered the oscilloscope which, in turn, triggered the simultaneous discharge of two xenon flash

tubes located inside the spray chamber for the illumination of the jet. The duration of this light output, also monitored by a fast response photocell, was adjusted prior to each run to prevent rewrite on the next mirror sweep (see Figure 6b). The liquid pressure during the injection was also displayed on the oscilloscope trace.

In most of the transient tests, the strobe flash and Polaroid camera were also used to obtain a single photograph of the same jet later in the injection, long past its transient as shown, for example, in Figure 5.

#### RANGE AND SCOPE OF EXPERIMENTS

One hundred steady state photographs and 55 transient sets of frames were taken so as to include the operating range of several practical injection systems. The experiments were conducted at 67 different sets of operating conditions, or Series, using the 14 nozzles shown in Figure 4. These designs include nozzles with  $L/d$  ratios from 85 to 0.5 with sharp and rounded inlets and  $d_0 = 0.34 \text{ mm}$ .

The chamber gases were air, nitrogen, helium and xenon with gas pressures up to 600 psia (40 atm) and the tests were made at about 300°K. The liquids tested were mixtures of water and glycerol (0, 50, 68, 80 and 100% glycerol wt.) and their use permitted a thousand-fold range in the liquid viscosity to be realized while the surface tension and liquid density remained with 20% of the values

of water 70 dyne/cm and  $1 \text{ g/cm}^3$  respectively. The liquid pressure ranged from about 500 to 2500 psia (33 to 166 atm) (a fixed value for each test). The test conditions are shown in Table 1. The runs are arranged in groups of tests with each injection nozzle and are organized within each group in order of increasing gas density. The number of tests performed in each series is indicated in the first two columns of the table.

Various quantities were measured from each of the photographs and are also included in Table 1. These include the angle of jet divergence, the spray angle  $\theta_s$ , and the distance from the nozzle exit to the point where the divergence is observed to begin,  $x_1$ . Measurements of the distance from the nozzle exit to the tip of the jet, made from transient pictures such as those of Figure 5, allowed the initial jet tip velocity  $U_T$  to be estimated for each run (Figure 7a). The jet tip velocity was found to be constant in all cases and is also included in Table 1.

The outline of the emerging jet taken from frames at different times after the onset of the injection were superimposed to help visualize the development of the flow field. Here, again, the jet intact length and a jet divergence angle  $\theta_T$  could be measured since

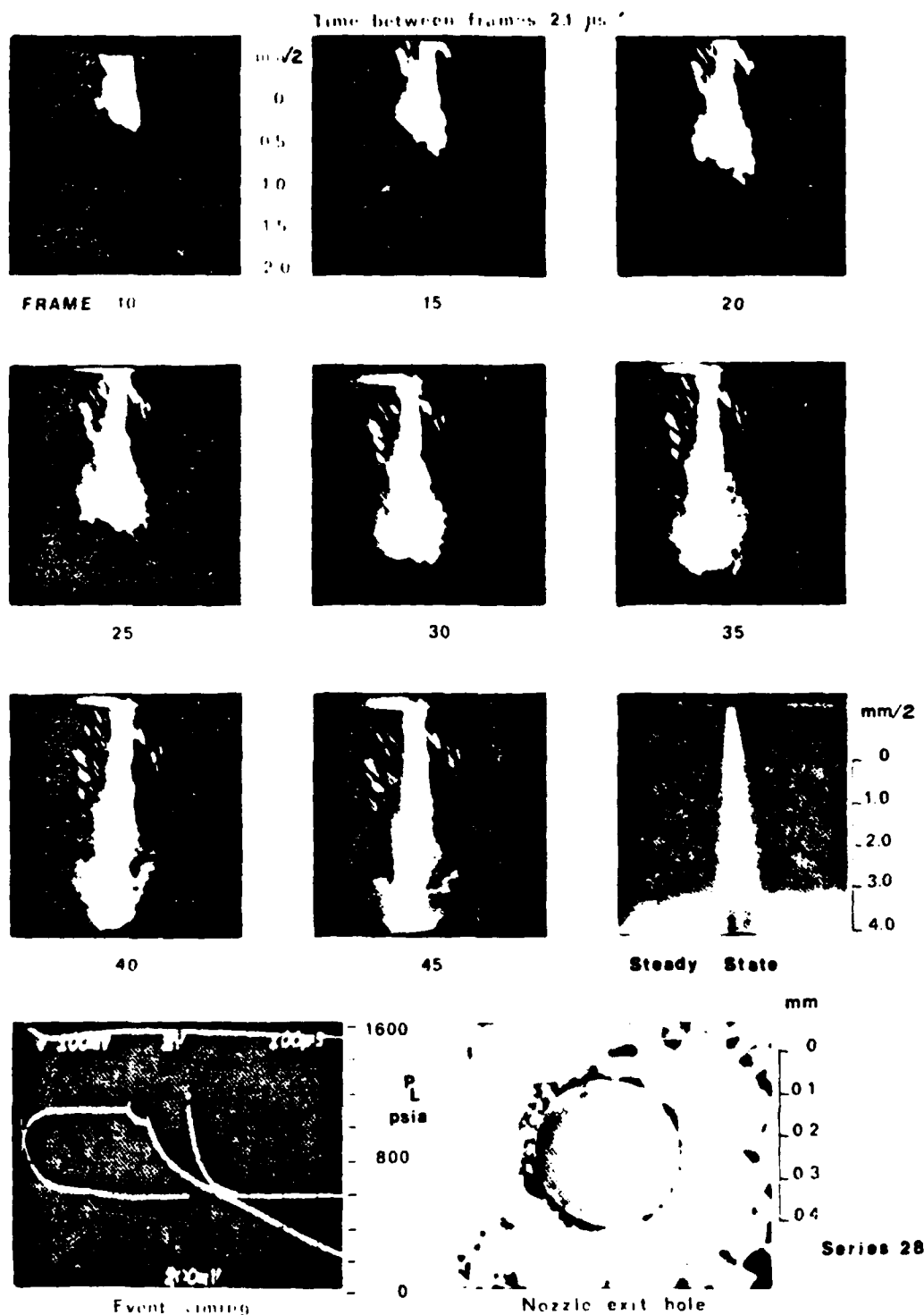
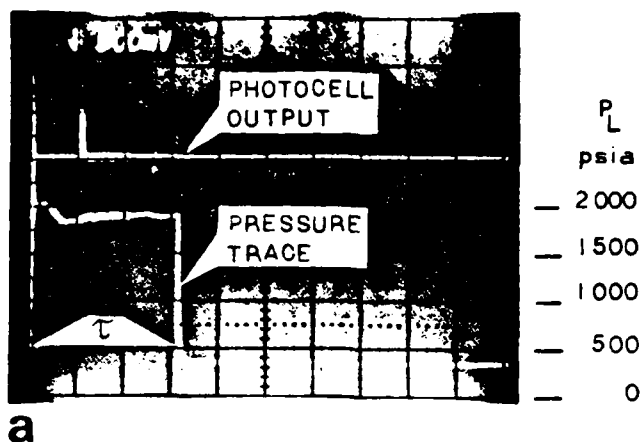
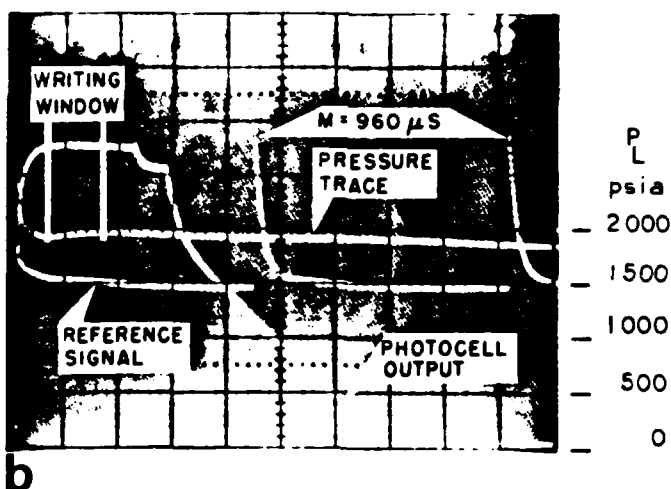


Fig. 5 - Photographs showing initial emergence and steady state jet (Series 28 - Liquid-water, Gas-nitrogen at 200 psia,  $\Delta P = 1600$  psia, Nozzle IX) and nozzle exit hole and event timing oscilloscope trace



a



b

Fig. 6 - a) Oscilloscope trace showing liquid pressure and event illumination sequencing for steady state tests. b) Oscilloscope trace showing liquid pressure and even sequencing details for transient tests

the jet divergence of the region behind the jets head was found to remain constant as the injection continued. This is shown in Figure 7b.

The nozzle coefficient of discharge was determined from the relation

$$C_D = \frac{V}{A_N \tau} \left( \frac{\rho_L}{2\Delta P} \right)^{1/2}$$

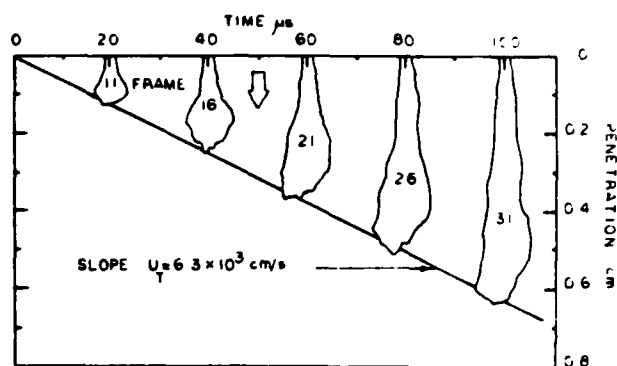
where  $\tau$  is the injection duration (see Figure 6a),  $V$  is the initial volume of the liquid in the reservoir,  $A_N$  is the nozzle exit cross-sectional area, and the liquid has been assumed to be incompressible.

Experiments made with nozzles which had plastic nozzle passages (nozzles VI, VII, VIII and XIII) were usually non-repeatable and their results were not used in deriving the conclusions of this study. Experiments conducted with metal nozzles (nozzles I, II, III, IX, X, XI, XII and XIV) and the glass nozzle IV were found to give consistent results. Most of these repeatable experiments (divergence angles agree within  $2^\circ$ ) were injections with injection pressures above 1500 psia (100 atm). In these tests, dimensions taken from the transient study photographs have an estimated accuracy of  $1^\circ$  for jet divergence angles, 50%  $d_0$  for jet intact lengths and 10% for jet tip velocities. Dimensions taken from the steady state photographs have accuracies of  $0.5^\circ$  for jet divergence angles and 25%  $d_0$  for jet intact lengths. Gas and liquid pressures were constant within 5% during a given test.

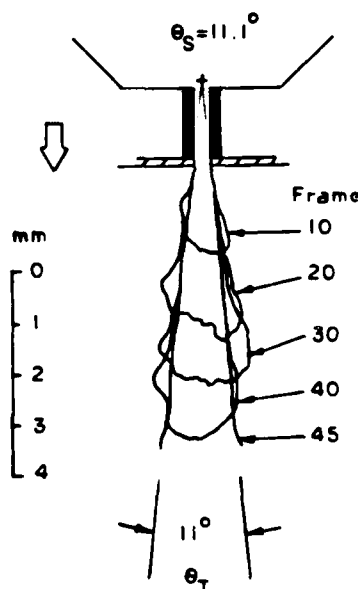
#### EXPERIMENTAL RESULTS

The measured jet divergence or spray angles were found to increase as the chamber gas was isothermally compressed up to a certain level, all other parameters being fixed. An increase in the spray angle with compression of the gas is consistent with the findings of other authors for fuel sprays (12). The results presented in Figure 8 demonstrate the effect of chamber gas compression on the spray angle for tests with the straight-sided converging nozzle XIV ( $L/d_0 \approx 0.5$ , sharp edged inlet nozzle passage) and with the constant diameter tube nozzle IX ( $L/d = 4$ , sharp-edged inlet). The series number is indicated next to each data point and the value of the injection pressure used in each test is also included in the figure (all runs in a given series are made at the same value of the injection pressure, see Table 1). The transient jet divergence angle measurements are indicated by an oblique line through a data point.

The spray angle is seen to increase up to gas pressures of 300 psia (20 atm) or a gas density of  $2.6 \times 10^{-2} \text{ g/cm}^3$ , after which further compression of the chamber gas has a relatively small effect on the jet divergence



(a)



(b)

Fig. 7 - a) Diagram showing transient jet outline penetration versus time. b) Composite diagram of superimposed frames showing transient jet development

for both nozzles. A close agreement between the spray angles measured from the transient and steady state data is also apparent. In addition, the results indicate that the 500 psia (33 atm) variation in the injection pressure ( $\sim 30\%$ ) for nozzle IX does not perceptibly influence the trend with respect to the changes in the gas pressure and density. The use of chamber gases of different molecular weights allowed the gas density and the gas pressure to be varied independently, with relatively minor changes in the physical properties of the gas. These experiments showed that the chamber gas density has a



[illegible]

**Table 1 - Sixty-seven Operating Conditions Employed in the Experiments**

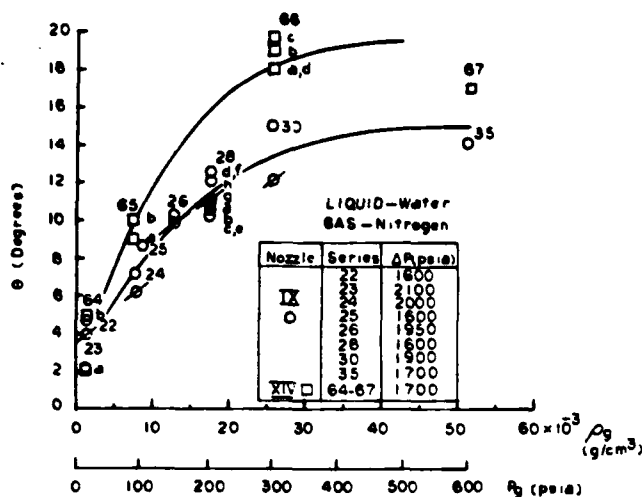


Fig. 8 - Graph showing effect of chamber gas compression on the spray angle for nozzles IX and XIV

predominant effect on the jet divergence angle for these tests, and that increases in jet divergence angle obtained by isothermally compressing the chamber gas in tests with a given nozzle are due to effects related to the increase in chamber gas density and not to those related to the increased chamber gas pressure (2).

Accordingly, the spray angle data of Figure 8 is shown plotted against the gas density in Figure 9. In this figure, an average value of the spray angle is plotted for repeated tests at the same operating conditions (series). The results of injections from nozzles XII, III, II and I are also included in the figure. These results confirm the increase in the spray angle with increasing gas density. The range of measured injection velocity for tests with a given nozzle is included in the figure. The open data points correspond to jets whose divergence is observed to begin at the nozzle exit. These jets may thus be classified as belonging to the Atomization Regime. The solid data points represent those runs where jet divergence was found to begin some distance from the nozzle exit. These jets thus belong to the Second Wind-Induced regime of breakup.

From this figure, it is apparent that, for a given nozzle, atomization occurs once the density of the chamber gas is increased beyond a certain level. Moreover, there is no evidence of an abrupt change in the spray angle between the Second Wind-Induced and Atomization breakup regimes. However, the transition is seen to occur at different chamber gas densities for different nozzles.

The experiments conducted using mixtures of water and glycerol as the test liquid allowed the effect of liquid viscosity on the

behavior of the jet to be explored with <20% changes in the liquid surface tension and density. The measured jet divergence angles are shown in Figure 10 plotted against a normalized liquid viscosity ratio  $\mu_L/\mu_{H_2O}$ . The open data points correspond to jets whose divergence begins at the nozzle exit plane, i.e., jets operating in the Atomization regime, while the solid data points represent jets whose divergence begins some distance downstream of the nozzle. These correspond to jets operating in the Second Wind-Induced regime of breakup.

The results of tests with nozzle IX ( $L/d_0 = 4$ , sharp-edged inlet) and with injection pressures of  $1750 \pm 150$  psia ( $117 \pm 10$  atm) reveal that the jet divergence angle decreases slightly as the liquid viscosity is increased from the value of water to  $\mu_L = 18.4 \mu_{H_2O}$  (the 68% glycerol and 32% water mixture Series 32). Beyond this point (Series 33 and 34) intact jets were obtained with no sign of jet breakup or divergence detected in the photographs.

Tests with nozzle XII ( $L/d_0 = 2.1$ , rounded inlet) and with injection pressures of  $1800 \pm 100$  psia ( $120 \pm 7$  atm) (Series 52-54), also shown in Figure 10, indicate again that intact, non diverging jets are obtained once the liquid viscosity is increased beyond a certain level. Injections from nozzle I ( $L/d_0 = 85$ , constant diameter tube nozzle) with injection pressures of 2100 psia (140 atm), Series 2 and 1800 psia (120 atm), Series 3, are also shown in Figure 10. Here no significant change in the jet divergence angle with increased liquid viscosity is detected for this nozzle in the range tested. The measured ranges of injection velocities  $U_{vol}$  for each nozzle are also given in Figure 10.

The results of Figure 10 indicate that, for a given nozzle, jet Atomization occurs when the liquid viscosity is reduced below a certain level and there is no evidence of an abrupt change in jet divergence angle accompanying the transition from the Second Wind-Induced to the Atomization breakup regimes. In addition, the results indicate that the transition occurs at different levels of liquid viscosity for each nozzle. The data of Figures 9 and 10 show obvious differences in the performance of jets injected from nozzles of different geometry. The effect of variations in nozzle design is further demonstrated in Figure 11. The four photographs show the steady state behavior of four water jets injected from four different nozzles, but with otherwise identical operating conditions.

The jet shown in Figure 11a was injected from nozzle I ( $L/d_0 = 85$ ) and the jet divergence is minimal. This photograph, as in the photographs of Figures 11b and 11d, was taken with backlighting of the jet long after the initiation of injection.

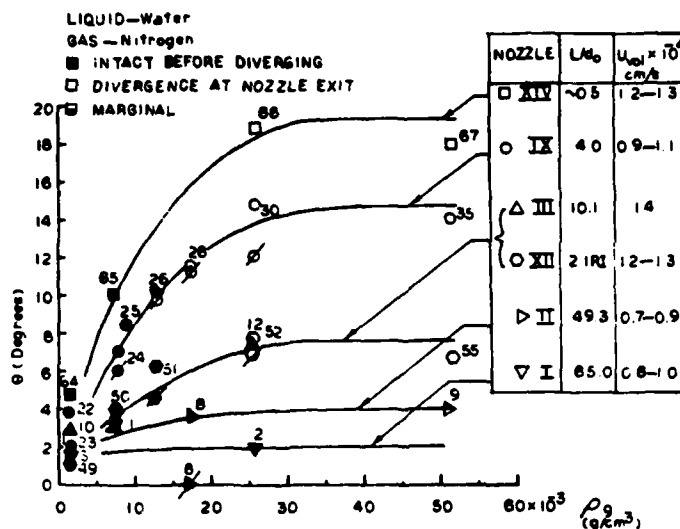


Fig. 9 - Graph showing effect of gas density on the spray angle and jet intact length for nozzles XIV, IX, III, XII, II and I

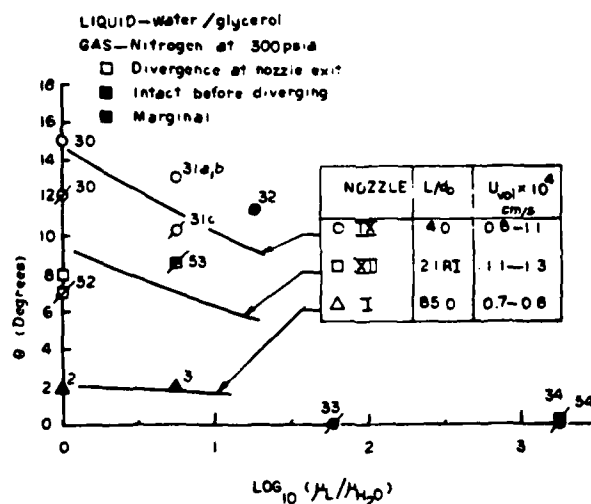


Fig. 10 - Graph showing effect of liquid viscosity on spray angle and jet intact length for nozzles IX, XII and I

The jet of Figure 11b was injected from nozzle III ( $L/d_0 = 10$ ) and larger divergence is observed. The photographs shown in Figure 11c was taken with a combination of front and backlighting. The nozzle used in this test was nozzle IX ( $L/d_0 = 4$ ). The jet is seen to have a similar overall appearance to that of the jet in Figure 11b but a larger angle of divergence. The photograph does show evidence of finely atomized particles and of divergence starting at the nozzle exit.

Finally, the jet shown in Figure 11d was injected from nozzle XIV ( $L/d_0 < 0.5$ ). Here a substantial divergence of the jet is seen to be present and to start immediately at the exit of the nozzle.

The photographic results of Figure 11 demonstrate that the nozzle passage length for these sharp-edged inlet nozzles has a large effect on the behavior of the liquid jet. In particular, the spray angle is seen to decrease as the nozzle passage length is

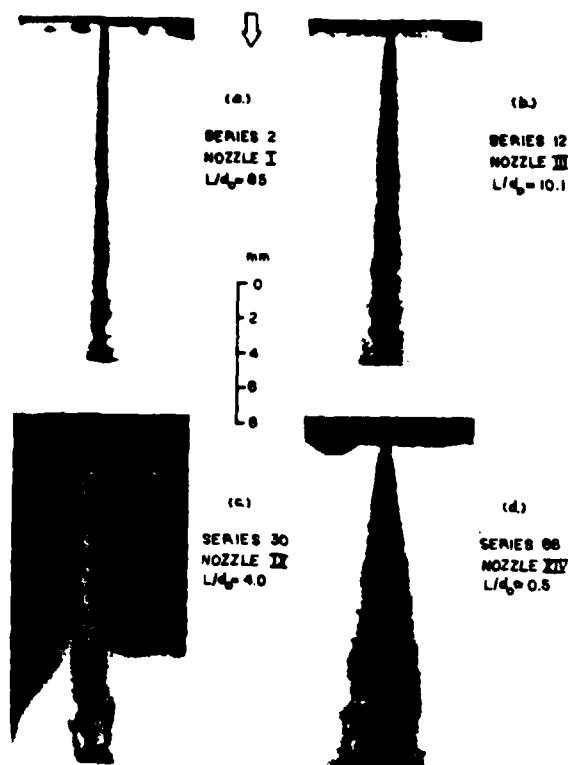


Fig. 11 - Photographs showing effect of nozzle passage length on steady state jet breakup - chamber gas-nitrogen at 300 psia,  $\Delta P \approx 1800$  psia, liquid-water

increased for these operating conditions. This trend is also apparent from the measured spray angles shown in Figures 8, 9 and 10. The effect of the design of the nozzle entrance is also shown in Figure 9. A comparison between the results of the rounded inlet nozzle XII ( $L/d_0 = 2.1$ ) and the sharp-edged inlet nozzle III ( $L/d_0 = 10.1$ ) reveals that those two nozzles have similar jet divergence angles in spite of the factor of 5 difference in the nozzle passage length. These results show that the effect of a rounded nozzle passage inlet on the jet is to stabilize the flow. Notice from the  $U_{vol}$  data presented in Figures 9 and 10 that there is no detectable consistent trend linking changes in the injection velocities to the performance of the various nozzles. This indicates that the observed trends in the jet divergence angles and the jet intact lengths, seen as the nozzle is changed, are due to effects over and above the changes in the injection velocity caused by coefficient of discharge variations.

The results of Figures 9 and 10 show that the transition between the Secon Wind-Induced and Atomization breakup regimes occurs at different gas density and liquid viscosity levels for each of the nozzles tested. In particular, the transition is seen to occur at higher gas density levels and lower liquid viscosity levels for those nozzles which produce jets with small jet divergence angles than for those nozzles which produce flows with consistently large spray angles. Therefore, any criterion used to predict the onset of jet atomization must include the details of the nozzle design. In particular, the criterion of Miesse (13) that  $We_g > 40.3$  for the onset of atomization is seen to be deficient since it does not include details of the nozzle design beyond the nozzle exit diameter.

#### DISCUSSION OF JET ATOMIZATION MECHANISM

An evaluation of the prominent jet atomization hypotheses was made using the experimental results and this revealed that most of

them, alone, could not explain the experimental results. The findings of this evaluation are presented in more detail in Reitz and Bracco (2) and are briefly summarized here:

1. If aerodynamic surface wave growth were the only mechanism controlling the jet divergence, the results should be independent of the nozzle geometry;
2. If pipe turbulence were the only controlling breakup agency, turbulent jets (from nozzles with large  $L/d_o$  ratios) should be the most unstable ones;
3. If the rearrangement of the cross-section axial velocity profile of the jet was the only mechanism of breakup, Poiseuille flows (high viscosity jets) should be the most unstable;
4. If the liquid supply pressure oscillations were the only agency, jet atomization should not have occurred in these experiments in which the supply pressure was kept constant;
5. If wall boundary layer exit velocity profile relaxation effects were the only mechanism, the jet breakup phenomena should be independent of the gas density.

Cavitation effects, alone, could possibly account for the observed trends in the Atomization regime if it is assumed that the mechanism of breakup changes from the Second Wind-Induced to the Atomization regimes. However, there is no evidence in the experimental results of such a discontinuity, but, instead, the results show a continuity in the jet divergence angle as the jet intact length tends to zero, i.e., as atomization is reached (see, for example, Figure 9). But it is still possible that liquid cavitation is the only agency controlling jet Atomization. It is also possible that jet Atomization is due to aerodynamic surface wave growth effects augmented by cavitation and/or wall boundary layer readjustment phenomena.

The aerodynamic surface wave growth mechanism is known to be responsible for the breakup of jets in the Second Wind-Induced regime and the fact that no discontinuity was detected when Atomization occurred suggests a continuity in breakup mechanism between the two regimes. An analysis of this possibility, which is presented in detail in Reitz and Bracco (2,14), shows that equations derived from the aerodynamic surface wave growth mechanism can reproduce the experimentally observed trends of gas density and liquid viscosity variations on the spray angle, and the insensitivity of the spray angle to relatively large variations in the jet velocity in the Atomization regime, if an additional mechanism is invoked to account for the effects of nozzle geometry. According to the aerodynamic surface wavetheory of jet breakup of Ranz (7), the spray angle is given by

$$\tan \theta/2 = \frac{1}{A} 4\pi \left( \frac{\rho_g}{\rho_L} \right)^{1/2} f \left( \frac{\rho_L}{\rho_g} \frac{Re_L}{We_L} \right)^2 \quad (1)$$

where the constant A must be obtained from a best fit of experimental data. Function (1) is plotted in Figure 12. The data shown previously in Figure 9 and 10 are compared with the prediction of Equation (1) in Figures 13 and 14. Here it is seen that agreement with the theoretical prediction can be maintained up to gas density levels of  $2.58 \times 10^{-2} \text{ g/cm}^3$  and liquid viscosities below about 0.2 g/cms provided that the constant A is permitted to be changed for each different nozzle.

In Reitz and Bracco (2), liquid cavitation and/or wall boundary layer rearrangement phenomena are introduced as possible agencies which could account for the required variation in the proportionality constant with nozzle geometry. Notice from Figure 13 that the flow cavitation number

$$K = \frac{P - P_v}{\rho_L \frac{V^2}{2g}}$$

which is included on the abscissa, is always greater than the critical cavitation numbers  $K_{crit}$  which were not measured in our experiments but could be estimated for the conditions of the present tests for nozzles XIV, IX and III from the data of Bergwerk (10). This indicates that cavitation phenomena are predicted to be present within each of these nozzles and it also may be significant that  $K_{crit}$  correlates with the value of the constant A.

Notice that these conclusions on the mechanism of jet Atomization were arrived at by varying  $\rho_g$ ,  $\rho_L$ ,  $P_L$ ,  $\mu_L$  and the nozzle geometry, but  $d_o$ ,  $\sigma$ ,  $\rho_L$  and the test environment temperature were not varied. Their variation may necessitate consideration of other effects in the Atomization mechanism. Indeed, had the nozzle geometry not been varied in these experiments, one could have concluded that the aerodynamic surface wave growth model, alone, was sufficient to explain the experimental results.

#### SOME APPLICATIONS OF THE RESULTS

Some applications considered in this section are single hole high pressure fuel injection systems and multiple hole (shower head) fuel injection nozzles if the holes are so apart from each other and so oriented as to minimize their interactions in the vicinity of the hole exits.

The effect of gas and liquid temperature changes on the jet atomization process may be important but was not studied in this work. This should be considered when using the results of the study for automotive and combustion applications, in which case the nozzle itself may be at a high temperature. However, according to Equation (1) the spray

angle should be insensitive to gas temperature changes for

$$\frac{\rho_L}{\rho_g} \left( \frac{Re_L}{We_L} \right)^2 > 1.$$

The other operating conditions varied in the present experiments do include those ranges commonly found in automotive applications. Standard diesel type injectors usually operate with injection pressures in the range 1500-4000 psia (100-260 atm) and gas densities between  $13 \times 10^{-3}$  to  $26 \times 10^{-3}$  g/cm<sup>3</sup> (C.R. 10-20) using constant diameter tube nozzles with  $L/d_o$  ratios from 2-6 and nozzle exit diameters in the range 0.015 - 0.05 cm (single hole and shower head nozzle designs). The liquids employed range from distillate fuels ( $\mu_L \approx 0.01$  g/cms) to residual fuels ( $\mu_L \approx 5$  g/cms) (values at 300°K) with liquid densities from 0.8 - 1.0 g/cm<sup>3</sup> and surface tension of about 25 dyne/cm (at 300°K).

The present study was performed with injection pressures from 1500-2100 psia (100-140 atm), gas densities from  $1.3 \times 10^{-3}$  to  $52 \times 10^{-3}$  g/cm<sup>3</sup>, constant diameter tube nozzles with  $L/d_o$  ratios of 0.5 to 85 and  $d_o = 0.034$  cm. The liquid viscosity varied from 0.01 g/cms to 17 g/cms; liquid density from 1.0 - 1.2 g/cm<sup>3</sup> and the surface tension was about 70 dyne/cm (at 300°K).

In the design of fuel injection systems, jet atomization is encouraged in order to increase mass transfer rates and to ensure efficient utilization of the injected fuel. In this case, one of the parameters of interest to the designer is the spray angle  $\theta$  which influences the extent of distribution of the fuel within the combustion chamber. The results of the present work show that this can be increased by increasing the chamber gas density (up to about  $2.6 \times 10^{-2}$  g/cm<sup>3</sup>) or reducing the liquid viscosity and by employing injection nozzles with  $L/d_o$  ratios between 0.5 and 4.0 and with sharp-edge inlets.

Abramowitz (15) and Newman and Brzustowski (16) argued that the divergence of the jet in the region at the nozzle exit may be estimated from a postulated similarity between a single phase injection of a turbulent jet of high density gas into a low density environment and the two phase liquid injection. In this case the spray angle is given by

$$\tan \theta/2 = 0.13 \left( 1 + \frac{\rho_g}{\rho_L} \right) \quad (2)$$

This equation is shown in Figure 15 together with the experimental results of nozzles I, II, III, IX, XII and XIV which were presented earlier in Figure 9. The

equation significantly overpredicts the jet spray angle for all nozzles at low chamber gas densities. In addition, Equation (2) does not allow the observed variation in the jet divergence angle, at a fixed gas density level but with different nozzles, to be predicted, since the gas jet turbulent mixing process is insensitive to changes in the internal geometry of the nozzle (16). The results of Figure 15 show that the commonly used "gas jet" estimate of the jet divergence angle cannot be used to predict the spray angle under most conditions. Instead, the aerodynamic theory prediction, Equation (1), should be used to estimate the spray angle. The constant A could be determined from the empirical formula

$$A = 3.0 + \frac{L/d_o}{3.6}$$

for sharp-edge inlet nozzles and for the operating conditions included by the present study.

In combustion applications, changes in the nozzle inlet geometry during operation produced mainly by cavitation could cause changes in the performance of the nozzle. Indeed, it is known that injection nozzles in oil burners and diesel engines need replacement after long periods of use because smoke emissions tend to increase. This need could be related to the increased jet stability (smaller dispersion) noticed in the present study for rounded inlet nozzles.

The penetration of the jet is also of interest to designers of fuel injection systems since it affects the extent of distribution of the fuel within the combustion chamber. Previous spray tip penetration measurements, reported, for example, in Giffen and Muraszew (12) and usually made from photographs with frame rates up to about  $5 \times 10^3$  frame/s, show that the spray tip penetration distance increases roughly proportionally to  $t^{1/2}$  for diesel fuel sprays in the range of distance of 200 to 1000  $d_o$  from the nozzle exit. The spray tip velocity is found to decrease rapidly ( $\propto t^{-1/2}$ ) with distance from the nozzle and is a small fraction of the injection velocity within the first few milliseconds from the start of the injection.

In the present transient jet breakup studies, the behavior of the jet was monitored up to about 20 nozzle exit diameters downstream of the nozzle exit (0.7 cm) for times less than a millisecond from the start of injection. The results show that the jet tip velocity is equal to the injection velocity for injections into a low gas density environment (see Table 1). For injections into environments at high gas densities (up to  $\rho_g = 2.6 \times 10^{-2}$  g/cm<sup>3</sup>) the jet tip velocity was found to be still constant but was less than

the injection velocity by as much as a factor of two. In spite of this reduction in velocity, the jet tip velocity is still much larger than characteristic gas velocities in engine applications. Therefore, the bulk motion of the gas (naturally occurring or induced, e.g., through swirl) can be expected to have an insignificant effect on the trajectory and the motion of the jet during this time. This result also has implications in the design of open chamber stratified charge engine combustion chambers. Hiroyasu (17) has found a change from linear to a square root penetration time dependence as the jet penetrates the chamber gas and this is consistent with the results of the present study.

In practical diesel injectors, the injection pressure is known to vary with time during the injection. Typical characteristic times for pressure variations are of the order of 100  $\mu$ s. The results presented in Figures 7b, 8, 9 and 10 showed that the steady and transient jet divergence angles  $\theta_S$  and  $\theta_T$  were quantitatively similar at the same operating conditions. The rapidity with which the region behind the emerging jets head, seen in the transient frames, approached its final jet divergence was discussed earlier and was illustrated in Figure 7b. From these results (Figure 7b) it can be seen that the final configuration is set up within a time no longer than that required for the tip of the jet to travel a distance of 3 to 7 nozzle exit diameters. For the jet tip velocities explored in this study, this shows that the final jet divergence is established in times less than 10 to 30  $\mu$ s. It follows that, if liquid supply pressure changes occur on time scales much longer than 10 to 30  $\mu$ s, the behavior of the jet at the nozzle exit will depend only on the corresponding, instantaneous upstream pressure.

Another parameter of importance to the fuel injection system designer is a measure of the average droplet size. This influences fuel vaporization times and pollutant emission levels and, in diesel combustion, the combustion rate. Although droplet sizes (distributions) were not measured in the present work, if the jet breakup process is assumed to be produced by the aerodynamically induced growth of surface waves in the range tested, then the results of Taylor (18) may be used to assess the effect of changes in the operating conditions on the average initial droplet size. In this analysis, the diameter of the recently formed droplet,  $2r$ , is assumed to be proportional to the wave length of the unstable surface wave from which it was formed, i.e.,

$$2r = \frac{4\pi B_1 \sigma x_m}{\rho_g U_o^2}$$

where  $B_1$  is a constant of order 1 and  $x_m$  is a dimensionless wave length which decreases with increasing

$$\frac{\rho_L}{\rho_g} \left( \frac{Re_L}{We_L} \right)^2$$

For

$$\frac{\rho_L}{\rho_g} \left( \frac{Re_L}{We_L} \right)^2 > 1,$$

$x_m$  is asymptotically equal to  $\frac{3}{2}$ .

It must be stressed that droplet sizes were not measured in this study, and that the given equation is, therefore, only an extension which is consistent with the aerodynamic hypothesis for the break up process. Notice that the predicted initial drop size would be insensitive to nozzle design changes. Nozzle design effects appear in Equation (1) for the spray angle since they would influence the surface wave growth rate but not necessarily the length of the most unstable of the surface waves which would be proportional to the average drop size. The length of the intact core of the jet is of interest in modeling that region of the spray close to the nozzle exit. Again, this was not measured in the present study but the length of the continuous liquid core of the jet may also be estimated from Taylor's (18) calculation of the rate at which liquid droplets remove mass from the liquid jet.

The length of the solid core of the jet,  $x_B$ , would then be given by

$$\frac{x_B}{d_o} = B_2 \sqrt{\frac{\rho_L}{\rho_g}} \cdot f \left( \frac{\rho_L}{\rho_g} \left( \frac{Re_L}{We_L} \right)^2 \right) \quad (3)$$

where the function  $f$  is shown in Figure 12 and  $B_2$  is a proportionality constant. It was found that Equation (3) could also be used to predict those operating conditions at which divergence commences at the nozzle exit, i.e., the boundary between the Atomization and Second Wind-Induced regimes, for the conditions of the present study. Here it was assumed that  $x_1 = 0$  corresponds to a critical value of  $x_B$ .

With this postulate, the criterion for the onset of jet Atomization from Equation (3) is

$$\sqrt{\frac{\rho_L}{\rho_g}} \leq k \text{ for } \frac{\rho_L}{\rho_g} \left( \frac{Re_L}{We_L} \right)^2 > 1 \quad (4)$$

and

$$\left( \frac{\rho_L}{\rho_g} \frac{We_L}{Re_L} \right)^{1/3} \leq k \text{ for } \frac{\rho_L}{\rho_g} \left( \frac{Re_L}{We_L} \right)^2 \rightarrow 0 \quad (5)$$

These formulae incorporate the effect of gas density and liquid viscosity and the effect of nozzle design changes may be included by

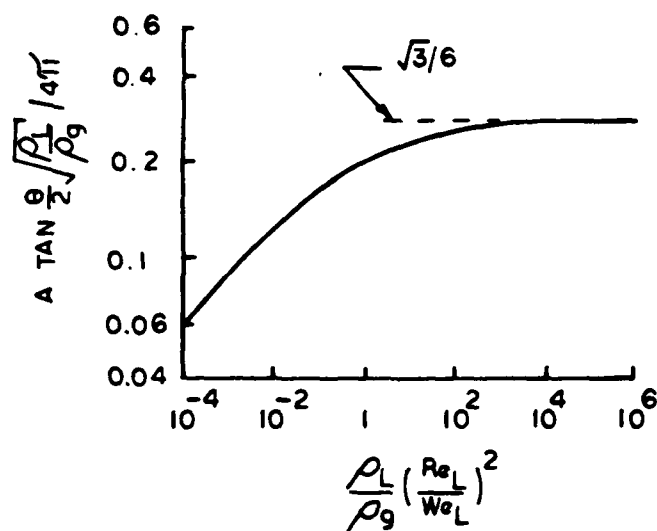


Fig. 12 - Theoretical dependence of the spray angle on the operating conditions for aerodynamic model of breakup, Equation (1)

allowing the constant  $k$  to vary with the different nozzles used. The empirical result  $k = 18.3/\sqrt{A}$  can be used to relate  $k$  to the constant  $A$  (see Table 2) for a particular nozzle. However, it is possible that  $k=k(U_0)$  as well. This was not determined in the present work but for fuel injection applications the injection velocities are similar to those of this study.

Equation (4) is shown in Figure 13 together with the experimental results of tests with nozzles I, II, III, IX, XII and XIV. The equation is seen to allow the location of the regime boundary to be represented satisfactorily for the conditions of that figure. For standard fuel injection applications of distillate fuels the design criterion to ensure jet atomization would be

$$\sqrt{\frac{\rho_L}{\rho_g}} < k$$

since in such applications it is often verified

that

$$\frac{\rho_L}{\rho_g} \left( \frac{Re_L}{We_L} \right)^2 > 1$$

However, for high viscosity fuels, where

$$\frac{\rho_L}{\rho_g} \left( \frac{Re_L}{We_L} \right)^2 < 1,$$

an alternate condition that could be used is that of Equation (5).

This equation is shown in Figure 14 for the conditions of the data in that figure and is seen to represent the location of the regime

Table 2 - Values of the Constants  $A$ ,  $K_{crit}$  and  $k$  for the Nozzles and the Range Tested

Nozzle	$L/d_o$	$A$	$K_{crit}$	$k$
I	85.0	28	---	3.45
II	49.3	13.4	---	4.99
III	10.1	8.0	2.8	6.46
IV	7*	4.1	---	9.02
VI	4.4	(-)	1.9	(-)
VII	4.3	(3.5)	1.9	(9.76)
VIII	4.3	(4.5)	1.9	(8.61)
IX	4.0	3.9	1.9	9.25
$X_N$	4.0	3.5	1.9	10.2
$X_O$	4.0	3.2	1.9	11.5
XI	4.3*	8.5	---	6.26
XII	2.1*	6.4	---	7.22
XIII	0.5	(4.1)	1.0	(9.02)
XIV	0.5	3.1	1.0	10.37

#### NOTES:

(-) Uncertain Values, Plastic nozzle passages.

\* Contoured

+ Rounded inlet

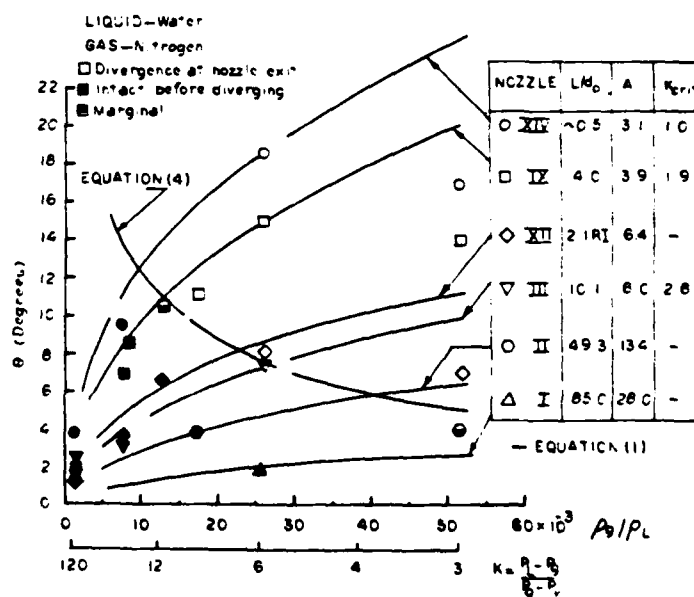


Fig. 13 - Graph of spray angle versus flow cavitation number and gas-liquid density ratio with theoretically predicted dependence, Equation (1)



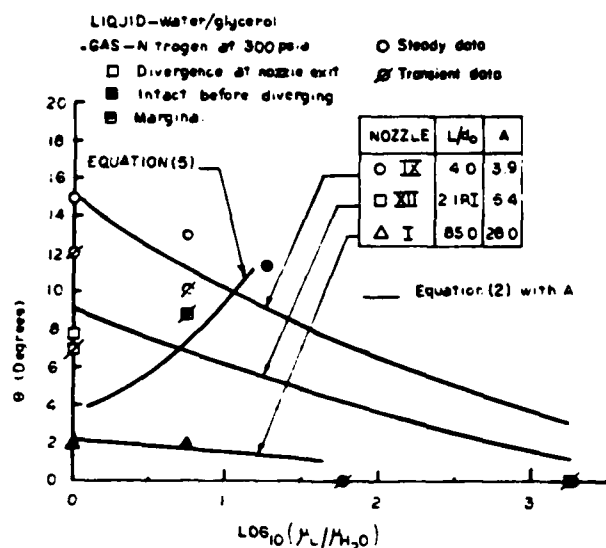


Fig. 14 - Graph of spray angle versus normalized liquid viscosity ratio with theoretically predicted dependence, Equation (1)

boundary with respect to changes in liquid viscosity, and to ensure jet atomization, in this case,

$$\left( \frac{\rho_L}{\rho_g} \frac{We_L}{Re_L} \right)^{1/3} < k.$$

The reader is reminded again that the above conclusions were reached by experiments in which the parameters were varied within specific, identified ranges. Extrapolation of the conclusions outside the tested ranges are difficult due to the complexity of the process.

#### SUMMARY

The Atomization of liquid jets influences combustion in direct injection stratified charge and diesel engines. At present, empiricism prevails in dealing with Atomization since the forces which control the breakup of liquid jets in this regime are unknown. In this study of the mechanism of Atomization, two photographic techniques were used to record the transient and steady behavior of high speed liquid jets in various gases. The transient behavior was recorded by a Cordin ultra high speed camera capable of up to  $10^6$  frames/second and the steady one by a technique similar to standard spark photography. The two techniques were often applied to the same jet. Except for temperature, which was kept at room value, the ranges of the experimental variable included those of practical interest. Constant liquid injection pressures from 500 psia (33 atm) to 2500 psia (166 atm) were employed with five mixtures of water and glycerol to vary the liquid viscosity. Air,

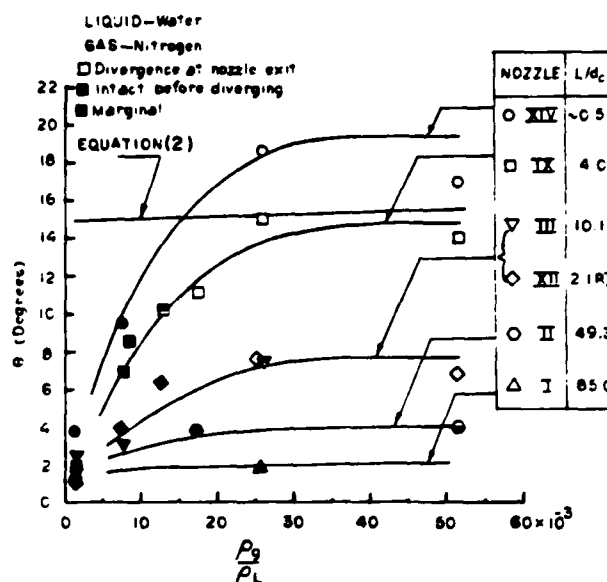


Fig. 15 - Single phase "gas jet" divergence angle, Equation (2), compared with the results of nozzles I, II, III, IX, XII and XIV

nitrogen, helium and xenon were used as chamber gases to separate gas pressure from gas density effects at pressures up to 600 psia (40 atm). The fourteen nozzle designs studied, all with an exit diameter of about 340  $\mu$ , include nozzles with length-to-diameter ratios from 85 to 0.5, and with sharp and rounded inlets. The quantities measured from the photographs include the jet diameter at the nozzle exit, the spray angle, the jet intact length, and the tip penetration rate.

The following trends were thus established within the tested range: 1. Jet divergence angles increase with increasing (isothermal) chamber gas compression; 2. Jet divergence begins progressively closer to the nozzle exit as the chamber gas is compressed, until it reaches the exit with no evidence of abrupt change; 3. These variations are due to effects related to increases in the gas density, not the gas pressure; 4. Jet divergence angles decrease with increasing liquid viscosity; 5. Jet divergence begins at the nozzle exit once the liquid viscosity is decreased below a certain level and there is no evidence of abrupt change; 6. Jet divergence angles decrease with increasing nozzle tube length; 7. For the same length rounded inlet nozzles produce less divergent jets than sharp edged inlet nozzles; 8. Jet divergence commences at the nozzle exit at different gas density and liquid viscosity levels as the nozzle design is changed; 9. The jet divergence angle and the jet intact length is quasi-steady with respect to changes in the operating conditions which occur on time scales greater than 10 to 30  $\mu$ s; 10. Relatively large variations in the injection

velocity (or injection pressure) have no detectable influence on the observed trends.

An evaluation of prominent jet Atomization hypotheses revealed that aerodynamic effects, liquid turbulence, jet velocity profile rearrangement effects and liquid supply pressure oscillations each could not alone explain the experimental results. It is possible that cavitation phenomena alone, or aerodynamic effects, supplemented by liquid cavitation and/or wall boundary layer velocity profile relaxation effects, combine to control the disruption of the jet in the Atomization regime. Some of the more practical applications of the results include the initial penetration of the jet in the region up to 0.7 cm from the nozzle exit, the effects of deterioration of the nozzle during its operation and the effect of liquid supply pressure variations. The criterion  $We_g > 40.3$  for the onset of atomization and the use of a gas jet correlation to predict the spray angle were shown to be inadequate and equations were presented for the prediction of the spray angle and of the onset of jet atomization in terms of the operating conditions. These equations are not claimed to be valid outside of the range of our experiments.

#### NOMENCLATURE

A	Dimensionless nozzle constant in Eq.(1)
$A_N$	Nozzle exit cross-sectional area
$B_{1,2}$	Proportionality constants
$C_D$	Nozzle coefficient of discharge = $U_o \left( \frac{\rho_L}{2\Delta P} \right)^{1/2}$
d	Jet diameter at the nozzle exit
$d_o$	Nozzle exit diameter
f	Function of $\frac{\rho_L}{\rho_g} \left( \frac{Re_L}{We_L} \right)^2$ shown in Figure 12
k	Nozzle regime boundary constant in Equations (4) and (5)
K	Flow cavitation number $\frac{P_L - P_g}{P_g - P_v}$
$K_{crit}$	Critical cavitation number. For $K < K_{crit}$ cavitation does not occur
L	Nozzle passage length
M	Framing camera mirror period of rotation
P	Pressure
$P_v$	Liquid vapor pressure
r	Droplet radius
Re	Reynolds number $\rho U_o d_o / \mu$
$U_o$	Jet average velocity over nozzle exit cross-section

$U_{vol}$	Measured injection velocity = $V/A_N T = U_o$
$U_T$	Transient jet tip velocity
V	Liquid reservoir initial volume
We	Weber number $\rho U_o^2 d_o / \sigma$
$x_B$	Distance from nozzle exit where liquid jet is no longer continuous (breakup length)
$x_I$	Distance from nozzle exit to point of jet divergence (intact length)
$x_m$	Wave length parameter $\lambda \rho U_o^2 / 2\pi \sigma$
$\Delta P$	Effective injection pressure $P_L - P_g$
$\theta$	Jet divergence or spray angle
$\lambda$	Surface wave wavelength
$\mu$	Viscosity
$\rho$	Fluid density
$\sigma$	Surface tension
$\tau$	Injection duration
Subscripts	
g	Based on gas properties
L	Based on liquid properties
S	Steady state value
T	Transient value

#### ACKNOWLEDGEMENTS

This work was supported under grants NSF-RANN AER75-09538 and DAAG 29-77-G-0146 of the Army Research Office.

#### REFERENCES

- Reitz, R. D. and Bracco, F. V., "Studies Toward Optimal Charge Stratification in a Rotary Engine," Combustion Science and Technology, Vol. 12, p. 63, 1976.
- Reitz, R. D. and Bracco, F. V., "On the Mechanism of Atomization of a Liquid Jet," submitted for publication to J. Fluid Mech., 1978.
- Reitz, R. D., Ph.D. Thesis, 1375, MAE Dept., Princeton University, 1978.
- Reitz, R. D. and Bracco, F. V., "Review-Atomization and Other Breakup Regimes of a Single Liquid Jet," submitted for publication to J. Fluids Eng., 1978.
- Lee, D. W. and Spencer, R. C., "Photomicrographic Studies of Fuel Sprays," NACA TR, 454, 1933.

6. Castleman, R. A., "Mechanism of Atomization of Liquids," U.S. Nat'l. Bureau of Std., J. Res., Vol. 6, p. 281, 1931.
7. Ranz, W. E., "Some Experiments on Orifice Sprays," Canad. J. Chem. Engng. Vol. 36, p. 175, 1958.
8. DeJuhasz, K. J. "Dispersion of Sprays in Solid Injection Oil Engines," Trans. ASME (OGP), Vol. 53, p. 65, 1931.
9. Schweitzer, P. H., "Mechanism of Disintegration of Liquid Jets," J. Applied Physics, Vol. 8, p. 513, 1937.
10. Bergwerk, W., "Flow Pattern in Diesel Nozzle Spray Holes," Proc. Instn. Mech. Engrs. Vol. 173, p. 655, 1959.
11. Rupe, J. H., "On the Dynamic Characteristics of Free-Liquid Jets and a Partial Correlation with Orifice Geometry," JPL, Tech Report, No. 32, p. 207, 1962.
12. Giffen, E. and Muraszew, A., "The Atomization of Liquid Fuels," John Wiley and Sons, 1953.
13. Miesse, C. C., "Correlation of Experimental Data on the Disintegration of Liquid Jets" Indust. Engng. Chem., Vol. 47, p. 1690, 1955.
14. Reitz, R. D. and Bracco, F. V., "Ultra High Speed Filming of Atomizing Jets," submitted for publication to The Physics of Fluids, 1978.
15. Abramowitz, G. N., "The Theory of Turbulent Jets" MIT Press, 1963.
16. Newman, J. A. and Brzustowski, T. A., "Behavior of a Liquid Jet Near the Thermodynamic Critical Region," AIAA Jour. Vol. 9, p. 1595, 1971.
17. Hiroyasu, H. Private Communication, 1978.
18. Taylor, G. I., "Generation of Ripples by Wind Blowing over a Viscous Fluid," Collected Works of G. I. Taylor, Vol. 3, Cambridge University Press, 1940.



**Society of Automotive Engineers, Inc.**  
400 COMMONWEALTH DRIVE, WARRENDALE, PA 15090

This paper is subject to revision. Statements and opinions advanced in papers or discussion are the author's and are his responsibility, not the Society's; however, the paper has been edited by SAE for uniform styling and format. Discussion will be printed with the paper if it is published

in SAE Transactions. For permission to publish this paper in full or in part, contact the SAE Publications Division.

Persons wishing to submit papers to be considered for presentation or publication through SAE should send the manuscript or a 300 word abstract of a proposed manuscript to: Secretary, Engineering Activities Board, SAE.

APPENDIX B

ULTRA HIGH-SPEED FILMING OF ATOMIZING JETS

R.D. Reitz and F.V. Bracco

# Ultra-high-speed filming of atomizing jets

R. D. Reitz and F. V. Bracco

Department of Mechanical and Aerospace Engineering, Princeton University, Princeton, New Jersey 08544  
(Received 5 June 1978; final manuscript received 11 December 1978)

In the atomization regime, a liquid jet breaks up into droplets of diameter much smaller than the nozzle exit diameter, within the nozzle or immediately upon entering the chamber gas. The mechanism of atomization is currently unknown. The initial emergence and breakup details of liquid jets at the onset of injection were recorded, apparently for the first time, by an ultra-high-speed framing camera (up to  $10^6$  frames/sec). Liquid pressure and viscosity, gas pressure and density, and the nozzle internal geometry were varied. The nozzle exit diameter, the liquid surface tension and density, and the gas and liquid temperatures were not varied significantly. Intact length, spray angle, penetration rate, and quasi-steadiness of the breaking jet are discussed. It is concluded that within the tested range, liquid cavitation or aerodynamic surface wave growth, augmented by liquid cavitation and/or boundary layer velocity profile relaxation phenomena, could explain the observed experimental trends adequately.

## I. INTRODUCTION

When a liquid jet is made to flow through a circular orifice into a chamber of stagnant gas, four main regimes of jet breakup are identified, Rayleigh, first wind induced, second wind induced, and atomization (Reitz and Bracco<sup>1</sup>). The forces controlling the breakup process in the various regimes have been both of fundamental and of practical interest for a considerable time. The investigation reported in this paper concerns mostly atomization, but the lack of a universally accepted terminology makes it advisable briefly to identify the other regimes as well.

Photographs of jets operating in the four breakup regimes from Lee and Spencer<sup>2</sup> and Reitz<sup>3</sup> are shown in Fig. 1. For sufficiently low jet velocities, the jet breakup, which occurs many nozzle exit diameters downstream of the nozzle, yields drops whose diameter exceeds that of the jet [Fig. 1(a)]. This is the Rayleigh regime and disruption of the jet is caused by the growth of axisymmetric oscillations on the liquid jet surface, induced by surface tension.

As the jet velocity is increased, or other operating conditions are appropriately changed, the inertial effects of the surrounding gas become important. The jet breakup, which occurs many diameters downstream of the nozzle, now yields drops whose diameter is of the order of the jet diameter [Fig. 1(b)]. In this case, the surface tension effect is augmented by the relative motion of the ambient gas and the jet, which produces a static pressure distribution across the jet accelerating the breakup process, (first wind-induced breakup regime). This mechanism was pointed out by Weber.<sup>4</sup>

With a further increase in the jet velocity, the jet breaks up into drops whose average diameter is very much less than the original jet diameter. The droplet formation, which is caused by the unstable growth of three-dimensional short wavelength waves on the jet surface, occurs some distance (intact length) downstream of the nozzle [Fig. 1(c)]. Beyond this point the liquid jet no longer has a cylindrical form, but rather, diverges as a spray (second wind-induced breakup regime).

The wave growth leading to the jet breakup is caused by the relative motion of the jet and the ambient gas, but wave growth is opposed by surface tension. Breakup in the second wind-induced breakup regime has attracted the attention of many researchers in connection with the problem of wave growth on the sea surface.<sup>5</sup> In addition, the works of Borodin,<sup>6,7</sup> Levich,<sup>8,9</sup> and Taylor<sup>10</sup> have contributed to an understanding of this type of jet breakup.

If jet velocity is further increased, or the operating conditions are appropriately changed, the fourth regime, the atomization regime, is encountered. This regime is the one of interest in this paper. The distinguishing feature in this regime is the absence of an intact jet length [Fig. 1(d)]. Breakup in this regime results in a spray which diverges immediately from the nozzle exit. The spray contains droplets whose average diameter is very much less than the nozzle diameter.

The agency responsible for jet disruption in this regime is unknown. The nature of the mechanism of atomization has been the subject of much speculation by a variety of authors. Some of the more prominent jet disruption hypotheses are outlined briefly here.

Castleman<sup>11</sup> and Ranz<sup>12</sup> proposed that aerodynamic interaction between the gas and liquid was responsible for jet breakup in this case. However, since no evidence of an intact length was found for jets in this regime, DeJuhasz<sup>13</sup> reasoned that the jet breakup process occurs within the nozzle itself. He argued that liquid turbulence could play an important role in this process. Schweitzer<sup>14</sup> proposed that the radial turbulent velocity components would disrupt the jet-gas interface, leading to the formation of droplets, as soon as the restraint imposed on the flowing liquid by the orifice wall ceases at the nozzle exit.

Bergwerk<sup>15</sup> noted that a cavitation region may occur within the nozzles. He suggested that large turbulent disturbances may be created in these cavitation regions and play a role in the jet disruption process. Rupe<sup>16</sup> postulated that the abrupt change in boundary condition experienced by the liquid flow at the nozzle exit could destabilize the jet, leading to its breakup.

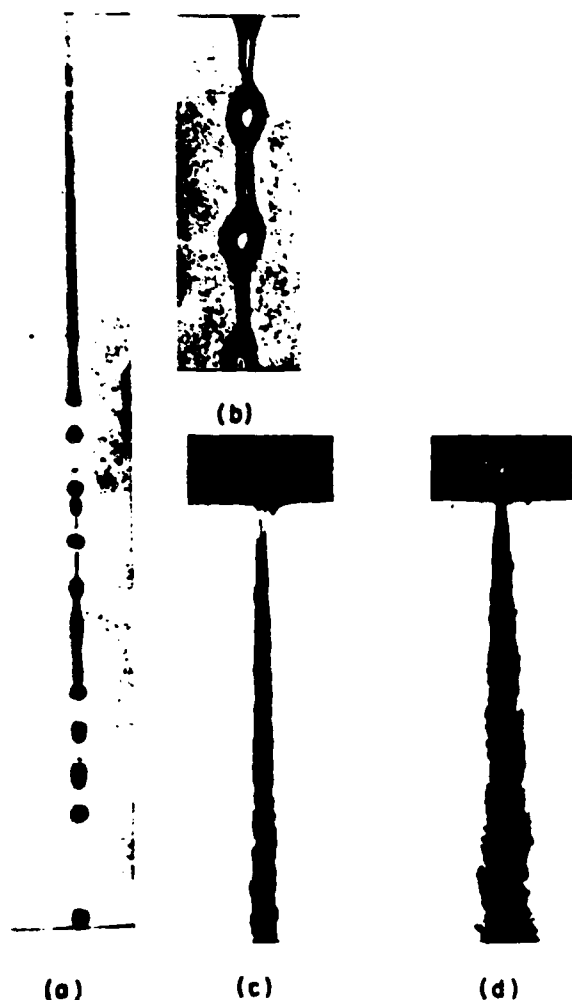


FIG. 1. Examples of the four jet breakup regimes from Lee and Spencer<sup>2</sup> and Reitz.<sup>3</sup>

In spite of these and other attempts to explain the process of atomization, no firm evidence so far has been provided in support of the various hypotheses, and no complete theory of atomization exists.

## II. EXPERIMENTAL DETAILS

A schematic diagram of the experimental apparatus used to study the atomization phenomenon is presented in Fig. 2. The individual components are described in this section (further details may be found in Reitz<sup>3</sup>). Referring to Fig. 2, the apparatus consisted of a framing camera (A), a spray chamber (B), an injection system (C and D), control units (E), and a set of nozzles. The high liquid injection velocities ( $\sim 10^4$  cm/sec) and the small length scales involved in this study (nozzle exit diameters  $d_0 \sim 0.3$  mm) necessitated the use of high framing rates for the resolution of breakup transients. The framing camera, manufactured by Cordin, model 117 and accessories, used a nitrogen driven turbine with highly polished rotating mirror to produce equivalent framing rates up to 1.25 million frames per second ( $0.8 \mu\text{sec}$  between frames). The image, taken through the lens to the surface of the rotating mirror, was reflected back through a bank of 60 focusing lenses, onto a stationary strip of film. This produced a "stationary"  $20 \times 20$  mm image (writing time approximately  $\frac{1}{2}$  interframe time) on each of the 60 frames of film. The spray chamber (25 cm and 45 cm length) allowed the injection process to be photographically studied through three 10 cm diam quartz windows. The injection system delivered  $40 \text{ cm}^3$  of the test liquid at a constant injection pressure. The test liquid in the liquid reservoir was separated from high pressure nitrogen (from a 10:1 pressure amplifier system) by a lightweight aluminum piston. The injection nozzles were designed so that they could be interchangeably mounted in two holders (see Fig. 3). With the unit assembled and mounted, the nozzle insert or extension

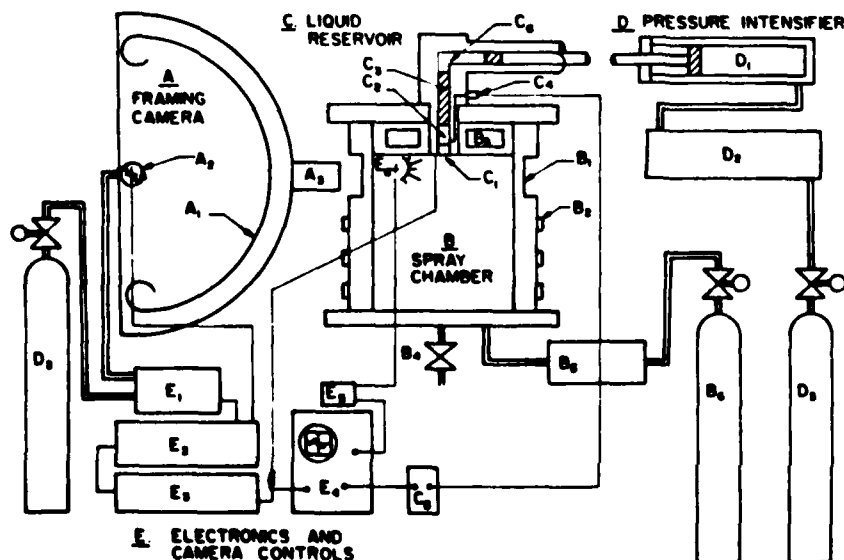


FIG. 2. Schematic diagram of apparatus. (A) Cordin model 117 camera (A<sub>1</sub> lens bank and stationary film strip, A<sub>2</sub> rotating mirror, and A<sub>3</sub> camera lens). (B) spray chamber (B<sub>1</sub> quartz windows, B<sub>2</sub> electrical heaters, B<sub>3</sub> water cooling jacket, B<sub>4</sub> drain and safety valves, B<sub>5</sub> electrical gas heater, and B<sub>6</sub> bottled gas). (C) liquid reservoir (C<sub>1</sub> nozzle holder, C<sub>2</sub> test liquid, C<sub>3</sub> piston, C<sub>4</sub> pressure transducer, C<sub>5</sub> charge amplifier, and C<sub>6</sub> driver gas). (D) pressure intensifier (D<sub>1</sub> pressure amplifier, D<sub>2</sub> accumulator, and D<sub>3</sub> bottled nitrogen). (E) electronics and camera controls (E<sub>1</sub> camera gas control unit, E<sub>2</sub> camera speed control unit, E<sub>3</sub> high energy pulse unit, E<sub>4</sub> oscilloscope, E<sub>5</sub> flash control unit, and E<sub>6</sub> xenon flash tubes).



Event illumination was accomplished by the simultaneous discharge of two xenon flash tubes positioned inside the spray chamber (see Fig. 2) (front lighting).

A storage oscilloscope and trigger unit were employed to monitor the liquid pressure and for event synchronization. The liquid pressure was indicated by the output of a fast response Kistler quartz pressure transducer. In addition, a single, short duration ( $\sim 1 \mu\text{sec}$ ), strobe flash served to illuminate the same jet much later in the injection so that its steady-state appearance was also recorded.

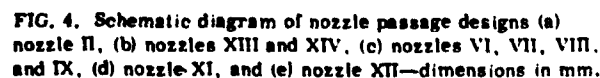






FIG. 5. Photograph showing nozzle exit hole taken after series 29.

#### A. Accuracy and limitations of measurements

Considerable time was devoted to perfecting the fuse technique for event initiation. Figure 5 is a typical example of the nozzle exit hole condition taken after a test.

The nozzle inlet and exit diameters were measured using a calibrated microscope to an estimated accuracy of 3%. Care was taken in the manufacture of the rounded inlet nozzles to insure that the internal circumference at any station was concentric with the nozzle exit hole. Nozzle tube internal surface roughness dimensions were visibly much less than this accuracy limit.

Jet divergence angles could be estimated from the photographs within  $1^\circ$  and jet intact lengths to within 50%  $d_0$ . The jet velocity was determined with an estimated accuracy of 10%.

The chamber gas pressure and the driver gas pressure remained constant within 5% during any given test.

### III. EXPERIMENTAL RESULTS

#### A. Range and scope of the experimental tests

Two different and complementing methods of investigation of the high velocity liquid jet breakup process were applied simultaneously. In the first, the initial emergence and breakup details of the liquid jet at the onset of injection were recorded by means of the high speed framing camera. This is referred to as the "transient" (T) method. In the second, or "steady-state" (S) method, a photograph was taken of the same jet about 1 sec after the initial emergence of the liquid jet into the spray chamber. Thirty-four different sets of test conditions, or series, were investigated as shown in Table I. These conditions were chosen to include the ranges of operating conditions of several practical fuel injection systems.

The nozzle exit diameter  $d_0$  was fixed at 0.34 mm, while the nozzle internal geometry was varied by making use of the nine nozzles depicted in Fig. 4. These nozzle designs included nozzles with length to diameter ratios ranging from  $\frac{1}{2}$  (nozzles XIII and XIV) to 50 (nozzle II) and allowed the effect of changes in nozzle inlet geometry and material of construction to

be studied.

The liquids tested were four different mixtures of water and glycerol (0%, 50%, 80%, and 100% wt. glycerol). This permitted a thousand-fold range in liquid viscosity  $\mu_L$  to be realized with relatively insignificant changes in the liquid density  $\rho_L$  and surface tension  $\sigma$ .

The liquid pressure  $p_L$  ranged from about 33 to 140 atm (a fixed value for a given test) and the chamber gas pressure  $p_g$  (nitrogen in these tests) range from 1 to 20 atm. The test environment was at room temperature.

The entries in Table I include the specification of the nozzle, the test liquid, the injection pressure  $\Delta p = p_L - p_g$ , and the computed jet exit velocity  $u_0$ . This is computed from the relation<sup>17</sup>

$$u_0 = C_d (2\Delta p / \rho_L)^{1/2},$$

where the  $C_d$  values were experimentally determined from the measured total injection duration. In addition, the Reynolds number  $Re_L = \rho_L u_0 d_0 / \mu_L$ , Weber number  $We_L = \rho_L u_0^2 d_0 / \sigma$ , and cavitation number  $K = \Delta p / (p_L - p_v)$  (where  $p_v$  is the liquid vapor pressure) corresponding to each series are included in the table.

#### B. Description of photographic results

A feature of the photographic results of the transient tests is that the appearance of the emerging jet changes very little from one frame to the next but, instead, changes become evident only when distant frames are compared. For this reason, the behavior of the emergence of the transient jet may be described and analyzed using a few selected frames instead of all of the 60 transient photographs, and this is the approach adopted in reporting the results.

The results of six of the series of experiments are presented in Figs. 6–11. They are series 51, 52, 31, 33, 8, and 47 of Table I, respectively. The photographic results of both the transient and steady-state pictures of the same jet are shown together for comparison in each case. The emerging jet is shown at approximately twice the magnification of the steady-state photograph in each figure.

The results shown in Figs. 6 and 7 demonstrate the effect of isothermal chamber gas compression on the behavior of the jet. Figure 6 shows the emergence and transient behavior of a water jet, injected into a 10 atm nitrogen environment with  $\Delta p = 130$  atm (series 51). The nozzle in this case is nozzle XII.

The head of the emerging jet in frames 15, 20, and 25 appears to be rounded, suggesting the existence of a primary vortex leading the jet and interacting with the chamber gas. In addition, the body of the jet in frames 20, 25, and 30 shows some increase in jet cross-sectional area from the exit plane up to the head of the emerging jet. There is evidence of many extremely fine particles traveling with the jet, particularly in the head region and the region of the flow immediately behind it. By frame number 55 the visible jet has reached a steady-state configuration. The jet shows evidence of being intact and cylindrical in form,

TABLE 1. Thirty-four operating conditions employed in transient jet breakup studies.

Series	Data T S		Nozzle	Liquid	$\Delta p$ (psi (absolute))	$p_t$	$U_0$ cm/sec	$U_T$ cm/sec	$Re_t$	$We_t$	$K$
7	3	0	II, $L/d_0 = 49.3$	H <sub>2</sub> O	720	100	$4.6 \times 10^3$	$4.6 \times 10^3$	$1.71 \times 10^4$	101.0	7.2
*8 <sup>a</sup>	1	1	II, $L/d_0 = 49.3$	H <sub>2</sub> O	1500	200	$7.0 \times 10^3$	$7.04 \times 10^3$	$2.46 \times 10^4$	420.0	7.5
16	4	4	VI, $L/d_0 = 4.4$	H <sub>2</sub> O	820	100	$5.3 \times 10^3$	$5.25 \times 10^3$	$2.4 \times 10^4$	198.0	8.2
17	1	1	VII, $L/d_0 = 4.3$	H <sub>2</sub> O	1400	100	$9.2 \times 10^3$	$7.8 \times 10^3$	$3.15 \times 10^4$	342.0	14.0
18	1	1	VII, $L/d_0 = 4.3$	H <sub>2</sub> O	1400	200	$8.8 \times 10^3$	$8.0 \times 10^3$	$3.01 \times 10^4$	627.0	7.0
20	2	2	VIII, $L/d_0 = 4.3$	H <sub>2</sub> O	1200	200	$8.7 \times 10^3$	$7.13 \times 10^3$	$2.98 \times 10^4$	613.0	6.0
21	1	1	IX, $L/d_0 = 4.0$	H <sub>2</sub> O	820	15	$7.1 \times 10^3$	$7.1 \times 10^3$	$2.43 \times 10^4$	30.5	54.7
22	1	1	IX, $L/d_0 = 4.0$	H <sub>2</sub> O	1600	15	$9.9 \times 10^3$	$1.11 \times 10^4$	$3.39 \times 10^4$	59.4	106.7
23	1	1	IX, $L/d_0 = 4.0$	H <sub>2</sub> O	2100	15	$1.14 \times 10^4$	$1.14 \times 10^4$	$3.9 \times 10^4$	78.8	140
24	1	1	IX, $L/d_0 = 4.0$	H <sub>2</sub> O	2000	90	$1.11 \times 10^4$	$6.35 \times 10^3$	$3.8 \times 10^4$	448.0	22.2
25	1	1	IX, $L/d_0 = 4.0$	H <sub>2</sub> O	1600	100	$9.7 \times 10^3$	$4.06 \times 10^3$	$3.32 \times 10^4$	380.0	16.0
26	1	1	IX, $L/d_0 = 4.0$	H <sub>2</sub> O	1950	150	$1.1 \times 10^4$	$8.2 \times 10^3$	$3.77 \times 10^4$	733.0	13.0
28	6	8	IX, $L/d_0 = 4.0$	H <sub>2</sub> O	1600	200	$9.2 \times 10^3$	$5.63 \times 10^3$	$3.15 \times 10^4$	685.0	8.0
29	1	1	IX, $L/d_0 = 4.0$	H <sub>2</sub> O	1300	300	$9.0 \times 10^3$	$5.42 \times 10^3$	$3.08 \times 10^4$	983.0	4.33
30	1	1	IX, $L/d_0 = 4.0$	H <sub>2</sub> O	1900	300	$1.09 \times 10^4$	$8.28 \times 10^3$	$3.73 \times 10^4$	$1.44 \times 10^3$	6.33
*31	1	3	IX, $L/d_0 = 4.0$	50% G + H <sub>2</sub> O	1700	300	$9.0 \times 10^3$	$6.3 \times 10^3$	$5.88 \times 10^3$	$1.02 \times 10^3$	5.67
*33	1	1	IX, $L/d_0 = 4.0$	80% G + H <sub>2</sub> O	1700	300	$4.5 \times 10^3$	$4.47 \times 10^3$	$3.3 \times 10^2$	280.0	5.67
34	1	1	IX, $L/d_0 = 4.0$	Glycerol	1600	300	$2.0 \times 10^3$	$2.0 \times 10^3$	5.5	71.3	5.33
*47	1	3	XI, $L/d_0 = 4.3$	50% G + H <sub>2</sub> O	1700	300	$1.0 \times 10^4$	$5.2 \times 10^3$	$6.53 \times 10^3$	$1.22 \times 10^3$	5.67
*49	2	2	XII, $L/d_0 = 2.1$	H <sub>2</sub> O	2000	15	$1.26 \times 10^4$	$1.03 \times 10^4$	$4.31 \times 10^4$	96.4	133
50	2	2	XII, $L/d_0 = 2.1$	H <sub>2</sub> O	2000	90	$1.26 \times 10^4$	$1.1 \times 10^4$	$4.3 \times 10^4$	570.0	22.2
*51	1	1	XII, $L/d_0 = 2.1$	H <sub>2</sub> O	2000	150	$1.26 \times 10^4$	$7.10 \times 10^3$	$4.31 \times 10^4$	956.0	13.3
*52	1	1	XII, $L/d_0 = 2.1$	H <sub>2</sub> O	1900	300	$1.2 \times 10^4$	$5.80 \times 10^3$	$4.31 \times 10^4$	$1.93 \times 10^3$	6.3
53	1	1	XII, $L/d_0 = 2.1$	50% G + H <sub>2</sub> O	1700	300	$1.1 \times 10^4$	$6.4 \times 10^3$	$7.2 \times 10^3$	$1.53 \times 10^3$	5.67
54	1	1	XII, $L/d_0 = 2.1$	Glycerol	1700	300	$5.8 \times 10^3$	$5.78 \times 10^3$	14.2	473.0	5.67
56	2	1	XIII, $L/d_0 = 0.5$	H <sub>2</sub> O	550	15	$7.8 \times 10^3$	$7.75 \times 10^3$	$2.4 \times 10^4$	30.0	36.7
57	1	0	XIII, $L/d_0 = 0.5$	H <sub>2</sub> O	1200	15	$1.01 \times 10^4$	$1.01 \times 10^4$	$3.53 \times 10^4$	64.4	80.0
58	2	0	XIII, $L/d_0 = 0.5$	H <sub>2</sub> O	2000	15	$1.34 \times 10^4$	$1.11 \times 10^4$	$4.59 \times 10^4$	109.0	133.0
59	1	0	XIII, $L/d_0 = 0.5$	H <sub>2</sub> O	500	100	$6.64 \times 10^3$	$6.6 \times 10^3$	$2.27 \times 10^4$	178.0	5.0
60	2	1	XIII, $L/d_0 = 0.5$	H <sub>2</sub> O	1300	100	$9.6 \times 10^3$	$7.63 \times 10^3$	$3.79 \times 10^4$	372.0	13.0
61	2	0	XIII, $L/d_0 = 0.5$	H <sub>2</sub> O	2000	100	$1.3 \times 10^4$	$8.0 \times 10^3$	$4.55 \times 10^4$	715.0	20.0
62	3	2	XIII, $L/d_0 = 0.5$	H <sub>2</sub> O	1500	200	$1.07 \times 10^4$	$7.43 \times 10^3$	$3.66 \times 10^4$	927.0	7.5
63	1	0	XIII, $L/d_0 = 0.5$	H <sub>2</sub> O	2000	200	$1.3 \times 10^4$	$1.0 \times 10^4$	$4.6 \times 10^4$	$1.4 \times 10^3$	10.0
64	3	1	XIV, $L/d_0 \approx 0.5$	H <sub>2</sub> O	1700	15	$1.2 \times 10^4$	$1.2 \times 10^4$	$4.1 \times 10^4$	87.0	113

<sup>a</sup>The asterisk means that the results are shown in Figs. 6-11.

near the nozzle exit. Close examination of frame 55 reveals, in addition, that the region beyond about five nozzle exit diameters downstream of the exit plane appears to diverge.

The steady-state photograph is shown for comparison. Here, the jet cross-sectional area is seen to increase in the direction of motion starting from about  $0.5 d_0$  from the nozzle exit plane.

Further compression of the chamber gas has a noticeable effect on the behavior of the head of the emerging jet. This is shown in Fig. 7, the results of series 52. Here, the chamber contains 20 atm nitrogen and all other operating conditions are similar to those of Fig. 6. In this case, the jet head vortex interaction with the surrounding gas has been increased. The region of the flow in the vicinity of the head of the jet comprises many finely atomized particles apparently

moving with the jet. Particularly striking in this set of results is the symmetry of the jet about the vertical axis. This suggests that the method of event initiation employed in these tests has a negligible disturbing influence on the subsequent emergence and breakup details of the jet.

Starting at the nozzle exit plane, the increase in jet cross-sectional area (jet divergence) is clearly apparent from frame number 25 onward. The steady-state photograph may be compared with frame 55 of the transient where the head of the jet is now out of the field of view. This comparison shows similar jet divergence angles in the two times.

In this case there is no evidence to suggest an intact or nondiverging region of the flow in the immediate vicinity of the nozzle exit in either frame 55 or in the steady-state photograph. These figures show that jet

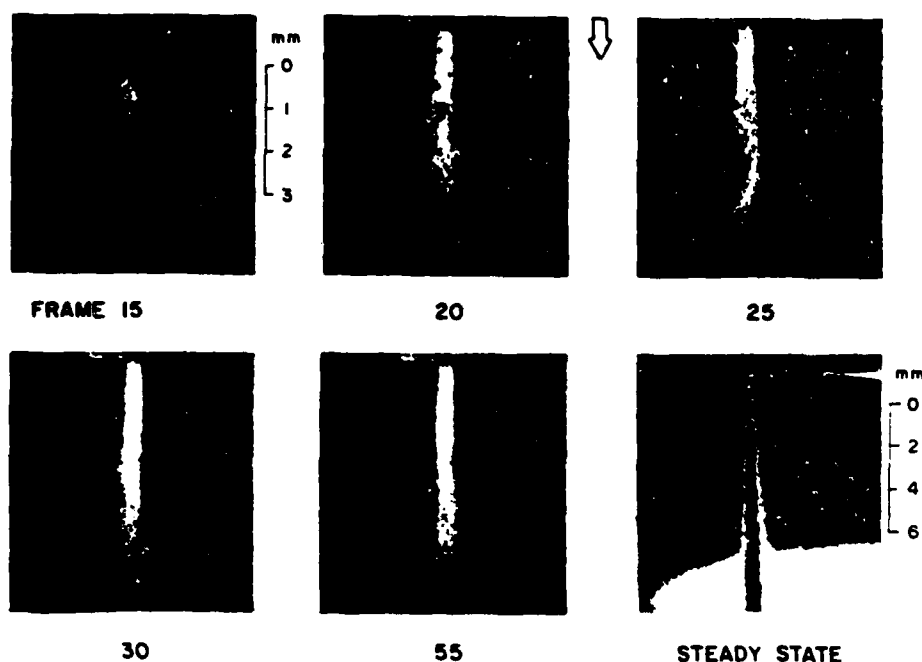


FIG. 6. Series 51. Water injection from nozzle XII ( $l/d_0=2.1$ , rounded inlet) into 10 atm nitrogen. Jet velocity  $7.1 \times 10^3$  cm/sec,  $2.5 \times 10^5$  frames/sec.

divergence starting at the nozzle exit can be achieved for these operating conditions if the chamber gas is progressively compressed.

The effect of changes in the test liquid are shown in the next two sets of photographs. Figure 8 (series 31) shows an injection of a 50% (wt.) mixture of water and glycerol ( $\mu_1 = 5.7 \mu_{H_2O}$ ) into 20 atm nitrogen from nozzle IX ( $L/d_0 = 4$ , sharp edged inlet). The injection pressure is 113 atm. The steady-state photograph of the jet has the appearance of an atomized jet with no visible intact or undiverging length. In frame 16 an outline of a jet is barely visible within and to the left

of what appears to be a cloud in the region of the nozzle exit hole. This cloud contains relatively slow moving droplets as can be seen by tracking its motion on the right-hand side of the frames 21, 26, and 31, until it gradually disappears.

The structure of the jet is similar to that of the previous two figures. It has a leading head region which continually sheds droplets (see, for example, frame 26) and interacts with the chamber gas. The region of the flow behind the head shows that the body of the jet diverges from the nozzle exit plane. A comparison between frame 56 and the steady-state photograph re-

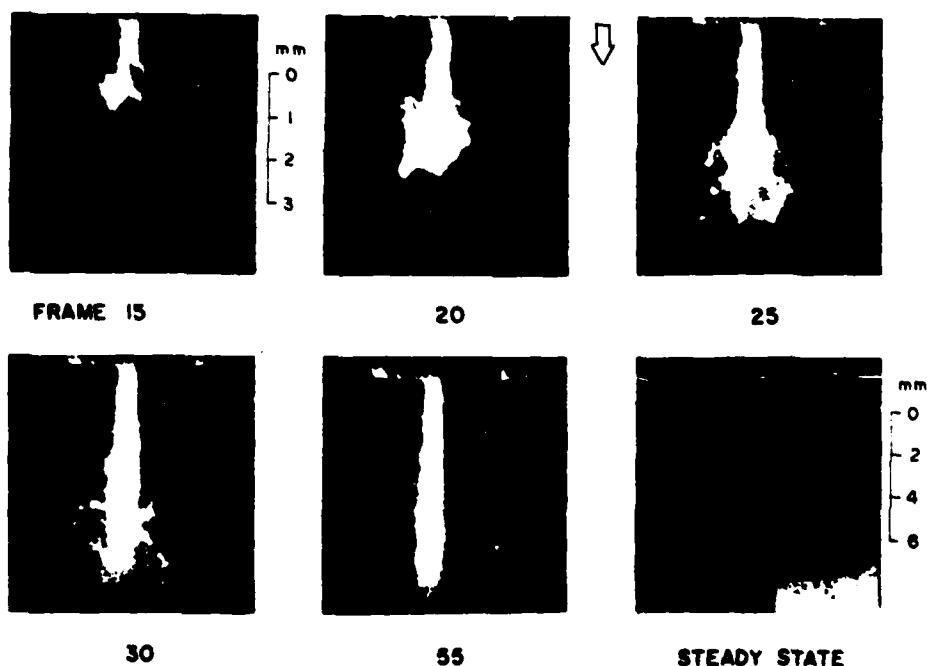


FIG. 7. Series 52. Water injection from nozzle XII ( $L/d_0 = 2.1$ , rounded inlet) into 20 atm nitrogen. Jet velocity  $5.8 \times 10^3$  cm/sec,  $2.5 \times 10^5$  frames/sec.

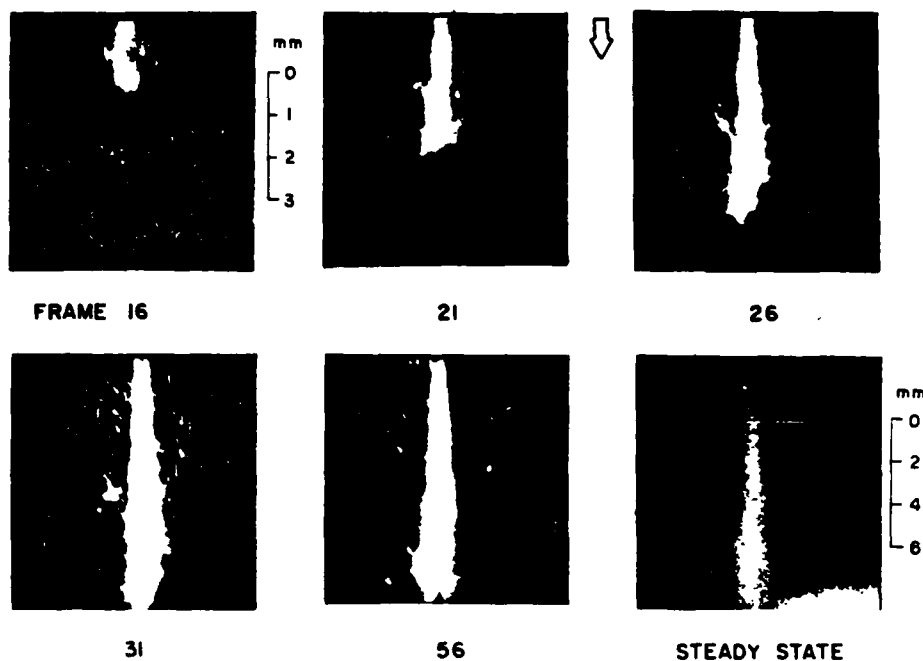


FIG. 8. Series 31. 50% water and glycerol mixture injected from nozzle IX ( $L/d_0 = 4.0$ , sharp inlet) into 20 atm nitrogen. Jet velocity  $6.3 \times 10^3$  cm/sec,  $2.5 \times 10^5$  frames/sec.

veals that the jet has a similar final divergence angle.

An injection with the same nozzle (series 33) and the same operating conditions is shown in Fig. 9, but the liquid in this case is a mixture of 20% water and 80% glycerol ( $\mu_l = 59.8 \mu_{H_2O}$ ). The ten times increased liquid viscosity has a dramatic effect on the details of the flow. The steady-state photograph shows that the liquid jet must have been completely detached (hydraulic flip) from the nozzle walls. The jet diameter estimated from this photograph was 55% of the nozzle

exit diameter.

Jet diameters measured in the transient frames show the jet diameter at the nozzle exit alternating between 70%–90% of the nozzle exit hole diameter. This could imply that transient reattachment phenomena were occurring within the nozzle. The head region of the jet does not appear to contain the finely atomized particles observed in Figs. 7, 8, and 9. These results shown that intact jets can be obtained with these operating conditions if the liquid viscosity is progressively in-

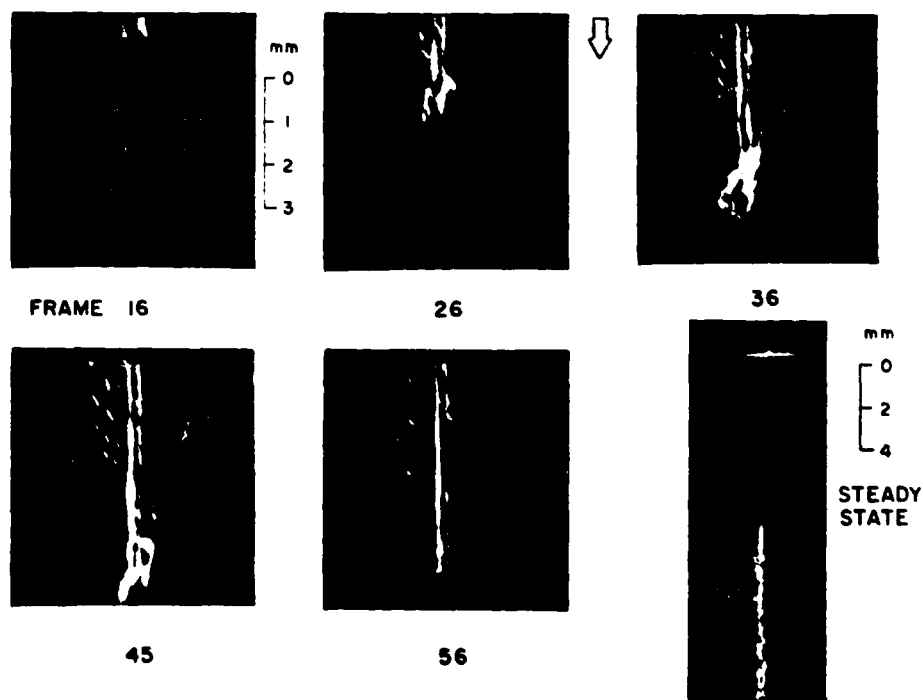


FIG. 9. Series 33. 20% water and 80% glycerol mixture injected from nozzle IX. ( $L/d_0 = 4.0$ , sharp inlet) into 20 atm nitrogen. Jet velocity of  $4.5 \times 10^3$  cm/sec,  $2.5 \times 10^5$  frames/sec.

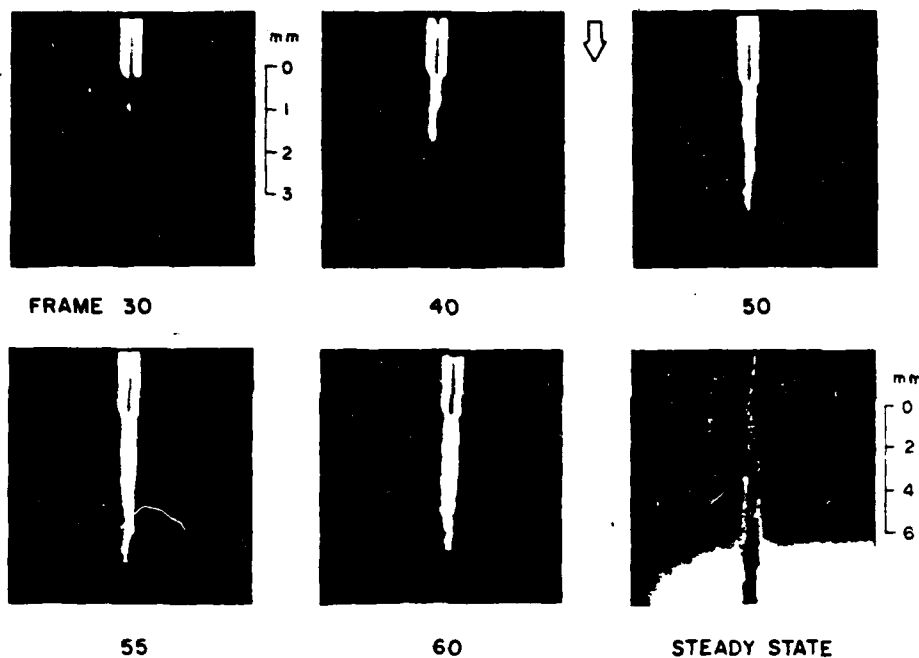


FIG. 10. Series 8. Water injection from nozzle II ( $L/d_0 \approx 49.3$ ) into 13 atm nitrogen. Jet velocity  $7.0 \times 10^3$  cm/sec.  $4.7 \times 10^5$  frames/sec.

creased.

The effect of nozzle passage geometry on the jet breakup process may be seen in Fig. 10. This shows series 8, a water injection from nozzle II ( $L/d_0 = 49.3$ ), with an injection pressure of 100 atm into a 13 atm nitrogen environment. The protruding nozzle tube [see Fig. 4(a)] is visible in all of the frames. A thin column of liquid is seen to precede the emergence of the jet and the emerging liquid jet shown in frames 40, 50, 55, and 60 of the transient frames shows a great deal of stability. The corresponding steady-state photograph

confirms this finding. The jet in this photograph is seen to exhibit minimal divergence.

Nozzle II with a  $L/d_0 = 49.3$  should produce a fully developed turbulent pipe flow at  $Re = 24,600$ .<sup>1</sup> The observed stability of these jets has implications on the role of liquid turbulence in the atomization mechanism.

The results shown in Fig. 11 also have implications on the atomization mechanism. This figure shows an injection from nozzle XI (rounded inlet nozzle,  $L/d_0 = 4.3$ ) of a 50% mixture of water and glycerol into a 20

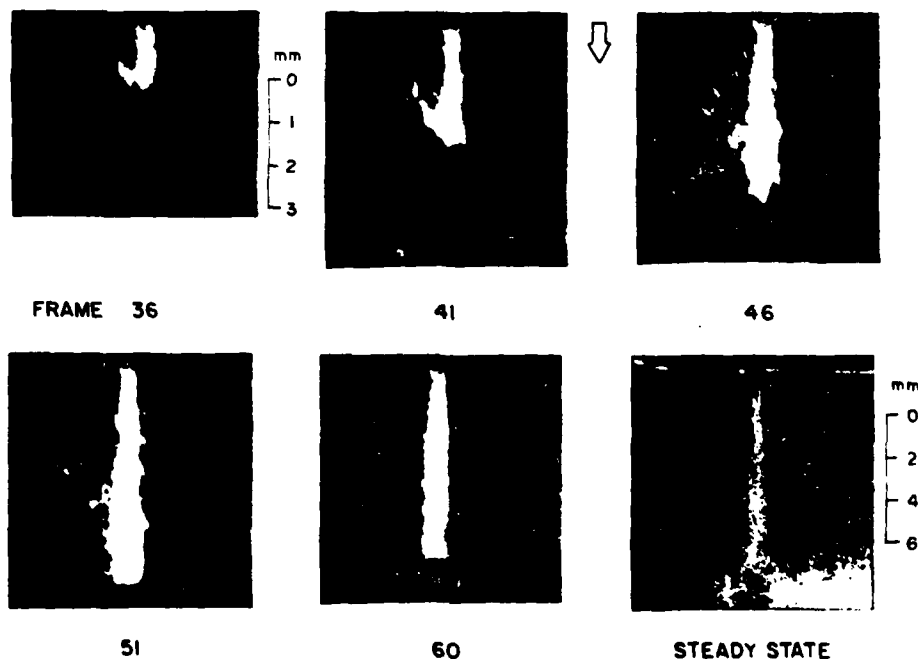


FIG. 11. Series 47. 50% water and glycerol mixture injected from nozzle XI ( $L/d_0 = 4.3$ , rounded inlet) into 20 atm nitrogen. Jet velocity  $5.2 \times 10^3$  cm/sec.  $2.5 \times 10^5$  frames/sec.

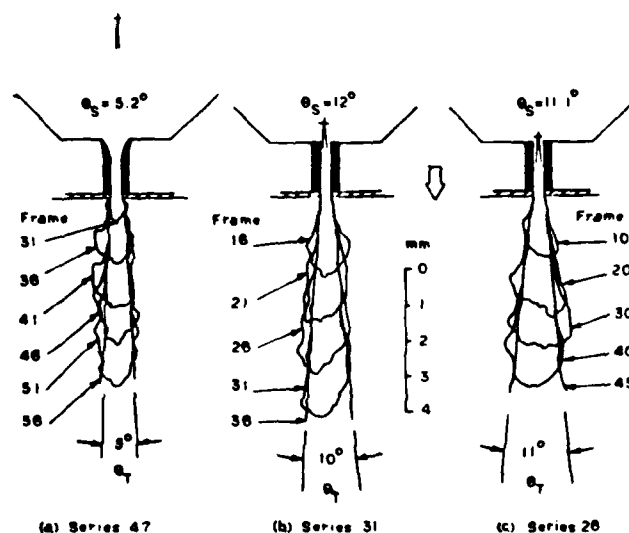


FIG. 12. Composite diagrams showing transient jet outline for series 47, 31, and 28.

atm nitrogen environment (series 47). This result could be compared with that shown in Fig. 8, an injection from the sharp edge inlet nozzle IX made at the otherwise same operating conditions. Immediately apparent is the difference detected in the steady-state photographs. In Fig. 11 the jet shows a substantial intact or undisturbed length, followed by divergence of the jet spray which suggests that the jet breakup may be classified as belonging to the second wind-induced regime. The comparison between the two transient studies, Fig. 8 corresponding to a jet in the atomization regime, reveals little difference in the overall appearance of the sets of photographs, apart from the droplet cloud referred to in the discussion of frames 16, 21, 26, and 31 of Fig. 8. In particular, a comparison of frame 46 of Fig. 11, with frame 26 of Fig. 8, reveals a striking similarity in the two results. This similarity could imply that no significant change in jet breakup mechanism has occurred; although the steady-state photographs, taken alone, could lead one to a different conclusion. Indeed, the conclusion that the transition from the second wind-induced regime to the atomization regime occurs smoothly is also reached from the quantitative analysis of the experimental trends presented in the next section.

#### IV. DISCUSSION OF THE RESULTS

A feature of the transient jet experimental results is the rapidity with which the emerging liquid approaches its steady-state configuration. This is further demonstrated in Fig. 12 which is a composite overlay of the jet outline from individual frames of the transient photographs and which allows one to visualize the initial development of the jet. Figures 12(a)–12(c), from series 47, 31, and 28, respectively, show that the region behind the head of the jet quickly assumes the final jet divergence angle,  $\theta_T$ , which then remains unaltered as the injection continues.

The corresponding steady-state jet divergence angle  $\theta_s$ , measured from the steady-state photograph, is printed at the top of each figure for comparison. A similar agreement between the transient and steady-state jet divergence angles was found in the majority of the tests.

Notice that, if the assumption is made that the magnitude of the spray angle is a direct measure of the breakup process, the measured quasi-steadiness of the angle also implies quasi-steadiness of the breakup mechanism.

The spray angle  $\theta$  was found to increase as the chamber gas was compressed. This trend, which can be seen by referring to Figs. 6 and 7 for example, is consistent with the findings of other authors (see for example Giffen and Muraszew<sup>18</sup>). Furthermore, it was also determined that it is the increased gas density, not the increased gas pressure, which results in larger spray angles upon compression of the gas. This was accomplished by using gases of different molecular weights.<sup>19</sup>

The results of the present study, supplemented with other results from Reitz and Bracco,<sup>19</sup> are presented in Fig. 13 to demonstrate this effect of gas density on jet divergence angle  $\theta$ . From this figure it is apparent that for a given nozzle, jet divergence commences at the nozzle exit (jet atomization) once a certain gas density level is reached. Moreover, no evidence of an abrupt transition from the second wind-induced regime (solid data points) to the atomization regime (open data points) is apparent. This transition from one regime to the next is seen to occur at different gas density levels for the different nozzles tested.

Notice that, for a given gas density level, the jet divergence angle is seen to decrease as the nozzle tube length (for the sharp edge inlet nozzles XIV, IX, III, II, and I) is increased. Moreover, for the same length, rounded inlet nozzles produce less divergent jets than sharp edged inlet nozzles.

The measured jet divergence angles presented in Fig. 13 can be quantitatively compared with the jet breakup theory of Ranz<sup>12</sup> and Taylor,<sup>10</sup> which attributes jet breakup to the aerodynamically induced growth of unstable surface waves. This theory, derived from consideration of infinitesimal surface waves on the liquid-gas interface, can be confidently applied in the second wind-induced regime (the solid data points) and it predicts that

$$\tan \frac{\theta}{2} = \frac{1}{A} 4\pi \left( \frac{\rho_l}{\rho_g} \right)^{1/2} f \left[ \frac{\rho_l}{\rho_g} \left( \frac{Re_l}{We_l} \right)^2 \right]. \quad (1)$$

In this equation, the constant of proportionality  $1/A$  must be obtained from experimental data. Ranz<sup>12</sup> used measured values of the jet divergence angle from his experiments to determine that  $A$  had a numerical value of 18 or 20, but pointed out that the jet divergence measurements of Schweitzer,<sup>20</sup> for fuel sprays, suggest that  $A$  has a value of about 3.

The group  $(A \tan \theta/2)/4\pi (\rho_l/\rho_g)^{1/2}$  is shown plotted against the group  $[(\rho_l/\rho_g) (Re_l/We_l)^2]$  in Fig. 14. From

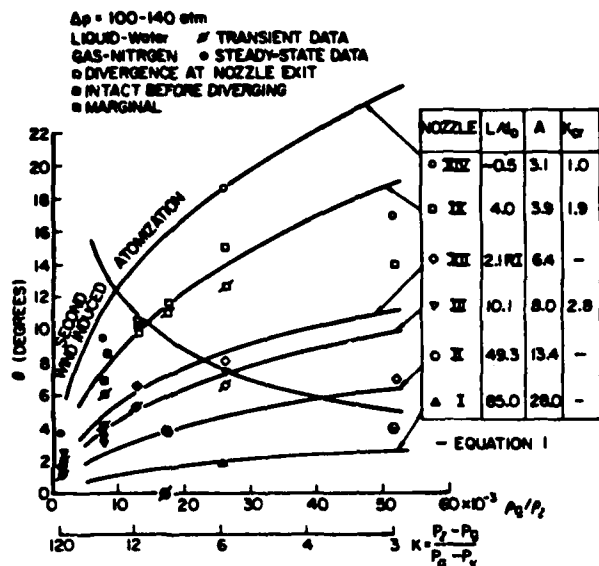


FIG. 13. Graph showing jet divergence angle versus flow cavitation number and gas-liquid density ratio for nozzles I, II, III, XII, IX, and XIV.

this figure it can be seen that Eq. (1) predicts that the jet divergence angle  $\theta$  increases with increasing gas density and decreases with increased liquid viscosity for the range of operating conditions of this work. This behavior is consistent with the experimental trends for tests with a given nozzle.

The comparison of the experimental results with the prediction of Eq. (1), also shown in Fig. 13, reveals that the predicted variation can be met for gas density levels up to about  $2.6 \times 10^{-2}$  g/cm<sup>3</sup> provided that the constant  $A$  is allowed to assume a different value ranging from 3.1 to 28 for each nozzle geometry in order best to match the experimental results. These findings indicate that additional phenomena, over and above the aerodynamic interaction between the liquid and gas flows as represented by Eq. (1), are at play in the jet breakup process; but this finding is equally true for jets operating in both the second wind-induced and atomization regimes, and therefore suggests a continuity in breakup mechanism in the two regimes.

The change in the value of the constant required as the nozzle is changed could possibly be caused by disturbances resulting from cavitation phenomena within the nozzle and/or wall boundary layer rearrangement effects within the liquid flow at the nozzle exit. The criteria of Bergwerk,<sup>15</sup> applicable to some of the sharp edge inlet nozzles of this study, predict that cavitation regions exist within these nozzles for the conditions of Fig. 13. This is because the flow cavitation number  $K$  (see Table I and Fig. 13) exceeds the critical values also shown in the figure. It may be significant that the magnitude of the constant  $A$  of the aerodynamic theory is seen to correlate with the value of  $K_{cr}$ , for those nozzles whose  $K_{cr}$  values could be estimated from the data of Bergwerk,<sup>15</sup> and that the discrepancy between the measured trends and those indicated by Eq. (1)

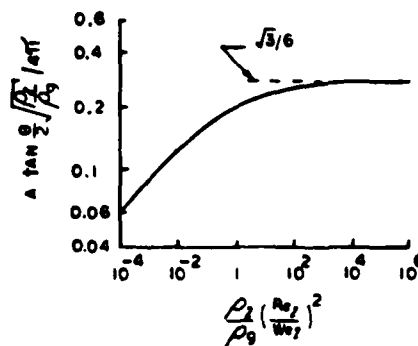


FIG. 14. Theoretical dependence of the jet divergence angle on the operating conditions from Ranz.<sup>12</sup>

for the divergence angle versus gas-to-liquid density ratio increases as the cavitation number approaches the critical one (see Fig. 13). In addition, the results of series 33 (Fig. 9) and other results reported in Reitz and Bracco,<sup>10</sup> show that non-cavitating jets (detached jets from sharp edge inlet orifices) exhibit increased stability.

An evaluation of other prominent hypotheses concerning the jet atomization mechanism is presented in more detail in Reitz and Bracco<sup>10</sup> using experimental results of both the transient and steady-state studies. However, from the results included in this paper, it can also be concluded that liquid pipe turbulence and liquid supply pressure oscillations each cannot alone control the jet disruption mechanism, due to the observed stability of turbulent jets (see Fig. 10) and the achievement of atomization under constant pressure injection. However, it cannot be excluded that cavitation alone could account for the observed trends.

## V. SUMMARY

Ultra-high-speed filming has been applied to study the initial transient in the process of atomization of high speed liquid jets. The technique was complemented by the simultaneous use of standard spark photography for a one-frame-picture of the atomizing jet past its transient (steady state).

The experiments were designed to include the operating range of several practical injection systems. Liquid injections from nine individual single hole nozzles of differing internal geometry but fixed exit diameter (0.34 mm) were studied in the tests. The injections were performed at room temperature in compressed nitrogen environments, maintained at a constant pressure for each experiment, between 1-20 atm. Four different mixtures of water and glycerol were used as the spray liquid. In each test the liquid pressure was kept constant and the range of pressures explored was 33-140 atm. Photographs of steady-state jets showed that the jet assumes an approximately conical shape which diverges in the direction of the flow. The angle of divergence  $\theta_s$ , the spray angle, was measured from traces of the jet outline in the photographs. The distance from the nozzle to the point where the divergence was observed to begin, the intact length,

$x_{10}$  was also measured. For the transient studies, the outline of the emerging jet was also traced and traces taken from frames at different times after the onset of the injection were superimposed to help visualize the development of the flow field. Here, again, the jet intact length and a jet divergence angle  $\theta_j$  could be measured since the divergence of the region behind the head of the emerging jet was found to remain constant as the injection continued. The transient and corresponding steady state divergence angles were found to agree.

This jet divergence angle was found to vary depending on the operating conditions. For a given nozzle, it increased with increasing chamber gas density and decreased slightly with increasing liquid viscosity. Beyond a certain liquid viscosity level, however, intact jets were obtained and cases of hydraulic flip were observed.

Jet atomization (jet divergence beginning at the nozzle exit) was achieved when the chamber gas density was increased beyond a certain level. Below this level, jet divergence commenced some distance from the nozzle exit and the jets corresponded to jets operating in the second wind-induced regime of breakup. No abrupt changes in the divergence angle were noticed between the two regimes.

Jet divergence angles, and the location of the region of transition from the second wind-induced regime to the atomization regime of breakup, were found to be greatly influenced by the nozzle design details. Jet divergence angles decreased as the nozzle  $L/d_0$  ratio was increased. Rounded inlet nozzles produced jets with smaller divergence angles than sharp edge inlet nozzles of the same length.

Within the tested range, aerodynamic interactions between the liquid and gas flows, enhanced by cavitation and/or wall boundary layer effects, would explain the measured trends and so could cavitation alone. Aerodynamic interactions, liquid turbulence, jet velocity profile rearrangements, and liquid pressure oscillations, each alone could not.

## ACKNOWLEDGMENTS

The authors would like to thank Dr. J. Petrowsky and Mr. L. Billard of the Naval Explosive Ordnance Disposal Facility, Indian Head, Maryland, for allowing us the use of the high speed framing camera and for the patience they showed during its delayed return. The authors gratefully acknowledge the support and stimulating interaction with Professor Martin Summerfield and the staff at the Princeton Combustion Laboratories, Princeton, New Jersey.

This work was supported under Grant NSF-RANN-AER 75-09538 (Dr. D. Senich, grant monitor) and DAAG 29-77-G-0146 of the Army Research Office, (Mr. J. J. Murray, grant monitor).

- <sup>1</sup>R. D. Reitz and F. V. Bracco (to be published).
- <sup>2</sup>D. W. Lee and R. C. Spencer, NACA TR 454 (1933).
- <sup>3</sup>R. D. Reitz, Ph.D. thesis, Princeton University (1974).
- <sup>4</sup>C. Weber, Z. Angew. Math. Mech. 11, 136 (1931).
- <sup>5</sup>O. M. Phillips, *The Dynamics of the Upper Ocean* (Cambridge University Press, Cambridge, 1966).
- <sup>6</sup>V. A. Borodin and Y. F. Dityakin, NACA TM 1281 (1951).
- <sup>7</sup>V. A. Borodin and V. I. Yagodka, J. Appl. Mech. Tech. Phys. 8, 46 (1967).
- <sup>8</sup>V. G. Levich, *Physicochemical Hydrodynamics* (Prentice-Hall, Englewood Cliffs, N.J., 1962).
- <sup>9</sup>V. G. Levich and R. S. Krylov, in *Annual Reviews of Fluid Mechanics* (Annual Reviews, Palo Alto, 1969), Vol. 1, p. 293.
- <sup>10</sup>G. K. Batchelor, editor, *Collected Works of G. I. Taylor* (Cambridge University Press, Cambridge, 1958).
- <sup>11</sup>R. A. Castleman, J. Res. Natl. Bur. Stand. 6, 281 (1931).
- <sup>12</sup>W. E. Ranz, Can. J. Chem. Eng. 36, 175 (1958).
- <sup>13</sup>K. J. DeJuhasz, Trans. A.S.M.E. 53, 65 (1931).
- <sup>14</sup>P. H. Schweitzer, J. Appl. Phys. 8, 513 (1937).
- <sup>15</sup>W. Bergwerk, Proc. Inst. Mech. Eng. 173, 655 (1959).
- <sup>16</sup>J. H. Rupe, Jet Propulsion Laboratory Technical Report 32 (1962), p. 207.
- <sup>17</sup>J. O. Hinze, *Turbulence* (McGraw-Hill, New York, 1959), p. 514.
- <sup>18</sup>E. Giffen and A. Muraszew, *The Atomization of Liquid Fuels* (Wiley, New York, 1953).
- <sup>19</sup>R. D. Reitz and F. V. Bracco (to be published).
- <sup>20</sup>P. H. Schweitzer, Pennsylvania State University Bulletin 40, (1932).



APPENDIX C

ON THE MECHANISM OF BREAKUP  
OF HIGHLY SUPERHEATED LIQUID JETS

K. -J. Wu, R.L. Steinberger, and F.V. Bracco

The Combustion Institute  
Central States Section  
1981 Spring Meeting, March 23-24  
General Motors Research Laboratories  
Warren, MI, 48098

ON THE MECHANISM OF BREAKUP  
OF HIGHLY SUPERHEATED LIQUID JETS

By

K.-J. Wu, R.L. Steinberger, and F.V. Bracco  
Department of Mechanical and Aerospace Engineering  
Princeton University  
Princeton, NJ 08544

#### ABSTRACT

Delay time and jet divergence angle measured from short-exposure, backlighted photographs, were studied for flashing jets at high degrees of superheat. n-Pentane, n-hexane, and ethanol were injected into nitrogen at two injection pressures and for three nozzle diameters. Proposed hypothesis for the delay time based on homogeneous nucleation are not confirmed by our experimental data. The assumption that the spray angle is related to the heat-transfer-controlled bubble growth appears to be supported by our data but important details concerning the number of bubbles in the jet and the state of the vapor in the bubble at breakup have not yet been properly explained. Both delay time and jet divergence angle are found to be sensitive to the degree of superheat and liquid properties, influenced by the liquid pressure and insensitive to jet diameter.

#### ACKNOWLEDGEMENTS

We are indebted to Dr. D.A. Santavicca, Mr. E. Griffith, and Mr. J. Semler for their advice and assistance. This work was supported by the Army Research Office under Grant DAAG 29-78-G-0132.

## INTRODUCTION

A liquid injected into a gas breaks up into droplets whose size depends on the mechanism of the breakup process. The mechanism of atomization of thermodynamically stable, and dynamically unstable, liquid jets has been extensively investigated, e.g. Reitz and Bracco (1979), but that of thermodynamically unstable jets has received much less attention. Thus, few studies have been reported of the breakup of superheated liquid jets.

Referring to Fig. 1, the flashing process can be divided into two consecutive stages: the nucleation of tiny bubbles inside the superheated liquid, to which the intact length of the jet and the corresponding delay time are associated; and the growth of these bubbles to a size large enough to shatter the jet, to which the angle of the resulting spray is related.

Brown and York (1962) investigated the effect of the Weber number and degree of superheat upon the mean drop size. Lienhard (1966) correlated the divergence angle of water jets with the degree of superheat by considering the transformation of thermal energy into kinetic energy of the droplets. Most researchers, Lienhard and Stephenson (1966), Lienhard and Day (1970), and Suzuki et al. (1978), concentrated on the stochastic distribution of the delay time and the bubble growth rate of the flashing process. Table 1 gives the experimental ranges of previous and present works.

For many applications, the delay time and the spray angle are important to control the spatial distribution of the liquid. In the present work, both parameters have been measured for different jet velocities, liquids, nozzle diameters and temperatures.

The experimental apparatus allowed jet configurations to be observed and photographed. Delay times and the divergence angles were measured from single, short-exposure photographs and they

are reported and discussed separately.

## EXPERIMENT

Figure 2 shows the experimental apparatus used for the observation of flashing jets. It was designed for liquid pressures and temperatures up to  $3.5 \times 10^7 \text{ N/m}^2$ , 500 K and gas pressures and temperatures up to  $7.0 \times 10^6 \text{ N/m}^2$ , 750 K.

The test liquid was housed in the reservoir, as shown in Fig. 3, between the piston and the nozzle attachment at the bottom of the liquid cylinder. Nitrogen gas was introduced above the piston to maintain the liquid pressure constant during injection. The drive nitrogen and the test liquid pressures were read from Heise-17555 and USG-1403 pressure gages. In addition, the liquid pressure trace during injection was recorded by a storage oscilloscope through a Kistler model 603A water cooled pressure transducer mounted on the liquid cylinder and a Kistler model 504D charge amplifier.

Eight, 650-watt immersion type electrical heaters were inserted into the cylinder wall. For a better control of the liquid temperature, a variable autotransformer was used to adjust the power input to the heaters.

The spray chamber had four windows and was filled with nitrogen gas maintained at  $1.29 \times 10^5 \text{ N/m}^2$  for all the tests. Two plexiglass windows on opposite sides of the chamber allowed the flashing process to be observed photographically. An aluminum plug in a side port was equipped with a Conax transducer and electrical conductor sealing glands which served as the connectors for thermocouple and heaters wires.

Single short-exposure backlighting photographs were taken. The camera used was a combination of a 1.05m long aluminum tube

with bellows, a Polaroid camera back, and a  $f/3.5$ , 200 mm Takumar lens system. The magnification factor of this system is about 5.6 and the field of view is about 1.5 cm x 2.0 cm. The jet configurations were recorded by Polaroid type 57 black and white 4x5 film at about 1 second after the initiation of the injection when a short duration spark light was triggered by an electrical signal from the oscilloscope. Based on these photographs, both the intact lengths and the divergence angles were measured. The measurements are estimated to be accurate to within 10 microns for intact lengths and 1 degree for spray angles to which these correspond. Maximum experimental errors are 5.5% for the delay time and 3.8% for the jet angle.

For most conditions, more than one photograph was taken. The average values of the delay time and the jet angle and the associated statistical standard deviations are shown in Table 4. Due to the stochastic character of the flashing phenomenon, standard deviations are generally greater than measurement errors.

In order to measure the relevant liquid temperature as accurately as possible, an Omega sub-miniature iron-constantan thermocouple probe with sheath O.D. of 500  $\mu\text{m}$  was soldered near the entrance of the nozzle. Fig. 3 shows the relative position between the orifice and the thermocouple head. The temperature of the liquid was read from an Omega model 400A digital readout when the spark light was flashing. The temperature readings are estimated to be accurate to within 1K.

Figure 3 also shows the geometry of the three nozzles tested. All the nozzles have the same configuration, i.e. simple cylindrical passage with sharp-edged entrance and exit. In order to check the dependence of the flashing process on the jet diameter, three nozzles with different sizes were chosen and their dimensions are given in Table 2. Due to difficulties in

drilling small orifices, nozzle No. 1 had an  $l/D_o$  ratio of 2.0, whereas the others had a ratio of 4.0. The entrance of each nozzle was carefully examined under a scanning electron microscope and the surface roughness was observed to be <5% of the diameter. A typical photograph of the nozzle entrance is shown in Fig. 4.

Three different hydrocarbon fuels were tested; they were n-pentane, n-hexane, and ethanol. The catalogue numbers and the manufacturers are included in Table 3. In all calculations the variation of liquid properties with temperature was considered based on the information from Gallant (1968). The temperature range of the present experimental work is also shown in Table 3 for each liquid. Generally broader ranges of superheat were studied than in previous works.

Another parameter that was varied is the injection pressure (and velocity). Two different values of  $\Delta P$  were employed,  $4.14 \times 10^6 \text{ N/m}^2$  and  $8.96 \times 10^5 \text{ N/m}^2$ , thus changing the jet velocity by a factor of about 2. However, the volumetric average velocities of the liquid jet were calculated from the volume of the liquid reservoir, the dimensions of nozzles, and the total injection time measured at room temperature.  $U_o$  may increase somewhat with temperature due to its influence on the liquid density, but the change is small and does not affect the results significantly.

## RESULTS AND DISCUSSION

Jet divergence angles and delay times were derived from each photograph for different liquids, injection pressures, nozzle diameters, and degrees of superheat. All the experimental conditions and data are listed in Table 4.

As the jet emerges from the nozzle, its pressure drops to that of the ambient gas. Under the conditions of our experiments, thermodynamically stable jets, i.e. cold jets, remain intact for long times. Figure 5(a) shows this type of jet for n-hexane at room temperature. But when appropriately superheated, the smooth jet breaks up suddenly into very fine droplets. Figure 5(b) shows a typical example of this type of jet. Comparison of Fig. 5 (c) with Fig. 5(b) reveals the temperature effects on the flashing phenomena. At higher superheat, the intact length becomes shorter and the divergence angle becomes wider due to the faster phase change of the liquid into vapor.

#### DELAY TIME

Lienhard and Day (1970) using homogeneous nucleation concepts obtained two dimensionless parameters from five variables ( $t_D$ ,  $\sigma_L$ ,  $\rho_L$ ,  $D_o$ ,  $(P_v - P_{amb})$ ) they chose in their dimensional analysis, a dimensionless delay time  $\phi$  and a dimensionless superheat  $\psi$ .

$$\phi = \frac{(P_v - P_{amb})^{5/2} D_o}{\sigma_L^2 \rho_L^{1/2}} t_D$$

and

$$\psi = \frac{D_o (P_v - P_{amb})}{\sigma_L}$$

The physical meaning of the two parameters becomes clear if they are seen as the products of several dimensionless quantities

$$\phi = \frac{3}{2} \cdot \frac{t_D}{t_o} \cdot \frac{4\pi\sigma_L D_o^2}{\Delta G} \cdot \frac{4\sigma_L/D_o}{P_v - P_{amb}} \quad (1)$$

$$\psi = 4 \cdot \frac{P_v - P_{amb}}{4\sigma_L/D_o} \quad (2)$$



$R_o = \frac{2\sigma_L}{P_v - P_{amb}}$  is the radius of a bubble in unstable equilibrium;

$\Delta G = \frac{4\pi\sigma_L}{3} R_o^3$  is the free energy required to trigger homogeneously a bubble in unstable equilibrium in a pure liquid, as shown by Frenkel (1955);

$t_o = \left( \frac{\rho_L R_o^3}{2\sigma_L} \right)^{1/2}$  is the characteristic time of the initial slow growth of the vapor bubble;  $4\pi\sigma_L D_o^2$  is the surface energy;

$\frac{4\sigma_L}{D_o}$  is the pressure difference across a spherical bubble with diameter of  $D_o$  at static balance; and  $P_v - P_{amb}$  corresponds to the degree of superheat of the liquid.

In Fig. 6, the dimensionless mean delay time is plotted versus the dimensionless superheat for n-hexane jets from three different nozzles at  $\Delta P = 8.96 \times 10^5 \text{ N/m}^2$ . In our experimental data no systematic dependence of the delay time on the cross sectional area of the jet was observed even though the area was changed by a factor of 27. This behavior is unlike that shown by Lienhard and Stephenson (1966) and Lienhard and Day (1970) at lower levels of superheat.

The data for n-hexane jets from two different nozzles with  $\Delta P = 4.14 \times 10^6 \text{ N/m}^2$  is shown in Fig. 7. The dependence of the delay time on the liquid pressure suggests that in our experiments heterogeneous nucleation may have been dominant. The fact that shorter delay times corresponded to higher liquid pressures could indicate that dissolved gases may have acted as heterogeneous sites. Moreover, according to Avedisian (1980) and Blander and Katz (1975), the homogeneous nucleation temperature is above any temperature used in our experiments and in the literature and only heterogeneous nucleation would be present.

Figure 8 shows the dimensionless delay time of n-pentane, n-hexane, and ethanol from the same nozzle No. II with  $\Delta P = 8.96 \times 10^5 \text{ N/m}^2$ . The data of each test liquid shows its own trend although they cluster together.

Figures 6-8 show that factors other than those included in  $\phi$  and  $\psi$  influence the delay time of flashing jets. Fig. 9 shows that the seven least-square fit straight lines of Figs. 6-8 can be correlated by an equation of the form

$$\phi\psi^k = c \quad (3)$$

Where  $k$  and  $c$  vary with jet diameter, pressure, and liquid properties due to unidentified effects. In principle, it is still possible that  $\phi$  and  $\psi$  include all the controlling effects of our data. For that,  $k$  and  $c$  would have to be shown to be unique functions of them. Instead, it is more likely that heterogeneous nucleation influences the initial stability ( $R_0$ ) and growth rate ( $t_0$ ) of the bubbles. An attempt to consider the initial gas content of the liquid within an existing theoretical framework (Lienhard, 1964; Ma and Wang, 1962) was undertaken but did not lead to a better correlation of the data.

#### JET DIVERGENCE ANGLE

Lienhard (1966) proposed that the superheat energy of a fraction of the liquid is transformed into kinetic energy of the spray thus determining, together with the jet velocity, the initial angle of the spray (see Fig. 1). For the spray angle he obtained

$$\sin \frac{\alpha}{2} = C' \frac{U_e}{U_0} = C' \left[ \frac{C_{p,L}}{T_{\text{sat}}(P_{\text{amb}})} \right]^{1/2} \frac{\Delta T}{U_0} \quad (4)$$

where  $C'$  is a dimensionless constant much less than unit.

In Fig. 10,  $\sin \frac{\alpha}{2}$  is plotted versus  $\left[ \frac{C_{p,L}}{T_{sat}(P_{amb})} \right]^{1/2} \frac{\Delta T}{U_o}$

for all the experimental conditions. It can be seen that Eq. (4) does not correlate the jet divergence angle completely and that effects of injection pressure, nozzle diameter, and liquid properties are not included. A comparison of the slope of each set of data shows that the experimental data can be rearranged into the form

$$\sin \frac{\alpha}{2} = C' \left[ \frac{C_{p,L}}{T_{sat}(P_{amb})} \right]^{1/2} \frac{\Delta T - \Delta T_o'}{U_o} \quad (5)$$

by introducing a different empirical constant  $\Delta T_o'$  for each set of data (Fig. 11). But the physical meaning of  $\Delta T_o'$  is unclear and its value for different experimental conditions cannot be predicted.

Another approach has been used to represent the spray angle data. The cross sectional area of jet can be considered as the sum of the parts occupied by liquid and bubbles,

$$A = \frac{\pi}{4} D_o^2 + \pi R^2 n \quad (6)$$

where  $R^2 \equiv r_{20}^2 \equiv \frac{\sum n_i r_i^2}{\sum n_i}$  is surface-mean radius of the bubbles,  $n = \sum n_i$  is the total number of bubbles in one cross-section of the jet, and  $n_i$  is the number of bubbles with radius  $r_i$  in one cross-section.

The expanding rate of the jet then can be found by differentiation of Eq.(6) with respect to time,

$$\begin{aligned} \dot{A} &= 2\pi R_s \dot{R}_s \\ &= 2\pi R \dot{R} n \end{aligned}$$

where  $R_s$  and  $\dot{R}_s$  represent the radius and expanding rate of the jet. At the beginning of breakup,  $R_s \approx D_o/2$  and, referring to Fig. 1

$$\begin{aligned} (\tan \frac{\alpha}{2}) \text{ at breakup} &= \frac{\dot{R}_s}{U_o} \\ &\approx n \frac{2R\dot{R}}{D_o} \end{aligned} \quad (7)$$

The asymptotic solution for the heat conduction controlled bubble growth, as shown by Forster and Zuber (1954), is

$$R = \left( \frac{C_{p,L} \Delta T}{h_{fg}} \right) \left( \frac{\rho_L}{\rho_v} \right) \sqrt{\pi \alpha_L t} \quad (8a)$$

We can also formulate the expression for the bubble growth rate phenomenologically as shown in Plesset and Prosperitti (1977).

The heat flux from the liquid into the bubble is approximately equal to  $4\pi R^2 (\alpha_L \rho_L C_{p,L}) \frac{\Delta T'}{\sqrt{\alpha_L t}}$ , where  $\Delta T' = T_L - T_{sat}(P_b)$  and  $P_b$  is no longer equal to  $P_{amb}$ . This energy is converted into the latent heat of vaporization,  $4\pi R^2 \dot{R} \rho_v h_{fg}$ , as the bubble grows. Equating the above two quantities, we obtain

$$\dot{R} \approx \left( \frac{C_{p,L} \Delta T'}{h_{fg}} \right) \left( \frac{\rho_L}{\rho_v} \right) \sqrt{\frac{\alpha_L}{t}} \quad (8b)$$

Equation (8b) differs from equation (8a) by a factor of  $\sqrt{\pi/4}$  and for having  $\Delta T'$  instead of  $\Delta T$ .

Hooper and Abdelmessih (1966), Mayinger and Hollborn (1977), and Suzuki et al. (1978) have observed, in their experiments, that Eq. (8a) overpredicts the bubble radius especially at higher degrees of superheat. This deviation is believed to be due to the bubble vapor pressure equilibrium assumption which is generally valid when the liquid temperature is just slightly above  $T_{\text{sat}}(P_{\text{amb}})$ .

Dalle, Donne and Ferranti (1975), by comparisons with numerical solutions for vapor bubble growth in sodium, also found that the use of a modified Jakob number, based on  $\Delta T'$ , leads to a significantly improved expression of the vapor bubble growth. We have adopted  $\Delta T'$  for the expressions of  $R$  and  $\dot{R}$ , but kept the linear dependence on the degree of superheat by introducing an empirical constant  $\Delta T_0$  which is equal to the difference between  $\Delta T$  and  $\Delta T'$ . Because of the uncertainty about  $P_b$ , the value of  $\Delta T_0$  is not known a priori.

Thus, the expressions for  $R$  and  $\dot{R}$  in the present work are

$$R = \left( \frac{C_{p,L}(\Delta T - \Delta T_0)}{h_{fg}} \right) \left( \frac{\rho_L}{\rho_v} \right) \sqrt{\pi \alpha_L t}$$

$$\dot{R} = \frac{1}{2} \left( \frac{C_{p,L}(\Delta T - \Delta T_0)}{h_{fg}} \right) \left( \frac{\rho_L}{\rho_v} \right) \sqrt{\frac{\pi \alpha_L}{t}}$$

and after substituting them in Eq.(7), the following relationship for the spray angle is obtained

$$\left( \tan \frac{\alpha}{2} \right)_{\text{at breakup}} \approx n\pi \left( \frac{\rho_L}{\rho_v} \frac{C_{p,L}(\Delta T - \Delta T_0)}{h_{fg}} \right)^2 \left( \frac{\alpha_L}{U_0 D_0} \right) \quad (9)$$

The jet divergence angle,  $(\tan \frac{\alpha}{2})^{1/2}$  is plotted versus  $\left(\frac{\rho_L}{\rho_v} \frac{C_{p,L} \Delta T}{h_{fg}}\right) \left(\frac{\alpha_L}{U_o D_o}\right)^{1/2}$  in Fig. 12; notice the use of  $\Delta T$  instead of  $(\Delta T - \Delta T_o)$ , and each set of data is seen to have its own trend. But if it is assumed that the number of bubbles at breakup is proportional to the jet diameter, that is

$$n\pi = C^* \left(\frac{D_o}{D_{o,I}}\right)$$

where  $D_{o,I}$  is the diameter of nozzle No. I and  $C^*$  is the same empirical constant for all the conditions, then Eq.(9) becomes

$$\tan \frac{\alpha}{2} \text{ at breakup} \approx C^* \left(\frac{D_o}{D_{o,I}}\right) \left(\frac{\rho_L}{\rho_v} \frac{C_{p,L} (\Delta T - \Delta T_o)}{h_{fg}}\right)^2 \left(\frac{\alpha_L}{U_o D_o}\right) \quad (10)$$

The jet divergence angle  $(\tan \frac{\alpha}{2})^{1/2}$  is now plotted versus  $\left(\frac{D_o}{D_{o,I}}\right)^{1/2} \left(\frac{\rho_L}{\rho_v} \frac{C_{p,L} \Delta T}{h_{fg}}\right) \left(\frac{\alpha_L}{U_o D_o}\right)^{1/2}$  in Fig. 13. Notice again the use of  $\Delta T$  instead of  $(\Delta T - \Delta T_o)$ . The data for three different nozzle diameters, two liquid pressures, and n-pentane and n-hexane are seen to coalesce, even though a pressure effect is still discernible, but those for ethanol are still uncorrelated. Since the chemical structures of n-pentane and n-hexane are similar, whereas that of ethanol is different, it may not be unreasonable to assume that the bubble vapor temperature at breakup is similar for the first two liquids and different for the third one, that is, to use one value of  $\Delta T_o$  for n-pentane and n-hexane, 45 K, and a different one for ethanol, 52.4 K. In Fig. 14, it is seen that Eq. 10 correlates all the data with the two values of  $\Delta T_o$  and  $C^* = 13.8$ . However, no explanation is available for the number of bubbles to be proportional to the jet diameter and no method is known to predict  $\Delta T_o$  for different liquids.

# NOTATIONS

$A$	=	cross sectional area of jet. ( $m^2$ )
$\dot{A}$	=	rate of change of jet cross-sectional area. ( $\mu m^2/s$ )
$c$	=	empirical constant in Eq. (3)
$C_{p,L}$	=	specific heat of liquid. ( $J/kg \cdot K$ )
$C'$	=	empirical constant in Eq. (4) and (5).
$C^*$	=	empirical constant in Eq. (10)
$D_o$	=	diameter of nozzle. ( $\mu m$ )
$D_{o,I}$	=	diameter of nozzle I. ( $\mu m$ )
$h_{fg}$	=	latent heat of vaporization. ( $J/kg$ )
$k$	=	empirical exponent in Eq. (3)
$L$	=	intact length. (mm)
$l$	=	length of orifice. (mm)
$n$	=	total number of bubbles in one cross-section of the jet.
$n_i$	=	number of bubbles with radius $r_i$ in one cross-section of the jet.
$P_{amb}$	=	pressure of ambient nitrogen. ( $N/m^2$ )
$P_b$	=	vapor pressure inside the bubble. ( $N/m^2$ )
$P_L$	=	liquid pressure. ( $N/m^2$ )
$P_v$	=	vapor pressure at liquid temperature $T_L$ . ( $N/m^2$ )
$R$	=	radius of bubble. ( $\mu m$ )
$\dot{R}$	=	rate of bubble growth, $R = \frac{dR}{dt}$ . ( $\mu m/s$ )

# NOTATIONS (CONT'D)

$R_o$	=	radius of an unstable equilibrium vapor bubble, $R_o = \frac{2\sigma_L}{P_v - P_{amb}} \cdot (\mu m)$
$R_s$	=	radius of jet. ( $\mu m$ )
$\dot{R}_s$	=	expanding rate of jet in the radial direction. ( $\mu m/s$ )
$r_i$	=	spectrum of bubble radius. ( $\mu m$ )
$r_{20}$	=	surface-mean radius of bubbles. ( $\mu m$ )
$T_L$	=	liquid temperature. (K)
$T_{sat}(P_{amb})$	=	saturation temperature of liquid at $P_{amb}$ . (K)
$T_{sat}(P_b)$	=	saturation temperature of liquid at $P_b$ . (K)
$t$	=	time (s)
$t_D$	=	delay time. ( $\mu s$ )
$t_o$	=	characteristic time of the initial growth of a vapor bubble, $t_o = (\rho_L R_o^3 / 2\sigma_L)^{1/2} \cdot (s)$
$U_e$	=	explosive velocity of a flashing jet. (m/s)
$U_o$	=	average velocity of jet. (m/s)
Greek Letters:		
$\alpha$	=	jet divergence angle. (degree)
$\alpha_L$	=	thermal diffusivity of liquid. ( $m^2/s$ )
$\Delta G$	=	free energy needed to create an unstable equilibrium vapor bubble.



# NOTATIONS (CONT'D)

$\Delta P$	=	effective injection pressure, $\Delta P = P_L - P_{amb}$ . (N/m <sup>2</sup> )
$\Delta T$	=	$T_L - T_{sat}(P_{amb})$ . (K)
$\Delta T'$	=	$T_L - T_{sat}(P_b)$ . (K)
$\Delta T_o$	=	$T_{sat}(P_b) - T_{sat}(P_{amb})$ . (K)
$\Delta T_o'$	=	empirical constant in Eq.(5). (K)
$\Delta \theta$	=	dimensionless temperature, $\Delta \theta = \frac{T_L - T_{sat}(P_{amb})}{T_{sat}(P_L) - T_{sat}(P_v)}$
$\rho_L$	=	density of liquid. (kg/m <sup>3</sup> )
$\rho_v$	=	density of vapor. (kg/m <sup>3</sup> )
$\sigma_L$	=	surface tension of liquid. (N/m)
$\phi$	=	dimensionless delay time, $\phi = \frac{(P_v - P_{amb})^{5/2} D_o}{\sigma_L \rho_L^{1/2}} t_D$
$\psi$	=	dimensionless superheat, $\psi = \frac{D_o (P_v - P_{amb})}{\sigma_L}$

## REFERENCES

- Avedisian, C.T., "Superheating and Boiling of Water in Hydrocarbons and of Hydrocarbon Mixtures," Princeton University, Ph.D. Thesis (1980).
- Blander, M. and Katz, J.L., "Bubble Nucleation in Liquids," *AIChE J.*, 21, 833 (1975).
- Brown, R. and York, J.L., "Sprays Formed by Flashing Liquid Jets," *AIChE J.*, 8, 149 (1962).
- Dalle Donne, M. and Ferranti, M.P., "The Growth of Vapor Bubbles in Superheated Sodium," *Int. J. Heat Mass Transfer*, 18, 477 (1975).
- Forster, H.K. and Zuber, N., "Growth of Bubble in a Superheated Liquid," *J. Appl. Phys.*, 25 (4), 474 (1954).
- Frenkel, J., "Kinetic Theory of Liquids," Ch. VII, Dover Publications, New York (1955).
- Gallant, R.W., "Physical Properties of Hydrocarbons," Vol. 1, Gulf Publishing Co., Houston, Texas (1968).
- Hooper, F.C. and Abdelmessih, A.H., "The Flashing of Liquids at High Superheats," *Proc. Third Int. Heat Transfer Conference*, Chicago, Vol. IV, 44 (1966).
- Lienhard, J.H., "An Influence of Superheat Upon the Spray Configurations of Superheated Liquid Jets," *J. Basic Eng., Trans. ASME, Series D*, 88, 685 (1966).
- Lienhard, J.H., "Some Generalizations of the Stability of Liquid-Gas-Vapor Systems," *Int. J. Heat Mass Transfer*, 7, 813 (1964).
- Lienhard, J.H. and Day, J.B., "The Breakup of Superheated Liquid Jets," *J. Basic Eng., Trans. ASME, Series D*, 92, 515 (1970).
- Lienhard, J.H. and Stephenson, J.M., "Temperature and Scale Effects Upon Cavitation and Flashing in Free and Submerged Jets," *J. Basic Eng., Trans. ASME, Series D*, 88, 525 (1966).
- Ma, J.T.S. and Wang, P.K.C., "Effect of Initial Air Content on the Dynamics of Bubbles in Liquids," *IBM J.* 6, 472, (1962).
- Mayinger, F. and Hollborn, E., "The Effect of Liquid Viscosity on Bubble Formation and Heat Transfer in Boiling," Ch. 17 of "Heat Transfer in Boiling," edited by Hahne, E. and Grigull, U., Hemisphere Publishing Co., Washington (1977).
- Plesset, M.S. and Prosperetti, A., "Bubble Dynamics and Cavitation," *Ann. Rev. Fluid Mech.*, 9, 145 (1977).
- Reitz, R.D. and Bracco, F.V., "Ultra High Speed Filming of Atomizing Jets," *Phys. Fluids*, 22 (6), 1054 (1979).
- Suzuki, M., Yamamoto, T., Futagami, N., and Maeda, S., "Atomization of Superheated Liquid Jet," *The 1st Int. Conference on Liquid Atomization and Spray Systems Proc.*, 37 (1978).

TABLE 1. Superheated Liquid Jet Experiments

Author	Test Liquid	$\Delta\theta$	Liquid Pressure (N/m <sup>2</sup> ) Gas and Pressure (N/m <sup>2</sup> )	Nozzle D <sub>o</sub> (μm) 1/D <sub>o</sub>	Measurement
Brown and York (1962)	Water and Freon-11	≈ 0.5	Air 1.01x10 <sup>5</sup>	500-2,000 0.8~3 with different surface roughness	Drop Size
Lienhard and Stephenson (1966)	Water	≈ 0.7	Air 1.01x10 <sup>5</sup>	2,400 4,000	Delay Time
Lienhard (1966)	Water	≈ 0.4	Air 1.01x10 <sup>5</sup>	3,200 66	Jet Angle
Lienhard and Day (1970)	Water and Liquid Nitrogen	≈ 0.7	Air 1.01x10 <sup>5</sup>	800 ~ 3,200	Delay Time
Suzuki, Yamamoto Futagami and Maeda (1978)	Water	≈ 0.7	(?) 1.01x10 <sup>5</sup> and 2.75x10 <sup>4</sup>	400 500 600	1.67~4.00 Delay Time and Bubble Growth Rate
Present Work	n-Pentane n-Hexane and Ethanol	0.25~0.99	1.02x10 <sup>6</sup> and 4.27x10 <sup>6</sup> Nitrogen 1.29x10 <sup>5</sup>	127 343 660	2.0 and 4.0 Delay Time and Jet Angle

TABLE 2. Dimensions of Nozzles

NO.	DIAMETER ( $\mu\text{m}$ )	$l/D_o$
I	127	2.0
II	343	4.0
III	660	4.0

TABLE 3. Test Liquids and Experimental Temperature Ranges

Test Liquid	Manufacturer	Temp. Range (K)
n-Pentane	Mallinckrodt, Inc., 6172	373 - 396
n-Hexane	Fisher Scientific Co., H-291 S	410 - 431
Ethanol	Dept. of Chemistry, Princeton University	425 - 432

TABLE 4. Experimental Conditions and Data

Run	No. of Data	Nozzle	Liquid	$\Delta P \times 10^{-5}$ (N/m <sup>2</sup> )	$U_o$ (m/s)	$T_L$ (K)	L (mm)	$t_D$ (us)		$\alpha$ (degrees)		
								Mean Value	Stan. Dev.	Mean Value	Stan. Dev.	
1	2	I	n-C <sub>6</sub> H <sub>14</sub>	8.96	22.0	419	2.86	130	4.1	49.9	12.6	
2	3	I				420	2.23	102	17.1	62.5	9.6	
3	2	I				421	1.12	50.7	22.5	65.9	0.1	
4	3	I				422	1.22	55.4	7.0	72.9	7.4	
5	3	I				423	0.94	42.7	7.4	69.9	5.8	
6	4	I				424	0.74	33.4	5.1	71.8	5.1	
7	5	I				425	0.60	27.4	3.8	71.0	10.0	
8	3	I				426	0.53	24.2	7.3	79.1	5.2	
9	5	I				428	0.36	16.2	5.5	86.2	5.7	
10	3	I				430	0.18	8.2	0.0	92.8	3.1	
11	2	II	"	"	21.2	410	5.58	263	73.8	17.0	5.6	
12	1	II	"	"		412	3.97	187	---	20.0	---	
13	4	II	"	"		413	3.86	182	110.0	23.1	6.5	
14	1	II	"	"		415	3.19	150	---	37.3	---	
15	2	II	"	"		418	2.32	110	5.0	45.2	0	
16	2	II	"	"		419	1.80	84.9	47.2	49.1	20.5	
17	2	II	"	"		423	0.69	32.5	4.8	69.9	3.8	
18	2	II	"	"		424	0.26	12.3	3.4	82.5	7.8	
19	1	II	"	"		428	0.08	3.8	---	90.0	---	
20	1	III	"	"		26.9	413	13.25	492	---	27.0	---
21	1	III	"	"	419		2.95	110	---	48.4	---	
22	2	III	"	"	421		2.79	104	3.3	55.6	1.9	
23	2	III	"	"	423		2.12	78.8	5.0	76.8	6.6	
24	3	III	"	"	424		0.98	36.4	15.1	87.9	14.3	
25	1	III	"	"	426		0.71	26.4	---	78.9	---	
26	2	III	"	"	427		0.73	27.1	7.2	90.0	11.2	
27	2	III	"	"	429		0.73	27.1	7.2	103.1	8.6	
28	2	I	"	41.4	46.2		415	2.86	61.9	2.7	8.0	0.0
29	2	I	"				"	420	2.00	43.3	2.4	14.3
30	1	I	"			"	428	0.85	18.4	---	34.8	---
31	2	I	"			"	430	0.68	14.7	0.3	40.2	8.8
32	1	I	"			"	431	0.56	12.1	---	47.0	---
33	3	II	"			"	410	5.14	115	49.8	6.7	0.7
34	1	II	"			"	412	4.73	107	---	8.8	---
35	2	II	"			"	414	3.50	78.9	1.7	12.2	0.3
36	2	II	"			"	418	1.78	40.1	0	20.0	1.4
37	3	II	"			"	430	0.69	15.6	0.6	42.1	1.4
38	1	II	n-C <sub>5</sub> H <sub>12</sub>	8.96	24.5	373	12.50	510	---	6.0	---	
39	1	II				374	14.25	582	---	7.0	---	
40	1	II				375	10.54	430	---	17.1	---	
41	2	II				378	5.45	222	116.6	22.5	10.6	
42	2	II				385	2.59	106	11.6	56.2	4.4	
43	1	II				387	1.64	66.9	---	62.0	---	
44	2	II				389	1.06	43.3	12.7	59.6	1.6	
45	2	II				391	0.77	31.4	12.4	77.4	0.8	
46	3	II				393	0.69	28.2	4.8	81.4	1.2	
47	1	II				394	0.71	29.0	---	74.8	---	
48	2	II	"	"	395	0.27	11.0	2.6	88.0	6.3		
49	2	II	"	"	396	0.28	11.4	4.3	97.5	3.2		
50	1	II	C <sub>2</sub> H <sub>5</sub> OH	19.9	425	8.75	440	---	24.0	---		
51	3	II			427	4.68	235	54.3	42.5	19.6		
52	3	II			429	4.07	204	218.0	67.7	11.7		
53	3	II			430	1.68	84.4	94.9	84.2	11.1		
54	2	II			431	0.95	47.7	25.9	87.0	3.2		
55	2	II			432	0.75	37.7	10.8	79.9	4.9		

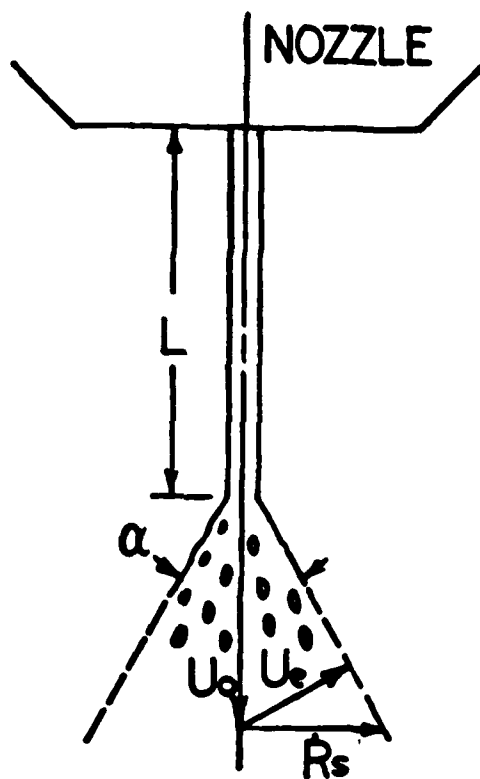


Fig. 1 Definitions of intact length and jet divergence angle (or spray angle).

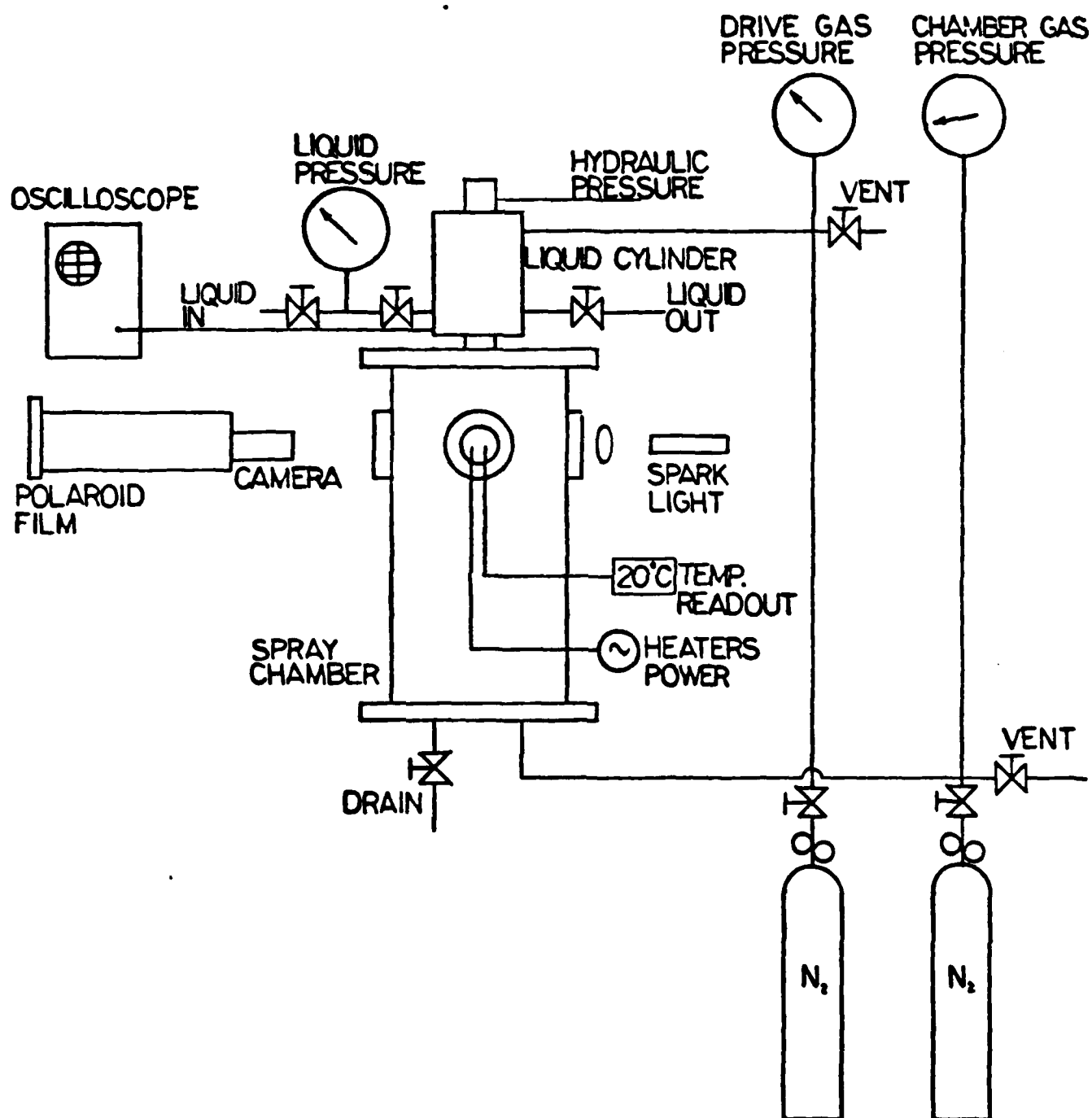


Fig. 2 Schematic diagram of the experimental apparatus.

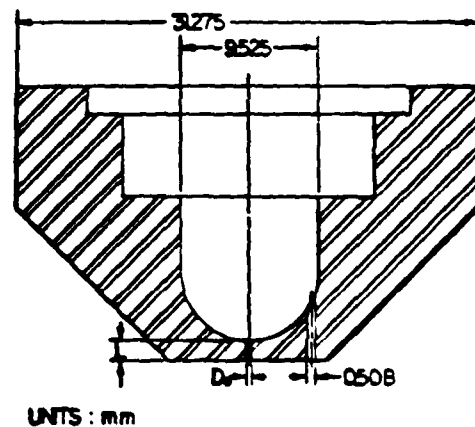
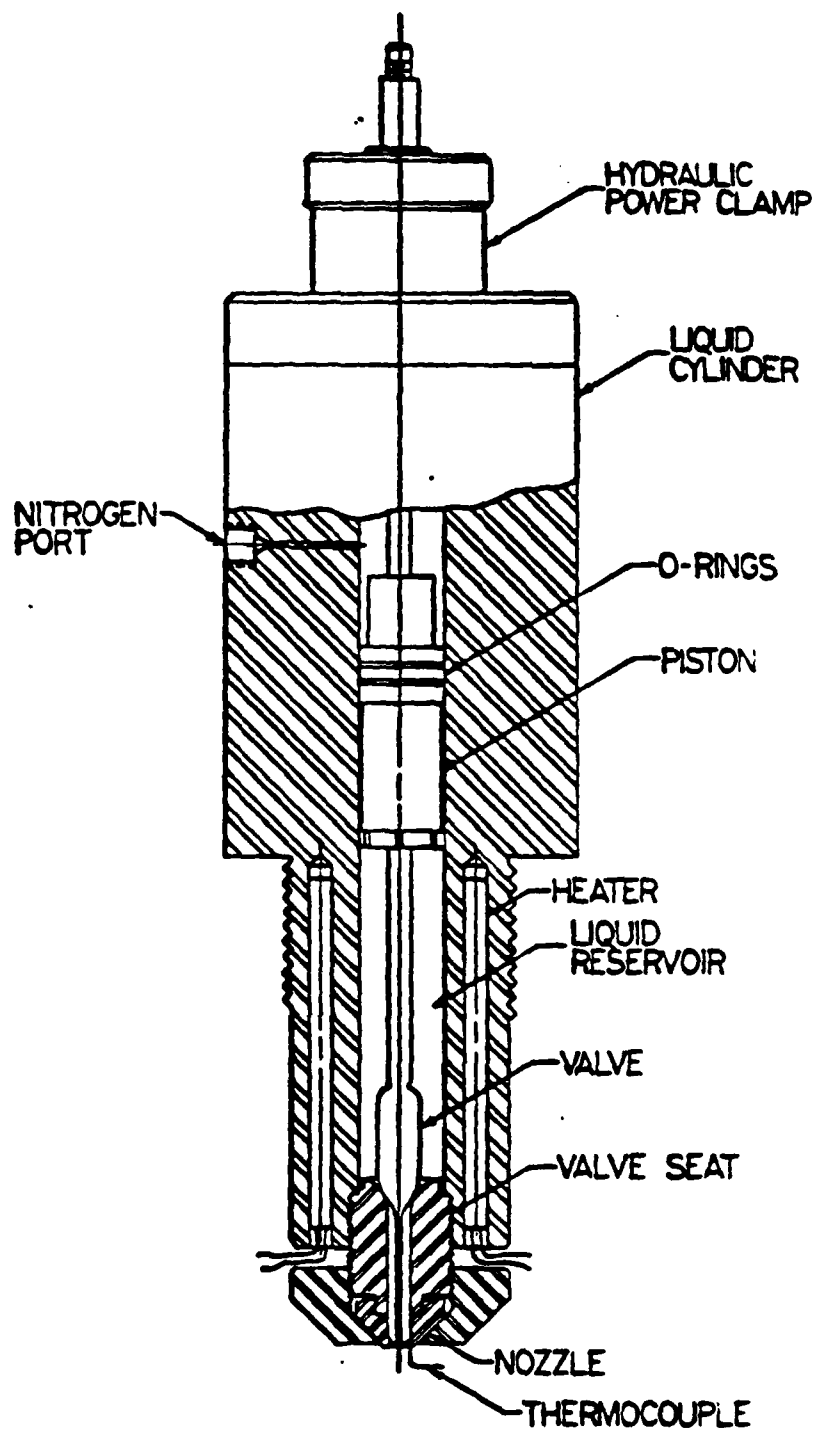


Fig. 3 Details of the liquid cylinder and nozzle.



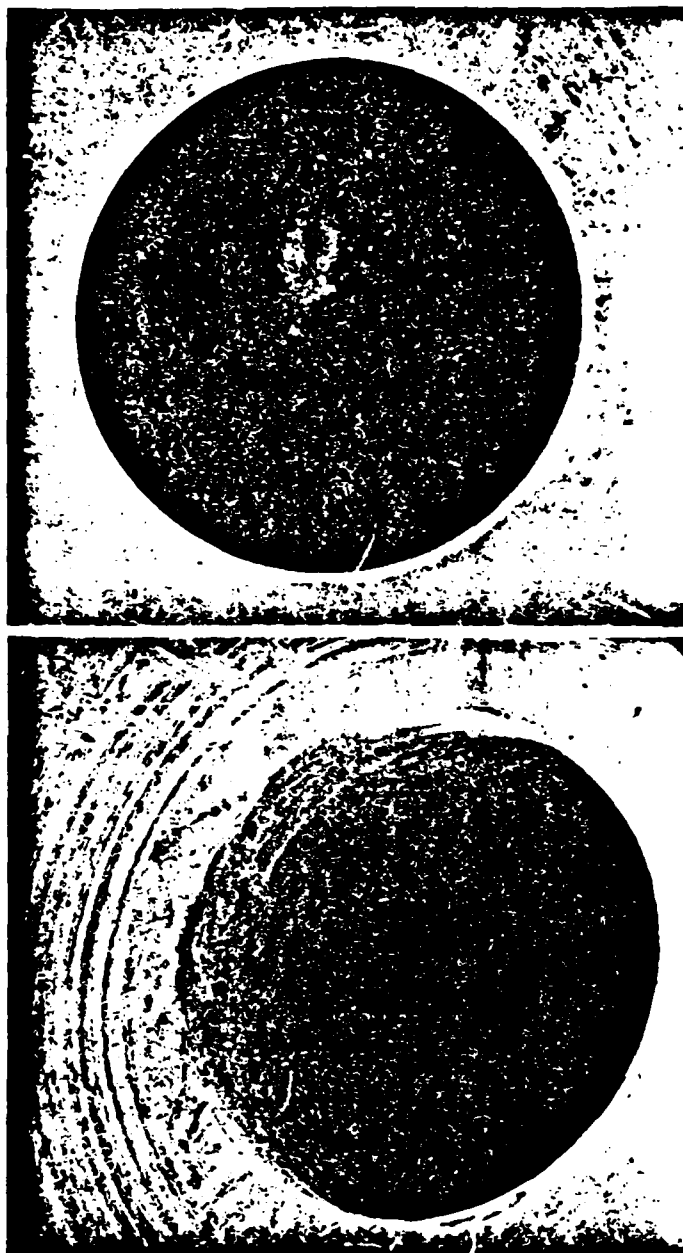


Fig. 4 Typical photographs of the nozzle entrance of Nozzle III.

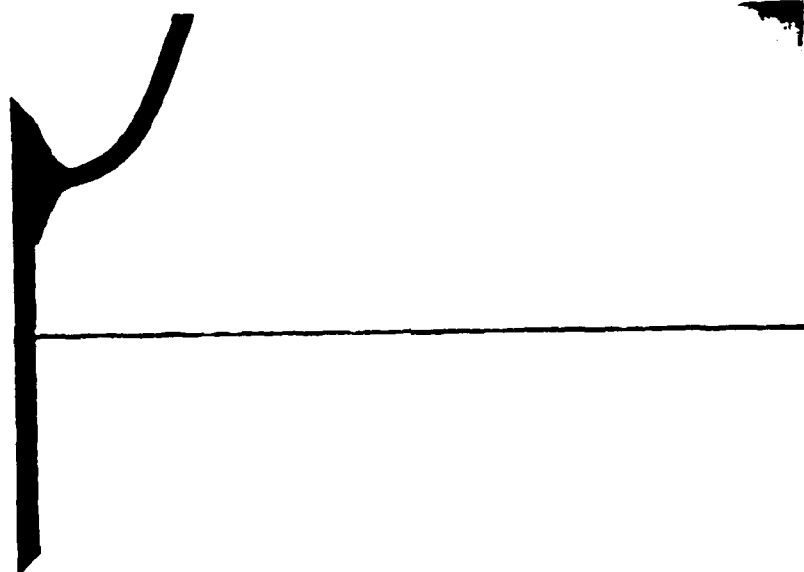


(a)

(b)

(c)

Fig. 5 Jet configurations at different degrees of superheat.  
 n-hexane, Nozzle I,  $\Delta P = 8.96 \times 10^5 \text{ N/m}^2$ ,  $P_{amb} = 1.29 \times 10^5 \text{ N/m}^2$ , (a)  $T_L = 293\text{K}$ , (b)  $T_L = 420\text{K}$  (c)  $T_L = 428\text{K}$ .







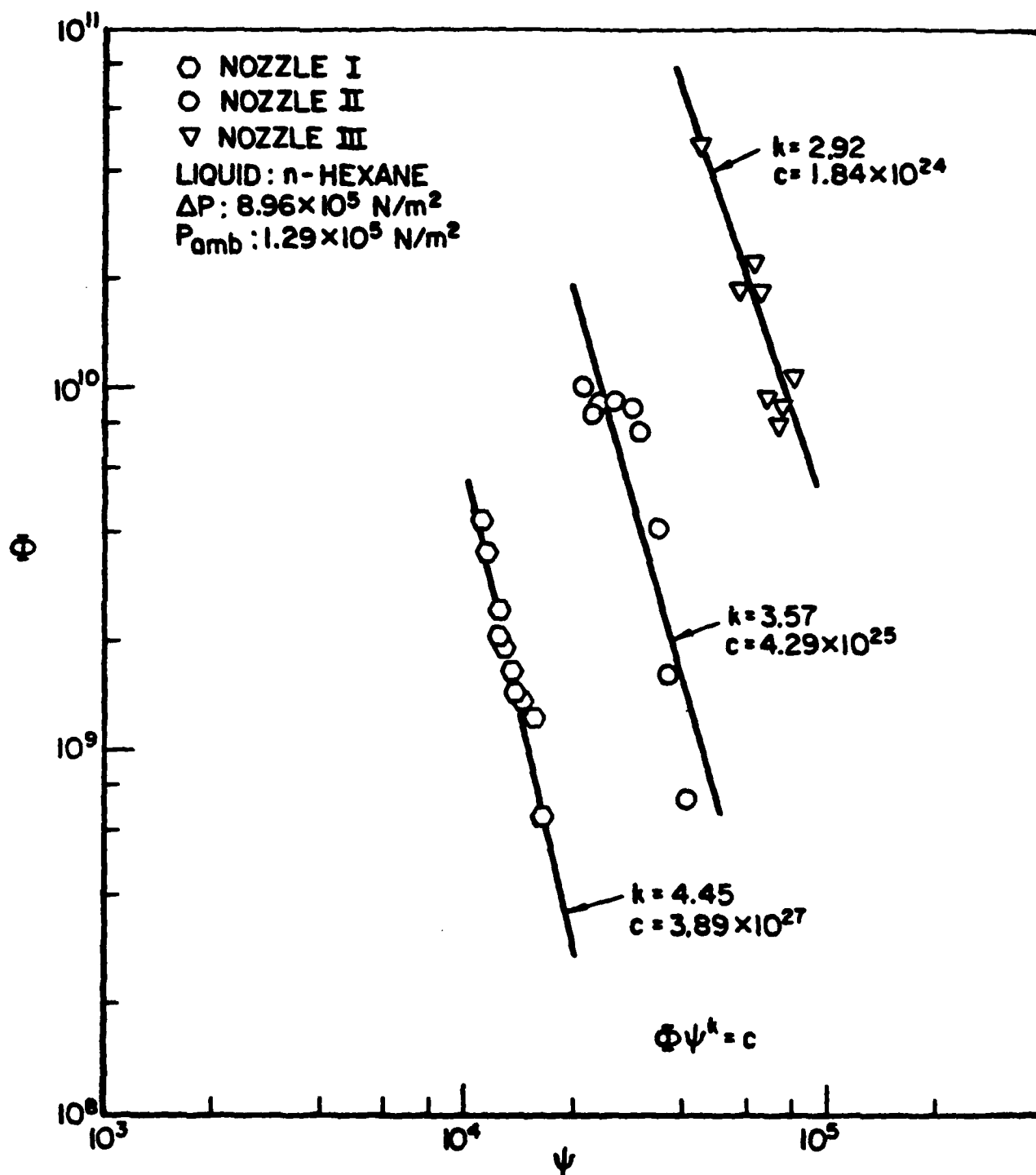


Fig. 6 Variation of dimensionless delay time with dimensionless superheat for different nozzle sizes at low injection pressure.

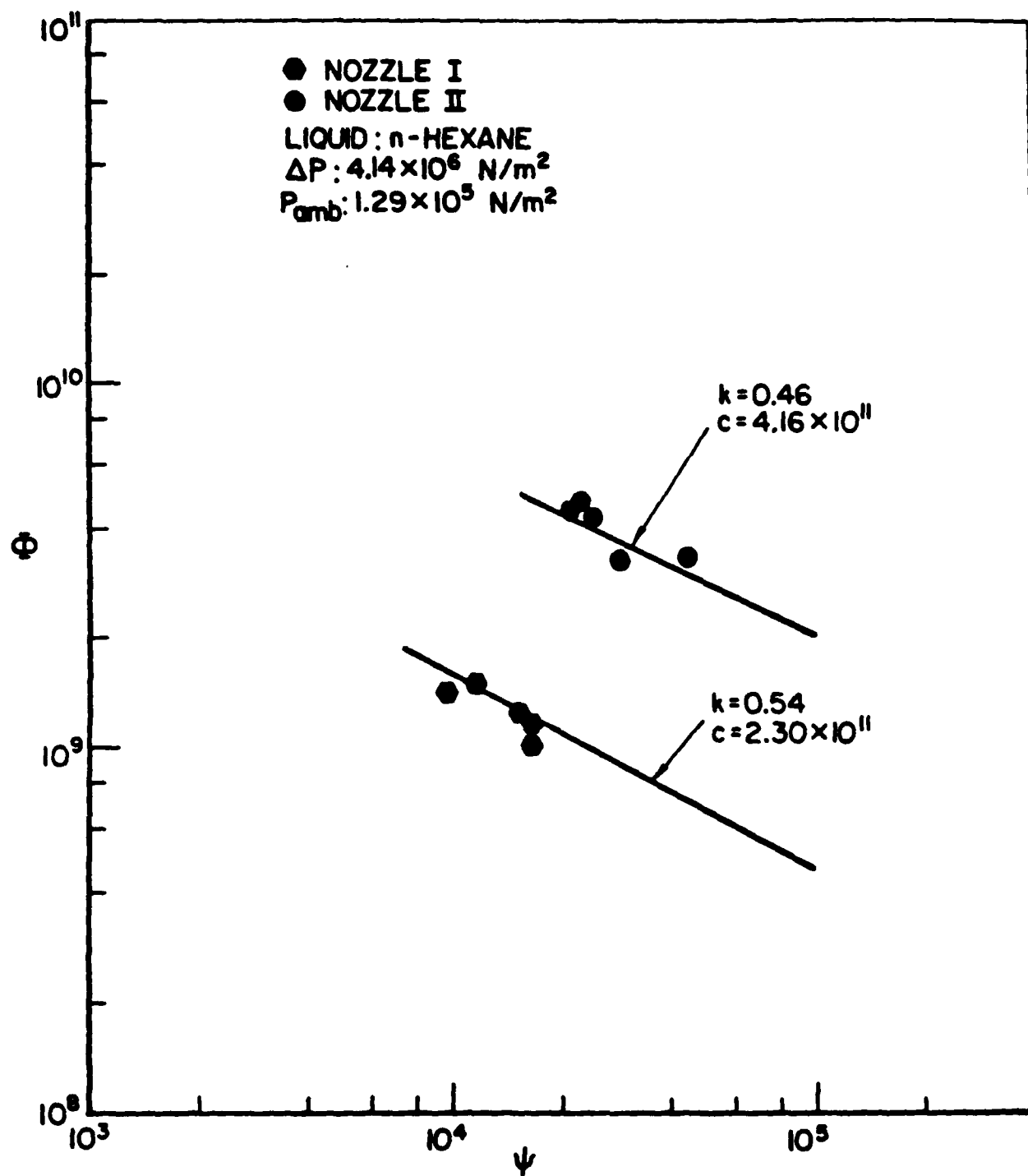


Fig. 7 Variation of dimensionless delay time with dimensionless superheat for different nozzle sizes at high injection pressure.

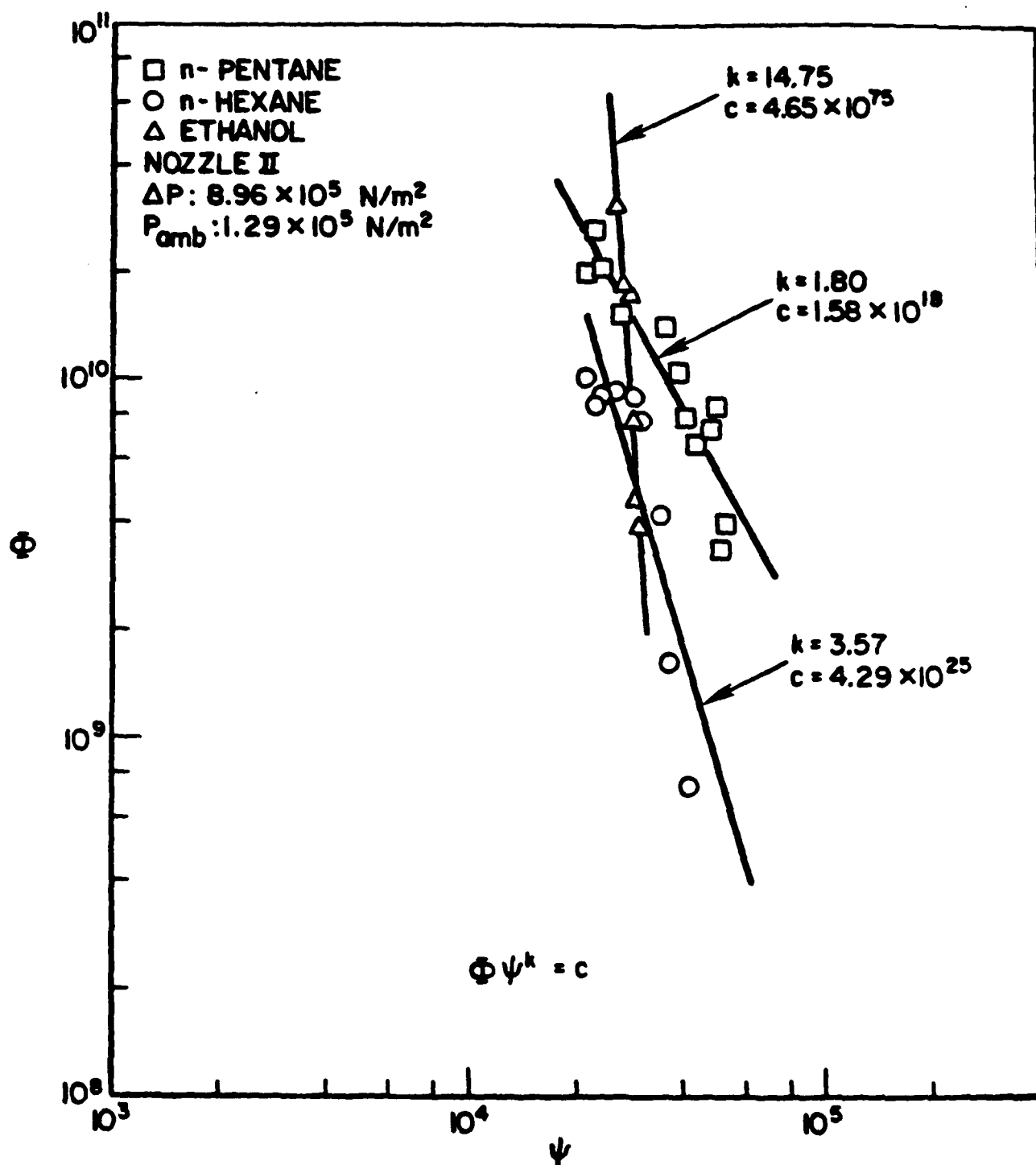


Fig. 8 Variation of dimensionless delay time with dimensionless superheat for different liquids.



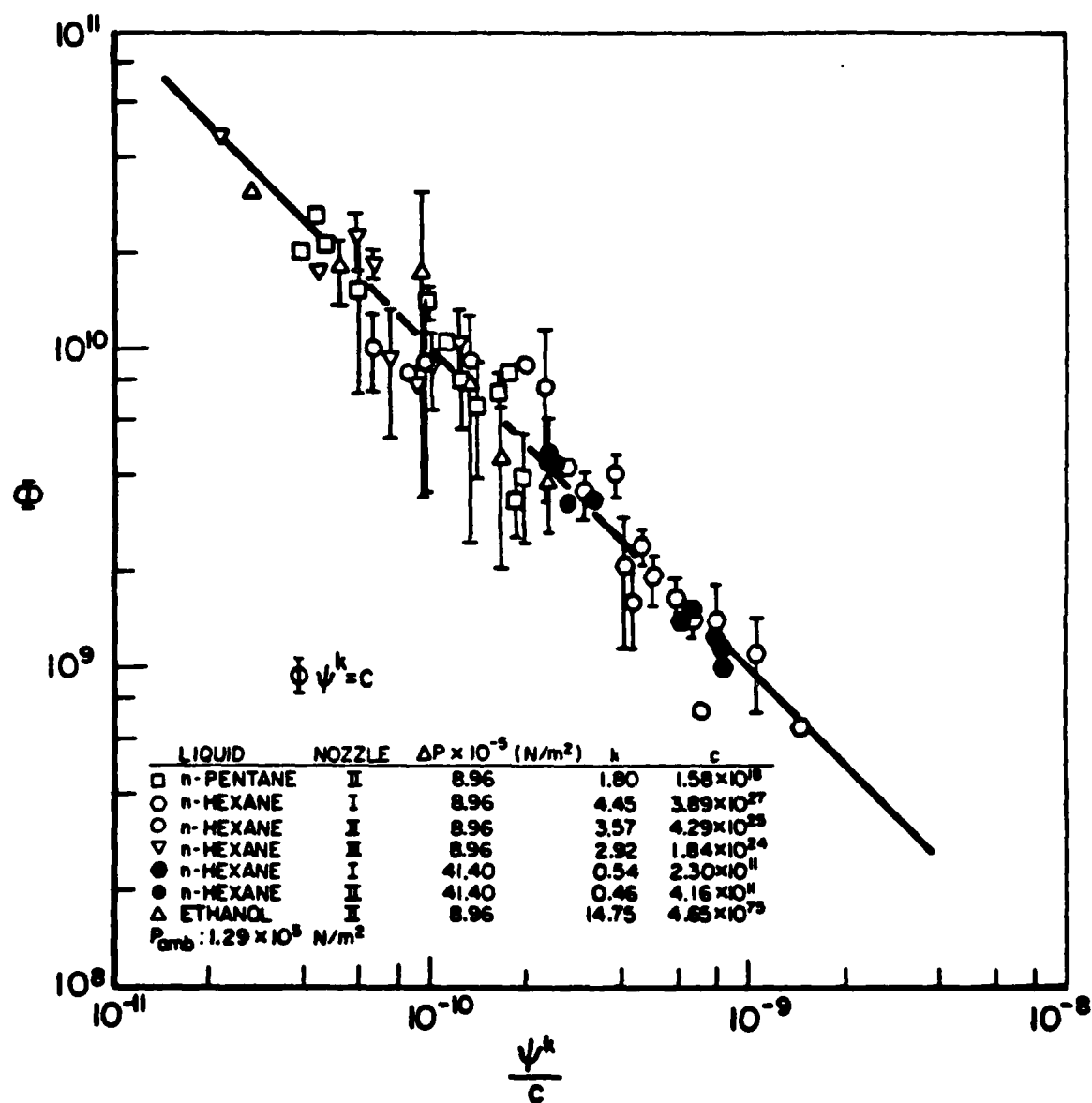


Fig. 9 Variation of dimensionless delay time with dimensionless superheat based on Eq.(3).

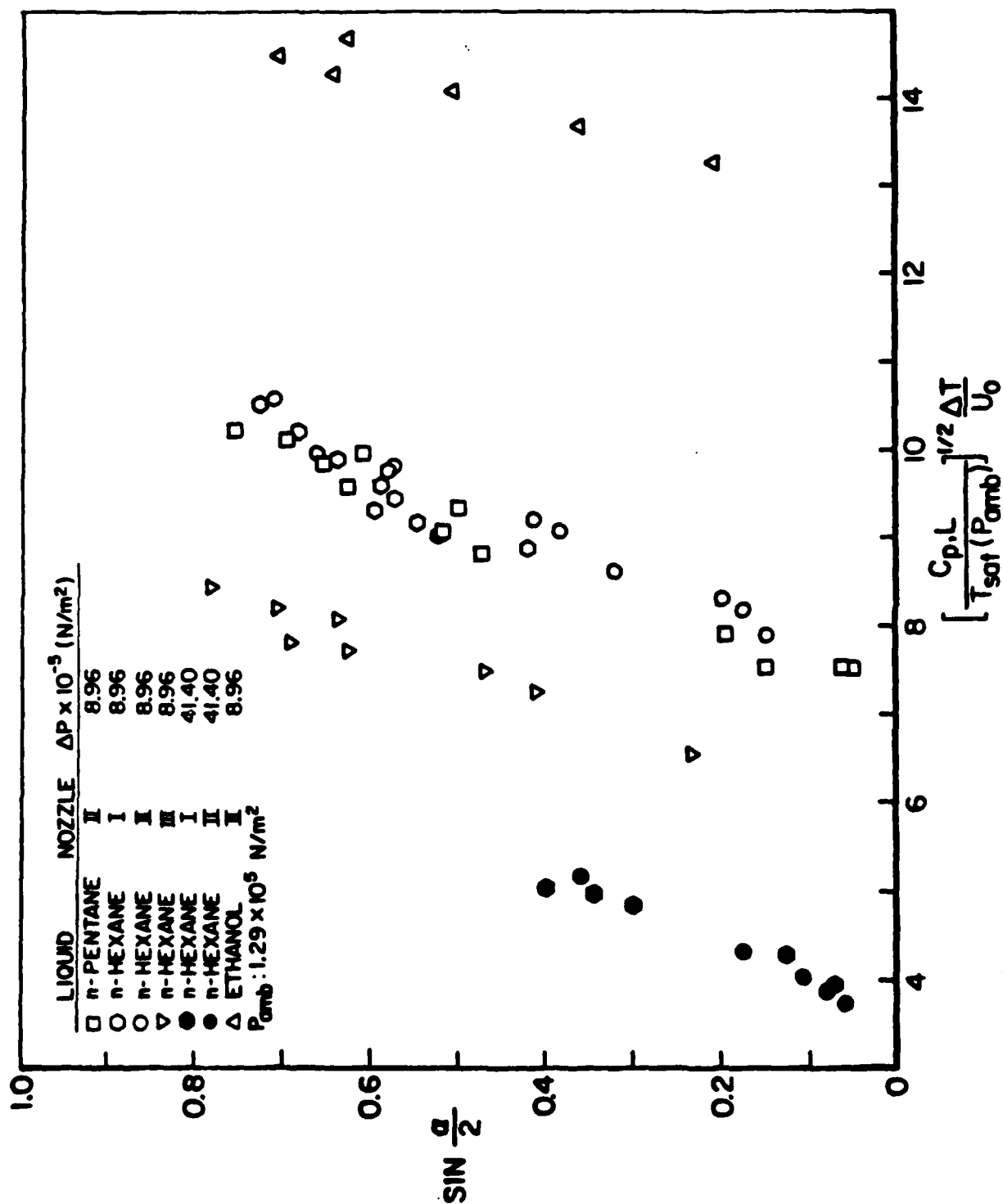


Fig. 10 Variation of jet divergence angle with degree of superheat based on Lienhard's (1966) expression.

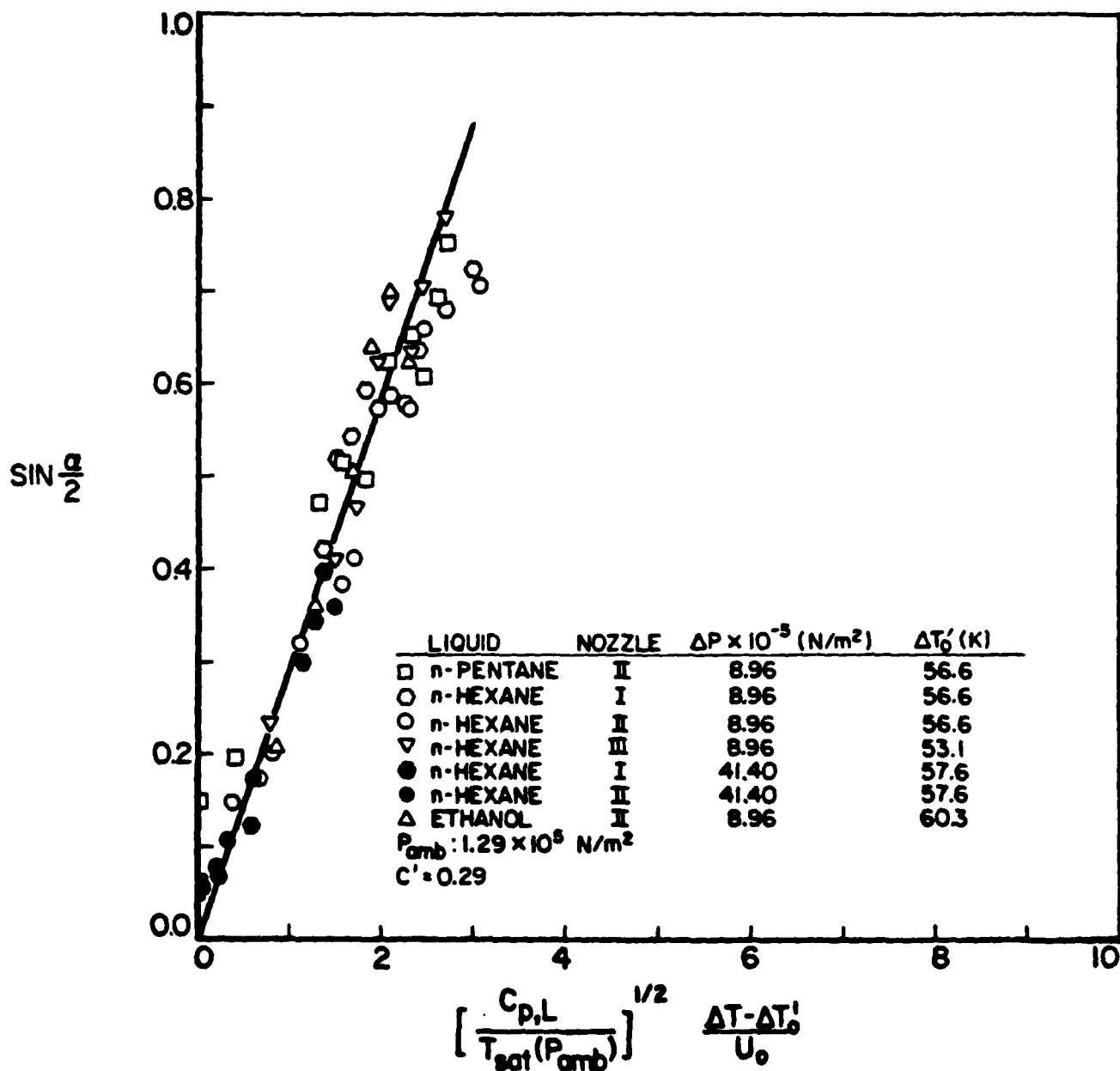


Fig. 11 Variation of jet divergence angle with degree of superheat based on a modified Lienhard's (1966) expression.

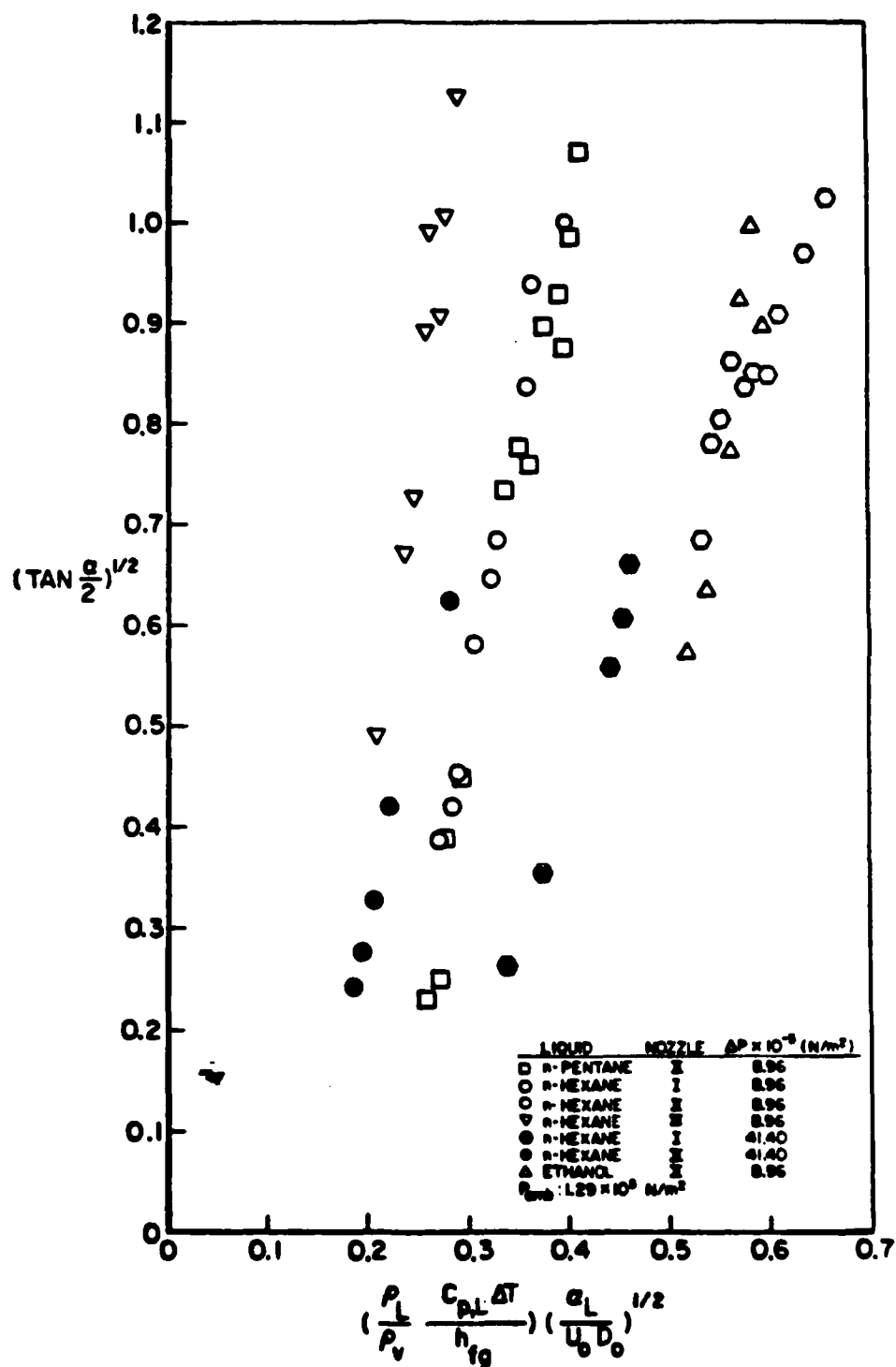


Fig. 12 Variation of jet divergence angle with degree of superheat based on consideration of heat-transfer-controlled bubble growth rate.

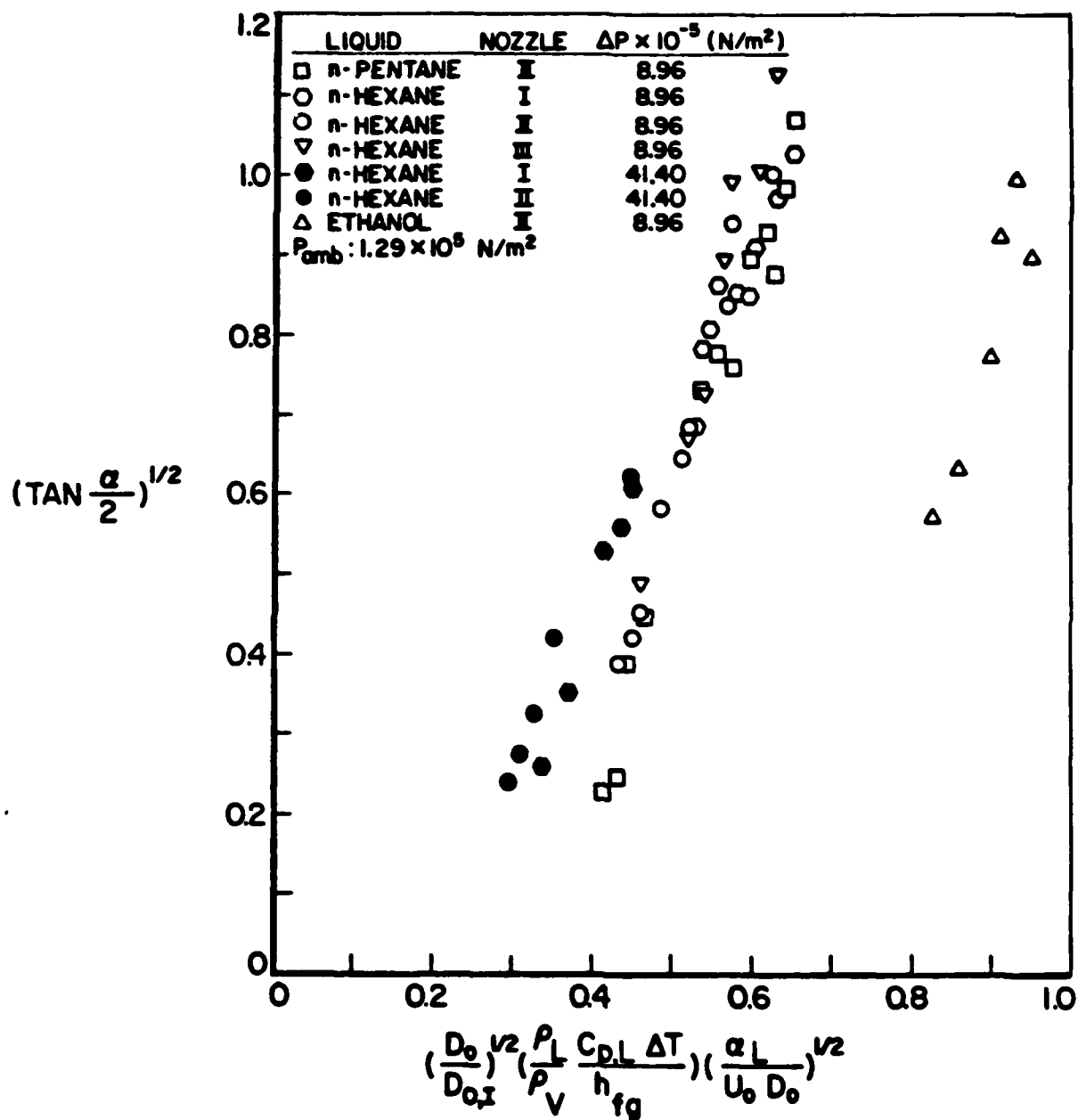


Fig. 13 Variation of jet divergence angle with degree of superheat considering bubble growth rate and number of bubbles in the jet cross-section.

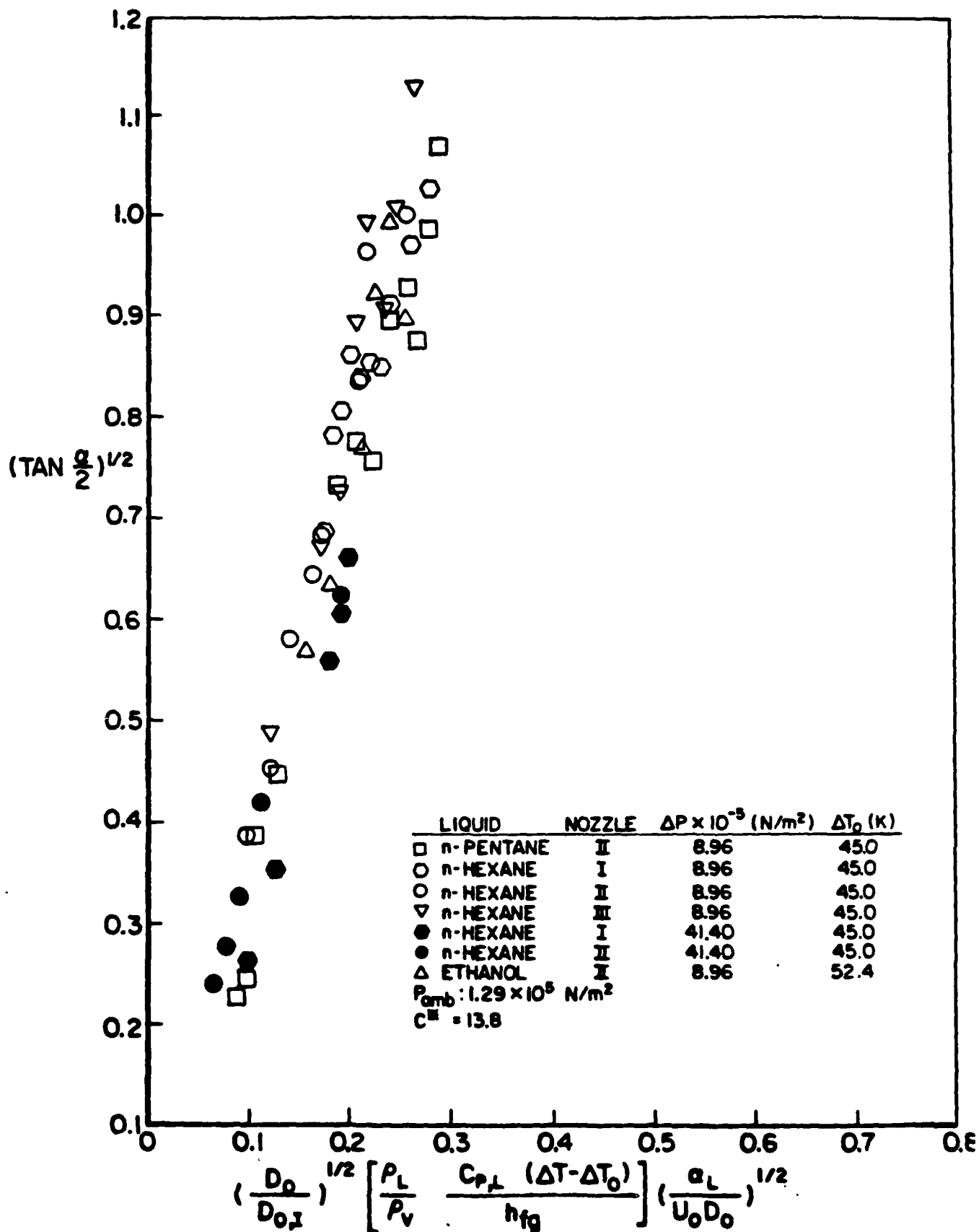


Fig. 14 Variation of jet divergence angle with modified degree of superheat considering bubble growth rate and number of

APPENDIX D

MEASUREMENT OF THE SPRAY ANGLE  
OF ATOMIZING JETS

C. -C. Su, K. -J. Wu, R.L. Steinberger  
D.A. Santavicca and F.V. Bracco

MEASUREMENTS OF THE SPRAY ANGLE OF ATOMIZING JETS

BY

C.-C. Su<sup>\*</sup>, K.-J. Wu<sup>\*</sup>, R.L. Steinberger<sup>\*\*</sup>  
D.A. Santavicca<sup>\*\*</sup>, and F.V. Bracco<sup>\*\*\*</sup>

Department of Mechanical and Aerospace Engineering  
Princeton University  
Princeton, N.J. 08544

Submitted for Publication to the  
Journal of Fluids Engineering

November 1981

<sup>\*</sup> Graduate Student

<sup>\*\*</sup> Research Staff Member

<sup>\*\*\*</sup> Associate Professor



## ABSTRACT

Liquid jets are considered issuing from single-hole, round nozzles into quiescent gases under conditions such that they break up into a well defined conical spray immediately at the nozzle exit plane. The initial angles of such sprays were measured at room temperature by a spark photography technique. Water, n-hexane, and n-tetradecane at pressures from 11.1 MPa to 107.6 MPa were injected into gaseous  $N_2$  at pressures from 0.1 MPa to 4.2 MPa through ten nozzles of different geometries. Under the test conditions, the spray angle is found to be a strong function of the nozzle geometry and the gas-liquid density ratio and a weak function of the injection velocity. The measured trends are then discussed in the light of possible mechanisms of the breakup process and shown to be compatible with the aerodynamic theory of surface breakup if modified to account for nozzle geometry effects.

## Introduction

The subject of this paper is very narrow: the initial angle of the sprays that are formed in diesel and stratified-charge engines when fuel is injected directly into the compressed air in their combustion chambers through cylindrical holes. Such angle is important because it influences the axial and radial distributions of the fuel and, ultimately, efficiency and emissions. Of interest is the dependence of the angle on the geometry of the nozzle, and the dynamic and thermodynamic states of liquid and gas at the moment of injection.

Typically, the injector head is made up of groups of straight, round holes (shower head) 200 to 600  $\mu\text{m}$  in diameter with length-to-diameter ratios between 2 and 8. The pressure difference is greater than 10 MPa, and in some designs is even higher than 100 MPa, so that the resulting initial jet velocity is greater than  $10^2$  m/s. Such jets are observed to breakup into drops 1 to 10  $\mu\text{m}$  in diameter within distances from the nozzle exit also of the order of 1 to 10  $\mu\text{m}$ . This is only one of many modes in which liquid jets breakup into drops and has been labelled [1] the atomization regime on account of the minute drops it forms and its suddenness.

Obviously more than the initial angle of the spray is of interest in IC engine applications. The initial distribution of drop radii and velocities are also very important quantities. But the small size, high speed, and high drop number density of atomizing jets make drop size and velocity measurements very difficult, even at the outer edge of the spray, and no technique seems to have been found to probe the jet inner structure where most of the drops are formed.

On the other hand the measured dependency of the spray angle on various parameters can be a clue to the mechanism of atomization, and if such mechanism is identified, predictions may be possible of the quantities that are difficult to measure.

An atomizing jet is shown in Figure 1 together with information that will be used later. In earlier work [1-3], the measured spray angle was found to follow the simple relationship

$$\tan \frac{\theta}{2} = \frac{1}{A} 4\pi \left( \frac{\rho_g}{\rho_l} \right)^{1/2} \frac{\sqrt{3}}{6} \quad (1)$$

where  $\theta$  is the spray angle,  $\rho_g$  the density of the gas,  $\rho_l$  the density of the liquid and  $A$  is a constant for a given nozzle geometry (Fig. 2). However four data points at the high density ratio of 0.0515 fell below the general trends. Also, although the range of parameters was rather broad (see Table 1), only water-glycerol mixtures were used, the exit diameter of all nozzles was approximately equal and cavitation was present in all tests. Finally, even though nine nozzle geometries were explored, all had sharp exit edges. Thus in the present work we explored a broader range of density ratios, and used different liquids, cavitation-free nozzles, and nozzles of different diameters and with rounded outlets. We also extended the measurements to higher injection pressures (up to 107.6 MPa). The narrower objective was to test the range of validity of Equation (1), the broader one was to collect additional information for the search for the mechanism of atomization.

This paper is organized as follows. First, experimental apparatus and procedure are described, then the range of the parameters explored and the measured spray angles are reported, and finally the possible implications of the measurements with respect to the mechanism of atomization are discussed.

## APPARATUS AND PROCEDURE

The experimental rig consisted of a spray chamber, a liquid pressurization system, a nozzle assembly, and instrumentation. Only a summary of the apparatus and the experimental procedure is given here. Details are available in [1] and [4].

**Spray Chamber.** The spray chamber was a cylindrical steel container, 19 cm ID and 48 cm in length, with four circular windows 10 cm in diameter. It was designed to withstand pressure up to 7.0 MPa at 750 K but the reported experiments were all conducted at room temperature. The liquid injections were along the axis of the chamber. The chamber was filled with Liquid Carbonic high purity nitrogen at the desired pressure. The gas density at all pressures was calculated based on the data in [5].

**Pressurization System.** Two techniques were used to pressurize the liquid. For liquid pressures up to 38.0 MPa, a local liquid reservoir was used with a valve mechanism (Fig. 3) that allowed a constant pressure, essentially motionless liquid, to be kept upstream of the nozzle. 41 MPa nitrogen gas from Matheson, after proper regulation with a Matheson model 3075 regulator, was used to pressurize the test liquid. The valve system included a solenoid controlled pressure amplifier, a hydraulic power clamp, and a valve rod. O-rings made of neoprene from Sandem Industries were used between the valve rod and the liquid reservoir for the sealing; a hand-lapped metal-to-metal seal was used between the valve rod and the valve rod seat. The solenoid controlled pressure amplifier was driven by the gas from the pressurized nitrogen tank and created high oil pressure to operate the hydraulic power clamp which in turn lifted the valve rod off its seat. When the nitrogen gas in the pressure amplifier was vented, the spring in the hydraulic power clamp forced the valve rod back to its seat.

For pressure between 38.0 MPa and 207 MPa the liquid reservoir was not immediately upstream of the nozzle and the test liquid flowed to the nozzle during the experiment through conduits of inner diameter no less than 6.9 times that of the nozzle (Fig. 4).

Test liquid was pumped into the liquid reservoir and the injection cylinder with a hand pump. Liquid and trapped air bubbles were bled out through two bleeding valves which were above any part of the liquid conduits, and the liquid inlet and outlet valves were closed, thus isolating the test liquid. Test liquid was then pressurized by the driver liquid (Diesel oil) which was in turn driven by a Miller Fluid Power H66R pressure intensifier.

A valve unit, housed in the injection cylinder, controlled the initiation and termination of injection. A hole of 0.635 cm diameter through the valve unit allowed the pressurized liquid to flow through. A piece of rubber was glued on the lower end of the valve unit and sealed the nozzle very well.

Nitrogen gas was used to control the movement of the valve unit. Initially, the upper control gas chamber was filled with nitrogen gas at about 1.0 MPa, thus keeping the valve unit in the closed position. The valve unit opened when nitrogen gas at higher pressure was introduced into the lower control gas chamber. As the gas in the lower control gas chamber was vented, the valve unit was forced back to its seat and stopped the injection.

**Nozzle Assembly.** Ten injection nozzles with seven different geometries, as listed in Table 2, were used in the experiments. The geometries could be divided into four groups: constant diameter tube with  $L/d$  ratio of 4.0, rounded outlet nozzle, straight sided diverging nozzle, and straight sided converging nozzle. The details of the geometries are shown in Fig. 5, and the reasons for selecting these geometries will be discussed later.

All the nozzles were made of SAE 303 stainless steel. The diameter of the orifices ranged from 254 to 660  $\mu\text{m}$  which is within the range of sizes used in Diesel engines. The orifice was drilled in the nozzle piece under an optical microscope with a microdrilling machine from National Jet.

Also, the entrance and exit of the nozzles were examined under a scanning electron microscope from different angles to assure that the desired sharpness (or roundness as may be the case) was obtained in the machining and not altered during the tests. The surface roughness was observed to be less than 5% of the diameter. Typical photographs of a nozzle are shown in Fig. 6.

Instrumentation and Accuracy. For the low liquid pressure apparatus, the driver nitrogen gas pressure was measured with a Heise-17555 gage, and chamber gas pressure was measured with a US Gage USG-132603 gage. The accuracy of the driver gas was  $\pm 0.2$  MPa and that for the chamber gas was  $\pm 0.03$  MPa.

In the ultra-high liquid pressure tests, the driver liquid pressure was measured at the pressure intensifier with a Heise-17555 gage having  $\pm 0.2$  MPa accuracy. Test liquid pressure was read from an AMINCO 47-18340 gage whose accuracy was  $\pm 0.3$  MPa.

In every test, the test liquid pressure during injection was also measured by a Kistler Model 307A pressure transducer, and Kistler Model 504 charge amplifier and the signal recorded by a Tektronix model 7313 oscilloscope with plug-in units 7A18 and 7835A. Figure 7 shows a typical photograph of the liquid pressure trace taken from the screen of the oscilloscope. The delay trigger out function of the oscilloscope was used to trigger the spark light after the liquid pressure had reached a steady value.

The sprays were illuminated by a high intensity short flash duration Xenon Model N-789B Nanolamp; a quartz lens was placed between the Nanolamp and the window on the spray chamber to collimate the light beam. The camera was an aluminum tube 107 cm long and was equipped with a Takumar 200 mm, f/3.5 lens, a mechanical shutter, and a Polaroid film back.

The magnification of this system was about 5.6 and the field of view was about 1.5 cm x 2.0 cm. The film used was Polaroid type 57 film. During the experiment, the Nanolamp was actuated by a preset delay trigger out signal from the oscilloscope. The time delay between valve opening and light flash was between 0.5 to 1.0 seconds as shown in Fig. 7. The shutter was opened manually before light flash and the exposure time of the back lighted photographs was determined by the flash duration of the Nanolamp, which was about 20 nanoseconds.

Water, n-hexane, and n-tetradecane were used as test liquids. Their sources and properties, obtained from [6] are listed in Table 3.

Spray angles were derived from photographs for each condition, as shown in Fig. 1. The accuracy of the measurement was within  $0.5^\circ$ . The arithmetic average of spray angles was calculated. The standard variation of each condition is shown by an error bar in the results.

It should be mentioned that in the high pressure rig, in which the test liquid upstream of the nozzle flowed during the test in conduits of inner diameter no less than 6.9 times that of the nozzle (Fig. 4), the Reynolds number in the upstream lines was estimated to range from 12,800, when the effective injection pressure was 11.0 MPa, to 24,000 when the effective injection pressure was 103.4 MPa. Since the distance between the liquid reservoir and the nozzle in the injection cylinder ( $\approx 70$  cm) was more than 100 times the diameter of the tube and the Reynolds number of the liquid in the tube was always in the turbulent range, the flow of the test liquid was turbulent before the liquid reached the nozzle. Therefore, a honeycomb of 0.08 cm hole diameter and 2.54 cm length was placed between the valve unit and the injection cylinder to guide the liquid back to laminar flow. However, the honeycomb was of poor construction and small pieces of it continually blocked the nozzle. Eventually the honeycomb was removed and all data were obtained without it, but still with a volume of  $4.7 \text{ cm}^3$  between the

upstream lines and the test nozzle in which the test liquid slowed down to negligible speed (50 cm/s). In any case, the results of the  $P_\ell = 15.3$  MPa series were compared with those of the  $\Delta p = 11.0$  MPa and 13.8 MPa series obtained from the low and moderate pressure system (Figures 10 and 13), and no difference was observed in the measured spray angle.



### MEASURED SPRAY ANGLES

The conditions of all tests are summarized in Table 1 with details given in Table 4.

High Density Ratio, Surface Tension, Nozzle Diameter. As pointed out in the introduction, earlier work [1-3] had indicated that, for a given nozzle geometry the spray angle is a function primarily of the density ratio (Equation (1)). However, there were four isolated data points at the highest density ratio (0.0515) of that work that did not fit Equation (1) and nozzle diameter, liquid density, and surface tension were not varied even though viscosity and pressure of the liquid, pressure and density of the gas and nozzle geometry were varied over broad ranges. Thus the first priority of this work was to assess the validity of Equation (1) in the high density ratio range and by varying the liquid surface tension and the nozzle diameter while keeping the same nozzle length-to-diameter ratio. The results of Figures 8 and 9 show that Equation (1) continues to be valid even for density ratios between  $26 \times 10^{-3}$  and  $61 \times 10^{-3}$  and that surface tension and nozzle diameter have no discernable effect on the initial angle of the spray.

High Injection Pressure. A recent trend in the design of Diesel injectors is toward the use of very high injection pressures, up to 207 MPa instead of the more traditional maximum pressures of 35 MPa. Thus it is of practical interest to know whether Equation (1) continues to hold at the higher injection pressures. The results of Fig. 10 (nozzles II(b) and II(c)) show that it does at least up to pressures of 107.6 MPa. (To make sure that the high injection pressures had not altered the nozzle, besides taking the standard electron microscope pictures of the nozzle entrance before and after the tests, the spray angle from low pressure injections was also measured before and after the high pressure ones, and no changes were found as shown in Figure 11.)

**Cavitation-Free Nozzles.** Another important question that had not been addressed directly by the earlier work is whether cavitation alone could be responsible for atomization, since nozzle designs and operation conditions were such that some degree of cavitation was expected in all tests. To see whether cavitation can be the only mechanism of atomization, it was necessary to use cavitation-free nozzles. Nozzles VI and VII are expected to be cavitation-free and produced atomized jets as shown in Figure 12. Thus cavitation cannot be the only mechanism of atomization. Also interesting is that the angle of the sprays from these nozzles continue to follow Equation (1).

**Rounded-Outlet Nozzles.** One parameter of the nozzle geometry that had not been previously tested for its possible effects on the spray angle is the radius of curvature of the exit edge of the nozzle (the radius of curvature of the entrance edge of the nozzle was tested and found to be very influential). Thus three nozzles (nozzles IV(a), IV(b), and V) with different exit geometries were employed and they gave the same spray angles as those with sharp outlets (Fig. 13).

## DISCUSSION

The data of this and earlier publications are valuable in that they can be used directly to predict the injection spray angle in Diesel engines. Since the residence time of the liquid within the nozzle generally is less than  $10^{-5}$  s, and that the initial breakup near the exit of the nozzle occurs on time scales of  $10^{-6}$  s, the instantaneous upstream pressure can be used and heating effects due to gas-liquid energy transfer are negligible [2].

The same data can also provide insight into the mechanism of disruption of the outer surface of the jet. However, this is a difficult step that requires assumptions that appear reasonable but cannot be fully supported. The first of such assumptions is that the larger the initial angle of the spray the more unstable is the outer surface of the jet. The statement is true in the limit, in that a jet that exhibits zero angle near the nozzle is stable there.

With the above assumption, in earlier work, it was concluded that each of many proposed mechanisms of breakup cannot explain the measured trends alone: if aerodynamic surface wave growth were the only mechanism, the spray angle should have been independent of nozzle geometry; if pipe turbulence were the only mechanism, jets from fully developed pipe flows should have been more unstable; if the rearrangement of the cross-section axial velocity profile of the jet were the only mechanism, then jets with laminar cores should have been more unstable; if upstream pressure oscillations were the only mechanism, then our jets should have been stable since the upstream pressure was constant in our experiments; and if wall boundary layer exit velocity profile relaxation effects were the only mechanism, then the breakup should have been independent of the gas density.

The data presented in this article further rule out cavitation as the only mechanism of breakup: if cavitation were the only agency of breakup, then nozzles VI and VII should have yielded intact jets since the flow within them was free of cavitation.

The fact that the spray angle was rather insensitive to the injection velocity is additional evidence that the disruption of the wall boundary layers at the nozzle exit is not a major factor in the atomization process. In a turbulent boundary layer, the wall stress increases roughly as the square of the flow stream velocity or, in our case, proportionally to  $\Delta p$ , which was varied by a factor of 9.4 (Figs. 10 and 13) with only minor effects on the spray angle. Similarly the rounding of the exit edge had no effect on the spray angle even though it is likely to have altered the rate of readjustment of the wall boundary layers.

Finally, the new data lends additional support to the hypothesis that aerodynamic interaction at the liquid-gas interface is a major component, but not the only component, of the mechanism of atomization. Indeed, for a fixed nozzle geometry, the measured spray angle behaves as predicted assuming that the aerodynamic interaction is the only mechanism of breakup.

Taylor [7] studied the rate of growth of the perturbations of planar liquid surfaces induced by gases flowing over it. He considered the limit  $\rho_g \ll \rho_l$  and included the effects of liquid viscosity and surface tension. Ranz [8] applied Taylor's results to round jets for the limit case in which the wave length of the fastest growing perturbation is much smaller than the jet diameter, and obtained the following expression for the spray angle

$$\tan \frac{\theta}{2} = \frac{1}{A} 4\pi \left( \frac{\rho_g}{\rho_l} \right)^{1/2} f \left[ \frac{\rho_l}{\rho_g} \left( \frac{Re_l}{We_l} \right)^2 \right] \quad (2)$$

where  $A$  is a constant not determined by the linear stability analysis and  $f$  is given in Fig. 14, and is seen to tend to  $\sqrt{3}/6$  when its argument is greater than unity. At this limit Equation 2 reduces to Equation 1.

For the data of Figures 8-13, the argument of  $f$  is no smaller than 0.4 so that the spray angle should be a function mostly of the density ratio. This is seen to be the case, for a given nozzle geometry at all density ratios including the high values which had not been adequately explored in our earlier work. Equations (1) and (2) reproduce the data also for different nozzle geometries provided that the constant  $A$  is given different values for different geometries. No element of the nozzle geometry enters the aerodynamic theory of Taylor and Ranz, and therefore such theory alone does not explain the process completely. The theory must be "supplemented" with a mechanism by which the nozzle geometry influences the breakup process. Such a mechanism has not yet been identified so that for the time being  $A$  must be considered an empirical constant.

Actually, there are hints that even the supplemented aerodynamic theory of atomization complies only with the most pronounced, and practically important, of the measured trends. Thus it would predict that the spray angle decreases monotonically with increasing jet velocity, tending to be independent of it in the limit:

$$\frac{\rho_l}{\rho_g} \left( \frac{Re_l}{We_l} \right)^2 \gg 1.$$

Figures 15 and 16 show that the measurements follow the predicted trend at sufficiently high density ratios but exhibit a mild opposite trend at lower density ratios. In fact, from Figures 8-13 it can be seen that Equation (2), which is predicted by the theory, does not represent the measured trends as well as Eq. (1) which is supposed to be less accurate.

AD-A113 892

PRINCETON UNIV NJ DEPT OF MECHANICAL AND AEROSPACE --ETC F/6 21/7  
HIGH PRESSURE ATOMIZATION.(U)  
MAR 82 F V BRACCO

DAA629-76-G-0264

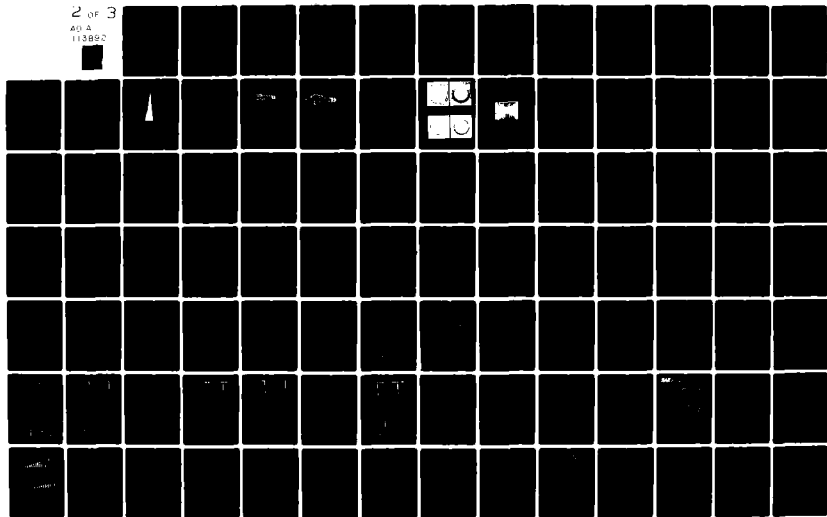
UNCLASSIFIED

ARO-13935.3-EX

NL

2 of 3

AD-A  
113892



In summary, the physical picture of atomizing jets that has emerged from this and earlier work can be stated briefly as follows. The surface of the liquid emerges from the nozzle already perturbed by events that occur within the nozzle itself and are affected by its geometry. The perturbations are selectively and rapidly amplified by the aerodynamic interaction with the gas until the outer surface of the jet breaks up into drops. The size of the drops and the intact length of the surface are much smaller than the jet diameter. The depth from the surface of the jet to which the above drop formation mechanism could possibly apply is not known, but the relative velocity between the two phases should decrease rapidly inside the jet. Since only isolated drops are found far downstream, the breaking up of the jet must continue even in its interior. However, initially the gas-volume-fraction at the core of the jet is so small that it is not likely that isolated drops exist within it separated by minute amounts of gas. It is more probable that liquid and gas form two mingled and fast changing continua (Fig. 1). This has been called the churning flow regime [9,10]. For typical spray angles of  $10^\circ$ , about ten diameters downstream of the nozzle exit the average gas-volume-fraction on the jet cross-section can be already 90%. Individual drops could exist even deep into the jet but they would be colliding and often recombining [9,10]. This has been called the thick spray regime [9,10] and lasts as far downstream as strong direct drop interactions persist. Finally, farther downstream in the thin spray regime, drops are so far apart from each other that they interact only indirectly through their collective effects on the entrained gas [9,10].

The above structure of the churning flow and thick spray regimes are only hypothetical since no measurements have been made in the inner part of the jet near the nozzle due to the small length and time scales of the process and the opacity of the core. But it is clear that the resulting downstream

distributions of drop sizes and velocities, and the effects that influence them at the various stages, are far from being well understood in spite of the attention they have received and of their long-established practical importance.



**ACKNOWLEDGEMENTS**

We wish to thank Mr. E.L. Griffith and Mr. J.H. Semler for their assistance in the design and the construction of the experimental apparatus.

This work was supported by the Army Research Office under Contract DAAG29-78-G-0132.

# NOMENCLATURE

A	=	dimensionless nozzle constant in Eqs. (1) and (2)
d	=	nozzle diameter, $\mu\text{m}$
f	=	function of $\frac{\rho_l}{\rho_g} \left( \frac{\text{Re}_l}{\text{We}_l} \right)^2$ , Fig. 14
K	=	cavitation number, $\frac{P_l - P_g}{P_g - P_v}$
L	=	nozzle passage length, $\mu\text{m}$
$P_g, P_l$	=	pressure of gas and liquid, MPa
$P_v$	=	vapor pressure of liquid, kPa
r	=	radius of curvature of nozzle exit edge, $\mu\text{m}$
$\text{Re}_l$	=	Reynolds number, $\frac{\rho_l U_{\text{vol}} d}{\mu_l}$
T	=	test liquid injection duration, s
$T_g, T_l$	=	temperature of ambient gas and test liquid
$U_{\text{ideal}}$	=	ideal jet velocity, cm/s
$U_{\text{vol}}$	=	volumetric averaged velocity of jet, cm/s
$\text{We}_l$	=	Weber number, $\frac{\rho_l U_{\text{vol}}^2 d}{\sigma_l}$
$\alpha$	=	nozzle inlet approach angle, degree
$\Delta p$	=	effective injection pressure, $P_l - P_g$ , MPa
$\theta$	=	spray full angle, degree
$\mu_g, \mu_l$	=	kinematic viscosity of gas and liquid, $\frac{\text{dyne} \cdot \text{s}}{\text{cm}^2}$
$\rho_g, \rho_l$	=	density of gas and liquid, $\frac{\text{g}}{\text{cm}^3}$
$\sigma_l$	=	gas-liquid surface tension, dyne/cm

## REFERENCES

1. Reitz, R.D., "Atomization and Other Breakup Regimes of a Liquid Jet," Ph.D. Dissertation, No. 1375-T, Dept. of Aerospace and Mechanical Sciences, Princeton Univ., 1978.
2. Reitz, R.D. and Bracco, F.V., "Ultra-High-Speed Filming of Atomizing Jets," Physics of Fluids, Vol. 22, No. 6, p. 1054, June 1979.
3. Reitz, R.D. and Bracco, F.V., "On the Dependence of Spray Angle and Other Spray Parameters on Nozzle Design and Operating Conditions," SAE Paper No. 790494, 1979.
4. Su, C.C., "Atomization of Round Liquid Jets," M.S. Thesis, No. 1502-T, Dept. of Mechanical and Aerospace Engineering, Princeton Univ., 1980.
5. Thompson, P.A., "Compressible Fluid Dynamics," McGraw-Hill, N.Y., 1972.
6. Weast, R.C., Ed., "Handbook of Chemistry and Physics," 58th ed; CRC Press, Cleveland, OH, 1977.
7. Taylor, G.I., "Generation of Ripples by Wind Blowing over a Viscous Fluid," Collected works of G.I. Taylor, Vol. 3, p. 244, 1940.
8. Ranz, W.E., "Some Experiments on Orifice Sprays," Canad. J. Chem. Engng., Vol. 36, p. 175, 1958.
9. O'Rourke, P.J., "Collective Drop Effects on Vaporizing Liquid Sprays," Ph.D. Dissertation, No. 1532-T, Dept. of Mechanical and Aerospace Engineering, Princeton University, Princeton, NJ, August 1981.
10. O'Rourke, P.J. and Bracco, F.V., "Modeling of Drop Interactions in Thick Sprays and Comparison with Experiments," Stratified Charge Automotive Engines Conference, The Institution of Mechanical Engineers, London, England, Nov. 1980.

TABLE 1. Summary of Test Parameters

	Ref. [1-3]	Present Work
Test Liquid	Water, Glycerol, and Their Mixtures	Water, n-Hexane, and n-Tetradecane
$\rho_l$	0.998 - 1.261	0.763 - 0.998
$P_l$	3.9 - 18.0	11.1 - 107.6
$\mu_l$	0.010 - 17.596	0.0032 - 0.0218
$\sigma_l$	63.0 - 72.8	18.4 - 72.8
$T_l$	room temp.	room temp.
Ambient Gas	N <sub>2</sub> , He, and Xe	N <sub>2</sub>
$\rho_g \times 10^3$	1.1 - 51.5	1.2 - 48.7
$P_g$	0.1 - 4.2	0.1 - 4.2
$\mu_g \times 10^4$	1.70 - 2.26	1.70
$T_g$	room temp.	room temp.
Nozzle Geometries	9	7
d	343	254, 343, and 660
L/d	0.5 - 85	≈ 0 and 4.0
Argument of f	$1.3 \times 10^{-4}$ - $1.6 \times 10^{-3}$	0.4 - 420
$\rho_g / \rho_l \times 10^3$	1.1 - 15.6	1.8 - 73.2

TABLE 2. Nozzle Geometries

NOZZLE	CLASS	d(μm)	DESCRIPTION		α(degree)
			L/d	r	
I	Constant Diameter Tube	254	4.0	-	180
II(a),(b), and (c)	Constant Diameter Tube	343	4.0	-	180
III	Constant Diameter Tube	660	4.0	-	180
IV(a) and (b)	Rounded Outlet	343	4.0	$\frac{1}{2}d$	180
V	"	343	4.0	d	180
VI	Straight Sided Diverging Nozzle	343	0	-	180
VII	Straight Sided Converging Nozzle	343	0	-	90

TABLE 3. Test Liquids and Their Properties

	WATER	n-HEXANE	n-TETRADECANE
Manufacturer and Catalogue Number	Tap Water	Fisher Scientific Co. H-291	Eastman Kodak Co. 13090
Density $\rho_l$	0.998	0.665	0.763
Surface Tension $\sigma_l$	72.8	18.43	26.7
Viscosity $\mu_l$	0.010	0.0032	0.0218
$(\frac{\sigma_l}{\mu_l})^2 \times 10^{-6}$	53.0	33.0	1.5
Vapor Pressure $P_v$	2.34	16.5	less than 0.14

TABLE 4. Conditions of the Experiments

Series	Data	Nozzle	P (atm)	$\rho \times 10^3$ (g/cm <sup>3</sup> )	Liquid	$\Delta p$ (atm)	K	$U_{ideal} \times 10^{-4}$ (cm/s)	T (°C)	$U_{vol.} \times 10^{-4}$ (cm/s)	$Re_f \times 10^{-4}$	$We_f \times 10^{-4}$	$\theta$ (deg)	$\frac{\rho}{\rho_f} \times 10^{-3}$	a	b	f
1	4	I	0.44	5.1	n-hexane	13.8	32.1	2.04	6.7	1.27	6.70	14.8	8.0	7.7	6.3	26.7	0.25
2	5	I	0.79	9.1	"	13.8	17.8	2.04	7.0	1.21	6.39	13.4	9.3	13.7	5.5	16.6	0.25
3	4	I	1.48	17.0	"	13.8	9.4	2.04	6.7	1.27	6.70	14.8	13.1	25.6	5.7	8.0	0.24
4	4	I	2.17	24.9	"	13.8	6.4	2.04	7.3	1.16	6.12	12.3	15.0	37.4	5.4	6.6	0.24
5	4	I	2.86	32.9	"	13.8	4.8	2.04	7.4	1.15	6.07	12.1	18.3	49.5	5.7	5.0	0.23
6	5	I	3.55	40.8	"	13.8	3.9	2.04	7.5	1.13	5.96	11.7	22.8	61.4	6.4	4.2	0.23
7	5	II(a)	0.10	1.2	"	11.0	130.1	1.82	4.3	1.08	7.70	14.4	5.5	1.8	9.0	158.8	0.27
8	4	II(a)	0.44	5.1	"	11.0	25.7	1.82	4.3	1.08	7.70	14.4	7.4	7.7	5.9	37.1	0.25
9	5	II(a)	0.79	9.1	"	11.0	14.2	1.82	4.2	1.11	7.91	15.2	9.2	13.7	5.5	19.8	0.25
10	4	II(a)	1.48	17.0	"	11.0	7.5	1.82	4.1	1.13	8.05	15.8	14.2	25.6	6.2	10.1	0.24
11	4	II(a)	2.17	24.9	"	11.0	5.1	1.82	3.9	1.19	8.48	17.5	17.1	37.4	6.2	6.3	0.24
12	4	II(a)	4.24	48.7	"	11.0	2.6	1.82	3.7	1.26	8.98	19.6	24.0	73.2	6.2	2.9	0.22
13	4	II(a)	0.44	5.1	water	13.8	31.1	1.66	4.4	1.06	3.63	5.3	2.3	5.1	2.2	92.6	0.26
14	4	II(a)	0.79	9.1	"	13.8	17.5	1.66	4.6	1.04	3.56	5.1	5.5	9.1	4.0	54.0	0.26
15	4	II(a)	1.48	17.0	"	13.8	9.3	1.66	4.5	1.03	3.52	5.0	8.0	17.0	4.3	29.4	0.25
16	4	II(a)	2.17	24.9	"	13.8	6.4	1.66	4.5	1.03	3.52	5.0	12.7	24.9	5.6	19.9	0.25
17	5	II(a)	2.86	32.9	"	13.8	4.8	1.66	4.6	1.04	3.56	5.1	16.2	32.9	6.2	14.7	0.24
18	5	II(a)	3.55	40.8	"	13.8	3.9	1.66	4.6	1.04	3.56	5.1	17.6	40.8	6.0	11.8	0.24
19	4	II(a)	0.44	5.1	n-hexane	13.8	32.1	2.04	4.6	1.04	7.41	13.4	7.8	7.7	6.2	39.8	0.26
20	4	II(a)	0.79	9.1	"	13.8	17.8	2.04	4.5	1.03	7.34	13.1	9.6	13.7	5.7	22.8	0.25
21	4	II(a)	1.48	17.0	"	13.8	9.4	2.04	4.4	1.06	7.56	13.9	12.8	25.6	5.6	11.5	0.24
22	4	II(a)	2.17	24.9	"	13.8	6.4	2.04	4.4	1.06	7.56	13.9	17.6	37.4	6.4	8.0	0.24
23	4	II(a)	2.86	32.9	"	13.8	4.8	2.04	4.7	0.99	7.06	12.1	20.0	49.5	6.3	6.8	0.24
24	4	II(a)	3.55	40.8	"	13.8	3.9	2.04	4.2	1.11	7.91	15.2	22.8	61.4	6.4	4.3	0.23
25	4	II(a)	0.44	5.1	n-tetradecane	13.8	30.9	1.90	4.4	1.06	1.27	11.0	4.7	6.7	4.0	2.0	0.22
26	4	II(a)	0.79	9.1	"	13.8	17.4	1.90	4.3	1.08	1.30	11.4	7.2	11.9	4.6	1.1	0.21
27	4	II(a)	1.48	17.0	"	13.8	9.3	1.90	4.0	1.16	1.39	13.2	10.2	22.3	4.8	0.5	0.20
28	5	II(a)	2.17	24.9	"	13.8	6.4	1.90	4.0	1.16	1.39	13.2	15.8	32.6	6.2	0.3	0.19
29	4	II(a)	2.86	32.9	"	13.8	4.8	1.90	3.9	1.19	1.43	13.9	17.2	43.1	5.8	0.2	0.18
30	4	II(a)	3.55	40.8	"	13.8	3.9	1.90	3.8	1.22	1.46	14.6	20.0	53.5	6.1	0.2	0.18
31	4	II(b)	0.10	1.2	n-hexane	15.2	178.9	2.14	—	1.46	10.4	26.4	3.4	1.8	5.6	86.4	0.26
32	3	II(b)	0.79	9.1	"	14.5	18.7	2.09	—	1.42	10.12	25.0	6.6	13.7	3.9	12.0	0.24
33	3	II(b)	1.48	17.0	"	13.8	9.4	2.04	—	1.39	9.91	23.9	13.9	25.6	6.1	6.7	0.24
34	3	II(b)	2.17	24.9	"	13.1	6.1	1.99	—	1.35	9.62	22.6	18.5	37.4	6.7	4.8	0.23

TABLE 4. Conditions of the Experiments

Series	Data	Nozzle	$P_g$ (MPa)	$\rho_g \times 10^3$ (g/cm <sup>3</sup> )	Liquid	$\Delta p$ (MPa)	K	$U_{ideal} \times 10^{-4}$ (cm/s)	T (s)	$U_{vol} \times 10^{-4}$ (cm/s)	$Re_L \times 10^{-4}$	$We_L \times 10^{-4}$	$\theta$ (deg)	$\frac{\rho_g}{\rho_L} \times 10^{4/3}$	a	b	f
35	3	II(b)	4.24	48.7	n-hexane	11.0	2.6	1.82	—	1.24	8.84	19.0	25.7	73.2	6.7	3.0	0.22
36	3	II(b)	0.10	1.2	"	37.9	447.2	3.38	—	2.30	16.39	65.5	4.5	1.8	7.7	34.8	0.25
37	3	II(b)	0.79	9.1	"	37.2	48.1	3.35	—	2.28	16.25	64.3	8.6	13.7	5.1	4.7	0.23
38	4	II(b)	1.48	17.0	"	36.5	25.0	3.32	—	2.26	16.11	63.2	12.6	25.6	5.5	2.5	0.22
39	4	II(b)	2.17	24.9	"	35.8	16.7	3.29	—	2.24	15.97	62.1	14.6	37.4	5.3	1.8	0.22
40	3	II(b)	4.24	48.7	"	33.8	8.0	3.19	—	2.17	15.47	58.3	19.9	73.2	5.2	1.0	0.21
41	4	II(b)	0.10	1.2	"	64.8	764.2	4.42	—	3.00	21.38	111.4	5.0	1.8	8.2	20.5	0.25
42	4	II(b)	0.79	9.1	"	64.1	82.8	4.40	—	2.99	21.31	110.6	9.4	13.7	5.6	2.7	0.22
43	4	II(b)	1.48	17.0	"	63.4	43.3	4.37	—	2.97	21.17	109.2	13.5	25.6	5.9	1.5	0.21
44	4	II(b)	2.17	24.9	"	62.7	29.1	4.35	—	2.96	21.10	108.4	13.5	37.4	4.9	1.0	0.21
45	4	II(b)	3.20	36.8	"	61.7	19.4	4.31	—	2.93	20.88	106.2	16.8	55.3	4.9	0.7	0.21
46	4	II(b)	4.24	48.7	"	60.6	14.4	4.28	—	2.91	20.74	104.8	18.8	73.2	4.9	0.5	0.20
47	4	II(b)	0.10	1.2	"	91.7	1081.3	5.26	—	3.58	25.52	158.6	5.4	1.8	8.8	14.4	0.24
48	4	II(b)	0.79	9.1	"	91.0	117.3	5.24	—	3.56	25.38	156.8	9.6	13.7	5.7	1.9	0.22
49	4	II(b)	1.48	17.0	"	90.3	61.7	5.22	—	3.55	25.30	156.0	12.9	25.6	5.6	1.0	0.21
50	4	II(b)	2.17	24.9	"	89.6	41.6	5.20	—	3.54	25.23	155.1	13.4	37.4	4.8	0.7	0.21
51	4	II(b)	3.20	36.8	"	88.6	27.8	5.17	—	3.52	25.09	153.4	16.2	55.3	4.8	0.5	0.20
52	4	II(b)	4.24	48.7	"	87.5	20.7	5.14	—	3.50	24.95	151.6	18.7	73.2	4.8	0.4	0.20
53	4	II(b)	0.10	1.2	"	15.2	178.9	2.14	—	1.46	10.41	26.4	3.2	1.8	5.2	86.4	0.26
54	3	II(b)	0.79	9.1	"	14.5	18.7	2.09	—	1.42	10.12	25.0	7.9	13.7	4.7	12.0	0.24
55	3	II(b)	1.48	17.0	"	13.8	9.4	2.04	—	1.39	9.91	23.9	11.4	25.6	5.0	6.7	0.24
56	4	II(b)	2.17	24.9	"	13.1	6.1	1.99	—	1.35	9.62	22.6	16.2	37.4	5.8	4.8	0.23
57	4	II(b)	3.20	36.8	"	12.1	3.8	1.91	—	1.30	9.27	20.9	21.3	55.3	6.4	3.6	0.23
58	4	II(b)	4.24	48.7	"	11.0	2.6	1.82	—	1.24	8.84	19.0	24.9	73.2	6.5	3.0	0.22



TABLE 4. Conditions of the Experiments

Series	Data	Nozzle	P <sub>g</sub> (MPa)	$\rho \times 10^3$ (g/cm <sup>3</sup> )	Liquid	$\Delta p$ (MPa)	K	$U_{ideal} \times 10^{-4}$ (cm/s)	T (s)	$U_{vol} \times 10^{-4}$ (cm/s)	$Re_L \times 10^{-4}$	$We_L \times 10^{-4}$	$\theta$ (deg)	$\frac{\rho_g}{\rho_L} \times 10^{13}$	a	b	f
59	3	II(c)	0.79	9.1	n-hexane	34.5	44.5	3.22	—	2.22	15.8	61.0	12.5	13.7	7.4	4.9	0.23
60	3	II(c)	1.48	17.0	"	34.5	23.6	3.22	—	2.22	15.8	61.0	14.4	25.6	6.3	2.6	0.22
61	3	II(c)	2.17	24.9	"	34.5	16.0	3.22	—	2.22	15.8	61.0	16.4	37.4	5.9	1.8	0.22
62	3	II(c)	2.86	32.9	"	34.5	12.1	3.22	—	2.22	15.8	61.0	16.6	49.5	5.6	1.6	0.22
63	3	II(c)	3.55	40.8	"	34.5	9.8	3.22	—	2.22	15.8	61.0	18.0	61.4	5.4	1.2	0.21
64	3	II(c)	4.24	48.7	"	34.5	8.2	3.22	—	2.22	15.8	61.0	18.9	73.2	4.9	0.9	0.21
65	4	II(c)	0.79	9.1	"	68.9	89.0	4.55	—	3.11	22.2	119.7	12.3	13.7	7.3	2.5	0.22
66	4	II(c)	1.48	17.0	"	68.9	47.1	4.55	—	3.11	22.2	119.7	14.3	25.6	6.2	1.3	0.21
67	4	II(c)	2.17	24.9	"	68.9	32.0	4.55	—	3.11	22.2	119.7	15.0	37.4	5.4	0.9	0.21
68	4	II(c)	2.86	32.9	"	68.9	24.2	4.55	—	3.11	22.2	119.7	15.5	49.5	5.2	0.8	0.21
69	4	II(c)	3.55	40.8	"	68.9	19.5	4.55	—	3.11	22.2	119.7	17.0	61.4	5.1	0.6	0.20
70	4	II(c)	4.24	48.7	"	68.9	16.3	4.55	—	3.11	22.2	119.7	18.2	73.2	4.7	0.5	0.20
71	4	II(c)	0.79	9.1	"	103.4	133.6	5.58	—	4.07	29.0	205.0	11.4	13.7	6.8	1.5	0.21
72	4	II(c)	1.48	17.0	"	103.4	70.6	5.58	—	4.07	29.0	205.0	14.2	25.6	6.2	0.8	0.21
73	4	II(c)	2.17	24.9	"	103.4	48.0	5.58	—	4.07	29.0	205.0	16.9	37.4	6.1	0.5	0.20
74	4	II(c)	2.86	32.9	"	103.4	36.4	5.58	—	4.07	29.0	205.0	17.4	49.5	5.9	0.5	0.20
75	4	II(c)	3.55	40.8	"	103.4	29.3	5.58	—	4.07	29.0	205.0	18.4	61.4	5.6	0.4	0.20
76	4	II(c)	4.24	48.7	"	103.4	24.5	5.58	—	4.07	29.0	205.0	18.9	73.2	4.9	0.3	0.19
77	4	III	0.44	5.1	n-hexane	13.8	32.1	2.04	1.0	1.26	17.3	37.8	6.6	7.7	5.2	27.2	0.25
78	4	III	0.79	9.1	"	13.8	17.8	2.04	1.0	1.26	17.3	37.8	8.8	13.7	5.2	15.3	0.25
79	4	III	1.48	17.0	"	13.8	9.4	2.04	1.0	1.26	17.3	37.8	13.8	25.6	6.0	8.2	0.24
80	4	III	2.17	24.9	"	13.8	6.4	2.04	1.0	1.26	17.3	37.8	16.4	37.4	5.9	5.6	0.24
81	4	III	2.86	32.9	"	13.8	4.8	2.04	1.0	1.26	17.3	37.8	18.5	49.5	6.2	4.2	0.23

TABLE 4. Conditions of the Experiments

Series	Data	Nozzle	P <sub>g</sub> (MPa)	$\rho_{gx}10^3$ (g/cm <sup>3</sup> )	Liquid	$\Delta p$ (MPa)	K	$U_{ideal}10^{-4}$ (cm/s)	T (s)	$U_{vol} \cdot 10^{-4}$ (cm/s)	$Re_L 10^{-4}$	$We_L 10^{-4}$	$\theta$ (deg)	$\frac{\rho_g}{\rho_L} \cdot 10^{+3}$	a	b	f
82	4	III	3.55	40.8	n-hexane	13.8	3.9	2.04	0.9	1.40	19.2	46.7	21.6	61.4	6.6	2.7	0.22
83	2	IV(a)	0.10	1.2	"	11.0	130.1	1.82	4.4	1.06	7.6	13.9	0.9	1.8	1.5	162.3	0.27
84	4	IV(a)	0.44	5.1	"	11.0	25.7	1.82	4.5	1.03	7.3	13.0	4.9	7.7	3.9	40.5	0.26
85	4	IV(a)	0.79	9.1	"	11.0	14.2	1.82	4.1	1.13	8.0	15.6	6.3	13.7	3.7	19.1	0.25
86	4	IV(a)	1.48	17.0	"	11.0	7.5	1.82	4.0	1.16	8.2	16.5	11.7	25.6	5.1	9.6	0.24
87	4	IV(a)	2.17	24.9	"	11.0	5.1	1.82	4.0	1.16	8.2	16.5	15.1	37.4	5.4	6.6	0.24
88	4	IV(a)	4.24	48.7	"	11.0	2.6	1.82	3.7	1.26	8.9	19.4	26.0	73.2	6.8	2.9	0.22
89	5	IV(b)	0.10	1.2	"	15.2	178.9	2.14	—	1.46	10.3	26.1	3.1	1.8	5.1	95.6	0.26
90	3	IV(b)	0.79	9.1	"	14.5	18.7	2.09	—	1.42	10.0	24.7	8.1	13.7	4.8	11.9	0.24
91	3	IV(b)	1.48	17.0	"	13.8	9.4	2.04	—	1.39	9.8	23.7	12.2	25.6	5.3	6.7	0.24
92	3	IV(b)	2.17	24.9	"	13.1	6.1	1.99	—	1.35	9.5	22.3	16.3	37.4	5.9	4.8	0.23
93	4	IV(b)	3.20	36.8	"	12.1	3.8	1.91	—	1.30	9.2	20.7	21.8	55.3	6.5	3.6	0.23
94	3	IV(b)	4.24	48.7	"	11.0	2.6	1.82	—	1.24	8.7	19.1	24.7	73.2	6.4	2.8	0.22
95	4	IV(b)	0.10	1.2	"	37.9	447.2	3.38	—	2.30	16.2	64.8	4.3	1.8	7.0	34.3	0.25
96	4	IV(b)	0.79	9.1	"	37.2	48.1	3.35	—	2.28	16.1	63.7	9.8	13.7	5.8	4.6	0.23
97	4	IV(b)	1.48	17.0	"	36.5	25.9	3.32	—	2.26	15.9	62.6	12.7	25.6	5.5	2.5	0.22
98	4	IV(b)	2.17	24.9	"	35.8	16.7	3.29	—	2.24	15.8	61.5	14.9	37.4	5.4	1.8	0.22
99	4	IV(b)	3.20	36.8	"	34.8	10.9	3.24	—	2.20	15.5	59.3	18.4	55.3	5.5	1.2	0.21
100	4	IV(b)	4.24	48.7	"	33.8	8.0	3.19	—	2.17	15.3	57.7	20.8	73.2	5.4	1.0	0.21
101	4	IV(b)	0.10	1.2	"	64.8	764.2	4.42	—	3.00	21.1	110.3	4.9	1.8	8.0	20.1	0.25
102	4	IV(b)	0.79	9.1	"	64.1	82.8	4.40	—	2.99	21.0	109.5	12.0	13.7	7.1	2.7	0.22
103	4	IV(b)	1.48	17.0	"	63.4	43.3	4.37	—	2.97	20.9	108.1	15.6	25.6	6.8	1.5	0.21

TABLE 4. Conditions of the Experiments

Series	Data	Nozzle	P <sub>g</sub> (MPa)	ρ <sub>g</sub> × 10 <sup>3</sup> (g/cm <sup>3</sup> )	Liquid	Δp (MPa)	U <sub>ideal</sub> × 10 <sup>-4</sup> (cm/s)	T (s)	U <sub>vol.</sub> × 10 <sup>-4</sup> (cm/s)	Re <sub>L</sub> × 10 <sup>-4</sup>	We <sub>L</sub> × 10 <sup>-4</sup>	θ (deg)	$\frac{\rho_g}{\rho_L} \times 10^{+3}$	a	b	f	
104	4	IV(b)	2.17	24.9	n-hexanes	62.7	29.1	4.35	—	2.96	20.9	107.3	17.2	37.4	6.2	1.0	0.21
105	6	IV(b)	3.20	36.8	"	61.7	19.4	4.31	—	2.93	20.6	105.2	19.2	55.3	5.7	0.7	0.20
106	4	IV(b)	4.24	48.7	"	60.6	14.4	4.28	—	2.91	20.5	103.7	19.9	73.2	5.2	0.5	0.20
107	4	IV(b)	0.10	1.2	"	91.7	1081.3	5.26	—	3.58	25.2	157.0	5.6	1.8	9.1	14.2	0.24
108	4	IV(b)	0.79	9.1	"	91.0	117.5	5.24	—	3.56	25.1	155.3	12.6	13.7	7.5	1.9	0.22
109	4	IV(b)	1.48	17.0	"	90.3	61.7	5.22	—	3.55	25.0	154.4	14.2	25.6	6.2	1.0	0.21
110	4	IV(b)	2.17	24.9	"	89.6	41.6	5.20	—	3.54	24.9	153.5	16.6	37.4	6.0	0.7	0.20
111	6	IV(b)	3.20	36.8	"	88.6	27.8	5.17	—	3.52	24.8	151.7	18.3	55.3	5.4	0.5	0.20
112	4	IV(b)	4.24	48.7	"	87.5	20.7	5.14	—	3.50	24.6	150.1	19.3	73.2	5.0	0.4	0.20
113	4	IV(b)	0.10	1.2	"	15.2	178.9	2.14	—	1.46	10.3	26.1	3.7	1.8	6.0	85.6	0.26
114	4	IV(b)	0.79	9.1	"	14.5	18.7	2.09	—	1.42	10.0	24.7	9.5	13.7	5.6	11.9	0.24
115	3	IV(b)	1.48	17.0	"	13.8	9.4	2.04	—	1.39	9.8	23.7	12.4	25.6	5.4	6.7	0.24
116	3	IV(b)	2.17	24.9	"	13.1	6.1	1.99	—	1.35	9.5	22.3	16.7	37.4	6.0	4.8	0.23
117	3	IV(b)	3.20	36.8	"	12.1	3.8	1.91	—	1.30	9.2	20.7	21.4	55.3	6.4	3.6	0.23
118	3	IV(b)	4.24	48.7	"	11.0	2.6	1.82	—	1.24	8.7	19.1	24.0	73.2	6.2	2.8	0.22
119	3	V	0.10	1.2	"	11.0	130.1	1.82	4.6	1.01	7.1	12.5	5.1	1.8	8.3	172.3	0.27
120	4	V	0.79	9.1	"	11.0	14.2	1.82	4.6	1.01	7.1	12.5	9.4	13.7	5.6	23.4	0.25
121	4	V	2.17	24.9	"	11.0	7.5	1.82	4.2	1.11	7.8	15.1	16.6	37.4	6.0	7.1	0.24
122	4	V	4.24	48.7	"	11.0	2.6	1.82	3.7	1.26	8.9	19.4	25.2	73.2	6.6	2.9	0.22
123	3	VI	0.10	1.2	"	11.0	130.1	1.82	3.8	1.22	8.6	18.2	0.7	1.8	1.1	122.7	0.27
124	4	VI	0.44	5.1	"	11.0	25.7	1.82	3.8	1.22	8.6	18.2	5.6	7.7	4.4	28.7	0.25
125	4	VI	0.79	9.1	"	11.0	14.2	1.82	3.8	1.22	8.6	18.2	7.4	13.7	4.4	16.2	0.25
126	4	VI	1.48	17.0	"	11.0	7.5	1.82	3.7	1.26	8.9	19.4	10.2	25.6	4.4	8.2	0.24
127	4	VI	2.17	24.9	"	11.0	5.1	1.82	3.7	1.26	8.9	19.4	12.5	37.4	4.5	5.6	0.24

TABLE 4. Conditions of the Experiments

Series	Data	Nozzle	P, (MPa)	$\rho \times 10^3$ (g/cm <sup>3</sup> )	Liquid	$\Delta p$ (MPa)	K	$U_{ideal} \times 10^{-4}$ (cm/s)	T (s)	$U_{vel} \times 10^{-4}$ (cm/s)	$Re_L \times 10^{-4}$	$We_L \times 10^{-4}$	$\theta$ (deg)	$\frac{\rho}{\rho_L} \times 10^{13}$	a	b	f
128	4	VI	4.24	48.7	n-hexane	11.0	2.6	1.82	3.6	1.29	9.1	20.4	15.0	73.2	3.9	2.7	0.22
129	3	VII	0.10	1.2	"	11.0	130.1	1.82	3.8	1.22	8.6	18.3	4.0	1.8	6.5	121.3	0.27
130	4	VII	0.79	9.1	"	11.0	14.2	1.82	3.8	1.22	8.6	18.3	8.1	13.7	4.8	16.0	0.25
131	4	VII	1.48	17.0	"	11.0	7.5	1.82	3.9	1.19	8.4	17.4	11.0	25.6	4.8	9.1	0.24
132	5	VII	2.17	24.9	"	11.0	5.1	1.82	3.8	1.22	8.6	18.3	13.6	37.4	4.9	5.9	0.24
133	5	VII	4.24	48.7	"	11.0	2.6	1.82	3.8	1.22	8.6	18.3	16.1	73.2	4.2	3.0	0.22

$$a = \left[ \tan \frac{\theta}{2} \sqrt{\frac{\rho_L}{\rho_g}} / \sin \theta \right] \times 10^2$$

$$b = \frac{\rho_L}{\rho_g} \left( \frac{Re_L}{We_L} \right)^2$$

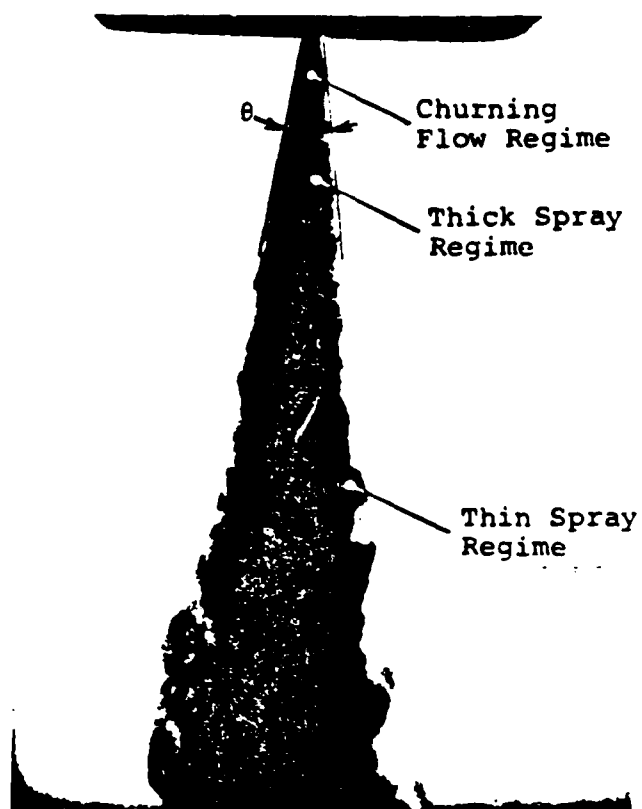


FIG. 1

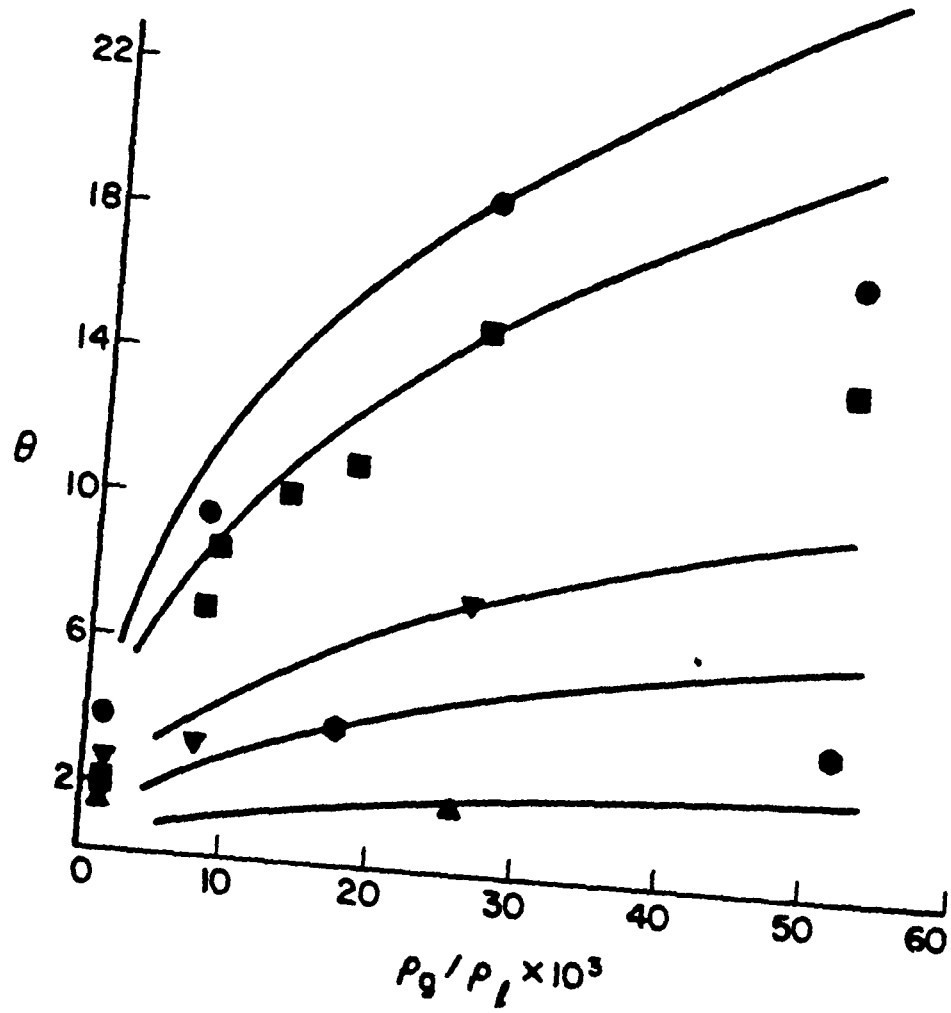
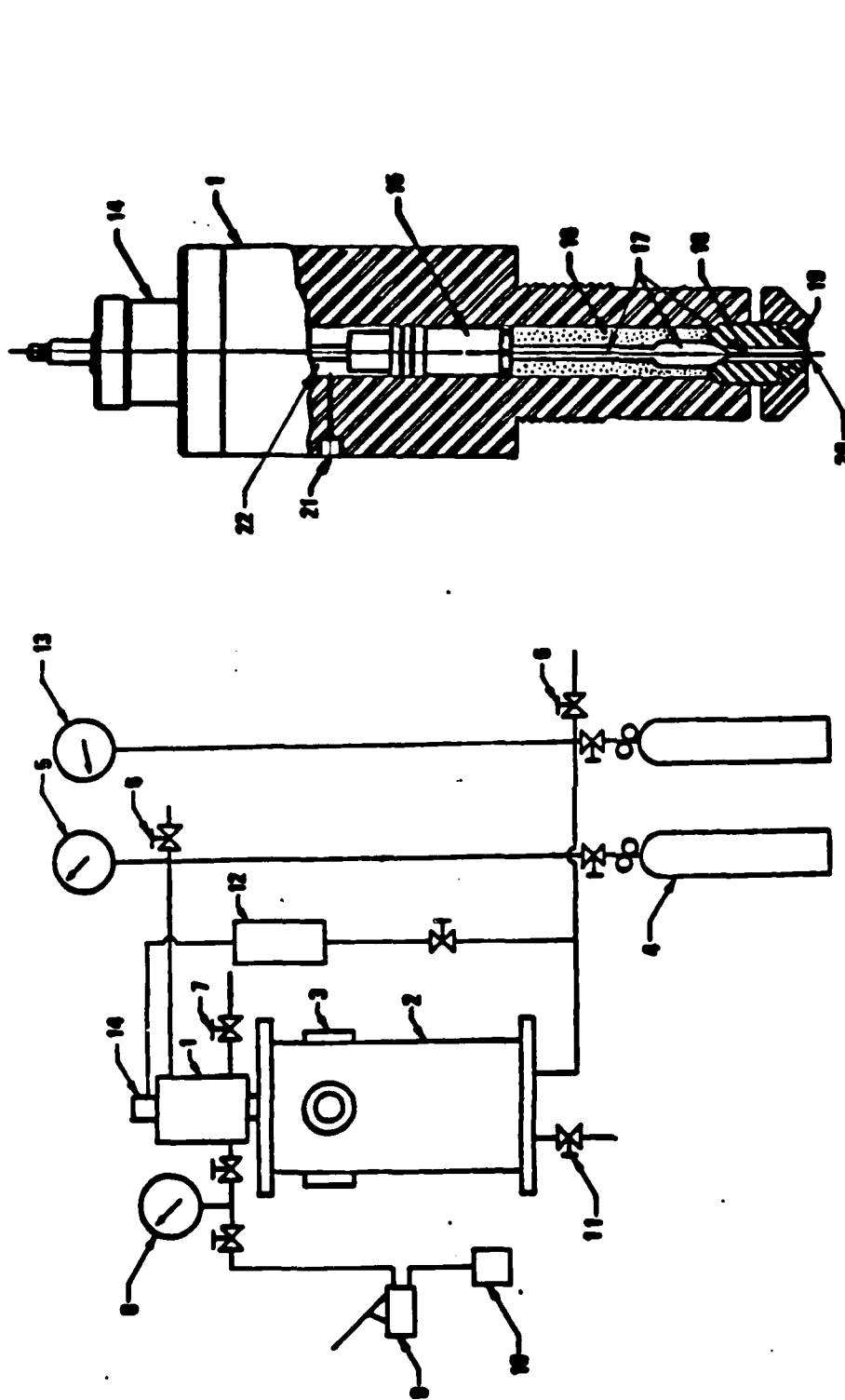
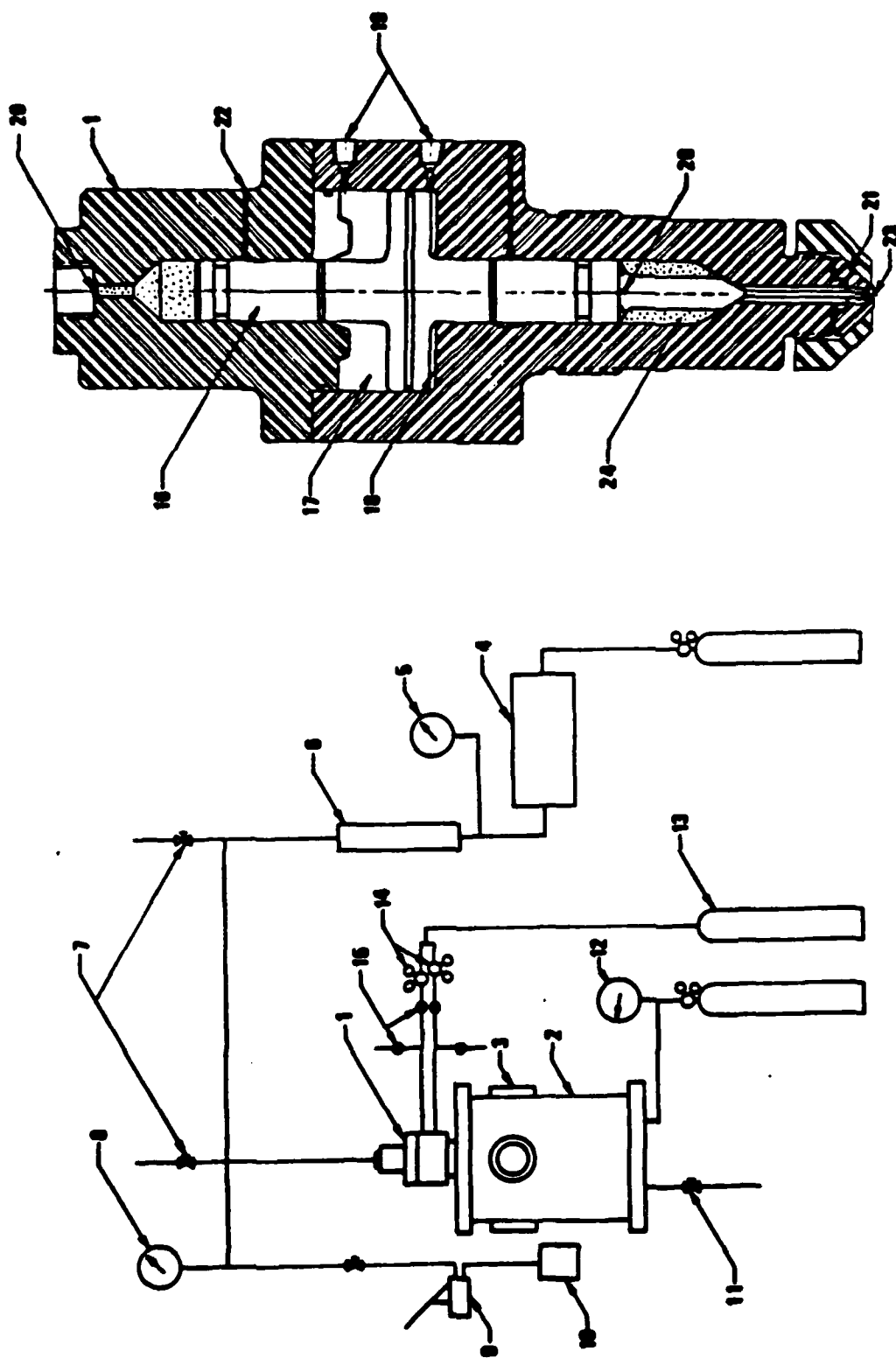


FIG. 2



- |                              |                               |                     |
|------------------------------|-------------------------------|---------------------|
| 1. INJECTION CYLINDER        | 10. TEST LIQUID TANK          | 19. NOZZLE PIECE    |
| 2. SPRAY CHAMBER             | 11. DRAIN                     | 20. NOZZLE          |
| 3. WINDOW                    | 12. PRESSURE AMPLIFIER        | 21. DRIVER GAS PORT |
| 4. NITROGEN CYLINDER         | 13. CHAMBER GAS PRESSURE GAGE | 22. DRIVER GAS      |
| 5. DRIVER GAS PRESSURE GAGE  | 14. HYDRAULIC POWER CLAMP     |                     |
| 6. VENT                      | 15. PISTON                    |                     |
| 7. BLEEDING VALVE            | 16. TEST LIQUID RESERVOIR     |                     |
| 8. TEST LIQUID PRESSURE GAGE | 17. VALVE                     |                     |
| 9. HAND PUMP                 | 18. VALVE SEAT                |                     |

FIG. 3



**FIG. 4**

- |    |                             |     |                           |     |                     |
|----|-----------------------------|-----|---------------------------|-----|---------------------|
| 1. | INJECTION CYLINDER          | 10. | TEST LIQUID TANK          | 19. | CONTROL GAS PORTS   |
| 2. | SPRAY CHAMBER               | 11. | DRAIN                     | 20. | TEST LIQUID CONDUIT |
| 3. | WINDOW                      | 12. | CHAMBER GAS PRESSURE GAGE | 21. | NOZZLE PIECE        |
| 4. | PRESSURE INTENSIFIER        | 13. | NITROGEN CYLINDER         | 22. | LEAK OFF            |
| 5. | DRIVER LIQUID PRESSURE GAGE | 14. | REGULATORS                | 23. | NOZZLE              |
| 6. | LIQUID RESERVOIR            | 15. | SOLENOID VALVES           | 24. | TEST LIQUID         |
| 7. | BLEEDING VALVES             | 16. | VALVE UNIT                |     |                     |
| 8. | TEST LIQUID PRESSURE GAGE   | 17. | UPPER CONTROL GAS CHAMBER |     |                     |
| 9. | HAND PUMP                   | 18. | LOWER CONTROL GAS CHAMBER |     |                     |
- FIG. 4



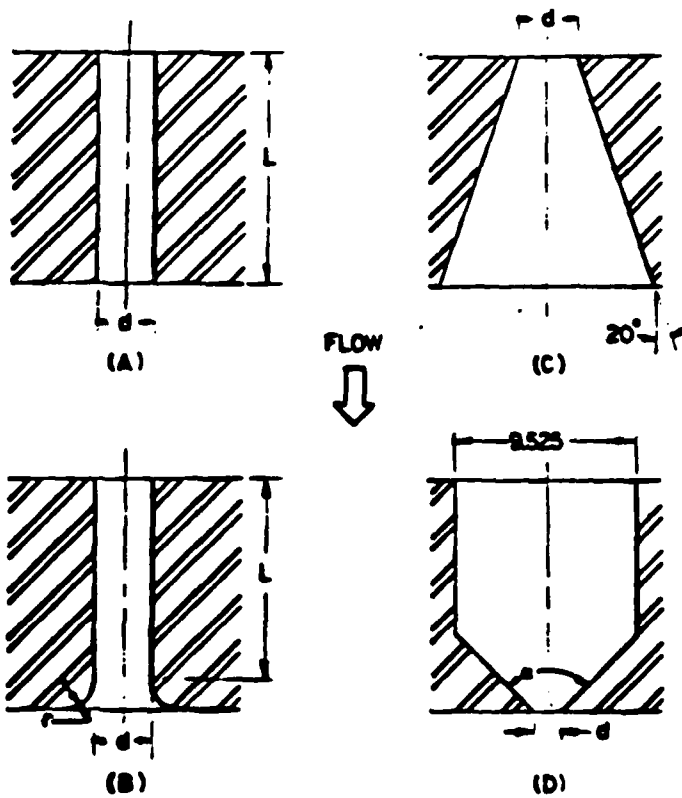
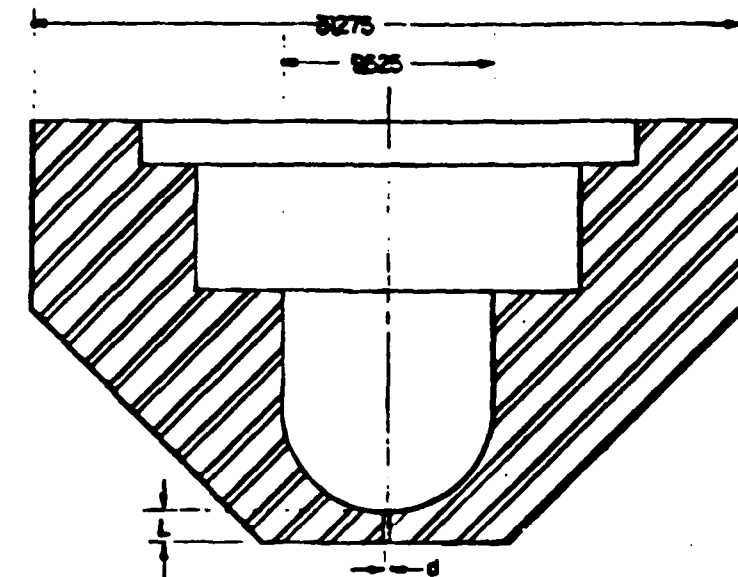
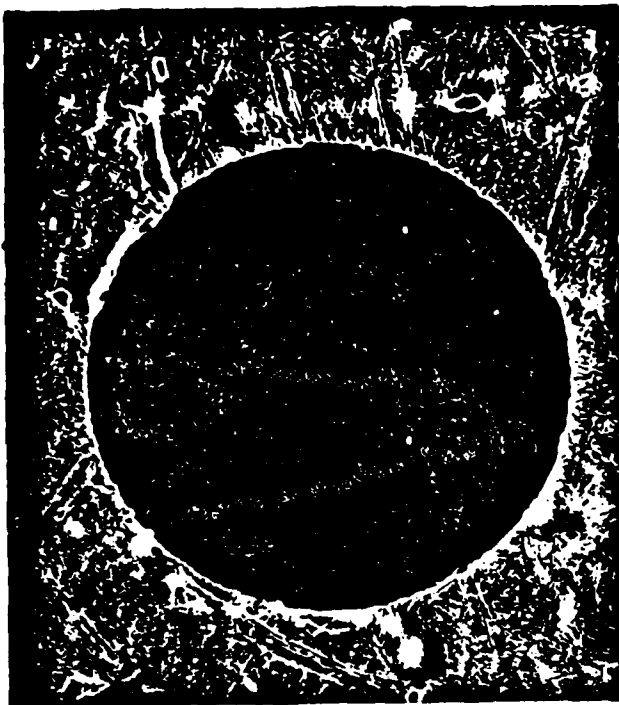
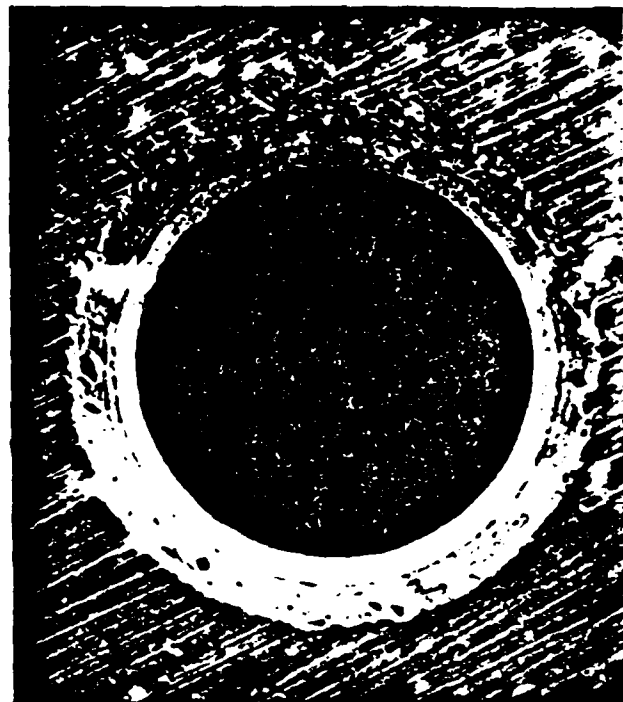


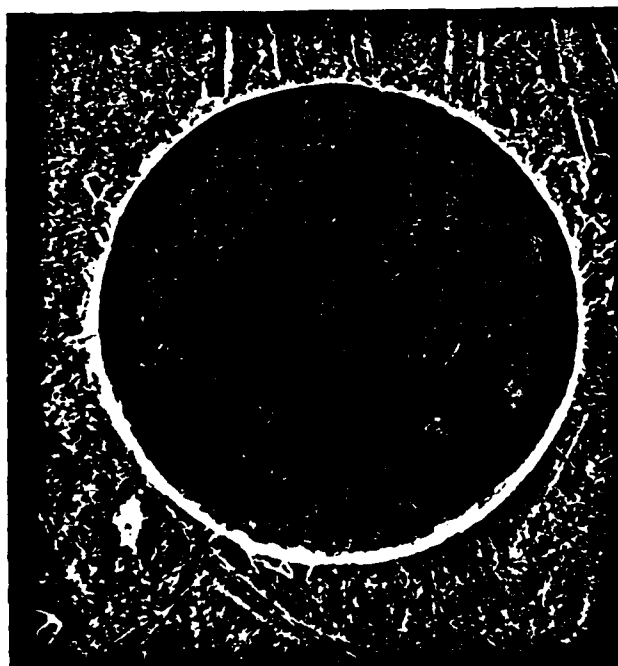
FIG. 5



(A) ENTRANCE, BEFORE ANY TEST



(B) EXIT, BEFORE ANY TEST



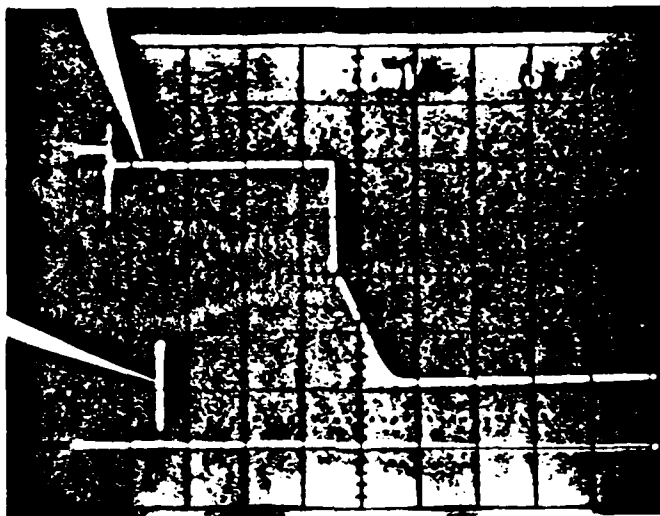
(C) ENTRANCE, AFTER  $P_l = 91.8$   
MPa TESTS



(D) EXIT, AFTER  $P_l = 91.8$   
MPa TESTS

TEST LIQUID PRESSURE TRACE

DELAY TRIGGER OUT  
SIGNAL FROM THE  
OSCILLOSCOPE



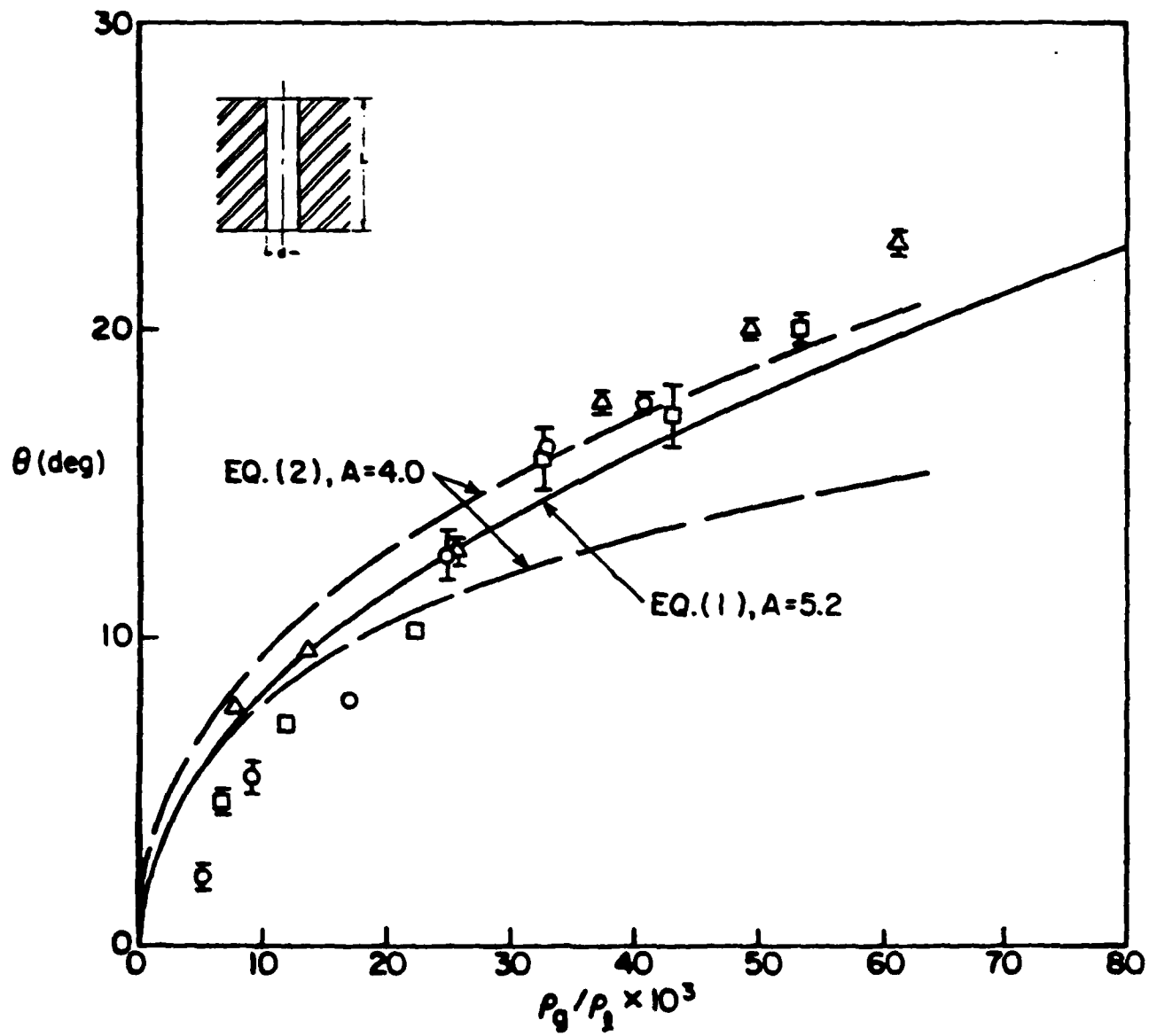


FIG. 8

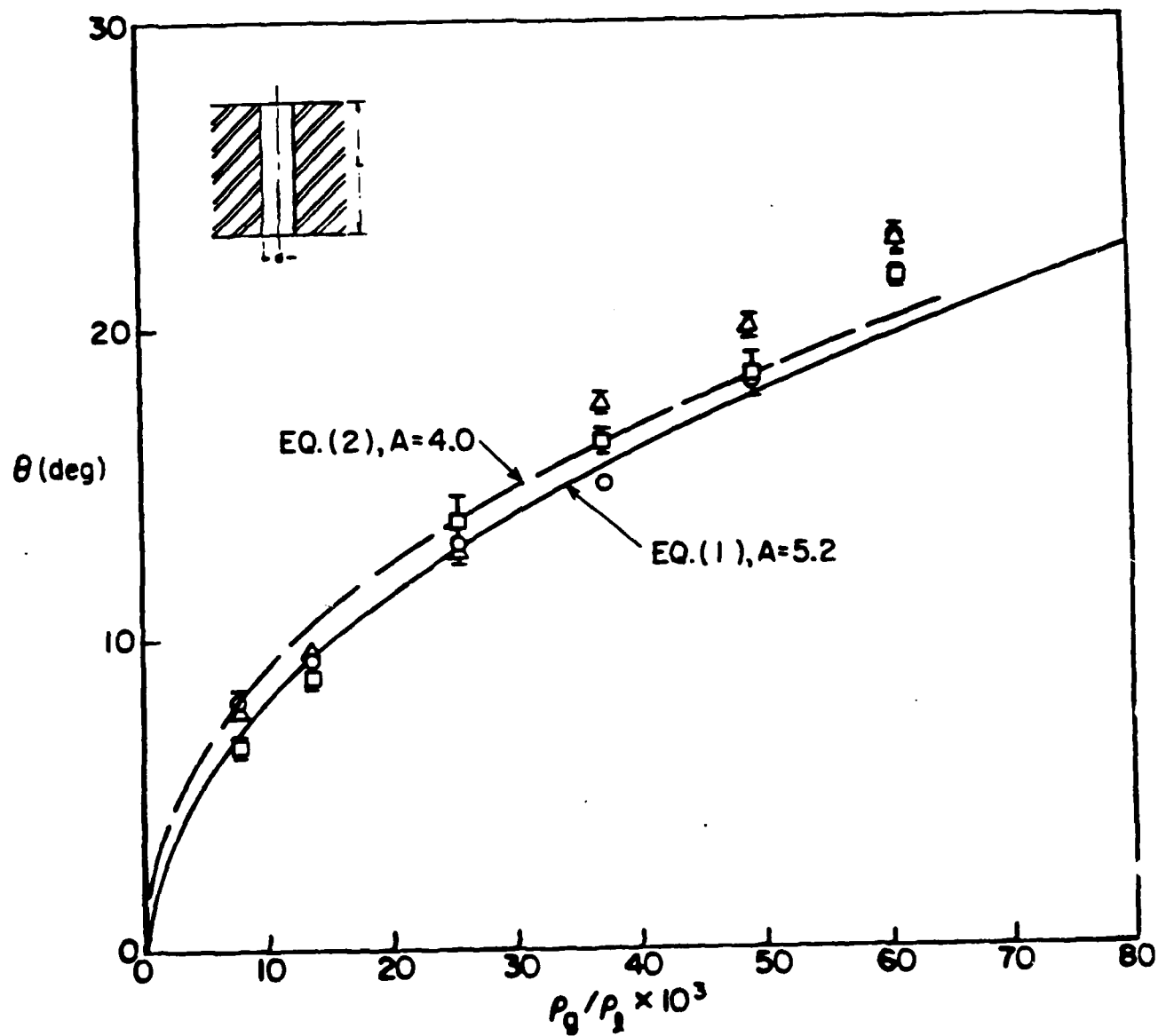


FIG. 9

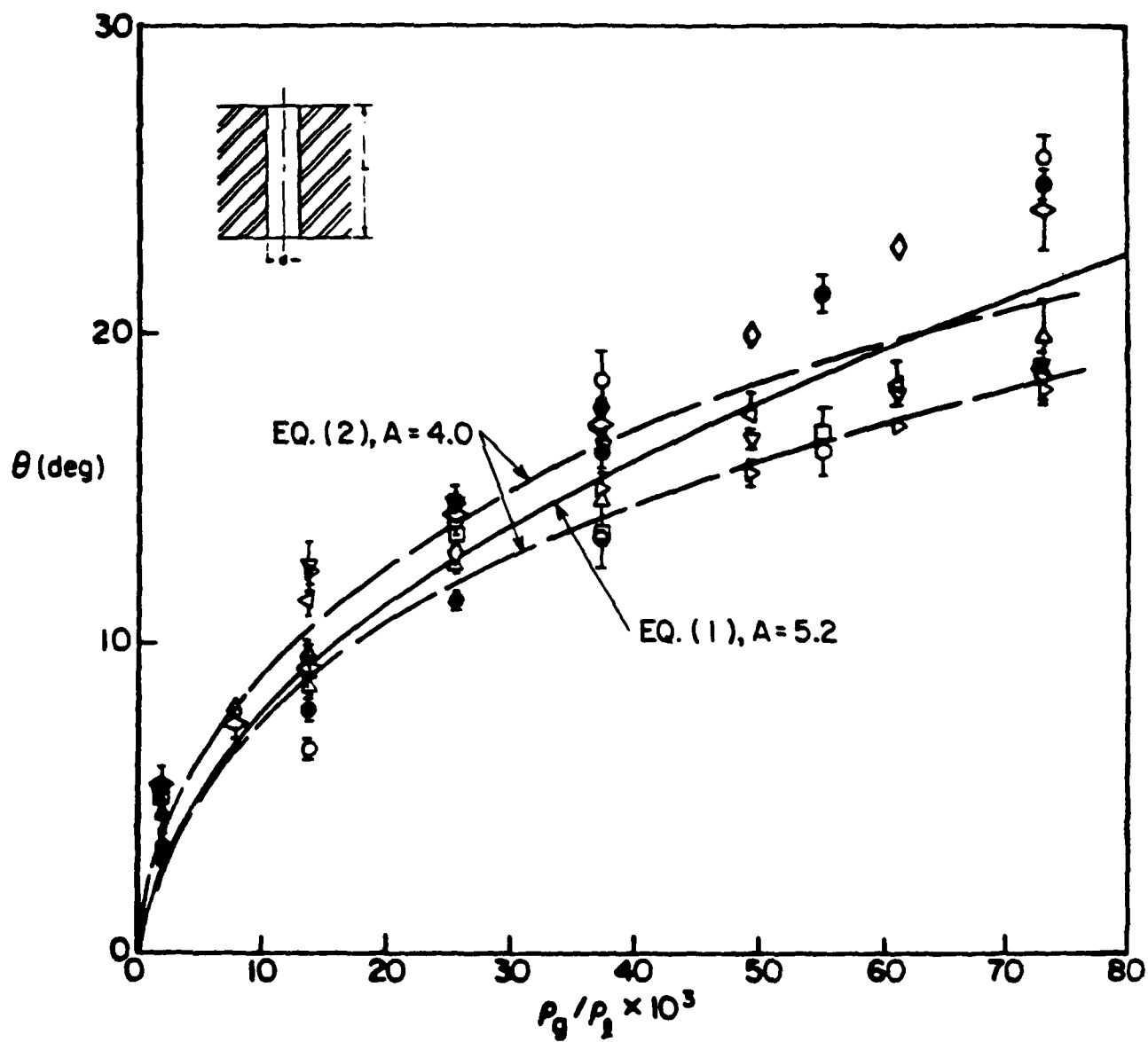


FIG. 10

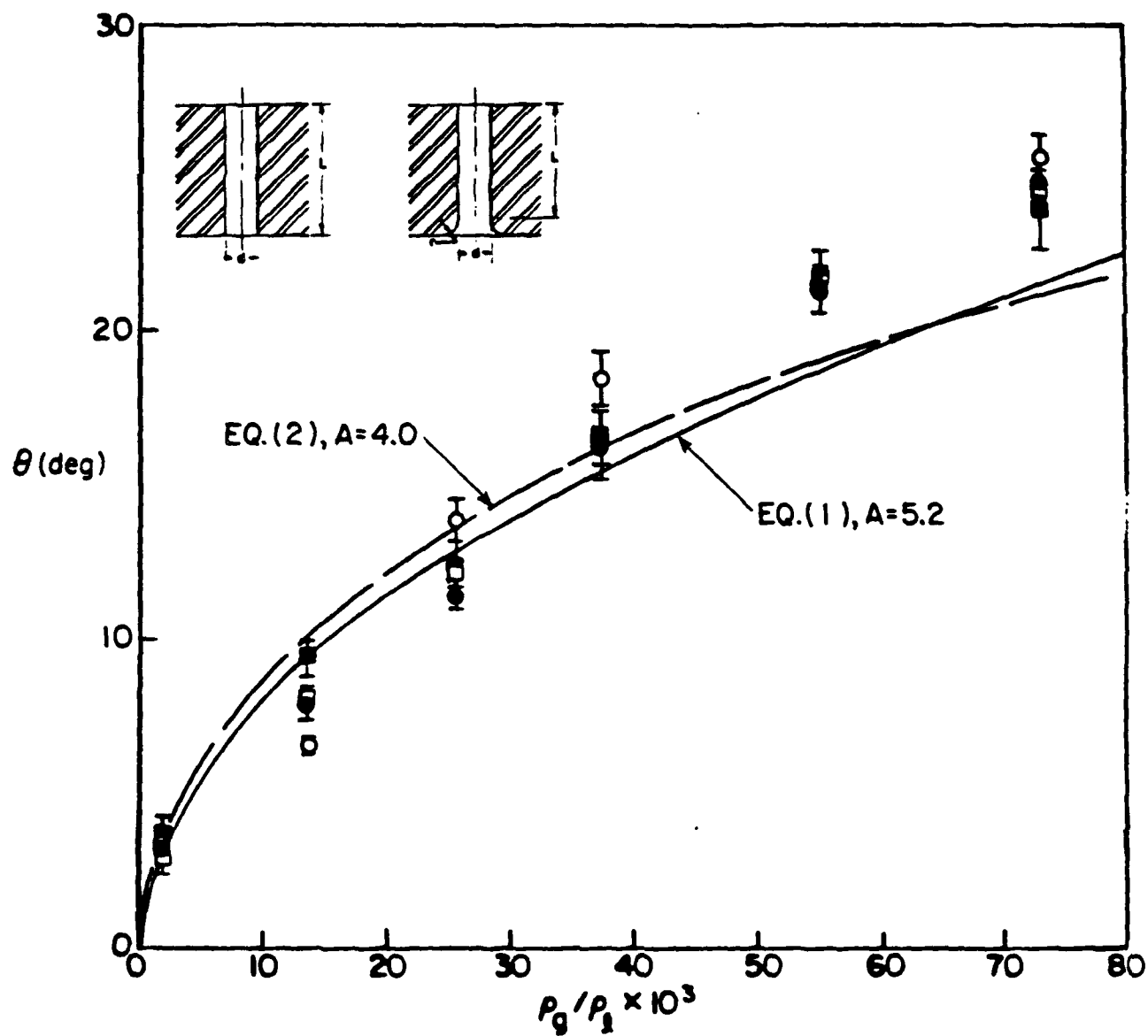


FIG. 11

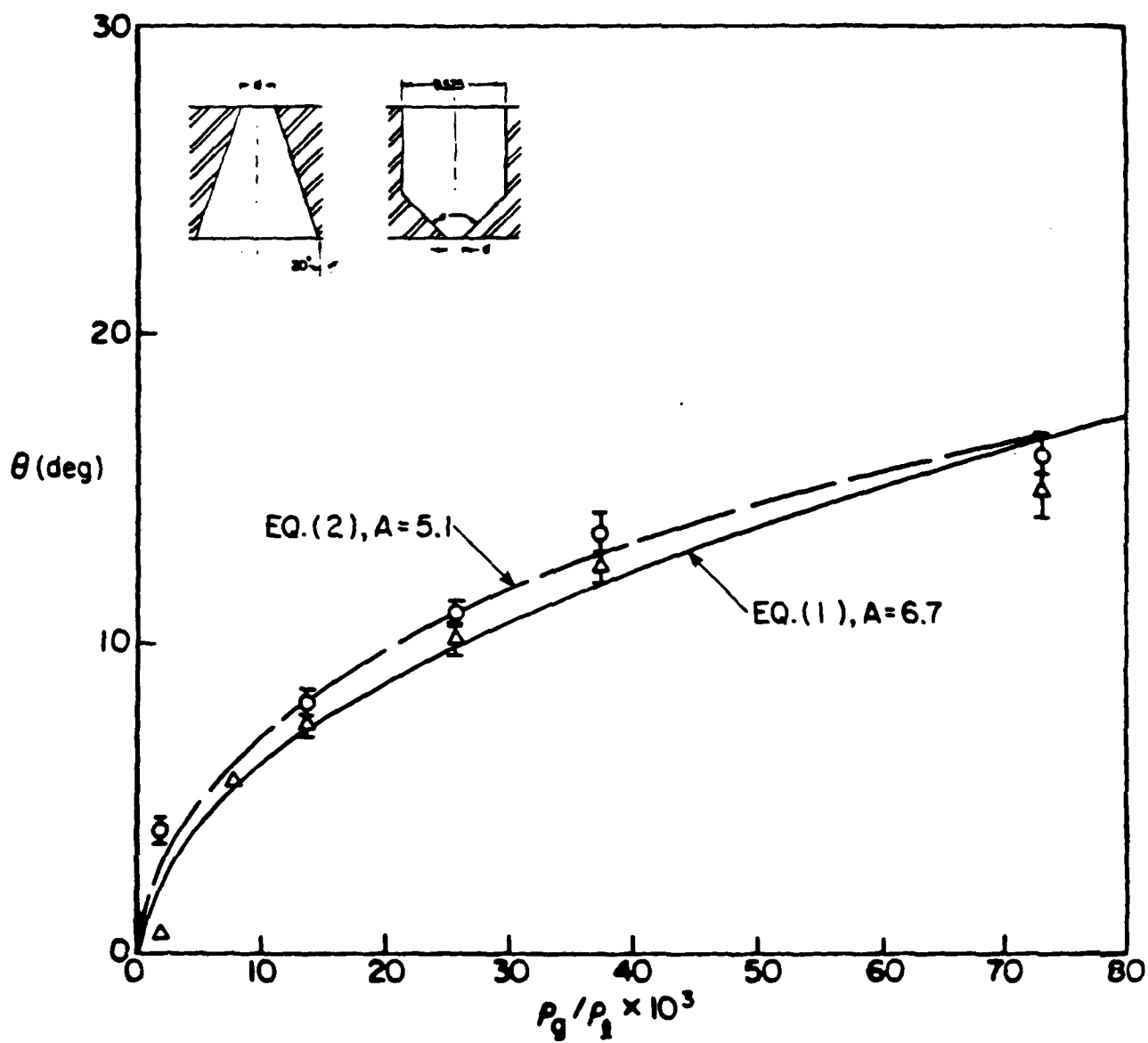


FIG. 12



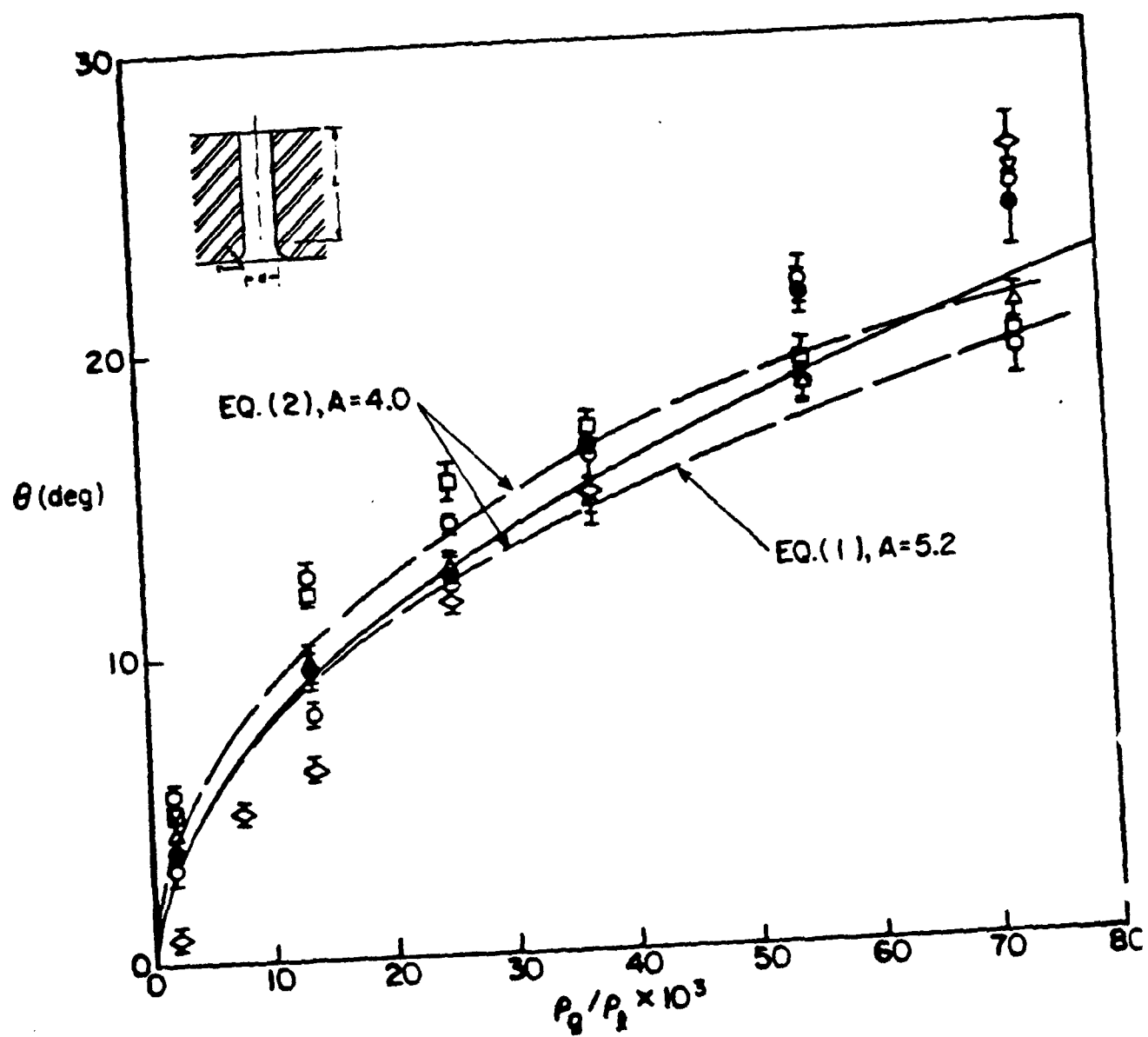


FIG. 13

$$\frac{A}{4\pi} \tan \frac{\theta}{2} \sqrt{\frac{\rho_l}{\rho_g}}$$

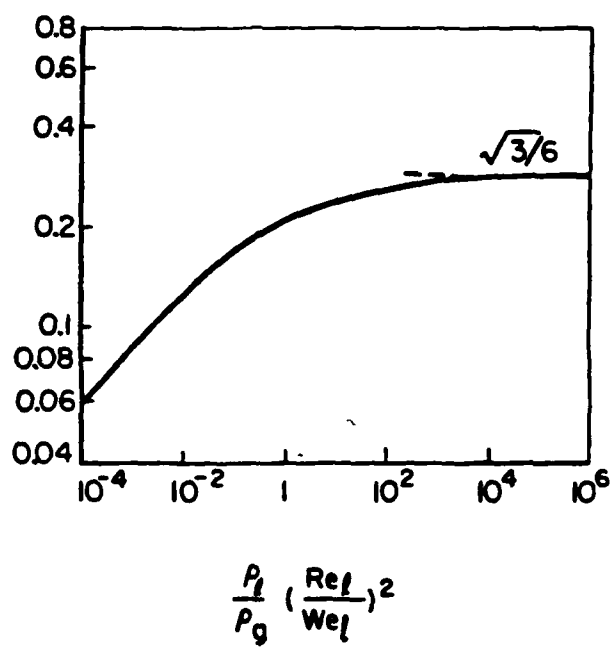


FIG. 14

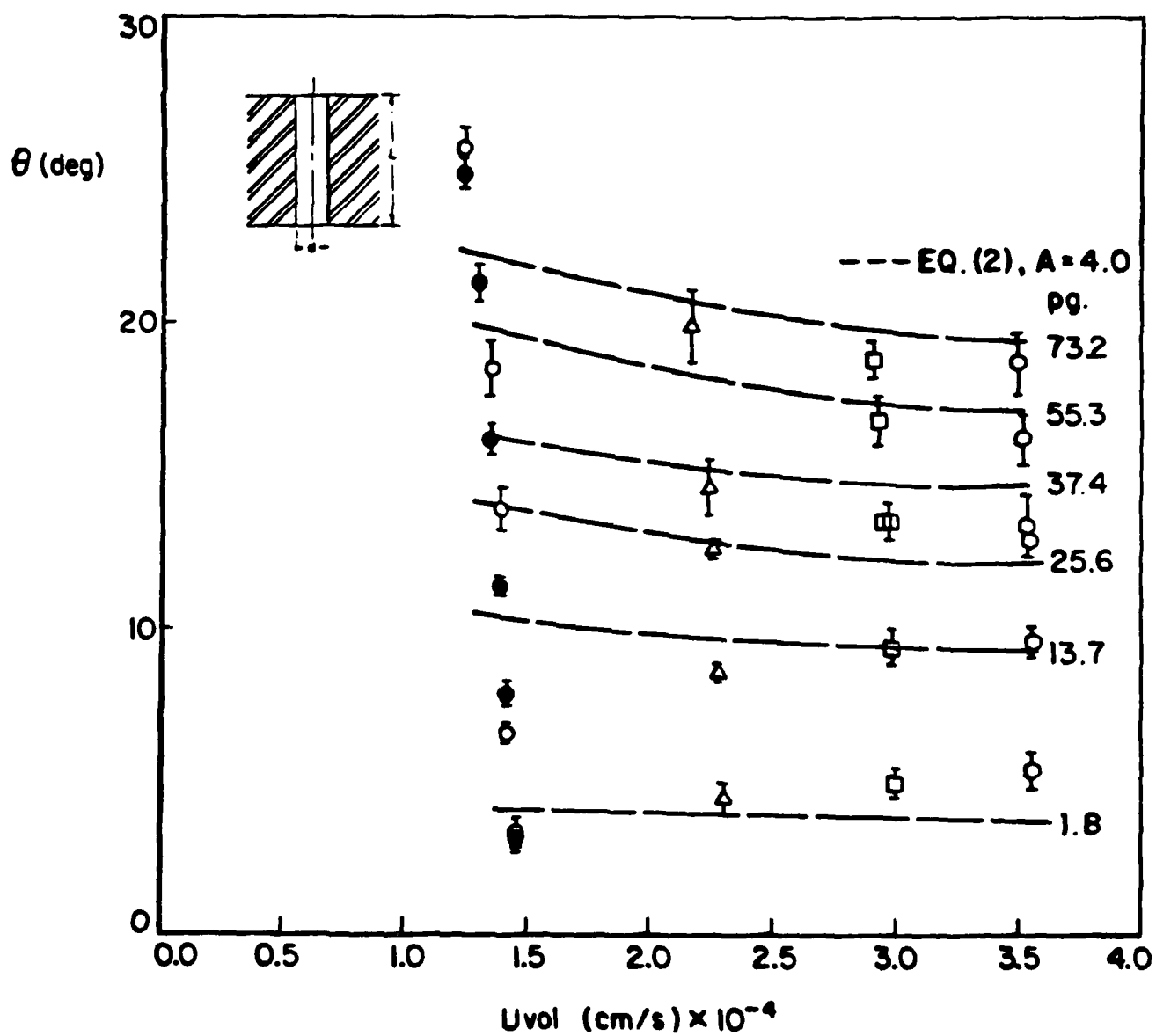


FIG. 15

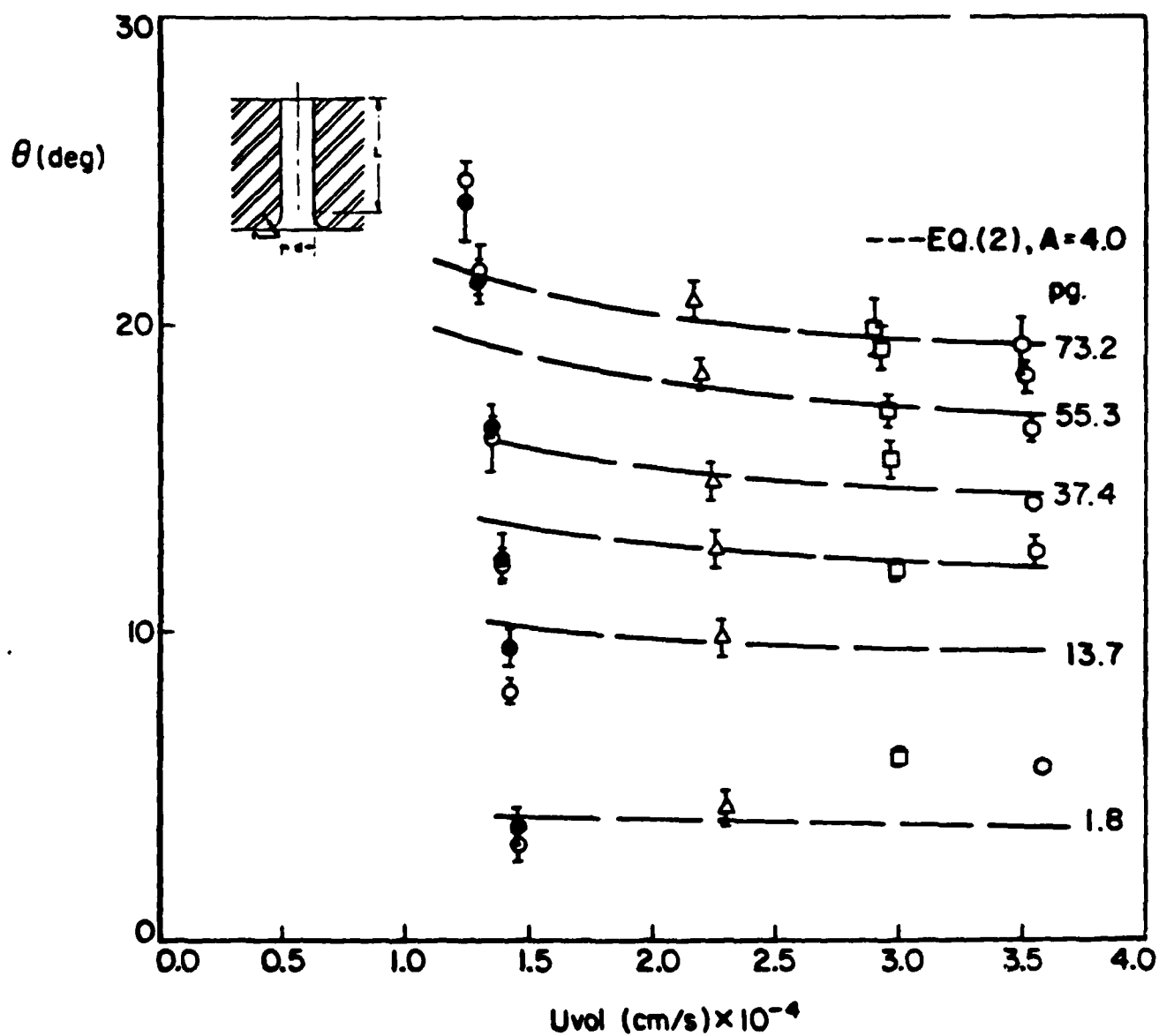


FIG. 16

# FIGURE CAPTIONS

Fig. 1. Typical atomizing jet

Fig. 2. Predicted (Equation 1) and measured spray angle versus gas-liquid density ratio [1]

Test liquid: water

Gas : nitrogen

Nozzle :  $d = 340 \text{ } \mu\text{m}$

● : straight sided converging nozzle,  $L/d = 0.5$ ,  $A = 3.1$

■ : constant diameter tube,  $L/d = 4.0$ ,  $A = 3.9$

▼ : constant diameter tube,  $L/d = 10.1$ ,  $A = 8.0$

● : constant diameter tube,  $L/d = 49.3$ ,  $A = 13.4$

▲ : constant diameter tube,  $L/d = 85.0$ ,  $A = 28.0$

Fig. 3. Schematic diagram of the system for liquid pressures up to 38.0 MPa with details of the injection cylinder.

Fig. 4. Schematic diagram of the system for liquid pressures between 38.0 and 207 MPa with details of the injection cylinder.

Fig. 5. Nozzle piece with details of nozzle geometries, unit : mm

(A) constant diameter tube nozzle: I, II(a), II(b), II(c), and III

(B) rounded outlet nozzle : IV(a), IV(b), and V

(C) straight sided diverging nozzle : VI

(D) straight sided converging nozzle : VII

Fig. 6. Typical electron microscope photographs of entrance and exit of nozzle IV(b) before and after ultra-high liquid pressure tests.

Fig. 7. Pressure trace of test liquid and delay trigger out signal from the oscilloscope.

Fig. 8. Spray angle for different test liquids

test liquid: ○ - water, ▲ - n-hexane, and □ - n-tetradecane

$\Delta p = 13.8 \text{ MPa}$

Nozzle = II(a)

FIGURE CAPTIONS (cont.d)

Fig. 9. Spray angle for different nozzle diameters

test liquid : n-hexane

$\Delta p = 13.8$  MPa

nozzle :  $\circ$ - I  $\Delta$ - II(a), and  $\square$ - III.

Fig. 10. Spray angle for nozzles II(a), II(b), and II(c) for injection pressures up to 107.6 MPa

test liquid : n-hexane

$\diamond$  : nozzle II(a),  $\Delta p = 11.0$  MPa

$\diamond$  : nozzle II(a),  $\Delta p = 13.8$  MPa

$\circ$  : nozzle II(b),  $p_l = 15.3$  MPa, before  $p_l = 91.8$  MPa tests

$\bullet$  : nozzle II(b),  $p_l = 15.3$  MPa, after  $p_l = 91.8$  MPa tests

$\Delta$  : nozzle II(b),  $p_l = 38.0$  MPa

$\square$  : nozzle II(b),  $p_l = 64.9$  MPa

$\circ$  : nozzle II(b),  $p_l = 91.8$  MPa

$\nabla$  : nozzle II(c),  $\Delta p = 34.5$  MPa

$\triangleright$  : nozzle II(c),  $\Delta p = 68.9$  MPa

$\triangleleft$  : nozzle II(c),  $\Delta p = 103.4$  MPa

Fig. 11 Spray angle for nozzles II(b) and IV(b) before and after ultra-high pressure tests

test liquid : n-hexane

$p_l = 15.3$  MPa

$\circ$  : nozzle II(b), before  $p_l = 91.8$  MPa tests

$\bullet$  : nozzle II(b), after  $p_l = 91.8$  MPa tests

$\square$  : nozzle IV(b), before  $p_l = 91.8$  MPa tests

$\blacksquare$  : nozzle IV(b), after  $p_l = 91.8$  MPa tests

FIGURE CAPTIONS (cont.d)

Fig. 12. Spray angle for cavitation-free nozzles VI and VII

test liquid : n-hexane

$\Delta p$  : 11.0 MPa

$\Delta$  : nozzle VI

O : nozzle VII

Fig. 13. Spray angle for rounded outlet nozzles IV(a), IV(b), and V

test liquid: n-hexane

$\diamond$  : nozzle IV(a),  $\Delta p = 11.0$  MPa

O : nozzle IV(b),  $P_l = 15.3$  MPa, before  $P_l = 91.8$  MPa tests

● : nozzle IV(b),  $P_l = 15.3$  MPa, after  $P_l = 91.8$  MPa tests

$\Delta$  : nozzle IV(b),  $P_l = 38.0$  MPa

$\square$  : nozzle IV(b),  $P_l = 64.9$  MPa

O : nozzle IV(b),  $P_l = 91.8$  MPa

$\nabla$  : nozzle V,  $\Delta p = 11.0$  MPa

Fig. 14. Predicted spray angle from Ranz [8]

Fig. 15. Effect of injection pressure on spray angle for nozzle II(b)

test liquid : n-hexane

O : nozzle II(b),  $P_l = 15.3$  MPa, before  $P_l = 91.8$  MPa tests

● : nozzle II(b),  $P_l = 15.3$  MPa, after  $P_l = 91.8$  MPa tests

$\Delta$  : nozzle II(b),  $P_l = 38.0$  MPa

$\square$  : nozzle II(b),  $P_l = 64.9$  MPa

O : nozzle II(b),  $P_l = 91.8$  MPa

FIGURE CAPTIONS (con.t)

Fig. 16. Effect of injection pressure on spray angle for nozzle IV(b)

test liquid : n-hexane

○ :  $P_l = 15.3$  MPa, before  $P_l = 91.8$  MPa tests

● :  $P_l = 15.3$  MPa, after  $P_l = 91.8$  MPa tests

△ :  $P_l = 38.0$  MPa

□ :  $P_l = 64.9$  MPa

○ :  $P_l = 91.8$  MPa



APPENDIX E

ON THE MECHANISM OF ATOMIZATION  
OF A LIQUID JET

R.D. Reitz and F.V. Bracco

On the Mechanism of Atomization  
of a Liquid Jet

R. D. Reitz and F. V. Bracco

Department of Mechanical and Aerospace Engineering  
Princeton University, Princeton, New Jersey 08544

In the atomization regime of a round liquid jet, a diverging spray is observed immediately at the nozzle exit. In this regime, the mechanism that controls the breakup of the jet has not yet been determined even though several have been proposed. The jet atomization mechanism was investigated experimentally using two photographic techniques to record the initial transient and the steady state behavior of high velocity liquid jets. Injections under constant liquid pressures from 500 psia (33 atm) to 2500 psia (166 atm) were studied with 5 different mixtures of water and glycerol. The atmosphere was nitrogen, helium, and xenon with gas pressures up to 600 psia (40 atm) at room temperature. Fourteen nozzles were used with length-to-diameter ratios ranging from 85 to 0.5 with sharp and rounded inlets, each with an exit diameter of about 340  $\mu$ . An evaluation of previously proposed jet atomization mechanisms shows that aerodynamic effects, liquid turbulence, jet velocity profile

rearrangement effects and liquid supply pressure oscillations each cannot alone explain the experimental results. From the results it is concluded that cavitation phenomena, alone, could possibly explain the results in the atomization regime, but the more likely mechanism combines aerodynamic effects with liquid cavitation and/or wall boundary layer profile relaxation phenomena. The conclusions were reached by varying the liquid pressure and viscosity, and gas pressure and density and the nozzle geometry as stated. However, the nozzle exit diameter, the liquid surface tension and density and the gas and liquid temperatures were not varied significantly. Their variations may necessitate consideration of additional effects in the mechanism of atomization.

## 1. INTRODUCTION

The injection of a liquid through a nozzle into an initially stagnant gas in the atomization regime results in a diverging spray immediately at the nozzle exit. Droplets are produced with sizes very much less than the nozzle exit diameter. Here the breakup mechanism is unknown.

Castleman<sup>1</sup> postulated that jet atomization is due to aerodynamic interaction between the liquid and the gas and Ranz<sup>2</sup> proposed that the drop sizes are related to the wavelengths of unstable aerodynamically induced waves growing on the surface of the liquid jet. This model of jet atomization has also been analyzed by Levich<sup>3</sup>. Various authors have objected to this model, reasoning that aerodynamically induced wave growth requires a

finite time to develop and therefore an intact (unbroken) length should be observed. Thus, DeJuhasz<sup>4</sup> proposed that the jet breakup process occurs within the nozzle itself and that liquid turbulence may play an important part. Schweitzer<sup>5</sup> suggested that the radial component of velocity in turbulent pipe flow could cause the immediate disruption of the jet at the nozzle exit. Other mechanisms based on liquid turbulence have been proposed by Holroyd<sup>6</sup> and Sitkei<sup>7</sup>.

Bergwerk<sup>8</sup> argued that the turbulent velocity components in the Reynolds number range of interest are not of sufficient magnitude to explain the observed atomization phenomenon. He concluded that liquid cavitation phenomena could create large amplitude pressure disturbances in the flow leading to atomization of the jet. Sadek<sup>9</sup> hypothesized that cavitation bubbles may influence the jet breakup process.

Rupe<sup>10</sup> observed that high velocity laminar liquid jets could be more unstable than fully developed turbulent jets. He believed that this instability is due to rearrangement in the cross-sectional velocity profile of the fully developed laminar jet once the constraint of the nozzle wall is removed at the nozzle exit. He reasoned that this redistribution of energy within the jet gives rise to radial velocity components which disrupt the jet. This rearrangement effect is minimal for jets with flat exit velocity profiles which explained the greater stability that he observed for turbulent jets.

Another suggested jet breakup agency is the acceleration

experienced by the fluid in the boundary layer on the nozzle wall at the nozzle exit caused by the abrupt change in boundary condition on the flow. Shkadov<sup>11</sup> investigated the effect of changes in interface tangential stresses in a boundary layer stability analysis and confirmed the existence of unstable short wavelength surface waves.

Finally, liquid supply pressure oscillations have been noted by Giffen and Muraszew<sup>12</sup> to have an effect on the outcome of the jet breakup process. Since these supply pressure oscillations are commonly found in injection systems, it has been suggested that they play an essential role in the jet breakup process itself.

## 2. EXPERIMENTAL DETAILS

The experimental apparatus used to study the jet atomization phenomenon is shown schematically in Fig. 1. Two spray chambers were used. The larger chamber (I.D. 19 cm) was used for tests with air and nitrogen and the smaller one (I.D. 3.5 cm) for xenon and helium. The liquid injection system allowed up to 40 cm<sup>3</sup> of a test liquid to be injected with nominally constant injection pressures during a given injection.

The system consisted of a piston which served to compress the test liquid and was in turn driven by high pressure gas from a pressure amplifier system. The test liquid was separated from the chamber gas by means of a variety of single hole nozzles mounted in nozzle holders. The nozzle exit diameter  $d_0$  was 0.34 mm to 0.39 mm for all of the nozzles used in the experiments.

Diagrams of the nozzle passages are shown in Figs. 2a and 2b. The fourteen injection nozzles used fell into two categories: constant diameter tube nozzles (nozzles I, II, III, VI, VII, VIII, IX and  $X_{O,N}$ ) shown in Fig. 2a, and convergent nozzles (nozzles IV, XI, XII, XIII, and XIV) shown in Fig. 2b. The nozzle length to diameter ratios ranged from less than 1/2 to 85 and the design included rounded and sharp edged nozzle inlets. Nozzles VI, VII, VIII, IX and  $X_{O,N}$  correspond to a sharp inlet configuration, with  $L/d_o \approx 4$ . Nozzles VI, VII and VIII were made from plastic and a length of 0.34 mm I.D. stainless steel tubing was glued into a plastic insert for nozzle IX. Nozzles  $X_O$  and  $X_N$  were made from brass.

Nozzles XI and XII were similar to nozzle IX, however, the inlet of the stainless steel hypodermic tubing was flared. For nozzle IV the nozzle passage was made from thin walled shaped glass tubing. Nozzle XIII was made from plastic and nozzle XIV was made of brass. The nozzle passages for nozzles I ( $L/d_o = 85$ ), II ( $L/d_o = 49.3$ ) and III ( $L/d_o = 10.1$ ) were made from stainless steel tubing with sharp edge inlets.

Two methods of event initiation were employed. In the first, flow of pressurized liquid was prevented prior to a test by gluing a 0.013 cm thick length of shaped tin fuse ribbon directly over the nozzle exit hole. In the case of nozzle II the fuse ribbon was sandwiched at the tube entrance as shown in Fig. 2a. A high energy short duration (~10  $\mu$ s) electrical discharge pulse was then supplied to the fuse in order to melt locally the metal in the immediate vicinity of the nozzle exit hole. In the second method,

the piston above the reservoir liquid was restrained by a retractable trigger pin. Removal of the pin caused the piston to compress the test liquid rapidly, and, after an initial unsteady phase, a constant injection pressure resulted and measurements were made.

Two optical systems were used in the experiments. In the first, the transient behavior of the liquid jet at the onset of injection was recorded by means of a Cordin model 117 high speed framing camera with frame rates up to  $1.25 \times 10^6$  frames/sec. The fuse technique of event initiation was used in these tests which allowed sixty frames of film to be obtained for each experiment. The jet was illuminated by the simultaneous discharge of two xenon flash tubes and the liquid pressure was monitored by a fast response pressure transducer. These experiments are referred to as "transient studies."

The second optical system used a strobe flash which allowed a single short exposure (41  $\mu$ s) photograph of the liquid jet to be taken about one second after its initial emergence into the chamber gas. These are the "steady state" studies. Two techniques were applied simultaneously to the same jet in most cases.

Further details of the experimental apparatus and experimental procedures are given by Reitz<sup>13</sup>.

### 3. SCOPE AND ACCURACY OF MEASUREMENTS

The operating conditions of the 100 steady state photographs (S) and the 55 transient studies (T) are summarized in Tables 1a and 1b. The experiments were conducted at 67 different sets of operating conditions, or series, with the number of repeated runs

indicated in the first two columns of the Tables. The missing series are reported in Reitz<sup>13</sup>. The series are organized into groups of tests with the same injection nozzle.

Injectors were performed in nitrogen, helium and xenon, and atmospheric air. The chamber gas pressures ranged from 15 to 600 psia (1 to 40 atm) and the test environment was at room temperature. The liquids tested were combinations of water and glycerol (0, 50, 68, 80 and 100% glycerol wt.) and their use permitted a thousand-fold range in liquid viscosity  $\mu_L$  to be realized with relatively insignificant changes (<20%) in the liquid density  $\rho_L$  and liquid surface tension  $\sigma$ . The liquid pressure  $P_L$  ranged from about 500 to 2100 psia (33 to 140 atm) (a fixed value for a given series) and the entries of a group in Tables I are made in order of increasing injection pressure  $\Delta P = P_L - P_g$ , for fixed gas density level. A high molecular weight polymer (Dow Separan AP 30; MW  $\sim 10^6$ ) mixed with water at concentrations of 100 ppm was used as the spray liquid in Series 1b, 12c and 66d, and carbonated water (saturated at 1 atmosphere) was used in Series 66c.

The angles of divergence of the steady and the transient jets  $\theta_s$  and  $\theta_T$ , i.e. the spray angles, were measured from the photographs. The distance from the nozzle to the point where the divergence was observed to begin, i.e., the intact lengths  $x_{IS}$  and  $x_{IT}$ , were also measured. These quantities can be seen in the photographs of the jet in Fig. 3, which shows some of the transient frames and the steady state photograph of series 47, for example. The nozzle exit is at the top of each photograph



and time increases from left to right in the figure. Measurements of the distance from the nozzle exit to the tip of the jet allowed the jet tip velocity  $U_T$  to be estimated for each run. The quantities are shown in the tables for each series. A more detailed discussion of the transient studies has already been given by Reitz and Bracco<sup>14</sup>.

The injection velocity  $U_{vol}$ , defined by  $U_{vol} = V/A_N \tau$ , was determined knowing the volume of the injected liquid, the area of the nozzle and by measuring the time taken to inject the fixed mass,  $\tau$ , in which case the orifice discharge coefficient is given by  $C_D = U_{vol}/U_{ideal}$ . The jet diameter measured at the nozzle exit is also presented in the tables. Other entries in Table I are dimensionless ratios formed using the liquid and gas properties, the nozzle diameter, and the injection velocity  $U_o = U_{vol}$ . These include the Reynolds number  $Re_L = \frac{\rho_L U_o d_o}{\mu_L}$ , the Weber numbers  $We_g = \frac{\rho_g U_o^2 d_o}{\sigma}$ ,  $We_L = \frac{\rho_L U_o^2 d_o}{\sigma}$  and the number  $\frac{\rho_L}{\rho_g} \left( \frac{Re_L}{We_L} \right)^2$  for each test condition.

Care was devoted to perfecting the fuse ribbon technique for event initiation. It was found to work extremely well when used with nozzles with metal nozzle passages. The photograph shown in Fig. 3 is typical of the condition of the nozzle exit hole after a test and shows that the nozzle exit area is unobstructed by the rest of the fuse material which remained on the exit face during the injection.

Experiments made with nozzles which had plastic nozzle passages, nozzles VI, VII, VIII and XIII, were found to be non-repeatable and their results are not given in Table I and were

not used in deriving conclusions in the study. Experiments conducted with metal nozzle passages, nozzles I, II, III, IX, X, XI, XII and XIV, and the glass nozzle IV were found to give consistent results (divergence angles agree within  $2^\circ$ ). In these tests dimensions taken from the photographs have an estimated accuracy of  $10\% d_0$  for jet diameters,  $1^\circ$  for jet divergence angles,  $50\% d_0$  for jet intact lengths,  $10\%$  for jet tip velocities.

Nozzle passage dimensions were measured to an estimated accuracy of  $3\% d_0$  and nozzle passage internal surface roughness dimensions were visibly much less than this accuracy limit. Both liquid and gas pressures remained constant within  $5\%$  during a given test.  $99\%$  pure bottled gases were used as the chamber gases and the tap water and glycerol mixtures used were made with proportions estimated to be accurate to  $1\%$ .

#### 4. EXPERIMENTAL RESULTS

The measured jet divergence, or spray angle, was found to increase as the chamber gas was isothermally compressed, all other parameters being the same. This trend can be seen by referring to the photographs of Figs. 4a, b, c and d which show that jet atomization can be achieved by increasing both the pressure and the density of the chamber gas at constant temperature.

The observed increase in the spray angle with compression of the gas is consistent with the findings of other authors<sup>12</sup>. Quantitative results which also demonstrate this trend are given in Fig. 5. This figure shows measured jet divergence angles corresponding to tests with nozzles I, II, III, IX, XII and XIV and the series numbers are included for reference to Tables 1a and b.

An average value of the jet divergence angle is used for repeated steady state tests at the same operating conditions. A close agreement between the spray angles measured from the transient and steady state jet breakup results, in the same series, is also apparent. This result implies quasi-steadiness of the spray angle<sup>14</sup>. The open data points correspond to jets whose divergence is observed to begin at the nozzle exit and are thus classified as belonging to the atomization regime. The solid data points represent those runs whose jet divergence was found to begin some distance from the nozzle exit. These jets apparently belong to an aerodynamically induced regime of breakup<sup>15</sup>. It is seen that, for a given nozzle, atomization occurs once the chamber gas is compressed beyond a certain level and that there is no evidence of an abrupt change in the spray angle between the aerodynamic and the atomization breakup regimes.

The results of Fig. 5 are presented for a range of injection pressures for each nozzle. However, the data show that relatively large variations in the injection pressure (~30%) have little perceptible effect on the observed spray angle as the chamber gas is compressed.

The use of chamber gases of different molecular weights allowed the gas density and the gas pressure to be varied independently, with relatively minor changes in the physical properties of the gas. Thus, for example, an examination of the photographs of Figs. 6a and b (Series 37<sub>o</sub> and 39<sub>o</sub>) reveals little difference in the appearance of the two jets in spite of the factor of 10 difference in chamber gas pressure between the two tests whereas

the gas densities are approximately the same. The jets of Figs. 6c and d (Series 41<sub>N</sub> and 44<sub>N</sub>) each have approximately the same gas pressure but the gas density now differs by a factor of about four. The increased gas density is seen to produce a marked increase in the jet divergence and evidence of atomized liquid particles in the flow. Similarly, the results of Series 36, 37 and 39-45 shown in Table 1b show that the chamber gas density has a predominant effect on the jet divergence angle, and that increases in jet divergence angle obtained by isothermally compressing the chamber gas are due to effects related to the increase in the gas density and not to those related to the increase in the gas pressure.

The four photographs shown in Fig. 7 demonstrate the effect of changes in liquid viscosity and, apart from the different liquids used, are each made at the same operating conditions. Large variations in liquid viscosity influence the jet breakup process, and a high value of the liquid viscosity results in an intact jet (Fig. 7d, Series 34). It may be observed that the jet divergence angles for the jets of Fig. 7a, b and c (Series 30, 31 and 32 respectively) are similar in spite of the corresponding factor of about 18 increase in the liquid viscosity for these jets. However, while the jet divergence appears to commence at the nozzle exit for the jets of Fig. 7a and b, the jet divergence of Fig. 7c begins some 2.5 nozzle exit diameters downstream of the nozzle exit and the jet exit diameter is measured to be only 0.85 of the nozzle exit diameter.

A summary of the effect of liquid viscosity on the jet divergence angle is shown in Fig. 8 where the measured jet divergence angle is plotted against a normalized liquid viscosity ratio  $\mu_L/\mu_{H_2O}$ . The open data points correspond to jets in the atomization regime, while the solid data points represent jets in an aerodynamic regime of breakup. The results of Series 52-54 also shown in the figure confirm that intact, non-diverging jets are obtained once the liquid viscosity is increased beyond a certain level. However, injections from nozzle I, Series 2 and Series 3, show no significant change in the jet divergence angle with increased liquid viscosity for the range tested.

The results of Fig. 8, for a given nozzle, also indicate that jet atomization occurs when the liquid viscosity is reduced below a certain level and there is no evidence of an abrupt change in jet divergence angle accompanying the transition from the aerodynamic to the atomization breakup regimes.

The photographs shown in Fig. 9 demonstrate the effect of different nozzle designs under the same operating conditions. The jet shown in Fig. 9a (Series 2) was injected from nozzle I ( $L/d_o = 85$ ) and diverges minimally compared with that of Fig. 9d (Series 66) nozzle XIV ( $L/d_o = 0.5$ ). If the details of the flow field within the nozzle were not important to the jet breakup process, no difference should be detected in jets from nozzles with the same exit diameter operating under the same conditions, and differing only in their internal design. But this was found not to be the case. For example, in Fig. 9 the divergence angle

is seen to decrease markedly as  $L/d_o$  increases. The same trend is shown more quantitatively in Fig. 8 for any fixed viscosity ratio and in Fig. 5 for any fixed gas density. Moreover, in Fig. 5, it can also be seen that nozzle XII, with  $L/d_o = 2.1$  and rounded inlet gives about the same divergence angle as nozzle III with  $L/d_o = 10.1$  and sharp inlet. Obviously, rounding the inlet of short nozzles has a stabilizing effect similar to that of lengthening the nozzle. Figures 5 and 8 also show that the transition from the aerodynamic to the atomization regimes occurs at different gas densities and viscosity ratios for different nozzle designs. Parenthetically the same figures also show that there is no detectable consistent trend linking changes in the divergence angle to up to 30% changes in injection velocity.

##### 5. EVALUATION OF PROPOSED JET ATOMIZATION MECHANISMS

The photograph shown in Fig. 9a indicates that the fully developed turbulent jet injected from nozzle I ( $Re_L = 2.8 \times 10^4$ ; Hinze<sup>16</sup>) has a marked degree of stability, in contrast to the expected behavior, if pipe turbulence were to control the breakup process as suggested by Schweitzer<sup>5</sup>. Moreover, the experimental results presented in Fig. 5 indicate that the jet divergence increases with reduced pipe turbulence levels obtained by decreasing the nozzle length at otherwise the same operating conditions (nozzles I, II, and III). Accordingly, these experimental results, obtained for a particular, well-defined class of turbulent flows imply that liquid pipe turbulence alone cannot be the mechanism of jet atomization. However, no other forms of liquid

turbulence were investigated.

The experimental results show that jet atomization can be achieved with constant liquid injection pressures. This implies that liquid supply pressure oscillations are not the sole agency responsible for the atomization of the jet.

The observed stability of the detached jets (Series 33, 36N, 37N, 40N) and of the fully developed turbulent jets of nozzles I and II (Series 1-9) is consistent with the experimental results of Rupe<sup>10</sup>. However, the cross-sectional velocity profile rearrangement jet atomization mechanism is contradicted by the results of Series 34 (Fig. 7d). Here the jet Reynolds number is 5.5 and the jet exit velocity profile is parabolic for those conditions<sup>17</sup>, and yet there is no evidence of jet breakup as would be predicted by the profile rearrangement mechanism. Also intact is the jet of Series 54, whose cross-sectional velocity profile is expected to be close to parabolic since its characteristic momentum diffusion time ( $d_o^2/23.0 \nu_L = 0.5 \text{ } \mu\text{s}$ ) within the nozzle [Batchelor<sup>18</sup>] is much less than the residence time ( $L/U_o = 12 \text{ } \mu\text{s}$ ). These results cast doubt on the hypothesis that the rearrangement of the jet's cross-sectional velocity profile is the only mechanism of jet atomization.

The instability analysis of Shkadov<sup>11</sup> shows that boundary layer velocity profile relaxation phenomena at the nozzle exit can generate surface waves of growing amplitude, and that their growth rate increases as the velocity gradient below the liquid surface increases. However, for incompressible fluids, the tangential stress at a gas-liquid interface is independent of the

gas density [Batchelor<sup>18</sup>]. Therefore, if this were the mechanism of atomization, the results of injections with the same jet exit velocity profile would be independent of the gas density, contrary to the observed trends. This may be seen by comparing the two jets of Fig. 6c and d, for example, which are expected to have the same velocity profile at the nozzle exit since they are produced using the same nozzle, the same liquid, the same injection and gas pressures, neither are detached, both have Mach numbers (based on the gas sound speed) less than 0.5 and they differ only in the gas densities. Consequently, the boundary layer profile relaxation phenomena cannot alone account for the observed behavior.

The same conclusion is also supported by the more qualitative observation that no change was detected in the appearance of the jets of Series 1b, 12c and 66d where high molecular weight polymers were added to the test liquid. The addition of such polymers would be expected to influence the boundary layer on the nozzle walls and hence the atomization process if such boundary layers were the only controlling mechanism. However, no quantitative analysis of this effect was performed.

Absence of cavitation can be assumed when complete detachment of the emerging jet from the tube wall (hydraulic flip) is observed. The stability noticed for the detached jets of Series 33, 36N, 37N and 40N is consistent with the results obtained by Bergwerk<sup>8</sup> and other authors. This result indicates that cavitation-free jets are stable. Liquid cavitation can occur within a



given nozzle when a critical value of the cavitation number,  $K_{crit}$ , is reached. For  $K = (P_L - P_g) / (P_g - P_v) < K_{crit}$  the flow remains cavitation free. ( $P_v$  is the vapor pressure).

Bergwerk<sup>8</sup> presented  $K_{crit}$  data as a function of nozzle  $L/d_o$  and these numbers have been used to typify critical cavitation numbers for nozzles III, IX and XIV of the present study. In Fig. 5 it is noticed that the criteria of Bergwerk<sup>8</sup> predict that cavitation occurs in all cases within those nozzles, i.e.,  $K$  is always greater than  $K_{crit}$  for each of nozzles XIV, IX and III. Since some of the jets of Fig. 5 do not belong to the atomization regime (solid data points), one can conclude that the presence of cavitation in itself does not guarantee atomization of the jet. However, since cavitation is also predicted for the jets which belong to the atomization regime, cavitation could be the agent of atomization above a certain threshold.

Parenthetically, it has been suggested that the gas content of the test liquid influences liquid cavitation phenomena. However, when liquids with undissolved gases are pressurized above about 1000 psia (65 atm), the gases are driven into solution and cavitation phenomena are insensitive to dissolved gases [Knapp<sup>19</sup>]. In this work, the liquid pressure was above 1500 psia (100 atm) for the experiments whose results were used to derive conclusions. Accordingly, the results are not expected to be influenced by the gas content of the liquids tested. This is also supported by the fact that no differences were detected in the four jets of Series 66 where jet 66c was from injection of carbonated water, saturated

at 1 atm pressure.

Ranz<sup>2</sup> argued that the jet divergence angle could be estimated from the aerodynamic wave growth theory of Taylor<sup>20</sup> by using the computed maximum wave growth rate and the corresponding wavelength from a dispersion relationship, to characterize the drop formation process. According to this model, the divergence of the jet is given by

$$\tan \theta/2 = \frac{1}{A} 4^{-} \left( \frac{\rho_g}{\rho_L} \right)^{1/2} f \left( \frac{\rho_L}{\rho_g} \left( \frac{Re_L}{We_L} \right)^2 \right) \quad (1)$$

where  $\theta$  is the jet divergence or spray angle. In this equation, the constant of proportionality  $1/A$  must be obtained from experimental data.

The group  $(A/4^{-}) \tan \theta/2 (\rho_L/\rho_g)^{1/2}$  is shown plotted against  $(\rho_L/\rho_g) (Re_L/We_L)^2$  in Fig. 10. It can be seen that Eq. (1) predicts that the jet divergence angle increases with increasing gas density and decreases with increased liquid viscosity for the range of operating conditions of this work. This is consistent with the experimental trends shown in Figs. 5 and 8 for tests with a given nozzle.

Moreover, for our water injections,  $(\rho_L/\rho_g) (Re_L/We_L)^2$  is always larger than 1 (see Table I) and therefore the divergence angle is predicted to be insensitive to variations in the injection velocity (see Fig. 10) which also is in agreement with the experimental trends. However, a quantitative comparison of the theoretical prediction of Eq. (1) with the experimental results can only be made if a numerical value is assigned to the constant  $A$ .

made if a numerical value is assigned to the constant A.

Fig. 11 shows the spray angle versus gas density data for nozzles XIV, IX, III, II and I and the prediction using Eq. (1) after having determined the constant A by a least square fit of the data for each nozzle. The comparison is made for density ratios up to  $30 \times 10^{-3}$ ; the inclusion of the four high gas density data points (67, 35, 55 and 9, see Fig. 5) led to slightly different values of A and quantitative agreement with the experimental results was not as good as that shown in Fig. 11. More detailed measurements and discussion of the high gas density region are given by Su<sup>23</sup>.

The values of A are given in Table II and are seen to range from 3.1 (nozzle XIV) to 28 (nozzle I). This range includes the values of Ranz<sup>2</sup> ( $A = 3 - 20$ ) but the value of the constant is required to decrease as the nozzle length is decreased (at constant tube diameter) for the sharp-edged inlet nozzles I-III, IX and XIV. Notice, however, that the flows from nozzles III ( $L/d_0 = 10.1$ ), II ( $L/d_0 = 49.3$ ), and I ( $L/d_0 = 85$ ) range from transition flows to fully developed turbulent flows, at the Reynolds numbers used in the experiments<sup>16</sup> and the aerodynamic surface wave growth theory makes the assumption of laminar flows.

The experimental results of Fig. 8 are shown in Fig. 12 together with the predicted spray angle versus liquid viscosity dependence of Eq. (1). Here the comparison is shown for tests with a particular nozzle using the constant A of Table II. In this case, quantitative agreement with the experimental results

is not as good as in Fig. 11, but the predicted trend is correct. However, a significant departure is noticed in the case of Series 33 (nozzle IX) in which the emerging jet was detached from the nozzle walls.

This analysis indicates that the theoretical prediction of Eq. (1) could explain the experimental results within the tested ranges provided that the constant  $A$  is allowed to assume a different value for each different nozzle geometry. However, the aerodynamic interaction theory alone and as represented by Eq. (1), would not predict the observed influence of nozzle geometry in both atomization and aerodynamic breakup regimes since it includes only the nozzle diameter and that is insufficient to characterize completely the nozzle geometry. Thus, the aerodynamic interaction mechanism alone (as represented by Eq. (1)) is also insufficient to explain the observed trends.

#### 6. POSSIBLE JET ATOMIZATION MECHANISMS

The aerodynamic surface wave growth mechanism can explain the experimentally observed trends of gas density and liquid viscosity variations on the spray angle, and the insensitivity of the spray angle to relatively large variations in the jet velocity in the atomization regime, if an additional mechanism is invoked to account for the effects of nozzle geometry. Moreover, the results of Figs. 11 and 12 show that the aerodynamic surface wave growth theory requires that such additional effects also be invoked to explain the results for jets in the aerodynamic breakup regime (jets with intact lengths) as well.

Ranz<sup>2</sup> reasoned that the constant  $1/A$  in Eq. (1) has the physical significance of an initial disturbance level and also that it could be interpreted as a measure of the trajectory of the motion of the surface upon which droplets are originally formed. Schweitzer<sup>5</sup> proposed that liquid turbulence gives rise to initial disturbances and if this were the cause of the variation in the constant  $A$ , it would be expected that  $1/A$  would increase with nozzle passage length and then level out once the fully developed turbulent state is reached. This behavior was not found, as was shown in Table II. In fact, it is of interest to notice that the aerodynamic theory of Eq. (1) could predict the increased stability of turbulent jets if the laminar viscosity  $\mu_l$  is replaced by a turbulent diffusion or eddy viscosity which is known to be much greater than the molecular one.

An additional source of disturbances could be cavitation phenomena which are of different intensity for different nozzle geometries and this could be the agency which complements aerodynamic effects. In this connection, it may be significant that the magnitude of the constant  $A$  in the aerodynamic theory correlates with the value of  $K_{crit}$  for those nozzles whose  $K_{crit}$  values could be estimated from the data of Bergwerk<sup>8</sup>. (See Table II). In addition, the relatively large values of  $A$  (implying relatively low initial disturbance levels) for the rounded inlet streamlined nozzles XI and XII are consistent with this trend since in these nozzles the occurrence of liquid cavitation should (ideally) be forestalled and therefore  $K_{crit}$  could be expected

to be high.

It is also possible that wall region boundary layer velocity gradient effects could supplement the aerodynamic jet breakup mechanism. The constant A in this case would be related to the adjustment of the flow at the nozzle exit. The fact that the wall region velocity gradient is likely to be steeper for the rounded inlet nozzle XI than for the turbulent flows of nozzles I and II<sup>21</sup>, and the rounded inlet nozzles produced jets with lower values of A (more unstable) is consistent with the expected trend from the analysis of Shkadov<sup>11</sup>.

Indeed, ultimately it could be concluded that both cavitation and wall region boundary layer velocity profile rearrangement effect contribute to the breakup process. The experiments of Schweitzer<sup>22</sup>, made with injection pressures up to 8,000 psia (530 atm) show that the spray angle increases with increasing injection velocity while the aerodynamic theory predicts that it decreases. This was not explored in the present study since the tests analyzed were performed in a relatively small range of injection velocities. It could be that the additional agency required by the aerodynamic theory to explain the results of the present study is also influenced by changes in the injection velocity. In particular, wall region velocity gradients could be expected to steepen with increases in the injection velocity and this effect would account for the trend reported by Schweitzer<sup>22</sup>.

The experimental results showed that detached, cavitation-free jets were stable (do not break up within the visible field

of view), but that the presence of a cavitation zone within a nozzle does not by itself guarantee jet atomization. However, since liquid cavitation zones are expected to be present also in all those cases in which jet atomization was found to occur (see Fig. 5), it is remotely possible that cavitation phenomena alone could still control the breakup under certain conditions.

First it is noticed that cavitation effects alone could not control the breakup of jets that exhibit an unbroken length. This is because the experimental results show that the jet breakup is influenced by effects related to gas density and not to gas pressure, for a given liquid, liquid pressure and nozzle. If cavitation were the only controlling mechanism, one would expect the jet breakup to be influenced by changes in  $K$ , which varies as  $p_g$  changed. Moreover there seems to be no means by which cavitation phenomena within the nozzle can be influenced by changes in the chamber gas density either, since the emerging jet remains intact in the vicinity of the nozzle exit.

Then, for liquid cavitation phenomena to be the only agency responsible for the breakup of jets in the atomization regime, one would have to postulate a discontinuity in the breakup mechanism between the two regimes. But, there is no evidence of such a discontinuity, (see Fig. 5). Furthermore, for cavitation to be the only mechanism of atomization, as observed in these experiments, other assumptions will have to be made. These include that cavitation effects produce a two-phase flow within the nozzle, and that the interaction between the closely packed drops and the

chamber gas is ultimately proved to be such as to explain the observed dependence of the jet divergence angle on the chamber gas density, liquid viscosity and the jet velocity<sup>13</sup>. Since the simultaneous validity of these assumptions cannot be disproved at this time it remains possible that liquid cavitation is the only agency controlling jet atomization.

The conclusions of this study, in general, and those about the mechanism of atomization, in particular, were obtained by varying the liquid pressure and viscosity, the gas pressure and density, and the nozzle geometry within specified ranges. Outside of these ranges, additional breakup mechanisms are known to exist. Moreover, the nozzle exit diameter, the liquid density and surface tension, and the gas and liquid temperatures were not varied significantly. Their variation may necessitate consideration of other effects in the atomization mechanism. Indeed, had the nozzle geometry not been varied in the present study, one could have concluded that the aerodynamic surface wave growth mechanism, alone, was fully able to explain the experimental results.

#### ACKNOWLEDGEMENTS

The authors gratefully acknowledge the support and stimulating interaction with Professor Martin Summerfield and the staff at Princeton Combustion Laboratories, Princeton, New Jersey.

This work was supported under grant DAAG 29-77-G-0146 of the Army Research Office, Mr. J. J. Murray, grant monitor.



## REFERENCES

- <sup>1</sup> R.A. Castleman, NACA Report 440 (1932).
- <sup>2</sup> W.E. Ranz, Canad. J. Chem. Engng., 36, 175 (1958).
- <sup>3</sup> V.G. Levich, *Physicochemical Hydrodynamics*, Prentice Hall, (1962).
- <sup>4</sup> K.J. DeJuhasz, Trans. ASME(OGP), 53, 65 (1931).
- <sup>5</sup> P.H. Schweitzer, J. Appl. Phys., 8, 513 (1937).
- <sup>6</sup> H.B. Holroyd, J. Franklin Inst., 215, 93 (1933).
- <sup>7</sup> G. Sitkei, Acta Tech. Acad. Sci. Hungaricae, 25, 87 (1959).
- <sup>8</sup> W. Bergwerk, Proc. Inst. Mech. Engrs., 173, 655 (1959).
- <sup>9</sup> R. Sadek, Proc. Inst. Mech. Engrs., 173, 671 communication to Bergwerk<sup>8</sup> (1959).
- <sup>10</sup> J.H. Rupe, JPL Tech. Report 32, 207 (1962).
- <sup>11</sup> V. Ya. Shkadov, Fluid Dynamics, 5, 473 (1970).
- <sup>12</sup> E. Giffen and A. Muraszew, *The Atomization of Liquid Fuels*, John Wiley and Sons (1953).
- <sup>13</sup> R.D. Reitz, Ph.D. Thesis 1375-T, AMS Dept., Princeton University (1978).
- <sup>14</sup> R.D. Reitz and F.V. Bracco, Phys. Fluids, 22, 1054 (1979).
- <sup>15</sup> R.D. Reitz and F.V. Bracco, (to be published)
- <sup>16</sup> J.O. Hinze, *Turbulence*, McGraw Hill (1959).
- <sup>17</sup> E.M. Sparrow and C.E. Anderson, J. Fluids Eng., 99, 556 (1977).

18

G.K. Batchelor, *Fluid Dynamics*, Cambridge University Press (1967).

19

R.T. Knapp, J.W. Daily, and F.G. Hammitt, *Cavitation*, McGraw Hill (1970).

20

G.I. Taylor, *Collected Works of G.I. Taylor*, Vol. 3 (1940).

21

A.R. Barbin and J.B. Jones, *J. Basic Eng.*, Trans. ASME, 85, DI, 29 (1963).

22

P.H. Schweitzer, *Bulletin No. 40*, Penn State University (1932).

23

C.C. Su, MS Thesis, MAE Dept., Princeton University (1980).




## TABLE AND FIGURE CAPTIONS

## Table

Ia	Experimental Data - Series 1 to 35.
Ib	Experimental Data - Series 36 to 67.
II	Nozzles and values of the constants, A and $K_{crit}$ .

## Figure

1	Schematic diagram of experimental apparatus
2	Nozzle passage design details a) constant diameter tube nozzles, b) converging nozzles (dimensions in mm)
3	Photographs showing initial emergence and breakup details for Series 47 with event synchronization oscilloscope trace and photograph showing nozzle exit hole condition after the test
4	Photographs showing effect of chamber gas com- pression on steady state jet breakup. Liquid- water, gas-nitrogen, $\Delta P = 1900$ psia nozzle XII ( $L/d_o = 2.1$ Rounded inlet)
5	Graph showing effect of chamber gas compression on spray angle and jet intact length for nozzles XIV, IX, III, XII, II and I. Liquid-water, gas- nitrogen, <input checked="" type="checkbox"/> intact before diverging, <input type="checkbox"/> divergence at nozzle exit, <input type="checkbox"/> marginal - $\circ$ steady state data, $\otimes$ transient data
6	Photographs showing effect of gas composition on

- steady state jet breakup. Liquid-water,  $\Delta p = 1600$  psia, nozzle  $X_0$  ( $L/d_0 = 4.0$ ).
- 7 Photographs showing effect of liquid viscosity on steady state jet breakup. Nozzle IX ( $L/d_0 = 4.0$ ), gas-nitrogen at 300 psia,  $\Delta p = 1800$  psia.
- 8 Graph showing effect of liquid viscosity on spray angle and jet intact length for nozzles IX, XII and I. Liquid-water/glycerol, gas-nitrogen at 300 psia,  divergence at nozzle exit,  intact before diverging,  marginal.
- 9 Photographs showing effect of nozzle passage length on steady state jet breakup. Liquid-water, gas-nitrogen at 300 psia.  $\Delta p = 1900$  psia.
- 10 Theoretical dependence of the spray angle on the operating conditions from Ranz<sup>2</sup> using the aerodynamic surface wave instability analysis of Taylor<sup>20</sup>.
- 11 Comparison of the measured spray angle-gas density dependence with the theoretical prediction of the aerodynamic surface wave mechanism - Equation (1).
- 12 Comparison with the measured spray angle - liquid viscosity dependence with the theoretical prediction of the aerodynamic surface wave mechanism - Equation (1).

Data	Nozzle	S	T	$\rho$ (g/cm <sup>3</sup> )	$p_0$ (psia)	Li salt	$\frac{c_p}{\rho} = \frac{c_p}{\rho}$		$\frac{c_p}{\rho} \times 10^{-6}$ cm/s	$\frac{c_p}{\rho} \times 10^{-6}$ cm/s	$\frac{c_p}{\rho} \times 10^{-6}$ cm/s	$\frac{c_p}{\rho} \times 10^{-6}$ cm/s	$\frac{c_p}{\rho} \times 10^{-6}$ cm/s	$\frac{c_p}{\rho} \times 10^{-6}$ cm/s	$\frac{c_p}{\rho} \times 10^{-6}$ cm/s	$\frac{c_p}{\rho} \times 10^{-6}$ cm/s	$\frac{c_p}{\rho} \times 10^{-6}$ cm/s	$\frac{c_p}{\rho} \times 10^{-6}$ cm/s	$\frac{c_p}{\rho} \times 10^{-6}$ cm/s	$\frac{c_p}{\rho} \times 10^{-6}$ cm/s	$\frac{c_p}{\rho} \times 10^{-6}$ cm/s	$\frac{c_p}{\rho} \times 10^{-6}$ cm/s	$\frac{c_p}{\rho} \times 10^{-6}$ cm/s	$\frac{c_p}{\rho} \times 10^{-6}$ cm/s	$\frac{c_p}{\rho} \times 10^{-6}$ cm/s	$\frac{c_p}{\rho} \times 10^{-6}$ cm/s	$\frac{c_p}{\rho} \times 10^{-6}$ cm/s	$\frac{c_p}{\rho} \times 10^{-6}$ cm/s	$\frac{c_p}{\rho} \times 10^{-6}$ cm/s	$\frac{c_p}{\rho} \times 10^{-6}$ cm/s	$\frac{c_p}{\rho} \times 10^{-6}$ cm/s	$\frac{c_p}{\rho} \times 10^{-6}$ cm/s	$\frac{c_p}{\rho} \times 10^{-6}$ cm/s	$\frac{c_p}{\rho} \times 10^{-6}$ cm/s	$\frac{c_p}{\rho} \times 10^{-6}$ cm/s	$\frac{c_p}{\rho} \times 10^{-6}$ cm/s	$\frac{c_p}{\rho} \times 10^{-6}$ cm/s	$\frac{c_p}{\rho} \times 10^{-6}$ cm/s	$\frac{c_p}{\rho} \times 10^{-6}$ cm/s	$\frac{c_p}{\rho} \times 10^{-6}$ cm/s	$\frac{c_p}{\rho} \times 10^{-6}$ cm/s	$\frac{c_p}{\rho} \times 10^{-6}$ cm/s	$\frac{c_p}{\rho} \times 10^{-6}$ cm/s	$\frac{c_p}{\rho} \times 10^{-6}$ cm/s	$\frac{c_p}{\rho} \times 10^{-6}$ cm/s	$\frac{c_p}{\rho} \times 10^{-6}$ cm/s	$\frac{c_p}{\rho} \times 10^{-6}$ cm/s	$\frac{c_p}{\rho} \times 10^{-6}$ cm/s	$\frac{c_p}{\rho} \times 10^{-6}$ cm/s	$\frac{c_p}{\rho} \times 10^{-6}$ cm/s	$\frac{c_p}{\rho} \times 10^{-6}$ cm/s	$\frac{c_p}{\rho} \times 10^{-6}$ cm/s	$\frac{c_p}{\rho} \times 10^{-6}$ cm/s	$\frac{c_p}{\rho} \times 10^{-6}$ cm/s	$\frac{c_p}{\rho} \times 10^{-6}$ cm/s	$\frac{c_p}{\rho} \times 10^{-6}$ cm/s	$\frac{c_p}{\rho} \times 10^{-6}$ cm/s	$\frac{c_p}{\rho} \times 10^{-6}$ cm/s	$\frac{c_p}{\rho} \times 10^{-6}$ cm/s	$\frac{c_p}{\rho} \times 10^{-6}$ cm/s	$\frac{c_p}{\rho} \times 10^{-6}$ cm/s	$\frac{c_p}{\rho} \times 10^{-6}$ cm/s	$\frac{c_p}{\rho} \times 10^{-6}$ cm/s	$\frac{c_p}{\rho} \times 10^{-6}$ cm/s	$\frac{c_p}{\rho} \times 10^{-6}$ cm/s	$\frac{c_p}{\rho} \times 10^{-6}$ cm/s	$\frac{c_p}{\rho} \times 10^{-6}$ cm/s	$\frac{c_p}{\rho} \times 10^{-6}$ cm/s	$\frac{c_p}{\rho} \times 10^{-6}$ cm/s	$\frac{c_p}{\rho} \times 10^{-6}$ cm/s	$\frac{c_p}{\rho} \times 10^{-6}$ cm/s	$\frac{c_p}{\rho} \times 10^{-6}$ cm/s	$\frac{c_p}{\rho} \times 10^{-6}$ cm/s	$\frac{c_p}{\rho} \times 10^{-6}$ cm/s	$\frac{c_p}{\rho} \times 10^{-6}$ cm/s	$\frac{c_p}{\rho} \times 10^{-6}$ cm/s	$\frac{c_p}{\rho} \times 10^{-6}$ cm/s	$\frac{c_p}{\rho} \times 10^{-6}$ cm/s	$\frac{c_p}{\rho} \times 10^{-6}$ cm/s	$\frac{c_p}{\rho} \times 10^{-6}$ cm/s	$\frac{c_p}{\rho} \times 10^{-6}$ cm/s	$\frac{c_p}{\rho} \times 10^{-6}$ cm/s	$\frac{c_p}{\rho} \times 10^{-6}$ cm/s	$\frac{c_p}{\rho} \times 10^{-6}$ cm/s	$\frac{c_p}{\rho} \times 10^{-6}$ cm/s	$\frac{c_p}{\rho} \times 10^{-6}$ cm/s	$\frac{c_p}{\rho} \times 10^{-6}$ cm/s	$\frac{c_p}{\rho} \times 10^{-6}$ cm/s	$\frac{c_p}{\rho} \times 10^{-6}$ cm/s	$\frac{c_p}{\rho} \times 10^{-6}$ cm/s	$\frac{c_p}{\rho} \times 10^{-6}$ cm/s	$\frac{c_p}{\rho} \times 10^{-6}$ cm/s	$\frac{c_p}{\rho} \times 10^{-6}$ cm/s	$\frac{c_p}{\rho} \times 10^{-6}$ cm/s	$\frac{c_p}{\rho} \times 10^{-6}$ cm/s	$\frac{c_p}{\rho} \times 10^{-6}$ cm/s	$\frac{c_p}{\rho} \times 10^{-6}$ cm/s	$\frac{c_p}{\rho} \times 10^{-6}$ cm/s	$\frac{c_p}{\rho} \times 10^{-6}$ cm/s	$\frac{c_p}{\rho} \times 10^{-6}$ cm/s	$\frac{c_p}{\rho} \times 10^{-6}$ cm/s	$\frac{c_p}{\rho} \times 10^{-6}$ cm/s	$\frac{c_p}{\rho} \times 10^{-6}$ cm/s	$\frac{c_p}{\rho} \times 10^{-6}$ cm/s	$\frac{c_p}{\rho} \times 10^{-6}$ cm/s	$\frac{c_p}{\rho} \times 10^{-6}$ cm/s	$\frac{c_p}{\rho} \times 10^{-6}$ cm/s	$\frac{c_p}{\rho} \times 10^{-6}$ cm/s	$\frac{c_p}{\rho} \times 10^{-6}$ cm/s	$\frac{c_p}{\rho} \times 10^{-6}$ cm/s	$\frac{c_p}{\rho} \times 10^{-6}$ cm/s	$\frac{c_p}{\rho} \times 10^{-6}$ cm/s	$\frac{c_p}{\rho} \times 10^{-6}$ cm/s	$\frac{c_p}{\rho} \times 10^{-6}$ cm/s	$\frac{c_p}{\rho} \times 10^{-6}$ cm/s	$\frac{c_p}{\rho} \times 10^{-6}$ cm/s	$\frac{c_p}{\rho} \times 10^{-6}$ cm/s	$\frac{c_p}{\rho} \times 10^{-6}$ cm/s	$\frac{c_p}{\rho} \times 10^{-6}$ cm/s	$\frac{c_p}{\rho} \times 10^{-6}$ cm/s	$\frac{c_p}{\rho} \times 10^{-6}$ cm/s	$\frac{c_p}{\rho} \times 10^{-6}$ cm/s	$\frac{c_p}{\rho} \times 10^{-6}$ cm/s	$\frac{c_p}{\rho} \times 10^{-6}$ cm/s	$\frac{c_p}{\rho} \times 10^{-6}$ cm/s	$\frac{c_p}{\rho} \times 10^{-6}$ cm/s	$\frac{c_p}{\rho} \times 10^{-6}$ cm/s	$\frac{c_p}{\rho} \times 10^{-6}$ cm/s	$\frac{c_p}{\rho} \times 10^{-6}$ cm/s	$\frac{c_p}{\rho} \times 10^{-6}$ cm/s	$\frac{c_p}{\rho} \times 10^{-6}$ cm/s	$\frac{c_p}{\rho} \times 10^{-6}$ cm/s	$\frac{c_p}{\rho} \times 10^{-6}$ cm/s	$\frac{c_p}{\rho} \times 10^{-6}$ cm/s	$\frac{c_p}{\rho} \times 10^{-6}$ cm/s	$\frac{c_p}{\rho} \times 10^{-6}$ cm/s	$\frac{c_p}{\rho} \times 10^{-6}$ cm/s	$\frac{c_p}{\rho} \times 10^{-6}$ cm/s	$\frac{c_p}{\rho} \times 10^{-6}$ cm/s	$\frac{c_p}{\rho} \times 10^{-6}$ cm/s	$\frac{c_p}{\rho} \times 10^{-6}$ cm/s	$\frac{c_p}{\rho} \times 10^{-6}$ cm/s	$\frac{c_p}{\rho} \times 10^{-6}$ cm/s	$\frac{c_p}{\rho} \times 10^{-6}$ cm/s	$\frac{c_p}{\rho} \times 10^{-6}$ cm/s	$\frac{c_p}{\rho} \times 10^{-6}$ cm/s	$\frac{c_p}{\rho} \times 10^{-6}$ cm/s	$\frac{c_p}{\rho} \times 10^{-6}$ cm/s	$\frac{c_p}{\rho} \times 10^{-6}$ cm/s	$\frac{c_p}{\rho} \times 10^{-6}$ cm/s	$\frac{c_p}{\rho} \times 10^{-6}$ cm/s	$\frac{c_p}{\rho} \times 10^{-6}$ cm/s	$\frac{c_p}{\rho} \times 10^{-6}$ cm/s	$\frac{c_p}{\rho} \times 10^{-6}$ cm/s	$\frac{c_p}{\rho} \times 10^{-6}$ cm/s	$\frac{c_p}{\rho} \times 10^{-6}$ cm/s	$\frac{c_p}{\rho} \times 10^{-6}$ cm/s	$\frac{c_p}{\rho} \times 10^{-6}$ cm/s	$\frac{c_p}{\rho} \times 10^{-6}$ cm/s	$\frac{c_p}{\rho} \times 10^{-6}$ cm/s	$\frac{c_p}{\rho} \times 10^{-6}$ cm/s	$\frac{c_p}{\rho} \times 10^{-6}$ cm/s	$\frac{c_p}{\rho} \times 10^{-6}$ cm/s	$\frac{c_p}{\rho} \times 10^{-6}$ cm/s	$\frac{c_p}{\rho} \times 10^{-6}$ cm/s	$\frac{c_p}{\rho} \times 10^{-6}$ cm/s	$\frac{c_p}{\rho} \times 10^{-6}$ cm/s	$\frac{c_p}{\rho} \times 10^{-6}$ cm/s	$\frac{c_p}{\rho} \times 10^{-6}$ cm/s	$\frac{c_p}{\rho} \times 10^{-6}$ cm/s	$\frac{c_p}{\rho} \times 10^{-6}$ cm/s	$\frac{c_p}{\rho} \times 10^{-6}$ cm/s	$\frac{c_p}{\rho} \times 10^{-6}$ cm/s	$\frac{c_p}{\rho} \times 10^{-6}$ cm/s	$\frac{c_p}{\rho} \times 10^{-6}$ cm/s	$\frac{c_p}{\rho} \times 10^{-6}$ cm/s	$\frac{c_p}{\rho} \times 10^{-6}$ cm/s	$\frac{c_p}{\rho} \times 10^{-6}$ cm/s	$\frac{c_p}{\rho} \times 10^{-6}$ cm/s	$\frac{c$
------	--------	---	---	-----------------------------	--------------	---------	---------------------------------------	--	--	--	--	--	--	--	--	--	--	--	--	--	--	--	--	--	--	--	--	--	--	--	--	--	--	--	--	--	--	--	--	--	--	--	--	--	--	--	--	--	--	--	--	--	--	--	--	--	--	--	--	--	--	--	--	--	--	--	--	--	--	--	--	--	--	--	--	--	--	--	--	--	--	--	--	--	--	--	--	--	--	--	--	--	--	--	--	--	--	--	--	--	--	--	--	--	--	--	--	--	--	--	--	--	--	--	--	--	--	--	--	--	--	--	--	--	--	--	--	--	--	--	--	--	--	--	--	--	--	--	--	--	--	--	--	--	--	--	--	--	--	--	--	--	--	--	--	--	--	--	--	--	--	--	--	--	--	--	--	--	--	--	--	--	--	--	--	--	--	--	--	-----------

Data	S	T	$\rho_g \times 10^3$ (g/cm <sup>3</sup> )	$p_g$ (psia)	Liquid	$K = \frac{p_L - p_v}{p_L - p_g}$	$U \times 10^{-4}$ cm/s	$Re_L \times 10^{-1}$	$We_g$ $\times 10^{-1}$	$\frac{Re_L}{Re_L^0} \left( \frac{We_L}{We_L^0} \right)^{0.1}$	$n$				$x_1/d_o$				$d/d_o$			
											$S^\circ$	$T^\circ$	$S$	$T$	$S^\circ$	$T^\circ$	$S$	$T$	$S^\circ$	$T^\circ$	$S$	$T$
1	1	0	X <sub>N</sub>	1.1	103 He	H <sub>2</sub> O	15.5	0.98	3.34	51	4.48	488.0	0.0	--	~40	--	--	--	0.65	--	--	--
1	1	0	X <sub>O</sub>	1.3	15 At.	H <sub>2</sub> O	106.7	0.96	5.15	51	3.97	489.0	4.0	--	2.5	--	--	--	1.0	--	--	--
4	0	0	X <sub>N</sub>	1.3	15 At.	H <sub>2</sub> O	106.7	0.88	5.00	50	3.10	489.0	0.0	--	~40	--	--	--	0.75	--	--	--
1	1	0	X <sub>O</sub>	1.3	15 At.	68%G	100.0	0.89	0.20	52	4.11	1.4	4.8	--	5.0	--	--	--	1.0	--	--	--
1	1	0	X <sub>O</sub>	1.7	150 He	H <sub>2</sub> O	10.7	1.00	3.42	78	4.70	318.0	5.0	--	0.5	--	--	--	1.0	--	--	--
2	0	0	X <sub>O</sub>	3.3	300 He	H <sub>2</sub> O	5.3	1.02	3.70	190	5.70	132.0	5.0	--	0.5	--	--	--	1.0	--	--	--
1	2	0	X <sub>N</sub>	3.3	300 He	H <sub>2</sub> O	5.3	1.10	3.70	190	5.70	132.0	0.0	--	30.0	--	--	--	0.75	--	--	--
1	2	0	X <sub>N</sub>	6.0	70 N <sub>2</sub>	H <sub>2</sub> O	21.4	0.96	3.29	260	4.33	96.1	3.0	--	15.0	--	--	--	1.0	--	--	--
1	1	0	X <sub>N</sub>	7.3	85 N <sub>2</sub>	H <sub>2</sub> O	17.7	0.97	3.32	323	4.42	77.3	1.5	--	5.0	--	--	--	1.0	--	--	--
2	0	0	X <sub>N</sub>	8.8	103 N <sub>2</sub>	H <sub>2</sub> O	14.6	0.97	3.29	383	4.33	65.0	3.0	--	3.0	--	--	--	1.0	--	--	--
1	1	0	X <sub>N</sub>	23.0	63 Xe	H <sub>2</sub> O	23.8	0.91	3.12	890	3.90	28.1	10.8	--	0.0	--	--	--	1.0	--	--	--
2	0	0	X <sub>N</sub>	25.8	300 N <sub>2</sub>	H <sub>2</sub> O	5.0	1.00	3.77	1170	5.68	17.1	12.5	--	0.0	--	--	--	1.0	--	--	--
1	1	0	X <sub>O</sub>	25.8	300 N <sub>2</sub>	68%G	5.0	0.48	0.11	300	1.37	0.2	9.0	--	0.4	--	--	--	0.8	--	--	--
3	1	XI	25.8	300 N <sub>2</sub>	50%G	5.7	1.10	0.52	0.65	1220	5.60	0.5	5.2	5.0	3.5	1.4	1.0	1.0	1.0	1.0	1.0	1.0
1	0	XI	51.5	600 N <sub>2</sub>	H <sub>2</sub> O	2.7	1.20	--	4.10	3560	6.90	6.9	9.0	--	0.0	--	--	--	1.0	--	--	--
2	2	XII	1.3	15 At.	H <sub>2</sub> O	133.0	1.26	1.05	4.31	96	7.45	259.0	2.0	1.5	~10	~20	1.0	1.0	1.0	1.0	1.0	1.0
2	2	XII	7.7	90 N <sub>2</sub>	H <sub>2</sub> O	22.2	1.26	1.10	4.31	57	7.45	43.3	3.6	3.0	2.0	8.0	1.0	1.0	1.0	1.0	1.0	1.0
1	1	XII	12.9	150 N <sub>2</sub>	H <sub>2</sub> O	15.3	1.26	0.71	4.31	956	7.45	26.2	6.5	4.5	0.5	7.5	1.0	1.0	1.0	1.0	1.0	1.0
1	1	XII	25.8	300 N <sub>2</sub>	H <sub>2</sub> O	6.5	1.26	0.53	4.31	1950	7.45	13.0	7.8	7.0	0.0	0.0	1.0	1.0	1.0	1.0	1.0	1.0
1	1	XII	25.8	300 N <sub>2</sub>	50%G	5.7	1.10	0.61	0.72	1530	6.64	1.3	19.0	9.0	0.0	0.0	3.2	1.0	1.0	1.0	1.0	1.0
1	1	XII	25.8	300 N <sub>2</sub>	G	5.7	0.58	0.58	1.47	475	2.25	1.6	0.0	0.0	~40	~20	1.0	1.0	1.0	1.0	1.0	1.0
1	0	XII	51.5	600 N <sub>2</sub>	H <sub>2</sub> O	3.0	1.21	--	1.11	3190	6.76	7.1	6.5	--	0.0	--	--	--	1.0	--	--	--
1	3	XIV	1.3	15 At.	H <sub>2</sub> O	113.0	1.21	1.20	1.10	87	6.76	387.0	1.9	0.0	25.0	~20	0.9	1.0	1.0	1.0	1.0	1.0
1	0	XIV	7.7	90 N <sub>2</sub>	H <sub>2</sub> O	18.9	1.21	--	1.15	615	6.76	10.6	9.5	--	5.0	--	--	--	1.0	--	--	--
1	0	XIV	25.8	300 N <sub>2</sub>	H <sub>2</sub> O	5.7	1.30	--	1.15	3050	7.91	12.2	18.7	--	0.0	--	--	--	1.0	--	--	--
1	0	XIV	51.5	600 N <sub>2</sub>	H <sub>2</sub> O	2.2	1.30	--	1.15	4100	7.91	6.1	17.0	--	0.0	--	--	--	1.0	--	--	--

Nozzle	$L/d_o$	A	$K_{crit}$
I	85.0	28	----
II	49.3	13.4	----
III	10.1	8.0	2.8
IV	7*	4.1	----
VI	4.4	----	1.9
VII	4.3	(3.5)	1.9
VIII	4.3	(4.5)	1.9
IX	4.0	3.9	1.9
$X_N$	4.0	3.5	1.9
$X_O$	4.0	3.2	1.9
XI	4.3 RI	8.5	----
XII	2.1 RI	6.4	----
XIII	0.5	(4.1)	1.0
XIV	0.5	3.1	1.0

(-) Uncertain Values

\* Contoured Nozzle

TABLE II

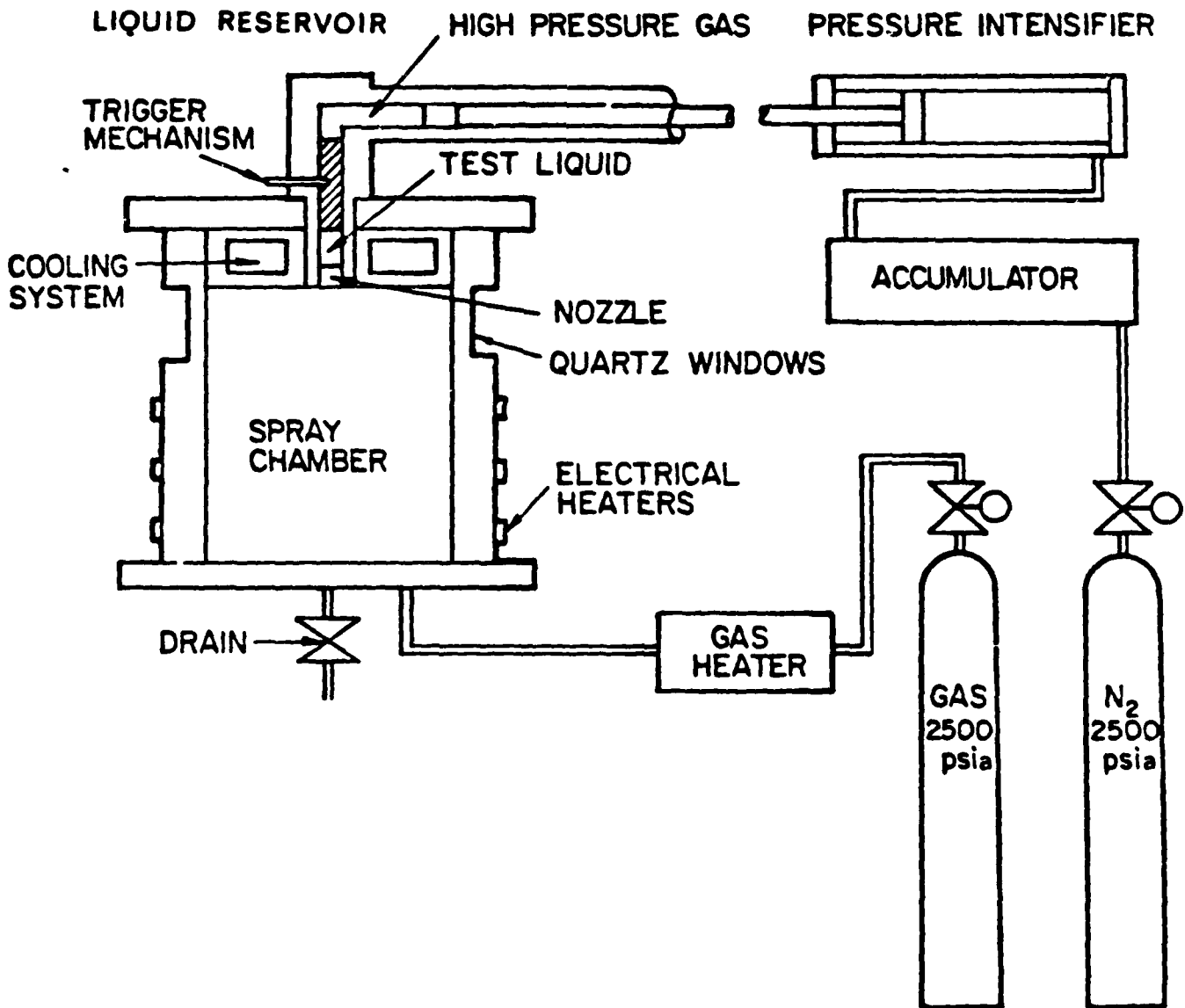


FIGURE 1

Fig. 1



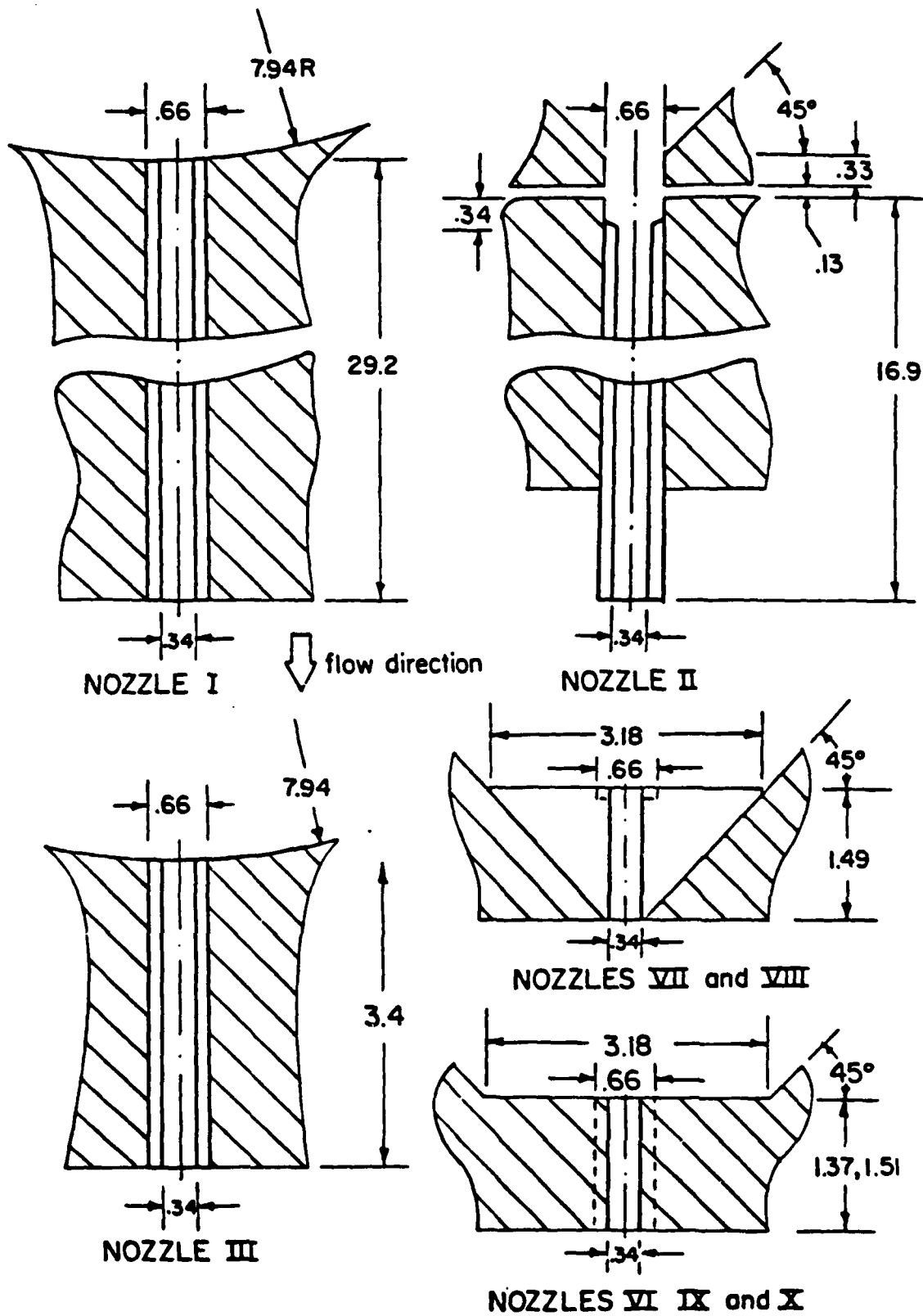
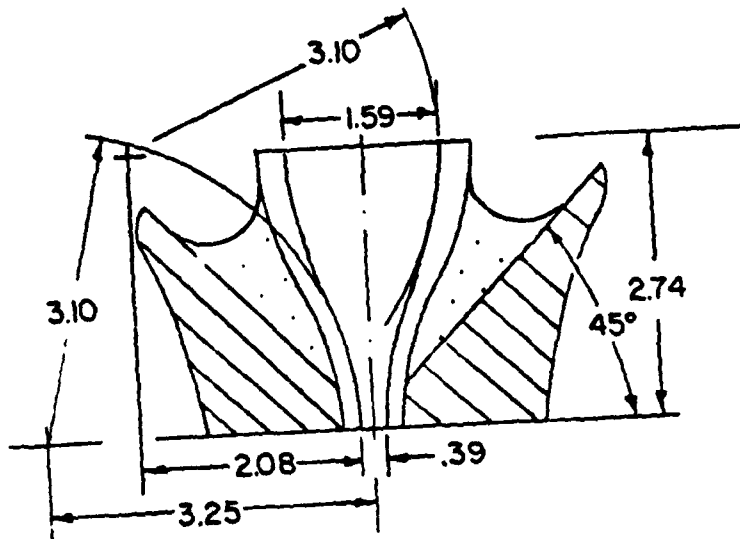
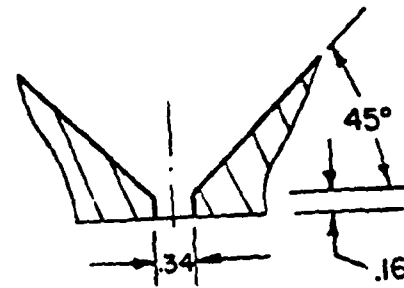


FIGURE 2a

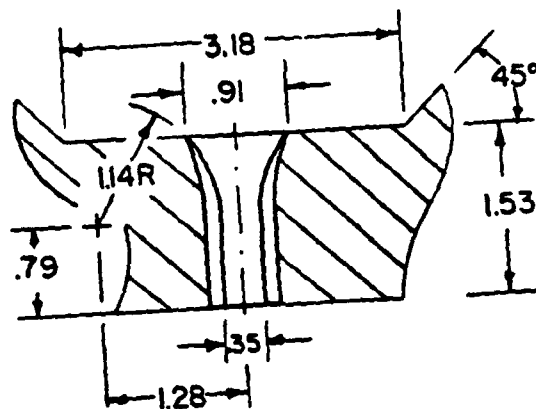


NOZZLE IV

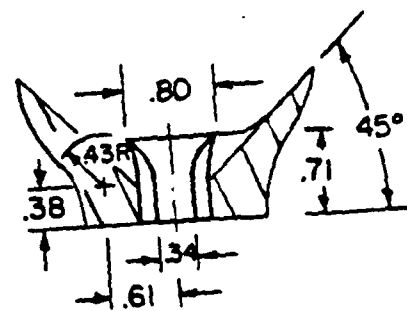


NOZZLES XIII and XIV

↓ flow direction

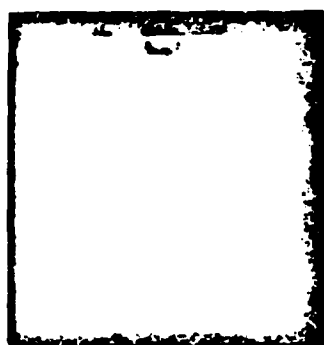


NOZZLE XI



NOZZLE XII

FIGURE 2b

Time between frames 4.0  $\mu$ s

FRAME 26

mm/2

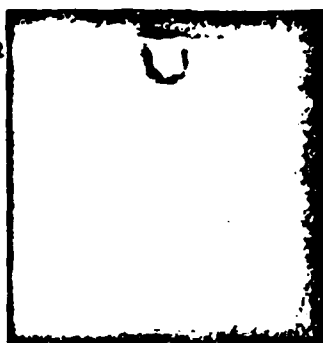
0

0.5

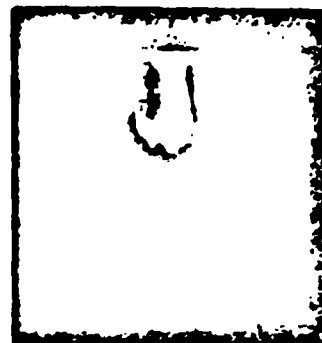
1.0

1.5

2.0



31



36



41



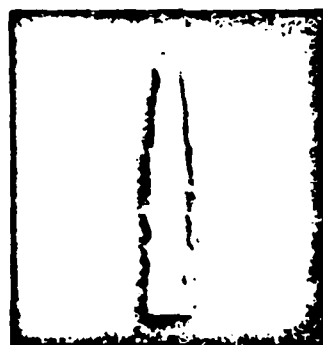
46



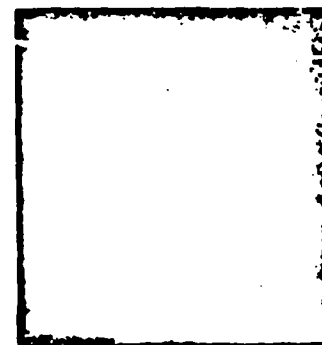
51



56



60



Steady State

mm/2

0

1.0

2.0

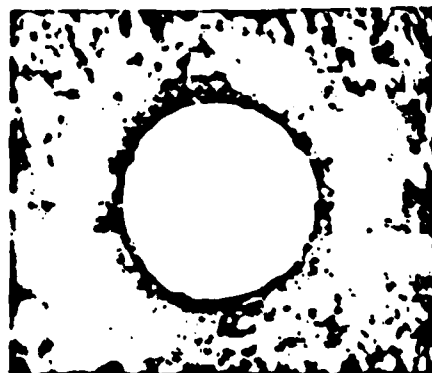
3.0

4.0



Event timing

$P_L$   
psia  
2000  
1500  
1000  
500  
0



Nozzle exit hole

mm

0

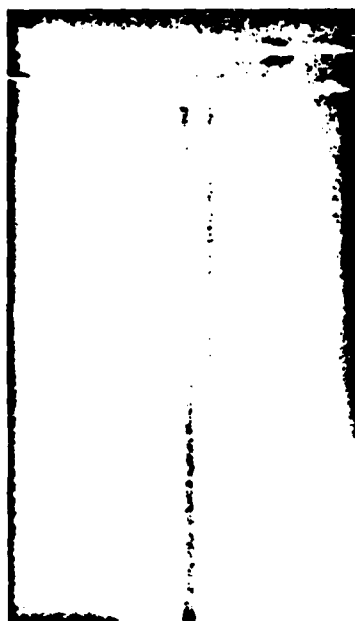
0.1

0.2

0.3

0.4

Series 47



(a.)

SERIES 49

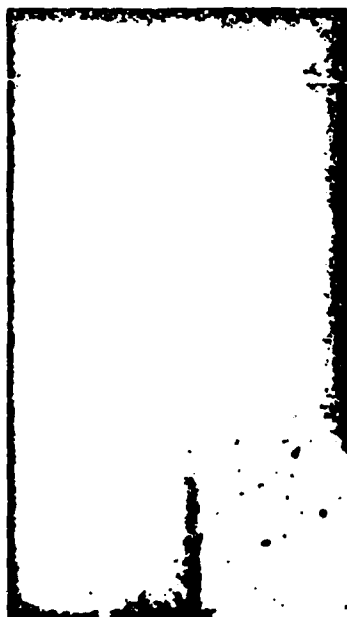
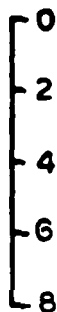
 $P_g = 15 \text{ psia}$  $\rho_g = 1.29 \times 10^2$   
(g/cm<sup>3</sup>)

(b.)

SERIES 51

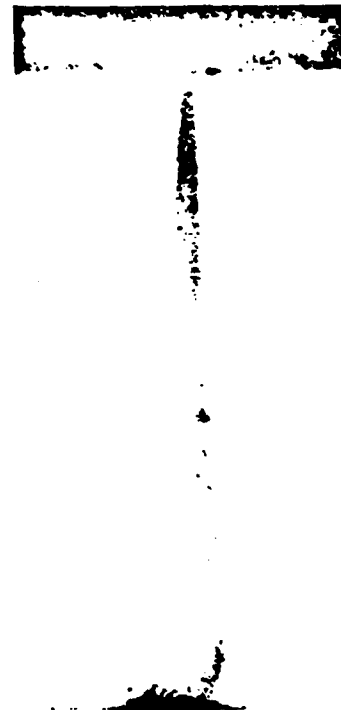
 $P_g = 150 \text{ psia}$  $\rho_g = 1.29 \times 10^2$   
(g/cm<sup>3</sup>)

mm



(c.)

SERIES 52

 $P_g = 300 \text{ psia}$  $\rho_g = 2.58 \times 10^2$   
(g/cm<sup>3</sup>)

(d.)

SERIES 55

 $P_g = 600 \text{ psia}$  $\rho_g = 5.15 \times 10^2$   
(g/cm<sup>3</sup>)

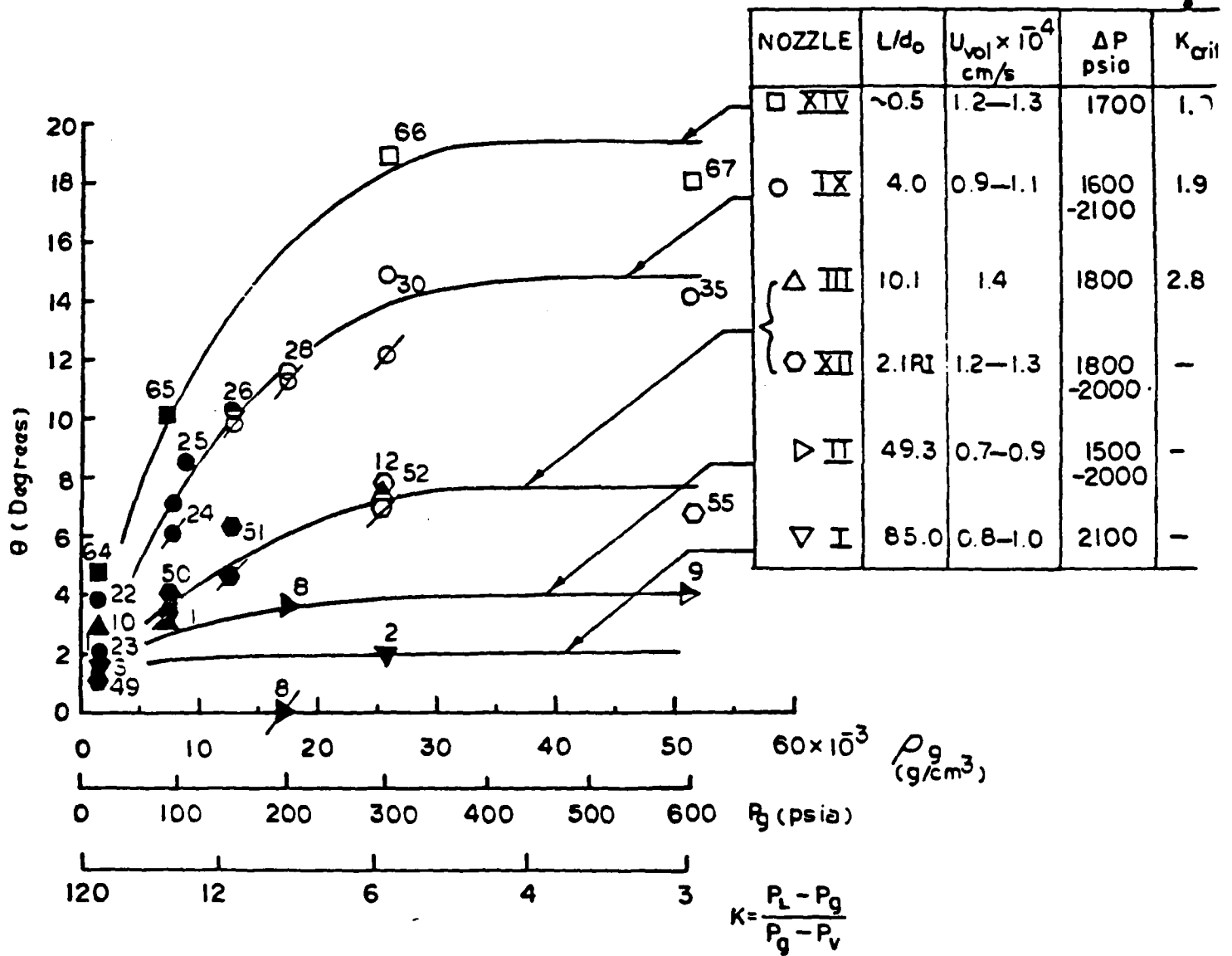
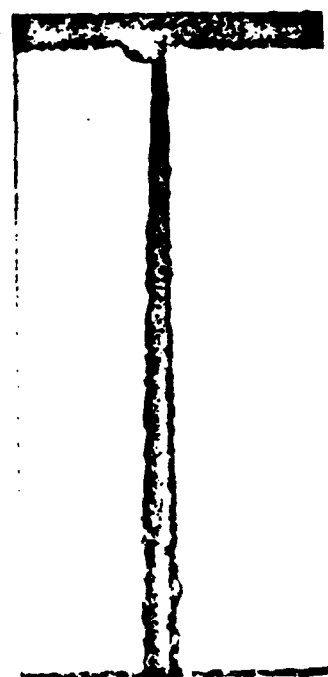


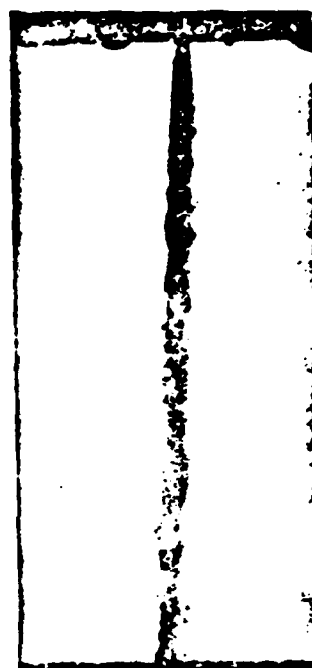
FIGURE 5



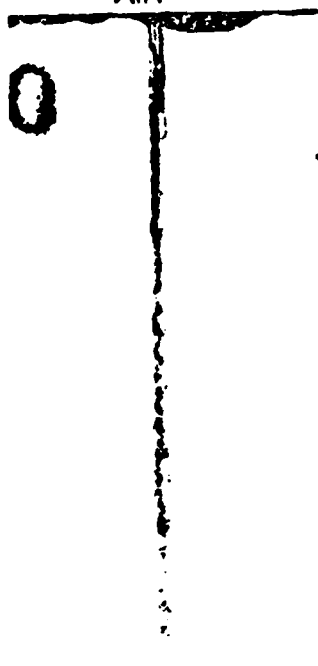
(a) SERIES 37<sub>0</sub>  
 $\rho_g = 1.29 \times 10^{-3} (\text{g/cm}^3)$   
 $P_g = 15 \text{ psia}$   
 AIR



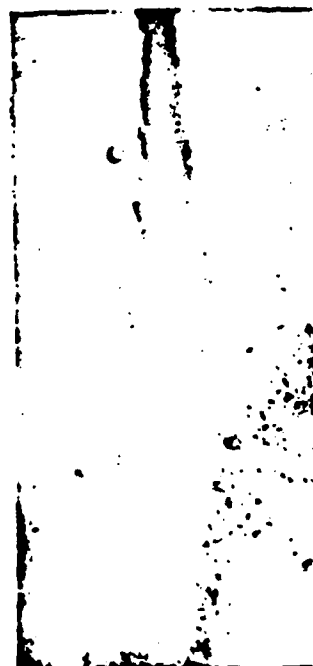
mm  
 0  
 2  
 4  
 6  
 8



(b) SERIES 39<sub>0</sub>  
 $\rho_g = 1.66 \times 10^{-3} (\text{g/cm}^3)$   
 $P_g = 150 \text{ psia}$   
 HELIUM



(c) SERIES 41<sub>N</sub>  
 $\rho_g = 6.0 \times 10^{-3} (\text{g/cm}^3)$   
 $P_g = 70 \text{ psia}$   
 NITROGEN



(d) SERIES 44<sub>N</sub>  
 $\rho_g = 23.0 \times 10^{-3} (\text{g/cm}^3)$   
 $P_g = 63 \text{ psia}$   
 XENON

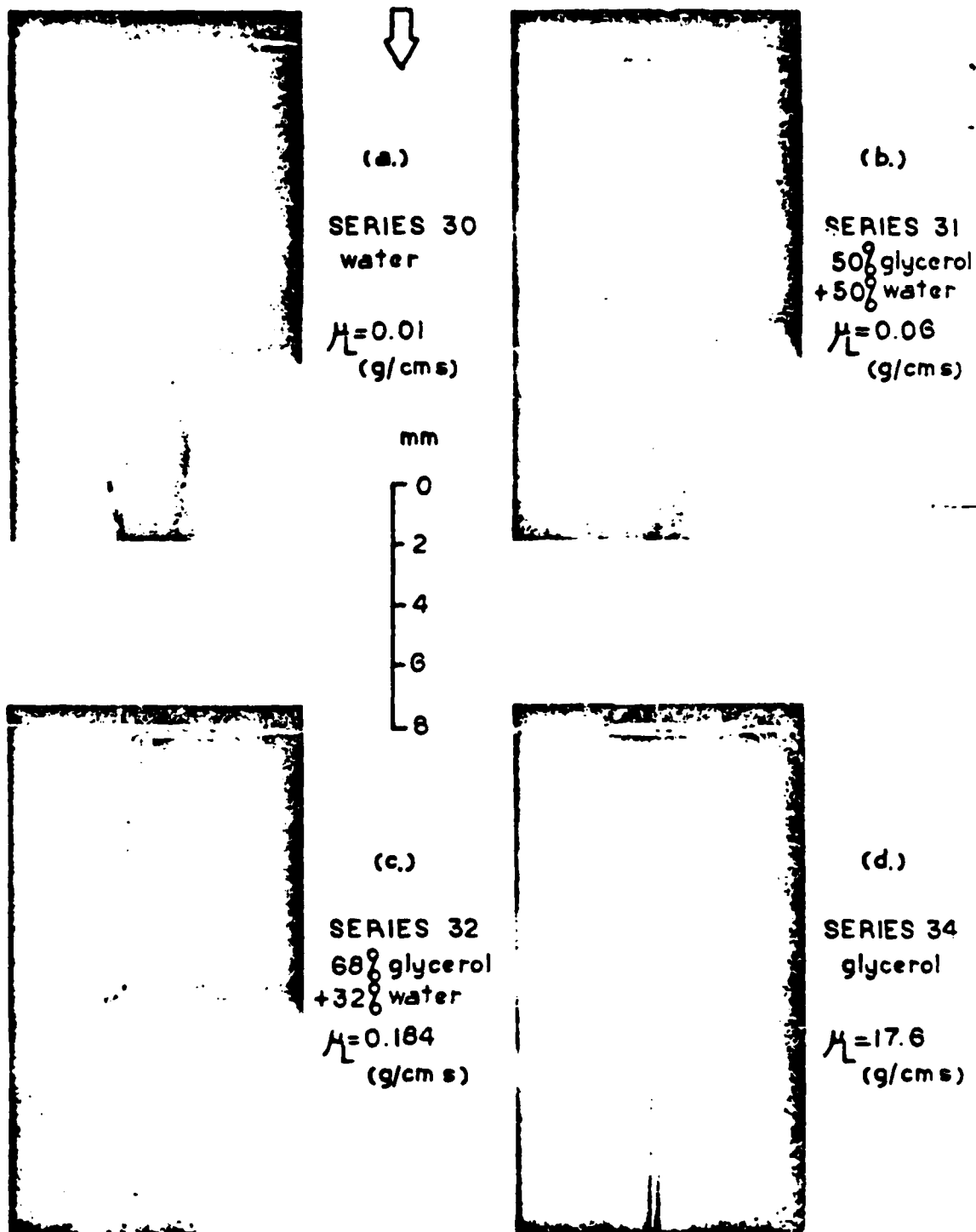


FIGURE 7

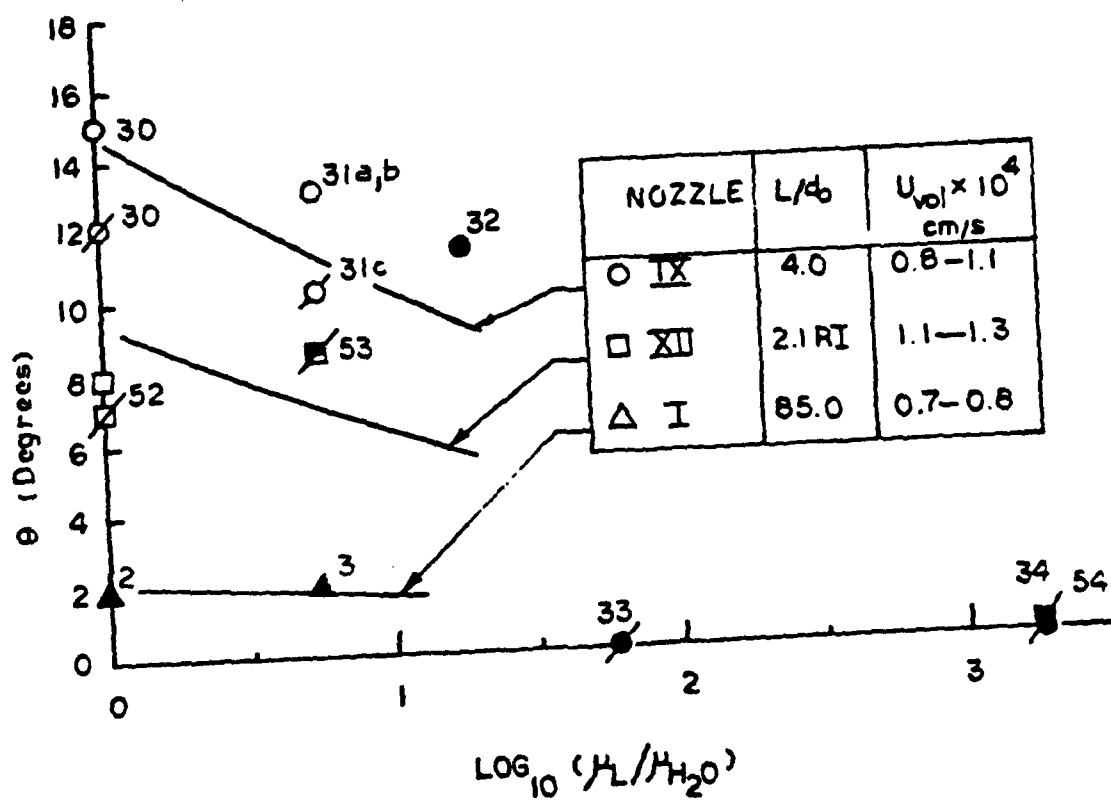


FIGURE 8



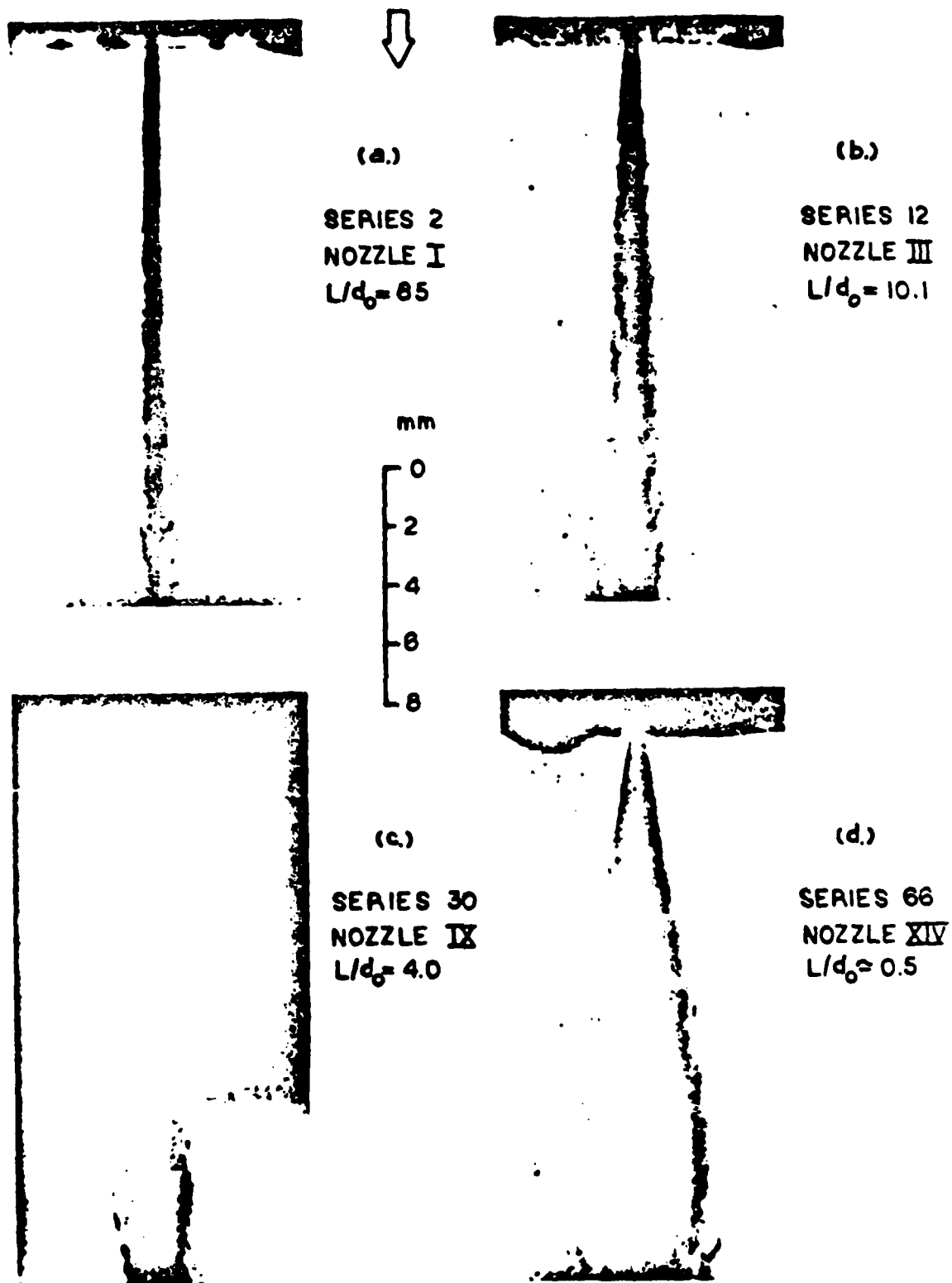


FIGURE 9

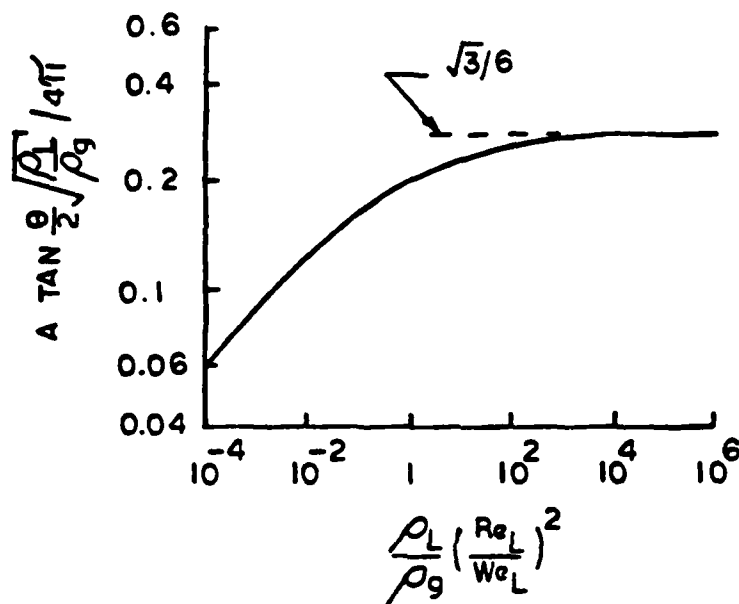


FIGURE 10

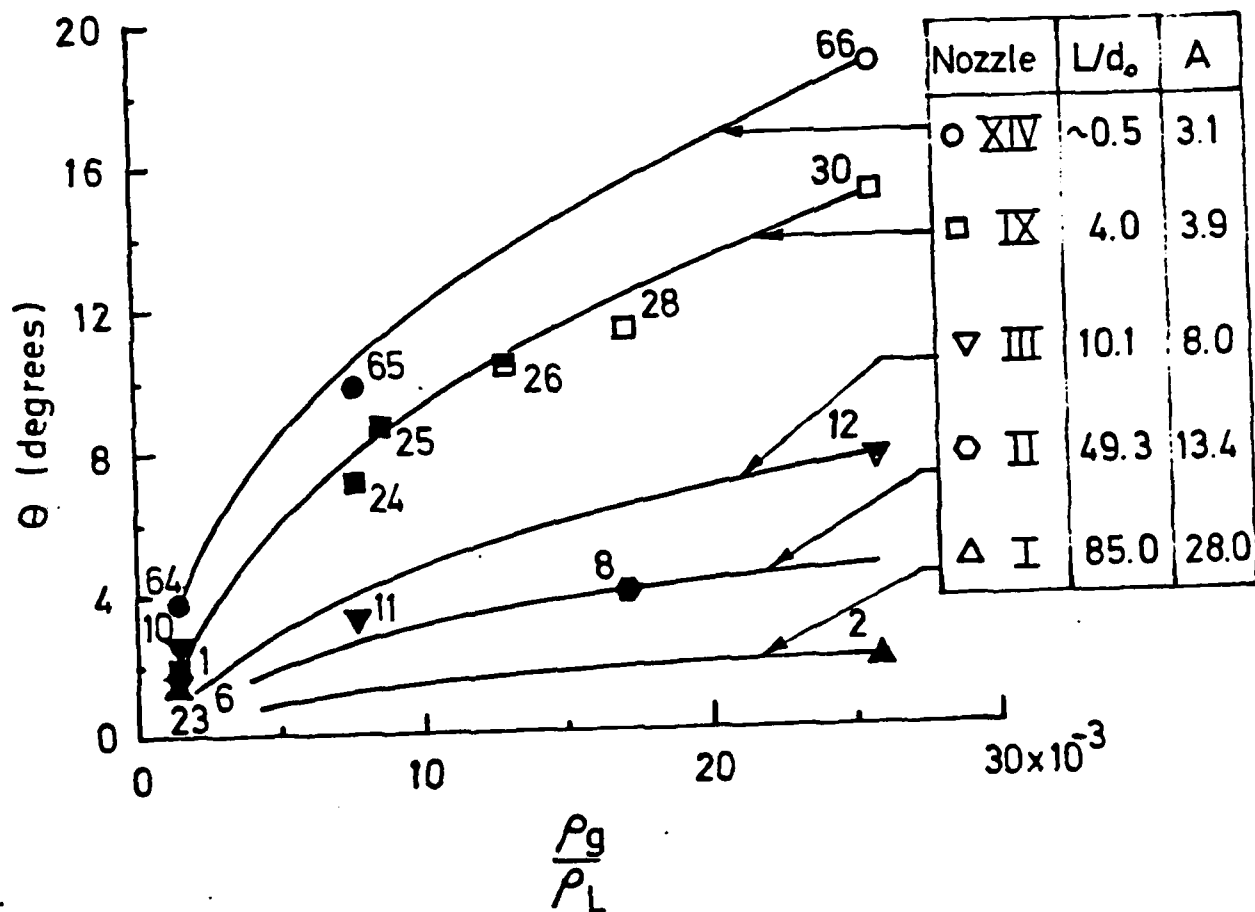


FIGURE 11

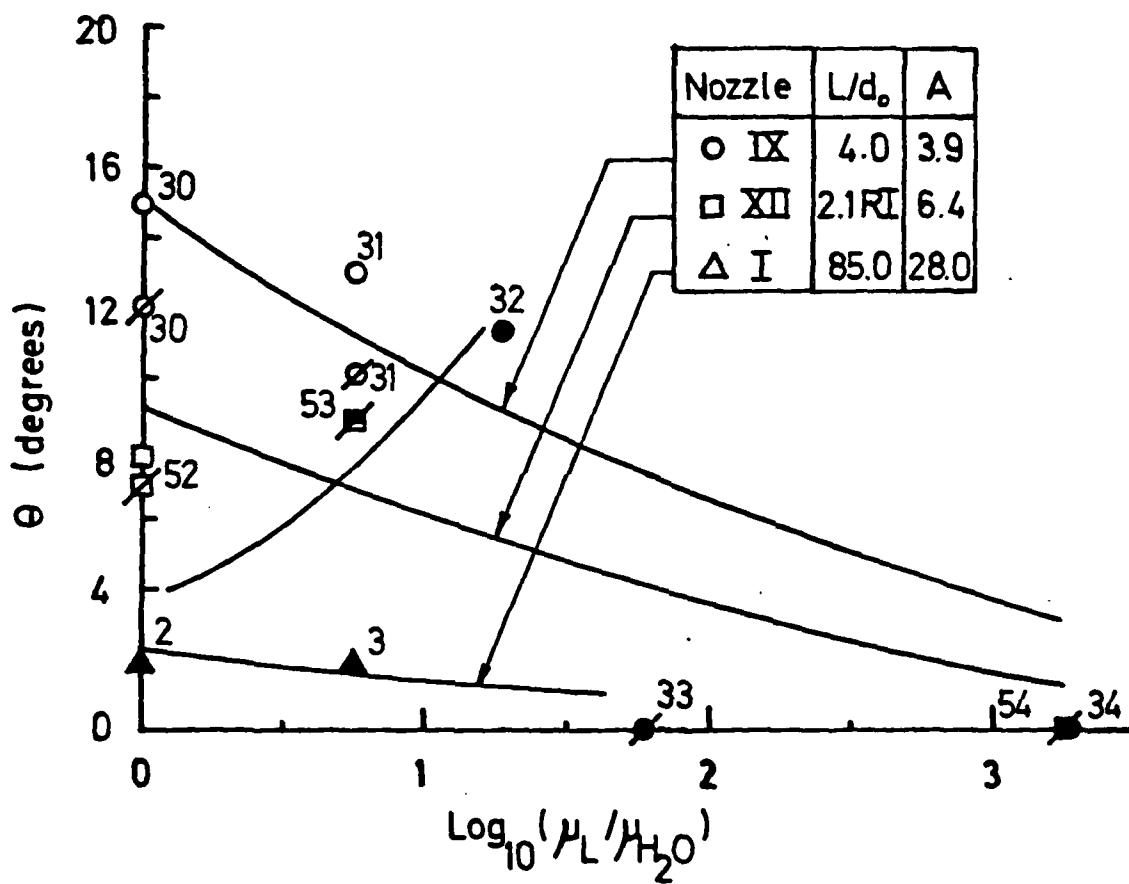


FIGURE 12

APPENDIX F

ON THE SCALING OF TRANSIENT  
LAMINAR, TURBULENT, AND SPRAY JETS

T.-W. Kuo and F.V. Bracco

# SAE Technical Paper Series

820038

## On the Scaling of Transient Laminar, Turbulent, and Spray Jets

**T.-W. Kuo and F. V. Bracco**

Dept. of Mechanical and Aerospace Engrg.  
Princeton Univ.  
Princeton, NJ

International Congress  
& Exposition  
Detroit, Michigan  
February 22-26, 1982

The appearance of the code at the bottom of the first page of this paper indicates SAE's consent that copies of the paper may be made for personal or internal use, or for the personal or internal use of specific clients. This consent is given on the condition, however, that the copier pay the stated per article copy fee through the Copyright Clearance Center, Inc., Operations Center, 21 Congress St., Salem, MA 01970 for copying beyond that permitted by Sections 107 or 108 of the U.S. Copyright Law. This consent does not extend to other kinds of copying such as copying for general distribution, for advertising or promotional purposes, for creating new collective works, or for resale.

Papers published prior to 1978 may also be copied at a per paper fee of \$2.50 under the above stated conditions.

SAE routinely stocks printed papers for a period of three years following date of publication. Direct your orders to SAE Order Department.

To obtain quantity reprint rates, permission to reprint a technical paper or permission to use copyrighted SAE publications in other works, contact the SAE Publications Division.

# On the Scaling of Transient Laminar, Turbulent, and Spray Jets

T.-W. Kuo and F. V. Bracco

Dept. of Mechanical and Aerospace Engrg.  
Princeton Univ.  
Princeton, NJ

IN THE FIELDS OF STRATIFIED CHARGE AND DIESEL ENGINES, TRANSIENT COMBUSTION-CHAMBER SPRAYS HAVE OFTEN BEEN THOUGHT OF AS GASEOUS JETS in part to simplify the problem, but also because of the belief either that vaporization occurs very rapidly or that the two types of jet behave similarly. The question of the vaporization time is addressed by us in a parallel paper (1)\*. In this manuscript we consider similarities and

differences in the transients of laminar and turbulent incompressible gas jets and non-vaporizing and vaporizing sprays.

Superficially, there are striking parallels among the transients of the three jets and equally noticeable differences. For example, in Fig. 1, the transients are given of a turbulent and a spray jet. Both exhibit a head vortex, a stem and seem to scale up in time in similar fashions. But in Fig. 2, the angle of steady sprays is shown to be a very strong function of the nozzle geometry and the ratio between the gas

\*Numbers in parentheses designate References at end of paper.

---

## ABSTRACT

---

Through numerical solutions of appropriate two-dimensional unsteady conservation equations, it is found that transient laminar incompressible jets, turbulent incompressible jets and non-vaporizing and vaporizing sprays reach steady state around the back of their head vortices. Thus, for many applications, the stems of such transient jets can be considered in steady state and steady state information can be applied to large fractions of transient jets. Equations are given for the penetration rate of such jets. In particular, an

equation is obtained for the penetration rate of the tip of sprays that compares favorably with measured ones. Also, scaling laws are reported that are obeyed by each of the three families of jets. Since the laws are somewhat different, no precise similarity exists among the three types of jet. However, one type of jet can still be approximately simulated by another but only with respect to certain parameters and within definite time and space ranges, given the acceptable error.



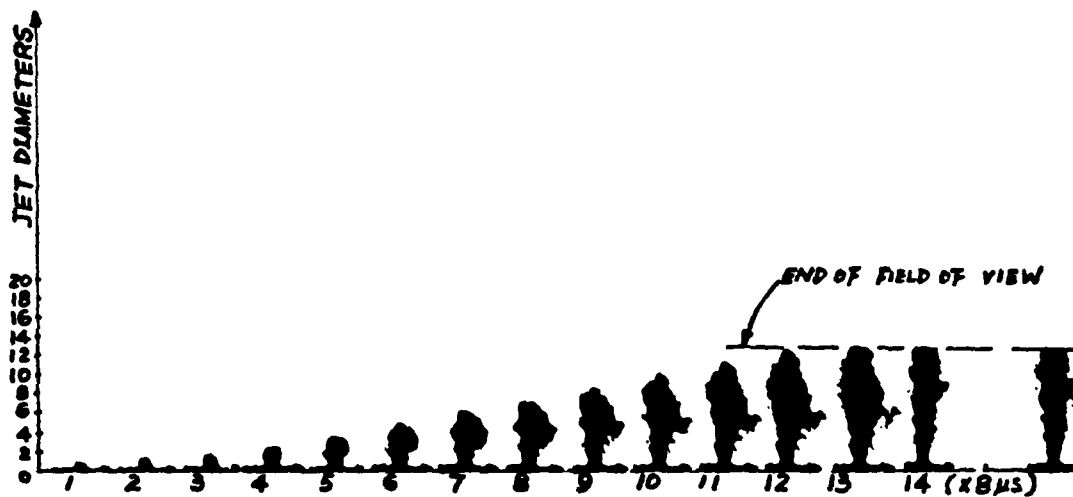
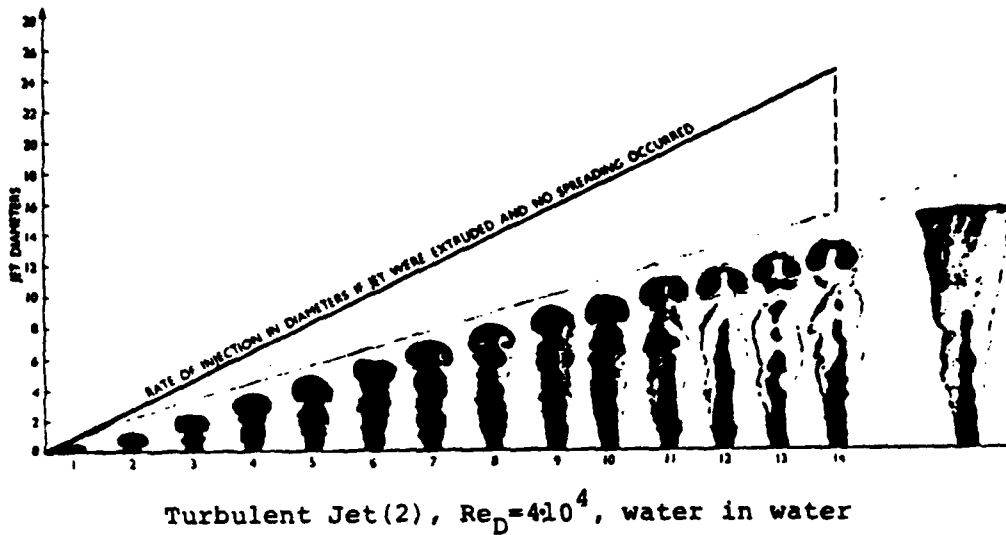


Fig. 1 - Transient development of a turbulent incompressible jet and a spray

and the liquid densities, whereas the angle of incompressible turbulent jets is very nearly a constant, thus the extent of and the reasons for the similarities need clarification.

The problem was approached through a large number of computations of the transient and steady state of laminar, turbulent and spray jets. In each case comparisons were made with experimental data whenever available. For each type of jet we attempted to determine the transient and steady state scaling parameters and steadying laws and then, by comparing them, to establish under what conditions and to what extent the three types of jet behave similarly.

The investigation was made difficult by the current limited knowledge of the structure of unsteady, or even steady, thick sprays. Also the transient of turbulent incompressible jets has received very little attention (4,5) even though their steady state has been thoroughly studied. And finally only one publication was found even on the transient of incompressible laminar jets (6). Nevertheless some progress was made in determining the scaling parameters and steadying laws for the three jets and some similarities and differences are now more clearly established.

The computations were made with different models for the three types of

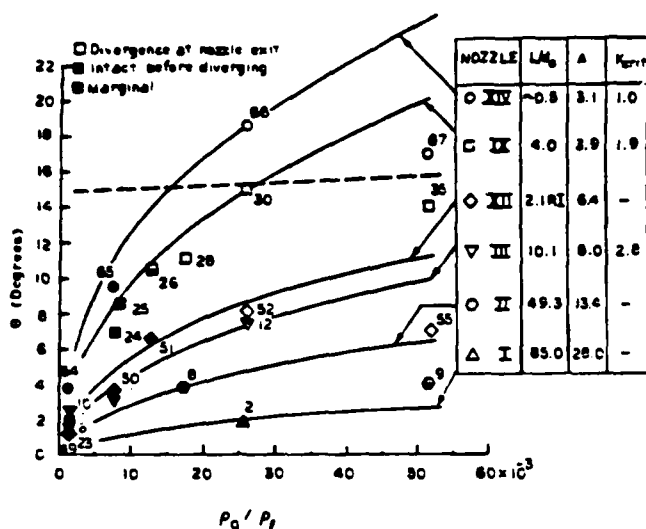


Fig. 2 - Single phase turbulent jet angle (dashed line) and spray angle (3) for different gas-liquid density ratios and nozzle geometries (water into N<sub>2</sub>)

jet and are reported in three separate sections. Then in two sections, comparisons are made of the three jets and examples of possible applications are given. In these sections the practical scope of the results becomes apparent. They were written so they could be read first. The details of the computations can be found in Reference 7 of which this paper is a partial and brief summary.

#### TRANSIENT INCOMPRESSIBLE LAMINAR JETS

THE MODEL - The governing equations of the model are:

$$\partial u / \partial x + 1/r \partial (rv) / \partial r = 0 \quad (1)$$

$$\begin{aligned} \rho \frac{\partial u}{\partial t} + \rho(u+U_e) \frac{\partial u}{\partial x} + \rho v \frac{\partial u}{\partial r} = \\ - \frac{\partial p}{\partial x} + \frac{\partial}{\partial x} \nu_1 \frac{\partial u}{\partial x} + \frac{1}{r} \frac{\partial}{\partial r} \nu_1 r \frac{\partial u}{\partial r} \end{aligned} \quad (2)$$

$$\rho \frac{\partial v}{\partial t} + \rho(u+U_e) \frac{\partial v}{\partial x} + \rho v \frac{\partial v}{\partial r} =$$

$$- \frac{\partial p}{\partial r} + \frac{\partial}{\partial x} \nu_1 \frac{\partial v}{\partial x} + \frac{\partial}{\partial r} \frac{\nu_1}{r} \frac{\partial (rv)}{\partial r} \quad (3)$$

where  $U_e$  is the coflow velocity.

The initial conditions were zero velocity everywhere except at the inlet plane. The boundary conditions were:

$$\begin{aligned} \text{at } r = 0, \quad \frac{\partial u}{\partial r} = 0, \quad v = 0 \\ \text{at } r = R, \quad \frac{\partial u}{\partial x} = 0, \quad \frac{1}{r} \frac{\partial (rv)}{\partial r} = 0 \end{aligned} \quad (4)$$

The above conditions are for an axisymmetric field and a finite domain of integration. Theoretically, the velocity goes to zero only as  $r$  tends to infinity. Our usual practice has been to choose  $R$  approximately equal to 3.5 times the maximum half-jet half-width,  $y_{1/2}$ , at the jet outlet plane. At the injector, two jet velocity profiles were studied and at the exit plane the axial velocity was obtained by integral mass balance and the radial velocity by setting its axial gradient equal to zero.

Solutions were obtained with a modified version of the computer code TEACH, developed at the Imperial College (8). This code, originally for steady two dimensional (planar and axisymmetric) flows, was modified to compute unsteady flows as well.

The grid system viewed in the  $r$ - $x$  plane is rectangular and with arbitrary spacing, as shown by the solid lines of Fig. 3. The dotted lines show a typical cluster of  $u$ ,  $v$  and scalar cells or control volumes. Each cell surrounds the location at which a variable is evaluated. Note that the variables are stored at different locations of the

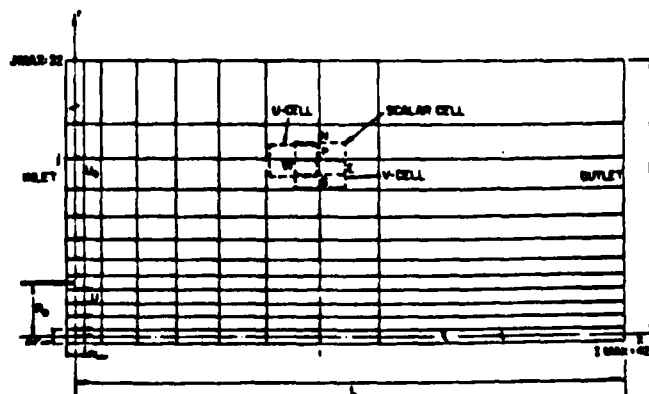


Fig. 3 - Computational mesh for incompressible jet studies

grid. The pressure and other scalars are evaluated at nodes, and velocities on the sides. With this staggered grid,  $u$ ,  $v$ ,  $p$  are easy to evaluate, and velocities are computed where they are needed for the calculation of convective flows (8).

A grid expansion technique was employed. Away from the nozzle exit, the size of the cells increase. In the axial direction, a cell expansion factor of 5% was used starting from the nozzle exit ( $I=2$ ). In the radial direction  $r$  is uniform within the pipe. Outside of the pipe, it expands by a factor of 7%. A total of 32 cells in the radial direction and 42 cells in axial one were employed. The reason for the expanding grid was to keep the number of nodes to a minimum, while guaranteeing that large velocity gradient in the free mixing region are properly resolved. Similarly the value of the time increment increased during the computations so as to keep the additional jet penetration during each time step approximately constant as the jet slows down.

For each flow configuration, a grid-independent solution can be sought by increasing the number of grid points until no further changes are observed in the final solution. This criterion was used in the present computations.

**SCALING** - The computed results for for the steady-state centerline velocity decay and transient jet tip penetration history were compared with those measured by Abramovich and Solan (6) in the Reynolds number range of 80 to 500. Results obtained starting from a parabolic exit velocity profile and with three different values of  $\bar{U}$ ,  $D$ ,  $\nu_l$ , but the same  $Re_D = 100$  are shown in Figs. 4 and 5. The dimensionless coordinates are those suggested by Abramovich and Solan, i.e.  $x^* = x/DRe_D^{1/2}$ ,  $t^* = 2t\nu_l Re_D^{1/2}/D^2$ . And  $t$  is defined as by Abramovich and Solan: It is the time needed for the centerline axial velocity  $u$  to reach 70% of its steady state value at any given downstream axial location.

In Figs. 4 and 5, it is observed that the computed solutions for a constant  $Re_D = 100$  and different values of  $\bar{U}$ ,  $D$ ,  $\nu_l$  are identical, and that the calculated results fit inside the experimental range. But computed steady and transient solutions for different  $Re_D = 70, 100, 500$ , do not coincide, when the non-dimensional parameters of Abramovich and Solan are used, and continue to show a systematic Reynolds

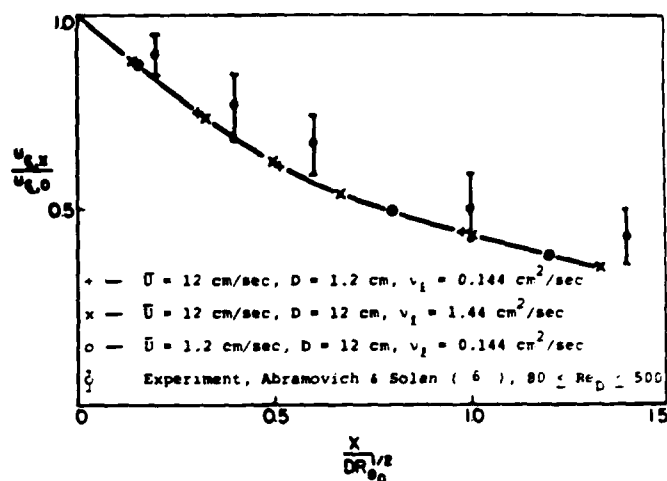


Fig. 4 - Incompressible laminar jets. Computed and measured steady-state centerline velocity with fixed Reynolds number ( $Re_D = 100$ ) using Abramovich and Solan length scale (6)

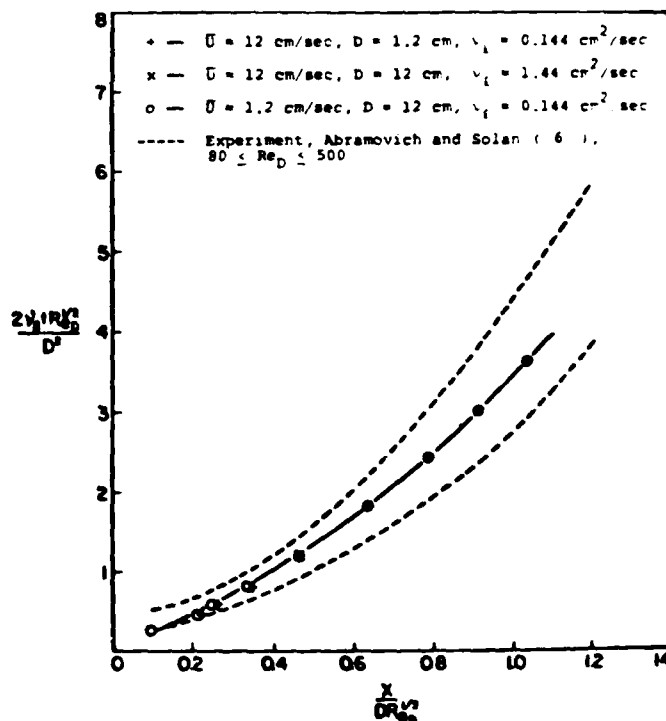


Fig. 5 - Incompressible laminar jets. Computed and measured transient jet tip penetration with fixed Reynolds number ( $Re_D = 100$ ) using Abramovich and Solan length and time scales (6)

number dependence as evidence in Figs. 6 and 7. Notice, however, that the computed curves for  $70 \leq Re_D \leq 500$  envelope the experimental measurements of Abramovich and Solan that were for  $80 \leq Re_D \leq 500$ . Thus we would like to suggest that what they considered experimental scattering may not be due wholly to experimental errors but also to improper account of the Reynolds number effect in their scaling parameters.

Indeed a dimensional analysis of a simplified version of Equations (1)-(4), obtained by making the boundary layer approximation (7), suggested that the proper time and length scales for this problem are  $D^2/\nu_L$  and  $DRe_D$  respectively instead of  $D^2/(2\nu_L Re_D^2)$  and  $DRe_D^2$  as proposed by Abramovich and Solan. This conclusion was confirmed by numerical solutions of the complete equations. For example, the results of Figs. 6 and 7 coalesce when plotted using the new scales as shown in Figures 8 and 9. Unfortunately the experimental data of Abramovich and Solan cannot be reported in the same figure because they did not identify the Reynolds numbers corresponding to each

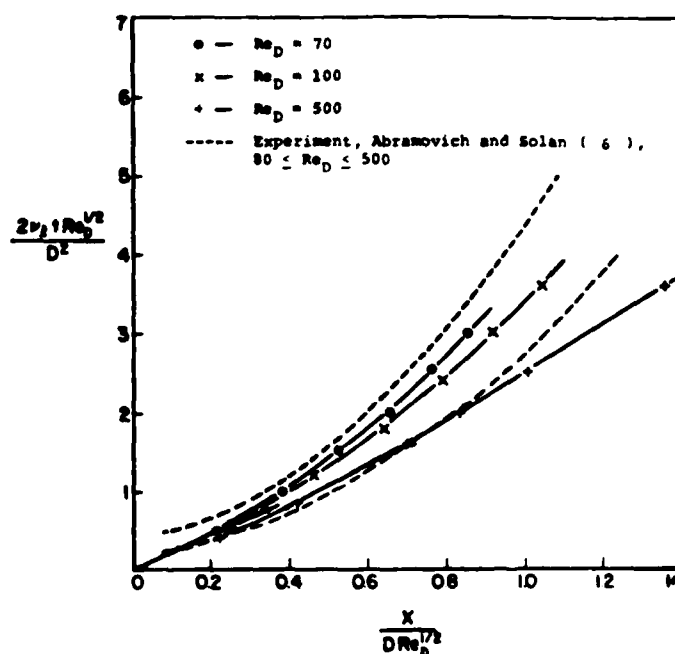


Fig. 7 - Incompressible laminar jets. Computed and measured transient jet tip penetration with different Reynolds numbers using Abramovich and Solan length and time scales (6)

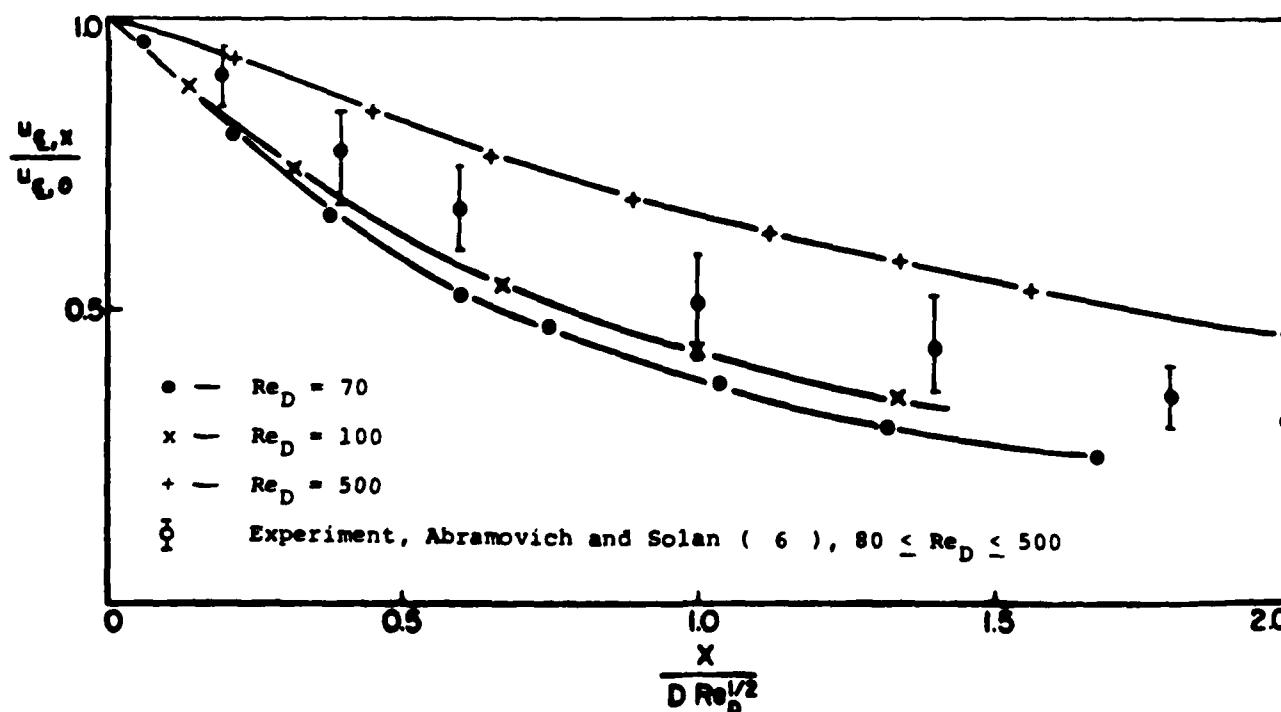


Fig. 6 - Incompressible laminar jets. Computed and measured steady-state centerline velocity with different Reynolds numbers using Abramovich and Solan length scale (6)

of their experimental data. However, in Fig. 8, measured and computed steady centerline velocity decay data of du Pless et al (9), Andrade et al (10), Pai et al (11) and Hatta et al (12) are reported in terms of the new length scale and seem to fall on a universal curve for each of the two initial velocity profiles.

For a given initial velocity profile, the universal curve of Fig. 9 changes if a percent other than 70 is selected to define achievement of steady state, but the characteristic time and length scales remain the same. This is illustrated in Figs. 10 and 11 for the case of uniform and parabolic exit velocities where the 70% curve is shown together with the 99.9%  $u_{CL, steady}$  and 99.9% steady momentum curves. The latter is obtained by imposing that the axial momentum reaches 99.9% of its steady value.

The curves of Figure 10, for the uniform exit velocity case, are fitted by the following equations:

$$\begin{aligned}
 &70\% u_{CL, steady} \\
 &t^* = 2.2x^* (x^* = 0.455 t^*) \quad x^* \leq 0.04 \\
 &t^* = 7.8x^{*1.42} (x^* = 0.235 t^{*0.7}) \\
 &\quad 0.04 \leq x^* \leq 0.2 \\
 &t^* = 13.2x^{*1.75} (x^* = 0.229 t^{*0.57}) \\
 &\quad x^* > 0.2 \\
 &99\% u_{CL, steady} \\
 &t^* = 16.2x^{*1.61} (x^* = 0.177 t^{*0.62}) \\
 &\quad x^* \geq 0.1 \\
 &99\% \text{ steady momentum} \\
 &t^* = 32x^{*1.61} (x^* = 0.116 t^{*0.62}) \\
 &\quad x^* \geq 0.075
 \end{aligned} \tag{5}$$

Also it is found that use of the 70%  $u_{CL, steady}$  and the 20% steady momentum definitions give similar axial locations, and that the 99.9%  $u_{CL, steady}$  and the 85% steady momentum conditions also occur simultaneously. Later we will find that the same quantities are related in the same way also for

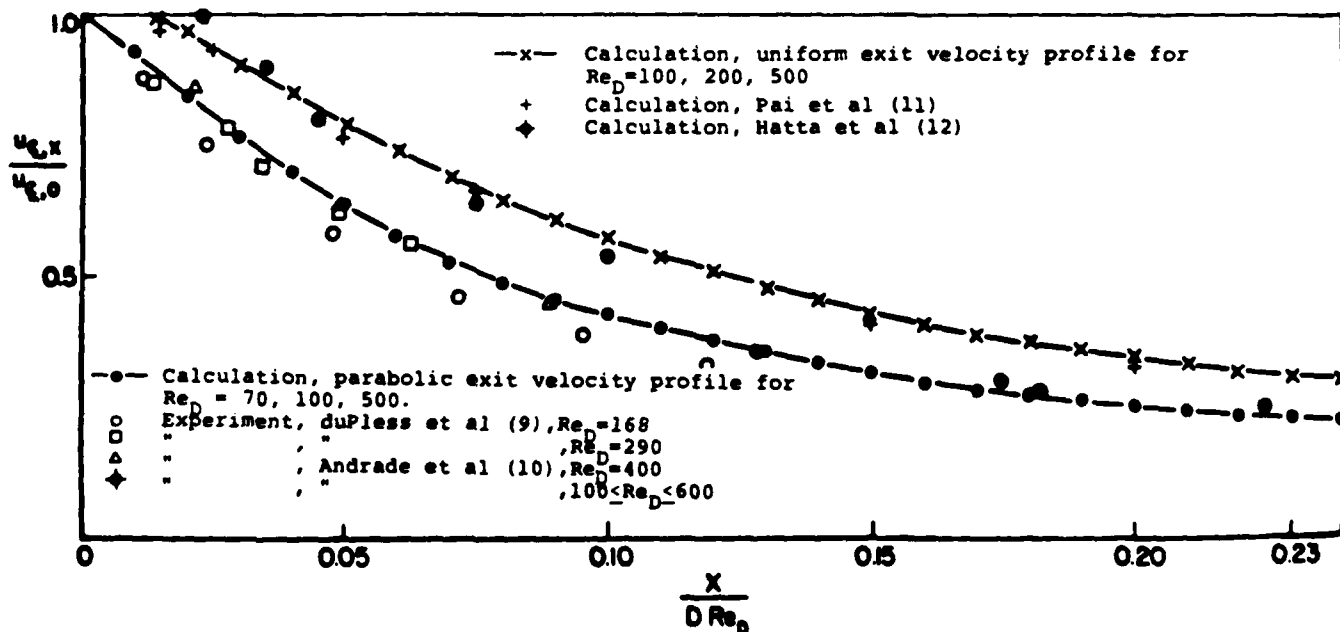


Fig. 8 - Incompressible laminar jets. Computed and measured steady-state centerline velocity using the new length scales

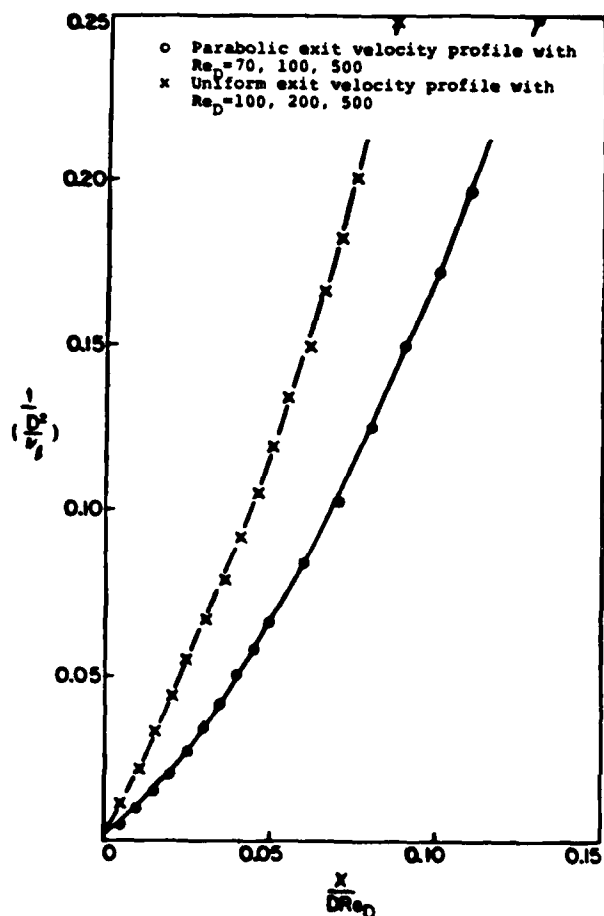


Fig. 9 - Incompressible laminar jets. Computed transient jet tip penetration using the new length and time scales

incompressible turbulence jets and for nonvaporizing and vaporizing sprays.

#### TRANSIENT INCOMPRESSIBLE TURBULENT JETS

**THE MODEL** - The equations of conservation of mass and momentum, and the two equations of the  $k$ - $\epsilon$  turbulence model (13), were solved simultaneously to obtain the mean dependent variables during the transient of two-dimensional, incompressible, turbulent, free jets. In cylindrical coordinates, the governing differential equations - including the semi-empirical turbulence model equations - can be put into the following general form (14,15)

$$\frac{\partial \phi}{\partial t} + \frac{1}{r} \left[ \frac{\partial}{\partial x} (r b \phi) + \frac{\partial}{\partial r} (r b v \phi) \right] =$$

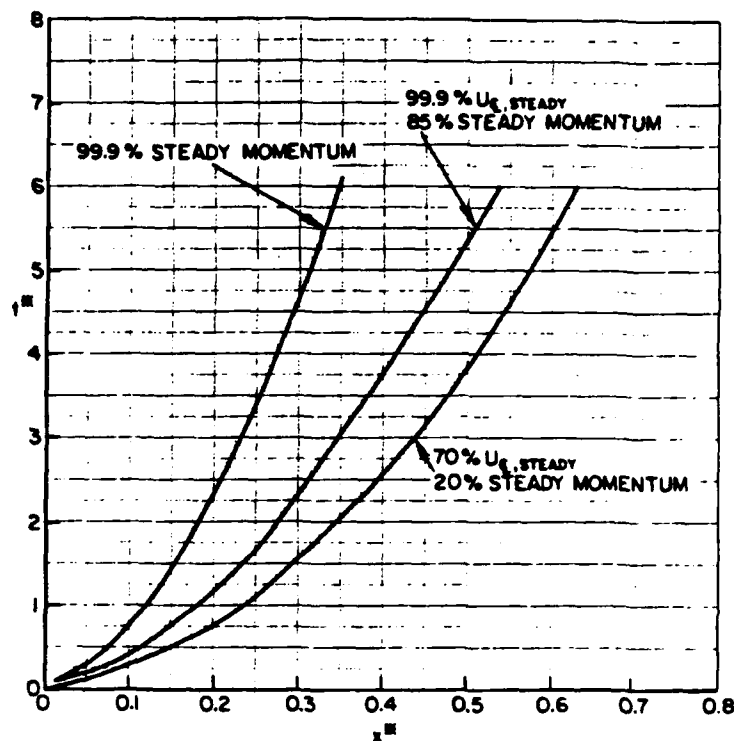


Fig. 10 - Incompressible laminar jet (uniform exit velocity profile). Steadying time curves, using different definitions for the achievement of steady-state and the new length and time scales

$$\frac{1}{r} \left[ \frac{\partial}{\partial x} (r b \frac{\partial \phi}{\partial x}) + \frac{\partial}{\partial r} (r b \frac{\partial \phi}{\partial r}) \right] + S_{\phi} \quad (6)$$

The meaning and form of the general dependent variable  $\phi$ , parameter  $b$ , and source term  $S_{\phi}$  are given in Table 1. The turbulent viscosity  $\mu_t$  used in the present calculation is modeled through  $k$  and  $\epsilon$  as shown in the same table.

The initial conditions were zero velocity everywhere except on the inlet boundary. The boundary conditions for the hydrodynamic variables  $u$  and  $v$  were:

$$\text{at } r = 0, \quad \partial u / \partial r = 0, \quad v = 0 \quad (7)$$

$$\text{at } r = R, \quad \partial u / \partial x = 0, \quad \frac{1}{r} \frac{\partial (r v)}{\partial r} = 0 \quad (8)$$

$$(u)_{r=R} = U_{\infty} \quad (9)$$

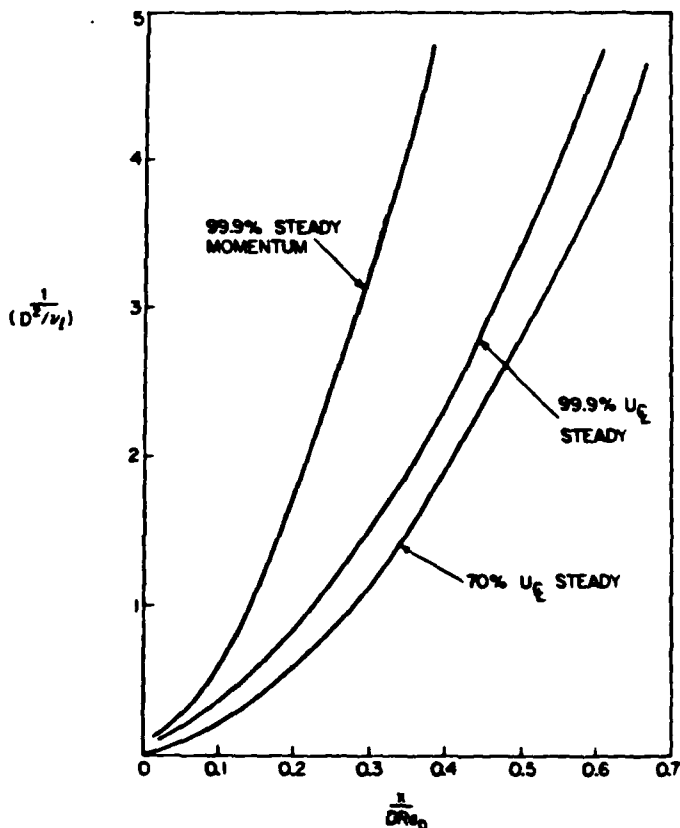


Fig. 11 - Incompressible laminar jet (parabolic exit velocity profile). Steadying time curves, using different definitions for the achievement of steady-state and the new length and time scales

The method of solution and the grid system were the same as in the laminar jet computations. At  $x = 0$ , two jet exit velocity profiles were used but only the results obtained with the uniform profile are summarized in the following paragraphs.

The conditions for  $k$  and  $\epsilon$  were as follows. At  $r = 0$ , the total normal fluxes for  $k$  and  $\epsilon$  were set equal to zero. At  $r = R$ , the values of  $k$  and  $\epsilon$  depended on the problem studied. Usually, a small value of  $k$  was used to simulate the natural turbulence level in the free stream. At  $x = 0$ , the distribution of  $k$  was prescribed and that of  $\epsilon$  was estimated through the expression (13)

$$\epsilon = k^{3/2} / l_0 \quad (10)$$

The outlet conditions were that the normal gradients be nil thus the computed flows are elliptic in space, but the results are not very sensitive to

the boundary conditions at the outlet plane as long as the head of the jet is away from that plane. In all our transient studies the head vortex remained within the computational domain.

**SCALING** - In Fig. 12 results are given for the steady state centerline velocity, with three different Reynolds numbers (based on the exit centerline velocity, orifice diameter, and kinematic laminar viscosity) and for the specified initial conditions. A systematic Reynolds number dependence is evidenced. However, it can be accounted for by scaling the axial distance with  $D Re_0^{0.053}$ . In Fig. 13, the transient results with three different Reynolds numbers are presented. Notice that the Reynolds number dependence disappears for large values of  $Re_0$ , i.e.  $Re_0 > 10^5$ . Also, the dependence of the transient on  $Re_0$  can be accounted for if the axial distance is scaled again by  $D Re_0^{0.053}$  and the steadying time by  $D Re_0^{0.053} / u_{CL,0}$  as shown in the same figure.

In Fig. 13,  $t$  is the time needed for the axial velocity  $u$  to reach 70% of its steady state value at any point  $x$  on the centerline of the suddenly-started turbulent jet. Again if a percent other than 70 is selected, the universal curve of Fig. 13 changes but not the characteristic time and length scales. This is illustrated in Fig. 14 where the 70% curve is shown together with the 99.9%  $u_{CL}$ , steady and 99.9% steady momentum curves.

The curves of Fig. 14 are fitted by the following equations.

$$\left. \begin{aligned} &70\% u_{CL, \text{steady}} \\ &t^* = 1.645x^* \quad (x^* = 0.608t^*) \quad x^* \leq 7 \\ &t^* = 0.235x^{*2} \quad (x^* = 2.06t^{*0.5}) \quad x^* \geq 7 \\ &99.9\% u_{CL, \text{steady}} \\ &t^* = 0.37x^{*2} \quad (x^* = 1.64t^{*0.5}) \quad x^* \geq 6 \\ &99.9\% \text{ steady momentum} \\ &t^* = 0.9x^{*2} \quad (x^* = 1.05t^{*0.5}) \quad x^* \geq 3 \end{aligned} \right\} \quad (11)$$

As for the laminar jets, it was found again that 70%  $u_{CL, \text{steady}}$  and 20% steady momentum are reached at the same time at all downstream planes and so are 99.9%  $u_{CL, \text{steady}}$  and 85% steady momentum.

For steady state free round jet flows, considerable experimental information is available. But for transient round jets the experimental data for comparisons with our computations is

Table 1. Governing differential equations for the study of turbulent incompressible jets

$$\frac{1}{r} \left[ \frac{\partial}{\partial x} (r \rho u \phi) + \frac{\partial}{\partial r} (r \rho v \phi) \right] + \frac{\partial \rho \phi}{\partial t} = \frac{1}{r} \left[ \frac{\partial}{\partial x} (r b \frac{\partial \phi}{\partial x}) + \frac{\partial}{\partial r} (r b \frac{\partial \phi}{\partial r}) \right] + S_\phi$$

Conservation of	$\phi$	b	$S_\phi$
Mass	1	0	0
Axial Momentum	u	$\nu_{eff}$	$\frac{\partial}{\partial x} (\nu_{eff} \frac{\partial u}{\partial x}) + \frac{1}{r} \frac{\partial}{\partial r} (\nu_{eff} r \frac{\partial v}{\partial x}) - \frac{\partial p}{\partial x}$
Radial Momentum	v	$\nu_{eff}$	$\frac{\partial}{\partial x} (\nu_{eff} \frac{\partial u}{\partial r}) + \frac{1}{r} \frac{\partial}{\partial r} (\nu_{eff} r \frac{\partial v}{\partial r}) - 2\nu_{eff} \frac{v}{r} - \frac{\partial p}{\partial r}$
Turbulent Kinetic Energy	k	$\frac{\nu_{eff}}{\sigma_k}$	$G - C_D \rho \epsilon$
Rate of Turbulent Energy Dissipation	$\epsilon$	$\frac{\nu_{eff}}{\sigma_\epsilon}$	$\frac{\epsilon}{K} (C_1 G - C_2 \rho \epsilon)$
$G = \nu_{eff} \left[ 2 \left( \left( \frac{\partial u}{\partial x} \right)^2 + \left( \frac{\partial v}{\partial r} \right)^2 + \left( \frac{v}{r} \right)^2 \right) + \left( \frac{\partial u}{\partial r} + \frac{\partial v}{\partial x} \right)^2 \right]$ $\nu_{eff} = \nu_l + \nu_t$ $\nu_t = C_\mu \rho k^2 / \epsilon$			

very limited. Recently, Witze (5) made some measurements in impulsively started air-into-air injections by hot-film anemometry. He measured both mean and fluctuation components of the axial velocity for both steady and transient cases, and presented four sets of experimental data using two nozzle exit conditions (Fig. 15). Only the jet arrival time he measured with nozzle A (See Table 2) was used for comparison with our transient computations because we cannot readily characterize the nozzle exit condition of nozzle B due to its screens.

It should be mentioned that from the measured arrival time at the various locations reported in Table 2, a common value of 0.35 ms was subtracted by Witze

to account for the response time of the equipment. In Fig. 16, the tabulated results are plotted in the coordinates  $(t/(D/u_{CL,0})); (x/D)$ , and a systematic Reynolds number dependence is evidenced. If use is made of the new length scale  $(D Re_D^{0.053})$  and the corresponding time scale  $(D Re_D^{0.053}/u_{CL,0})$ , the two curves tend to coalesce as shown in Fig. 17. The discrepancy is larger very near the injector where the experimental measurements showed broader scatter.

A visual correlation based on two experimental transient jet penetration pictures of Rizk (2) and Dedeoglu (16) is shown in Fig. 18. The center of the vortex shaped structure at the head of the jet was chosen to identify the location and time at which 70% of the cen-



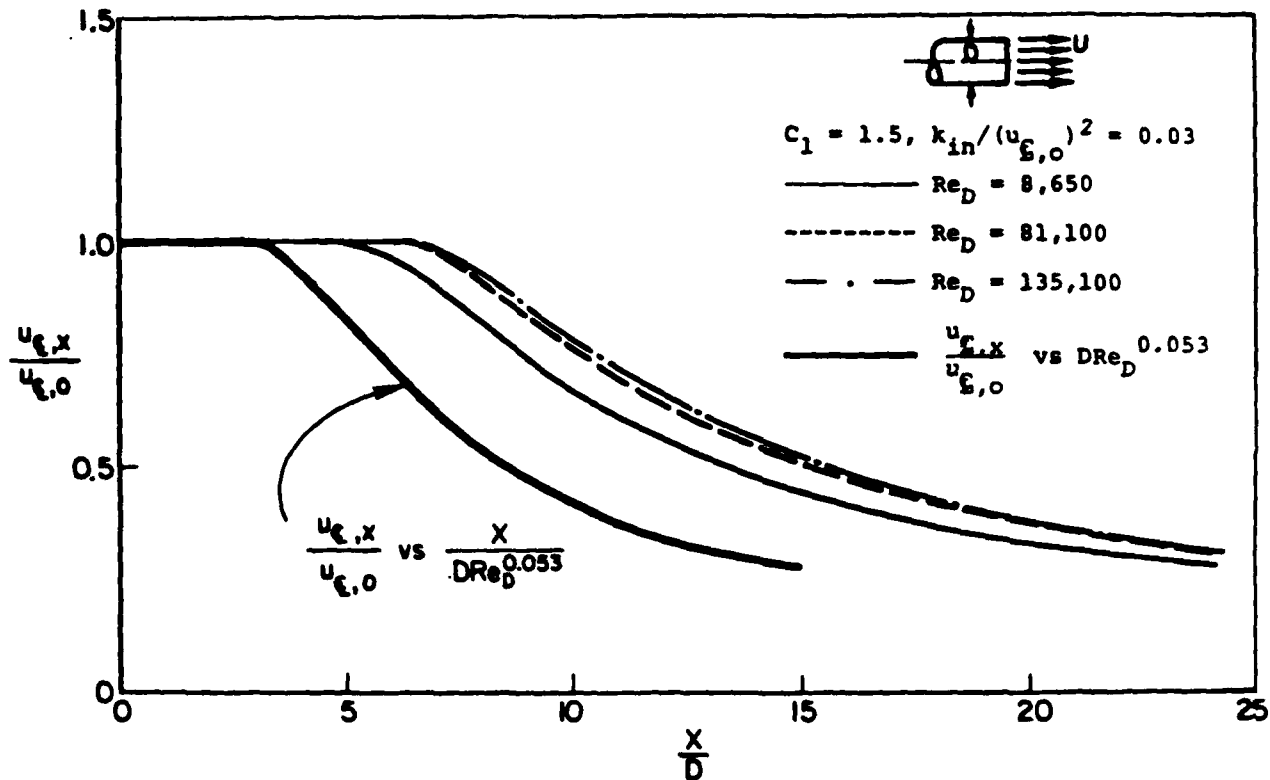


Fig. 12 - Incompressible turbulent jets. Computed steady-state centerline velocity distribution with three different Reynolds numbers

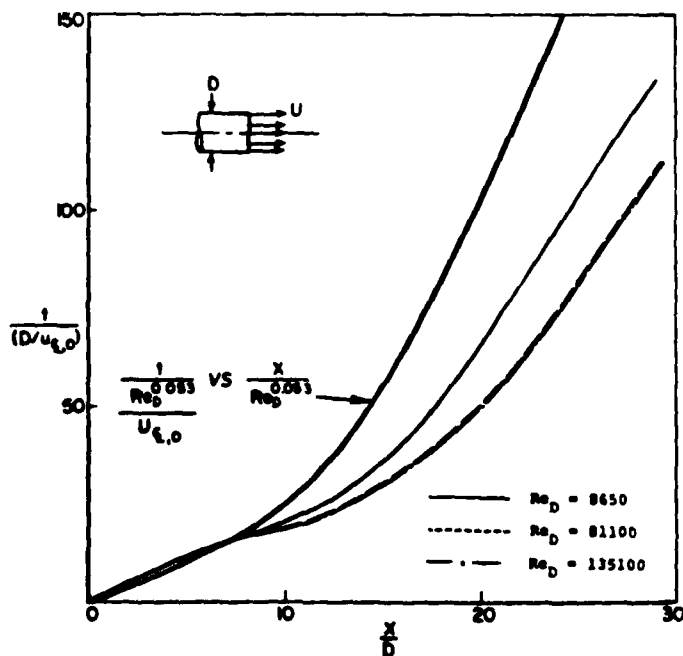


Fig. 13 - Incompressible turbulent jets. Calculation results on transient jet tip penetration with three different Reynolds numbers

terline steady state velocity is reached. These locations and arrival times thus correspond to the computed ones with which they are seen to compare favorably. In the transient laminar jet experiments of Abramovich and Solan (6), 70% of the centerline steady state velocity was also used to define the penetration of the center of the head vortex. It is also interesting that, working with fuel sprays, Borman and Johnson (17) and Taylor and Walsham (18) pointed out that the spray tip penetration rate can be closely estimated using a value between 68% and 72% of the steady state centerline velocity of the spray.

#### TRANSIENT THICK SPRAYS

**THE MODEL** - The equations of the model for the transient and steady state of nonevaporating and evaporating sprays are those of O'Rourke and Bracco (19). They are:

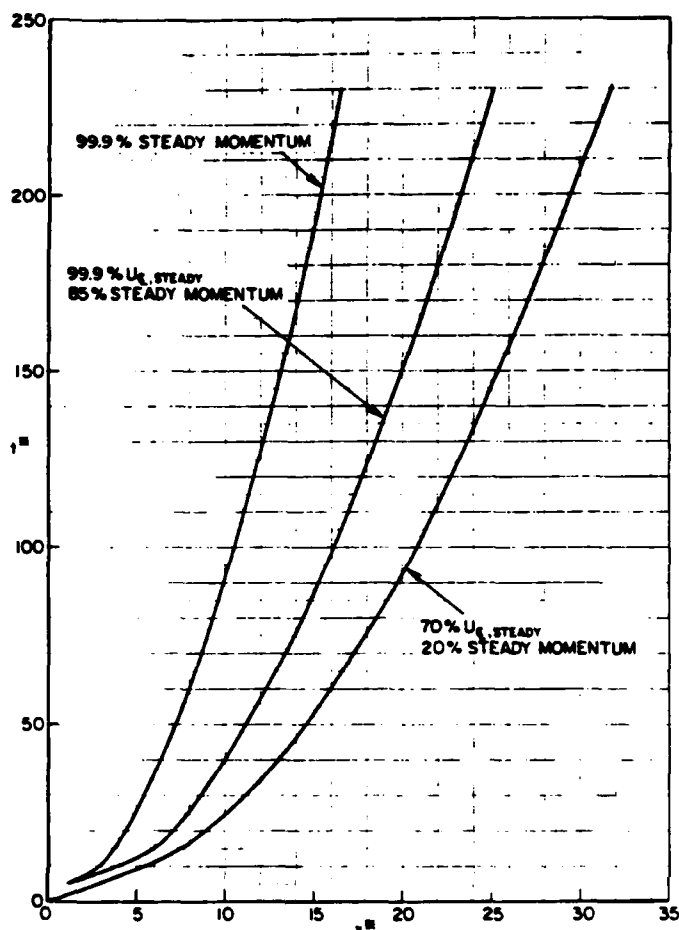


Fig. 14 - Incompressible turbulent jets. Steadying time curves using different definitions for the achievement of steady-state

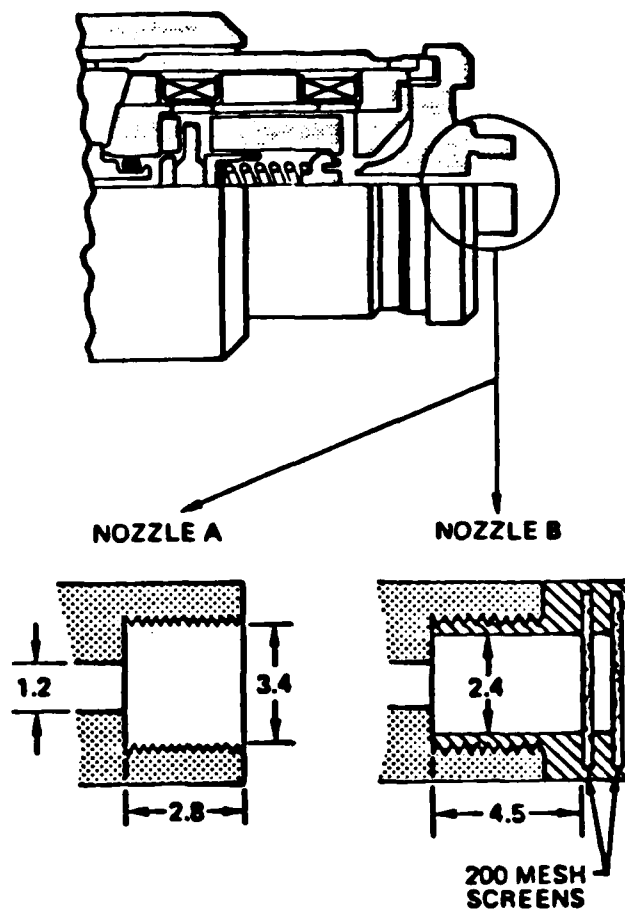


Fig. 15 - Solenoid-actuated valve and nozzle configurations used by Witze (5) - dimensions in mm

### Spray Equation

$$\frac{\partial f}{\partial t} + \underline{v} \cdot \nabla_{\underline{x}} (f \underline{v}) + \underline{v} \cdot \nabla_{\underline{v}} (f \underline{v}) + \frac{\partial}{\partial r} (f r) + \frac{\partial}{\partial T_d} (f T_d) =$$

$$1/2 \iint f(\underline{x}, \underline{v}_1, r_1, T_{d1}, t) f(\underline{x}, \underline{v}_2, r_2, T_{d2}, t)$$

$$v(r_1 + r_2)^2 |\underline{v}_1 - \underline{v}_2| E_{12}(\underline{x}, \underline{v}_1, r_1, \underline{v}_2, r_2, t)$$

$$\{ \sigma(\underline{v}, r, T_d, \underline{v}_1, r_1, T_{d1}, \underline{v}_2, r_2, T_{d2}, \underline{x}, t)$$

$$- \delta(r - r_1) \delta(\underline{v} - \underline{v}_1) \delta(T_d - T_{d1})$$

$$- \delta(r - r_2) \delta(\underline{v} - \underline{v}_2) \delta(T_d - T_{d2}) \}$$

$$dr_1 dv_1 dT_{d1} dr_2 dv_2 dT_{d2} \quad (12)$$

### Gas Phase Mass Equation

$$\frac{\partial \rho'}{\partial t} + \nabla \cdot (\rho' \underline{u}) = - \iiint 4\pi r^2 R_{p2} f dr dv dT_d \quad (13)$$

Table 2 - Transient Arrival Times Measured by Witze (5)

CASE 1 ( $U_{g,o} = 53$ m/sec, $D = 1.2$ mm)	
t (ms)	x (mm)
0.1222	2.87
0.3167	9.22
1.2097	15.57
2.9667	28.27
5.3667	40.97
8.5972	53.67
12.8556	66.37
17.9083	79.07

CASE 2 ( $U_{g,o} = 103$ m/sec, $D = 1.2$ mm)	
t (ms)	x (mm)
0.0014	2.87
0.0236	9.22
0.2083	15.57
1.2986	28.27
2.4472	40.97
3.9722	53.67
5.7861	66.37
8.0694	79.07

Vapor Mass Equation

$$\frac{\partial \rho'_g v}{\partial t} + \nabla \cdot (\rho'_g v u_g) = - \iiint 4\pi r^2 \rho_{g,i} f dr dv dT_d + \nabla \cdot [\rho'_g D_t \nabla Y_v] \quad (14)$$

Gas Phase Momentum Equation

$$\frac{\partial \rho'_g u}{\partial t} + \nabla \cdot (\rho'_g u u_g) + \nabla(p_g) = - \iiint [4\pi r^2 R v + \frac{4}{3} \pi r^3 \underline{f}] \rho_{g,i} f dr dv dT_d + \nabla \cdot \underline{I}_t \quad (15)$$

$$\text{where } \underline{I}_t = \rho'_g D_t [\nabla u_g + \nabla u_g^T - \frac{2}{3} \nabla \cdot u_g \underline{I}]$$

Gas Phase Energy Equation

$$\begin{aligned} \frac{\partial \rho'_g h}{\partial t} + \nabla \cdot (\rho'_g h u_g) = 0 \left( \frac{\partial p_g}{\partial t} + u_g \cdot \nabla p_g \right) \\ - \iiint \rho_{g,i} [4\pi r^2 R (h_i(T_d) + \frac{1}{2} (v - u_g)^2) \\ + \frac{4}{3} \pi r^3 (\underline{f}_i \cdot (v - u_g) + c_{p,i} \dot{T}_d)] dr dv dT_d \\ + \underline{I}_t : \nabla u_g + \nabla \cdot [\rho'_g c_{p,g} D_t \nabla T_g] \end{aligned} \quad (16)$$

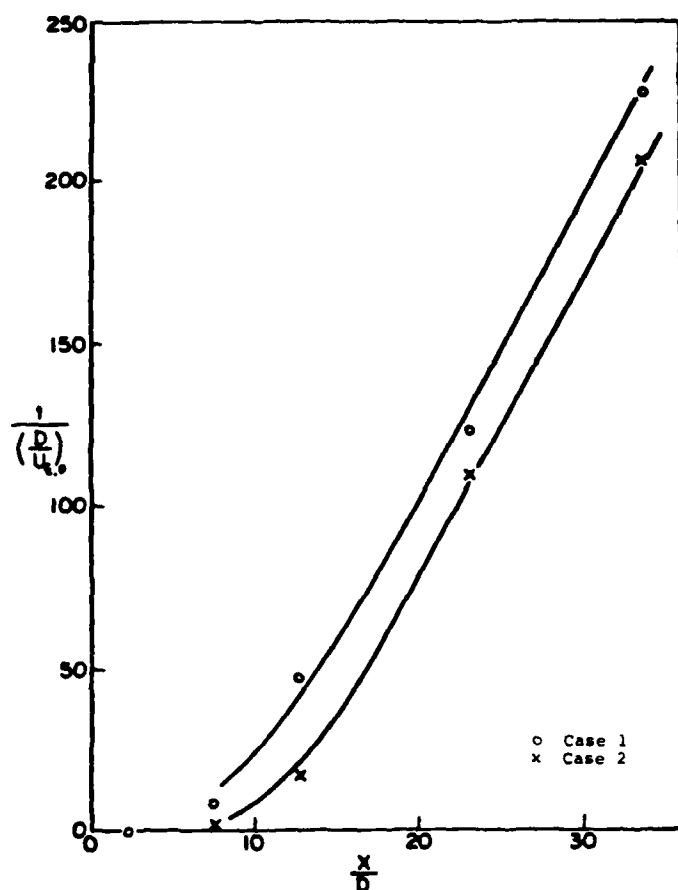


Fig. 16 - Witze's experimental transient jet tip penetration (5) (See Table 2)

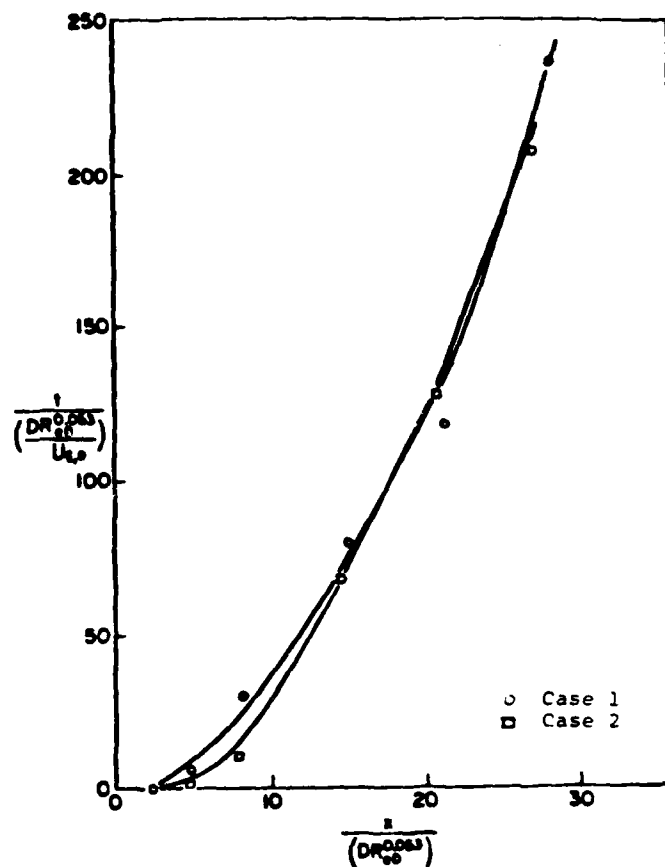


Fig. 17 - Witze's experimental transient jet tip penetration (5) in terms of the proposed length and time scales

#### Equations Determining Exchange Rates

$$-\rho_L R = \frac{\lambda_g}{c_{p_g}} \frac{Nu_g}{2r} \frac{Y_{v_g} - Y_{v_s}}{1 - Y_{v_s}} \quad (17a)$$

$$-\rho_L R = \frac{\lambda_g}{c_{p_g}} \frac{Nu_g}{2r} \left\{ \frac{c_{p_g}}{l(T_g)} \left[ (T_g - T_s) - \frac{Nu_g \lambda_g}{Nu_s \lambda_s} (T_s - T_d) \right] \right\} \quad (17b)$$

$$\frac{\frac{Y_{v_g}}{v_g}}{\frac{Y_{v_g}}{w_g} + \frac{Y_{v_s}}{w_s}} = \frac{p_v(T_g)}{p_g} \quad (17c)$$

$$\dot{T}_d = \frac{3}{2} \frac{\lambda_g}{\rho_L c_L r^2} Nu_L (T_s - T_d) + 3(R/r) (T_s - T_d) \quad (17d)$$

$$\begin{aligned} \bar{F} &= \frac{3}{8} \frac{\rho_g}{\rho_L} \frac{|u_g + u'_g - v|}{r} (u_g + u'_g - v) c_D \\ -\frac{1}{\rho_L} \nabla p_g &= \bar{F}_a - \frac{1}{\rho_L} \nabla p_s \end{aligned} \quad (17e)$$

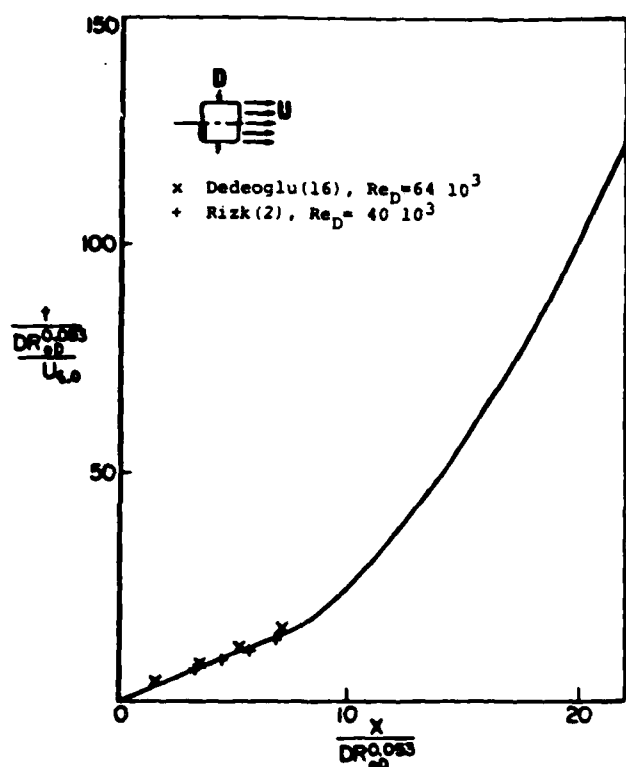


Fig. 18 - Incompressible turbulent jets.  
Comparison of predicted and observed  
jet tip arrival times

#### Equations of State

$$p_g = p_g R T_g \left( \frac{Y_v}{W_v} + \frac{Y_I}{W_I} \right) \quad (18a)$$

$$h_g = (c_{p_v} Y_v + c_{p_I} Y_I) T_g = c_{p_g} T_g \quad (18b)$$

$$h_l(T_d) = c_{p_v} T_d - L(T_d) \quad (18c)$$

$$L(T_d) = L_{ref} + (c_{p_v} - c_{p_l})(T_d - T_{ref}) \quad (18d)$$

Equation 12 is the traditional spray equation (20) plus two new terms that account for the heating of drops and for drop collisions and coalescence. The term  $\partial(f\dot{m}_d)/\partial T_d$  was tested for the first time in the present study and accounts for the effects of unsteady drop heating and a distribution of drop temperatures. The integral on the right hand side

accounts for the effects of drop collisions. The collision efficiency  $E_{12}$ , which has been demonstrated by O'Rourke and Bracco to have essentially a value of 1 in the present application, modifies the following collision frequency between drops having velocities, sizes and temperatures in the implied range:

$$f(\underline{x}, \underline{v}_1, r_1, T_{d1}, t) f(\underline{x}, \underline{v}_2, r_2, T_{d2}, t) \\ \pi(r_1 + r_2)^2 |\underline{v}_1 - \underline{v}_2| \\ d\underline{v}_1 dr_1 dT_{d1} d\underline{v}_2 dr_2 dT_{d2}.$$

The portion of the integrand within the brackets gives the sources (given by the transition probability function,  $\sigma$ ) and the sinks (given by the delta functions,  $\delta$ ) of drops of velocity  $\underline{v}$ , radius  $r$ , and temperature  $T_d$ , due to collisions between drops with subscript 1 properties and those with subscript 2 properties. The transition probability function gives the outcome of a collision and has a complicated mathematical expression (21). Physically, it determines whether the outcome of a collision is coalescence or separation. The criterion for drop separation after collision is that the rotational energy of the coalesced drop pair exceeds the surface energy required to reform the original drops from the coalesced pair. For the coalescence efficiency,  $E_{coal}$ , which is the probability of coalescence given that collision has occurred, O'Rourke and Bracco give the expression

$$E_{coal} = \min(2.4 f^* \left(\frac{r_2}{r_1}\right) \frac{1}{We}, 1.0) \quad (19)$$

$$\text{where } We = \frac{\rho_l |\underline{v}_1 - \underline{v}_2|^2 r_1}{\sigma_l}, \quad r_1 \leq r_2 \quad (18b)$$

and  $\sigma_l$  is the surface tension coefficient. The function  $f^*$

$$f^* \left(\frac{r_2}{r_1}\right) = \left(\frac{r_2}{r_1}\right)^3 - 2.4 \left(\frac{r_2}{r_1}\right)^2 + 2.7 \left(\frac{r_2}{r_1}\right) \quad (20)$$

has the value of 1.3 for  $r_2/r_1 = 1$  and 3.8 for  $r_2/r_1 = 2$ , and behaves as  $(r_2/r_1)^3$  when  $r_2/r_1$  approaches infinity. The process of drop re-separation (called grazing collision by O'Rourke and Bracco) is important. Without it, that is if all collisions are assumed to result in coalescences, unphysically

large drops result (21).

In the gas phase mass, momentum and energy conservation equations, the integrals on the right-hand sides represent the exchange functions. They are the sum over all drops at point  $x$  and time  $t$  of the rate of mass, momentum, and energy exchanges between each drop and the gas; thus they involve the rate of drop radius change  $R$ , velocity change  $\underline{F}$ , and temperature change  $\dot{T}_d$ .

The rate of drop radius change  $R$  is found by solving equations (17a)-(17c) simultaneously for the unknown drop surface temperature  $T_s$ , surface vapor mass fraction  $Y_{vs}$ , and  $R$ . After  $R$  and  $T_s$  are found, the rate of drop temperature change  $\dot{T}_d$  is obtained from (17d). The drop acceleration  $\underline{F}$ , given by equation (17e), has two contributions: one due to aerodynamic drag  $\underline{F}_a$  and the other due to the mean pressure gradient which has been shown to be important in some applications by O'Rourke (21). In Equations (17a)-(17e), there are three unknown functions; the drag coefficient  $C_D$ , and the gas and liquid phase Nusselt numbers,  $Nu_g$  and  $Nu_l$ , respectively. After a detailed survey of experimental and theoretical studies of fluidized beds, heat transfer in regular arrays of spheres, and packed beds, O'Rourke proposed the following correlations to account for the effect of the gas volume fraction,  $\epsilon$ ,

$$C_D(\epsilon, Re) = \frac{24}{Re} \left( \epsilon^{-2.65} + \frac{Re^{2/3}}{6} \epsilon^{-1.78} \right) \quad (21)$$

$$Nu_g = [2\epsilon^{-1.75} + 0.6 \left( \frac{Re}{\epsilon} \right)^{1/2} Pr^{1/3}] \frac{\ln(1+B)}{B} \quad (22)$$

$$\text{where } B = \frac{Y_{vs} - Y_v}{1 - Y_{vs}} \text{ is the transfer number.}$$

Equations (21) and (22) were used in the present non-evaporating and evaporating studies with the  $Nu_l = 1$  and  $Pr = 0.7$ .

The effect of turbulence on the gas phase are accounted for by the terms involving  $D_t$  in Eq. (14)-(16), where  $D_t$  is the turbulent diffusivity, and was assumed to be equal to that of turbulent gas jets and related to the kinematic momentum (22)

$$D_t = 0.0161 \left( \frac{\pi D^2}{4} u_{inj}^2 \right)^{1/2} \quad (23)$$

The turbulence effects on the drops are calculated by adding to the mean gas velocity,  $\underline{u}_g$ , a fluctuating component,  $\underline{u}'_g$ , when computing the aerodynamic drag force  $\underline{F}_a$  and the gas phase Nusselt number  $Nu_g$ .  $\underline{u}'_g$  is chosen randomly from an isotropic Gaussian distribution with mean square deviation  $2/3k$ , where  $k$  is the turbulence kinetic energy and is assumed to be a fixed fraction ( $C = 0.20$ ) of the local mean flow kinetic energy, as is the case, approximately, in the downstream part of steady gaseous jets

$$k = C \frac{3}{2} \underline{u}_g^2 \quad (24)$$

For each drop, after a turbulent correlation time  $\tau_t$ , a new value of  $\underline{u}'_g$  is chosen. Dukowicz (23) took this correlation time  $\tau_t$  to be constant. O'Rourke (21) took  $\tau_t$  to be the residence time of a drop in a turbulent eddy of size  $l$  found from

$$D_t = C_l k^{1/2} l \quad (25)$$

with the optimized constant  $C_l = 0.045$ .  $\tau_t$  is then given by

$$l = \int_t^{t+\tau_t} |\underline{v}(t') - \underline{u}_g(t')| dt' \quad (26)$$

where  $\underline{u}_g(t')$  is the mean gas velocity at the drop position at time  $t'$ .

A detailed derivation and discussion of the equations of the thick-spray model is given in Reference 21.

The axisymmetric transient motion of a liquid spray is computed from the beginning of the thick spray regime to a downstream region where the spray is very thin. The computational mesh used is shown in Fig. 19. For all the cases studied, the cells were smallest near the nozzle exit, where  $\Delta r = 0.05$  cm and  $\Delta x = 0.1$  cm. Away from the nozzle exit, the size of the cells increased in both the axial and radial direction with corresponding expansion factors of 4% and 7%. A total of 44 cells in the

AD-A113 892

PRINCETON UNIV NJ DEPT OF MECHANICAL AND AEROSPACE --ETC F/G 21/7  
HIGH PRESSURE ATOMIZATION.(U)  
MAR 82 F V BRACCO

DAAG29-76-6-0264

UNCLASSIFIED

ARO-13935.3-EX

NL

3 OF 3

AD A  
113892

END  
DATE  
FILMED  
05-82  
DTIC

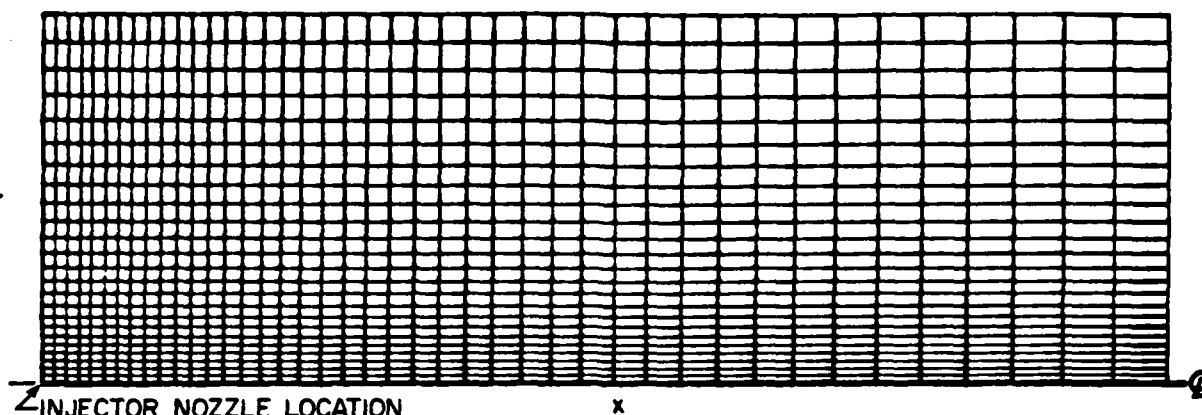


Fig. 19 - Computation mesh for spray studies

axial direction and 26 cells in the radial direction were used, giving the computational domain a length of 9.5 cm and width of 3.2 cm.

The top and right boundaries were treated as open boundaries, the left boundary as a solid wall and drops and gas injected from the cell of the left boundary next to the axis of symmetry. The condition on the top boundary allows for free entrainment from the surroundings. The pressure at the top and right boundary were assumed to be uniform and equal to the ambient value to simulate the free spray conditions.

All the computations were initiated at that axial location of the spray where the initial gas volume fraction,  $\phi_0$ , is approximately 0.9. Gas and liquid were injected with equal axial velocity  $U_0$ , computed by using conservation of momentum, that is somewhat lower than the liquid injection velocity,  $U_{inj}$ , in turn calculated with a discharge coefficient,  $C_{dis}$ , estimated from the experimental data of Bergwerk (24). The procedure to compute  $U_0$  was explained by O'Rourke and Bracco (19). The initial spray angle and mean size of the drops was computed using correlations proposed by Reitz and Bracco (25) for the atomization process. They were able to show that under the condition of

$(\rho_l/\rho_g)(Re_l/We_l)^2 \gg 1$ , the measured initial spray half angle,  $\theta_{1/2}$ , is correlated well by

$$\tan \theta_{1/2} = \frac{1}{C_6} [4 - (\rho_g/\rho_l)^{1/2} \frac{\sqrt{3}}{6}] \quad (27)$$

where the proportionality constant,  $C_6$ , depends on the geometry of the nozzle. For example, for straight round holes,  $C_6$  increases when the length-to-diameter

ratio of the nozzle increases. Reitz and Bracco argued that the corresponding initial mean drop size should be correlated by

$$SMR_0 = B [4 - (\rho_l/\rho_g U_{inj}^2)^{1/2}]^{3/2} \quad (26)$$

where the constant  $B$  is independent of the nozzle geometry and of order one, but no experimental verification of Equation 28 has yet been provided. Note that in this expression, the initial mean drop size  $SMR_0$  is predicted to decrease when the chamber gas density increases. However the computed downstream mean drop size is found to increase with increasing gas density due to collisions and recombination (19) and in agreement with the measurements of Hiroyasu and Kadota (26).

The computer code LDEF (Lagrangian Drop-Eulerian Fluid) developed by O'Rourke (21) was employed for the present study with some modifications. This code incorporates the basic methodology of the stochastic parcel method of Dukowicz (23) as well as additional features added by O'Rourke to improve its accuracy and extend its applicability. Typical examples are: compressibility effects were included by a modified form of the ICE technique, the momenta equations were cast in conservation form, and the swirl velocity equations were added for the liquid and gas. Use of the ICE method obviates the need to observe the Courant sound speed restriction on the size of the computational time step. Detailed description of the iteration procedure used in the code and the momentum exchange calculation are given in Reference 21.

The modifications we have made to O'Rourke's code for the present study



include: 1) a numerically more efficient grazing collision calculation procedure; 2) a new implicit iteration scheme to compute the time advanced liquid parcel temperature for evaporating sprays; 3) gravitational acceleration in the computation of the liquid parcel velocity; 4) and algorithm for the evaluation of the drop velocity distribution function and the axial distribution of mean drop size. More information on these modifications and other spray computations can be found in Reference 7.

**SCALING** - To assess the accuracy of the model, O'Rourke and Bracco (19,21) compared its result with the tip penetration rate and the downstream drop size distribution measured by Hiroyasu and Kadota (26) in one Diesel-type injection and with drop size and velocity distributions measured by Groeneweg et al (27) at several locations within a spray from a swirl atomizer. More comparisons have since been made with more of the data of Hiroyasu and Kadota.

In Fig. 20, computed and measured tip penetration rates are given for the

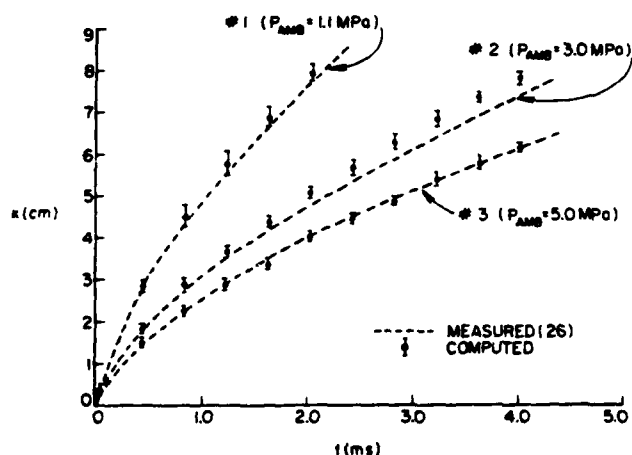


Fig. 20 - Computed ensemble averaged spray tip penetration curves of cases #1, 2, and 3 of Table 3

different gas pressures (and densities since the experiments were at room temperature) of 1.1, 3.0, and 5.0 MPa. The agreement is seen to be good. The computed and measured downstream drop size distributions and corresponding Sauter mean radii for the three cases are also shown in Fig. 21 in the coordinates of incremental volume fraction,  $(1/V_T)dV(r)/dr$ , versus drop radius  $r$ . It is observed that both computed Sauter mean radii and computed distributions compare favorably with the measured ones. All computations were made with

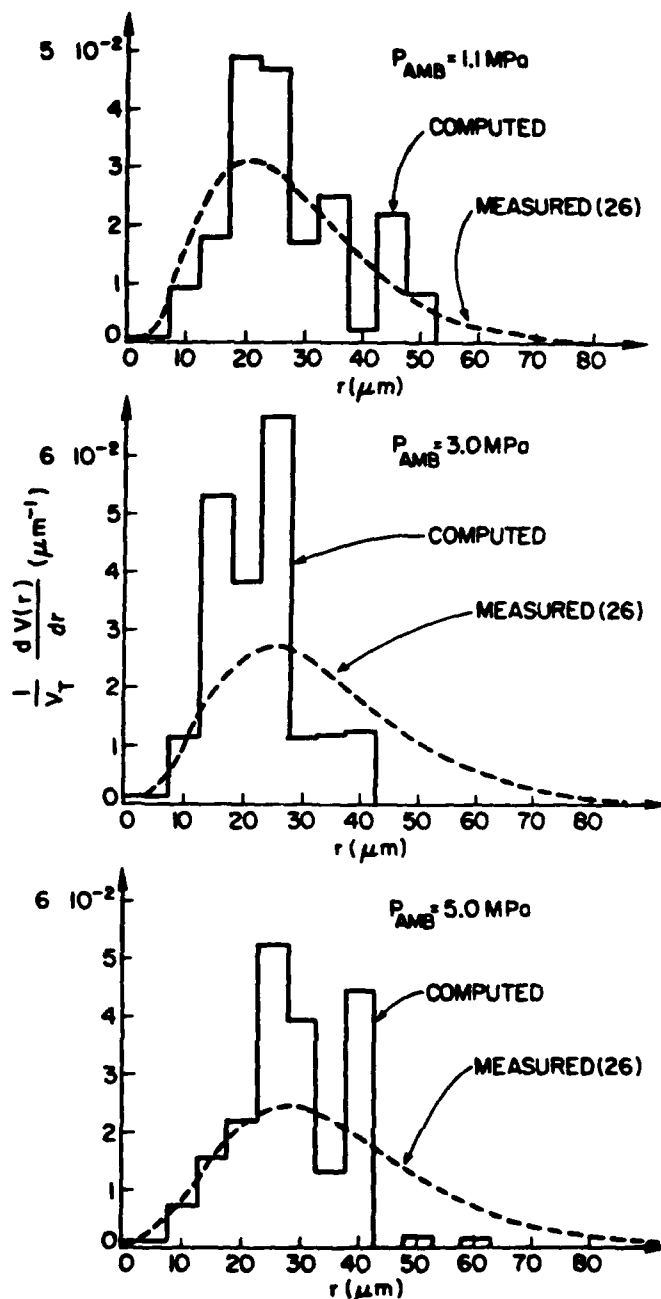


Fig. 21 - Computed and measured drop incremental volume fractions versus drop radius at three gas pressures (cases #1, 2, 3 of Table 3)-measured SMR = 21, 24, 27  $\mu\text{m}$  - computed SMR = 23, 20, 25  $\mu\text{m}$

the same model.

In the scaling studies (see Table 3) we varied separately the orifice diameter, to study the effect of orifice size at constant geometry (Cases #1 and 9); the injection velocity (Cases #1 and 10); the spray angle, to evaluate the effect of orifice geometry at constant orifice diameter (Cases #1, 2, 3 and

Table 3. Input parameters of the spray computations

CASE #	P <sub>inj</sub> MPa	P <sub>amb</sub> MPa	C <sub>DIS</sub>	U <sub>inj</sub> cm/ms	U <sub>o</sub> cm/ms	θ <sub>o</sub>	SR <sub>o</sub> um	θ <sub>1/2</sub> Rad	$\frac{l}{D}$	D <sub>t</sub> cm <sup>2</sup> /ms	P <sub>STATE</sub> ms <sup>-1</sup>	δt us	D cm	T <sub>g</sub> K	ρ <sub>g</sub> g/cm <sup>3</sup>	T <sub>l</sub> K	ρ <sub>l</sub> g/cm <sup>3</sup>
1	9.9	1.1	0.7	10.2	8.92	0.9	3	.0785	6.67	.0043	900	0.5	0.03	300	.0126	300	0.84
2	9.9	3.0	0.7	9.03	6.91	0.88	1.5	.0993	6.67	.0039	900	0.5	0.03	300	.0344	300	0.84
3	9.9	5.0	0.8	8.64	5.92	0.87	1.2	.1220	6.67	.0037	900	0.5	0.03	300	.0577	300	0.84
4	12.9	6.0	0.7	9.03	6.91	0.88	1.5	.0993	6.67	.0039	900	0.5	0.03	600	.0344	300	0.84
5	10.45	1.65	0.7	10.2	8.92	0.9	3	.0785	6.67	.0043	900	0.5	0.03	450	.0126	300	0.84
6	11.0	2.2	0.7	10.2	8.92	0.9	3	.0785	6.67	.0043	900	0.5	0.03	600	.0126	300	0.84
7	11.0	2.2	0.7	10.2	8.92	0.9	3	.0785	6.67	.0043	900	0.5	0.03	600	.0126	300	0.84
8	34.0	3.4	0.65	16.2	13.13	0.923	0.9	.1047	4.0	.0046	900	0.5	0.02	700	.0164	300	0.84
9	9.9	1.1	0.7	10.2	7.073	0.968	3	.0785	6.67	.0022	900	0.5	0.015	300	.0126	300	0.84
10	18.7	1.1	0.7	14.43	12.74	0.9	1.5	.0785	6.67	.0062	900	0.5	0.03	300	.0126	300	0.84
11	9.9	1.1	0.7	10.2	8.92	0.9	3	.1312	6.67	.0043	900	0.5	0.03	300	.0126	300	0.84
12	9.9	3.0	0.7	9.03	6.91	0.88	1.5	.1745	6.67	.0039	900	0.5	0.03	300	.0344	300	0.84
13	9.9	5.0	0.8	8.64	5.92	0.87	1.2	.2182	6.67	.0037	900	0.5	0.03	300	.0577	300	0.84
14	13.8	5.0	0.7	10.2	7.0	0.873	0.6	.1220	6.67	.0043	900	0.5	0.03	300	.0577	300	0.84
15	9.9	3.0	0.7	11.71	7.51	0.86	0.9	.1220	6.67	.005	900	0.5	0.03	300	.0344	300	0.50

#11,12,13, respectively); the gas density (Cases #1 and 14); and the liquid density (Cases #1 and 15). After each variation, we looked for characteristic length and time scales so that the dimensionless location at which a selected fraction of steady state is reached remains the same before and after the variation at all dimensionless times. It was also checked that the selected scales do not change when different fractions of steady state are employed. In looking for the characteristic length and time scales we were guided by our findings for laminar and turbulent jets. There the characteristic velocity was always found to be the injection velocity so that the characteristic time became determined as soon as the characteristic length was identified. The characteristic lengths, in turn were  $D \text{ Re}_D$  for laminar jets and  $D \text{ Re}_D^{0.053}$  for turbulent jets, but both of them can be written as  $D/\tan \theta_{1/2}$  since for laminar jets  $\tan \theta_{1/2} \sim \text{Re}_D^{-1}$  and for turbulent jets  $\tan \theta_{1/2} \sim \text{Re}_D^{-a}$  ( $a \sim 0.053$ ). Thus the injection velocity, the diameter of the orifice and the initial angle of the spray were suspected to be important in the scaling of sprays as well. Indeed they were found sufficient to scale the effects of nozzle size, nozzle geometry, and injection velocity. Moreover the effects of gas and liquid densities were surmised to be expressible through their ratio since this ratio influences the initial angle of the spray (25) and is also important in compressible turbulent jets (28).

Finally changing the gas temperature at constant gas density changes the vaporization rate and the transfer number  $\text{Br} = c_{p_l} (T_g - T_l) / L$  was considered for the scaling and found adequate (7).

The conclusion of the parametric study is that the characteristic length, velocity, and time scales for the transient and steady state of thick sprays are:

Characteristic Length:

$$d_{\text{eff}} = D (\tan \theta_{1/2})^{-0.25} (\rho_l / \rho_g) (1 + \text{Br}_T)^{-0.45}$$

Effect of Nozzle Size    Effect of Nozzle Geometry    Effect of Liquid & Gas Density    Effect of Vaporization

Characteristic Velocity:

$U_{\text{inj}}$

Effect of Injection Velocity

Characteristic Time:

$d_{\text{eff}} / U_{\text{inj}}$

(29)

Moreover, just as for laminar and turbulent jets, we found that the characteristic time and length scales do not change when different definitions for the achievement of steady state are adopted (see Figure 22), and that 70%

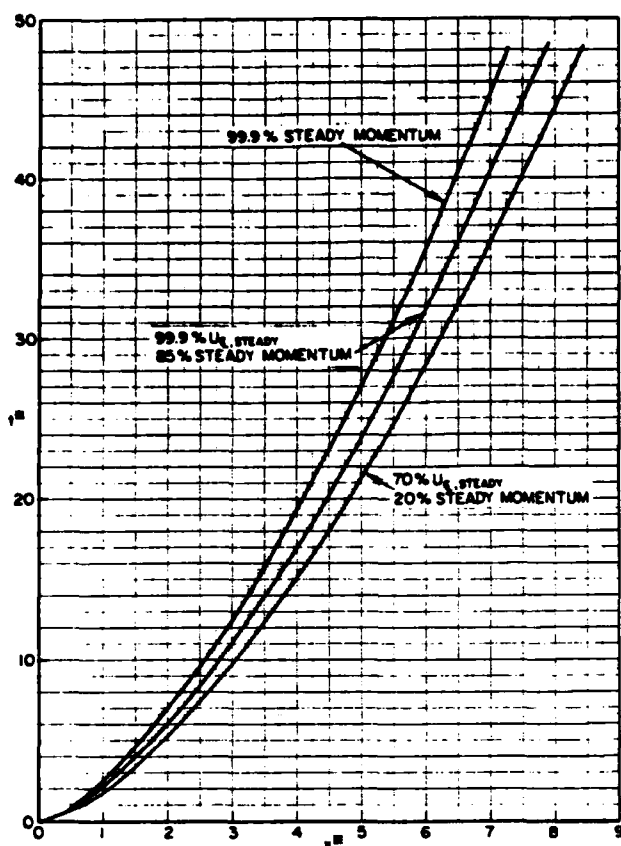


Fig. 22 - Spray steadying time curves using different definitions for the achievement of steady-state. See Eq. 29 for reference length and time scales

$u_{CL, steady}$  and 20% steady momentum are achieved at the same time at all axial locations and so are 99.9%

$u_{CL, steady}$  and 85% steady momentum.

The curves of Fig. 22 are fitted by the following equations:

70%  $u_{CL, steady}$

$$t^* = 1.457x^* \quad (x^* = 0.686t^*) \quad x^* \leq 0.6$$

$$t^* = 1.89x^{*1.51} \quad (x^* = 0.656t^{*0.662}) \quad x^* \geq 0.6$$

99.9%  $u_{CL, steady}$

$$t^* = 2.2x^{*1.49} \quad (x^* = 0.589t^{*0.671}) \quad x^* \geq 0.6$$

99.9% steady momentum

$$t^* = 2.5x^{*1.48} \quad (x^* = 0.538t^{*0.676}) \quad x^* \geq 0.6$$

(30)

When  $U_{inj}$  and the expression for  $deff$  (Equation (29)) are replaced in the equation for the trajectory of the

70%  $u_{CL, steady}$  point (Equation (30)) and terms are regrouped so as to isolate the various parameters, exponents of the parameters are derived that can be compared with the exponents of tip penetration rate correlations proposed by other authors and obtained through theoretical considerations or curve fits of experimental data. The comparison is made in Table 4. It can be seen that the proposed signs of the exponents are in general agreement but that magnitudes differ. However, our correlation is in reasonably good agreement with the experimental ones of Schwitzer (29), Parkset al (33), and Taylor et al (35). In particular, it is interesting that the correlations proposed by other authors on theoretical considerations let  $x$  go as  $t^{0.5}$ , in obvious analogy with turbulent gas jets, whereas our computations and the experiments indicate that the exponent of  $t$  should be between 0.59 and 0.66.

#### SIMILARITIES AND DIFFERENCES OF LAMINAR, TURBULENT, AND SPRAY JETS

The conclusions of the numerical studies described in the previous sections are summarized in Table 5. There the characteristic length, velocity, and time scales are given for the transient and steady state of incompressible laminar and turbulent jets and nonvaporizing and vaporizing sprays together with the fits for the steadying times (Equations 5, 11, and 30 corresponding to the curves of Figures 10, 14, and 22).

Although the equations of Table 5 contain all the necessary information, we would like to illustrate their meaning and the general behavior of the transient of the three jets with the help of Figure 23. The three curves of this figure are typical of the universal steadying curves that we have found for the three families of jets (Figures 10, 14, and 22) and that are represented by the equations of Table 5. Sketched on top of them is the corresponding jet at two subsequent times from its impulsive start. (The shape and position of the head vortex is only approximate since its structure was not studied directly in this work due to difficulties in identifying its boundaries precisely in the numerical results). The three curves identify which part of the jet has achieved what fraction of steady state given either the time from its impulsive start or its instantaneous position.

For all three families of jets, the

Table 4 - Powers of the Independent Parameters of the Tip Penetration Function

PROPOSER OF CORRELATION	POWER OF PARAMETER									
	$\Delta P$	D	$\rho_g$	$T_g$	t	$\rho_l$	$v_l$	$t_g$	Tan $\theta_h$	Remarks
SCHWEITZER (29)	0.2936	0.4127	-0.4127	—	0.5873	—	—	—	—	exp.
LYSHEVSKIY (30)	0.3	0.4	-0.5	—	0.5	0.4	0.3	—	—	theor.
WAKURI, ET AL (31)	0.25	0.5	-0.25	—	0.5	—	—	—	-0.5	theor.
SITKEI (32)	0.39	0.82	-0.35	—	0.48	-0.04	-0.3	—	—	theor.
PARKS, ET AL (33)	0.3	0.4	-0.4	0.6	0.6	—	—	—	—	exp.
HAKKI OZ (34)	—	—	—	—	0.5	—	—	—	—	theor.
TAYLOR, ET AL (35)	0.32	0.18	-0.32	—	0.64	—	—	0.18	—	exp.
DENT (36)	0.25	0.5	-0.25	-0.25	0.5	—	—	—	—	theor.
WILLIAMS (37)	0.25	0.5	-0.25	—	0.5	—	—	—	—	theor.
CHIU, ET AL (38)	0.25	0.5	-0.35	—	0.6	0.4	—	—	—	exp.
HIROYASU, ET AL (39)	0.25	0.5	-1	—	0.5	—	—	—	—	$t > t_{break}^*$
	0.5	—	—	—	1	-0.05	—	—	—	$t < t_{break}^*$
PRESENT STUDY	0.331	0.338	-0.338	-0.152	0.662	0.0	—	—	-0.085	$x^* > 0.6$
	0.5	—	—	—	1	-0.05	—	—	—	$x^* < 0.6$

$$*t_{break} = 28.65 \rho_l D / (\rho_g \Delta P)^{1/2}$$

transition to steady state is accomplished mostly within the head vortex. It is realized that the diffusional component of the process strictly would require infinite time for complete steady state to be reached. But practically high fractions of steady state values are already achieved at the back of the head vortex. What fraction is considered sufficient depends on the specific application. For this reason we have given curves corresponding to five different fractions.

For all three types of jet, the velocity achieves a given fraction of its steady state value faster along the axis than off the axis as shown, for example, by 70% of the steady state centerline velocity being achieved at the same cross-section at which only 20% of the steady state axial momentum is obtained. At the back of the vortex, using any definition, a large fraction of the steady configuration has already been achieved.

Extremely important is that the characteristic steadying time and length scales are the same for all fractions of steady state for each family of jets (but are different for the three families). This is necessary to be able to conclude that all transient jets scale in time.

Very interesting is that for each of the three types of jet the cross-section at which 70% of the steady state centerline velocity is obtained remains identical with that at which 20% of the steady momentum is achieved throughout the propagation. Since this is a section of the head vortex, one must conclude that the head vortex itself scales in time and that its length and time scales are proportional to those given in Table 5. But, as previously stated, the scaling of the head vortex was not studied explicitly and this conclusion remains to be checked.

Thus, in general, the three families of jets are similar in that at



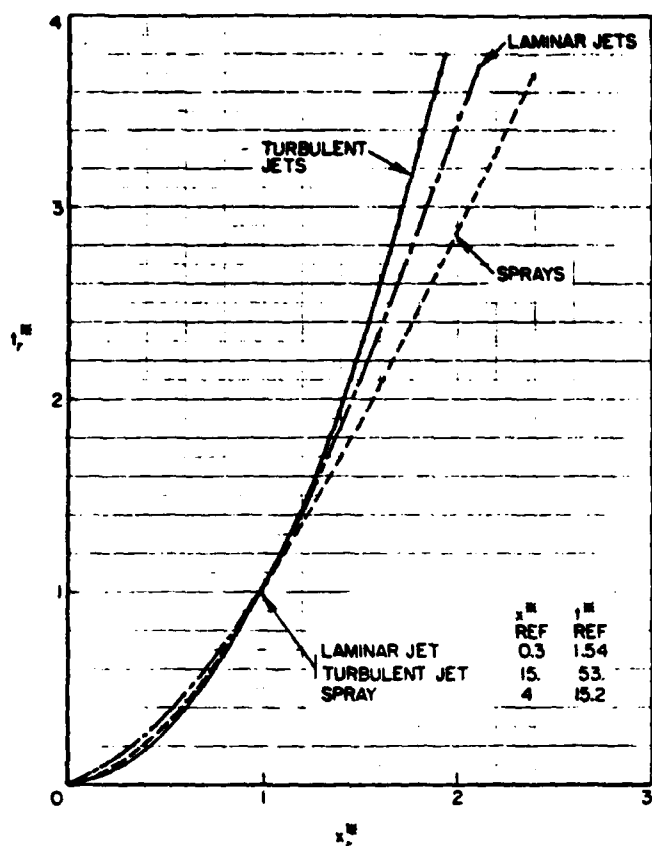


Fig. 24 - Reduced dimensionless steadying time versus reduced dimensionless steadying length using 70%  $u_{CL}$ , steady

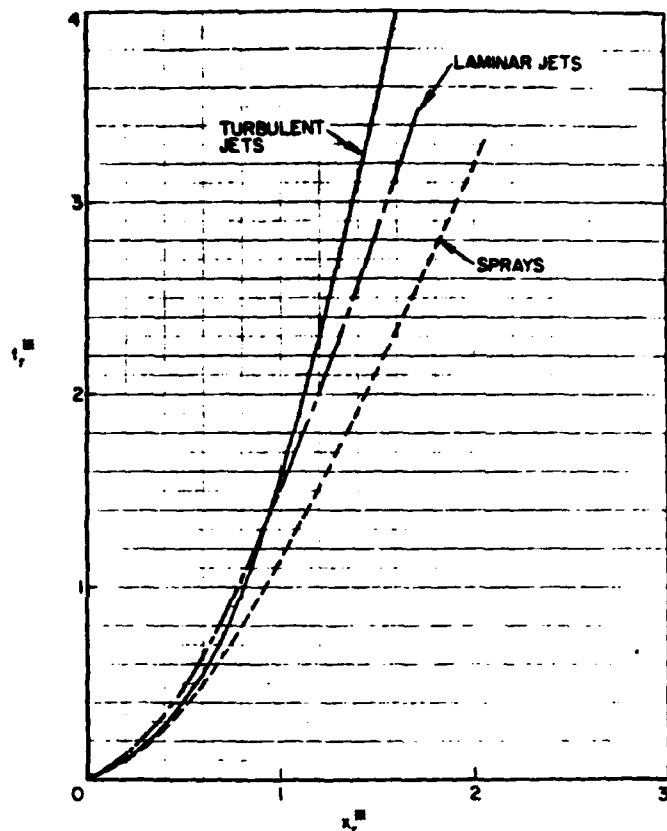


Fig. 25 - Reduced dimensionless steadying time versus reduced dimensionless steadying length using 99.9%  $u_{CL}$ , steady

the 99.9%  $u_{CL}$ , steady and 99.9% steady momentum positions are tracked (see Figures 25 and 26). This is particularly true for the difference between the gas jets and the spray. It means that even though one can determine a turbulent gas jet that has the same tip penetration rate as the spray (having identified the tip with the point at which the 70%  $u_{CL}$ , steady is first reached), between the tip and the orifice the two jets will have different axial distributions and the difference will change with time.

Finally, the radial distributions are in general different, if for no other reason, because the angles of the turbulent jet and of the spray are different. However, under certain conditions even the angles can be similar (see Figure 2).

#### SAMPLE APPLICATIONS

To help understand and use the curves of Figures 10, 14, and 22, that

are fitted by the equations of Table 5, a few examples are now given. Consider the non-vaporizing spray measured by Hiroyasu and Kadota in a gas pressure of 3.0 MPa (Case #2 of Table 3). How long does it take to the center of the head vortex to penetrate 2.5 cm? The quantities needed, and their values from Table 2 are:  $D = 0.03$  cm;  $\theta_1 = 5.7^\circ$ ;  $\rho_g = 0.0344$  g/cm<sup>3</sup>;  $\rho_l = 0.84$  g/cm<sup>3</sup>;  $B_T = 0.90$ ;  $U_{inj} = 9.03$  cm/ms. With these quantities we can compute the length scale  $d_{eff} = 1.3$  cm, and the time scale  $d_{eff}/U_{inj} = 0.144$  ms from the equations of Table 5. Since the given penetration is 2.5 cm, the dimensionless penetration is  $2.5/1.3 = 1.92$ . Entering Figure 22, or the corresponding curve fits, with  $x^* = 1.92$ , we read three values of  $t^*$ . Using the time scale of 0.144 ms, the three values of  $t$  become 0.72, 0.82, and 0.96 ms. The first is the arrival time at  $x = 2.5$  cm of the center of the head vortex. The second is the time for the axial velocity at  $x = 2.5$  cm to reach 99.9% of its steady state value, and for

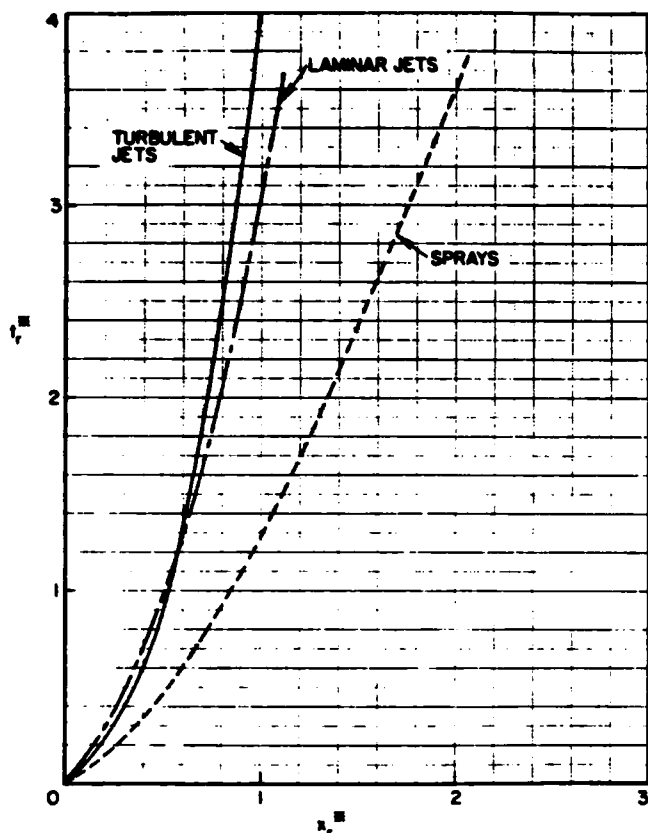


Fig. 26 - Reduced dimensionless steadying time versus reduced dimensionless steadying length using 99.9% steady momentum

the axial momentum to reach 85% of its steady value, and corresponds roughly to the back of the head vortex. The third is the time for the spray to reach complete steady state between the orifice and  $x = 2.5$  cm. Alternatively fixing the time at 0.72 ms, we read from Figure 22 that the center of the vortex is at 2.5 cm, the back of the vortex is at about 2.25 cm, and between the injector and location 2 cm, the spray is in complete steady state.

Now suppose we want to simulate the above non-vaporizing spray with an incompressible turbulent gas jet. We cannot have the two tips penetrate exactly at the same rate at all times but we can have them reach any one penetration depth at the same time (slightly different penetration depths will be reached at different times around the selected one but at times very different from the selected one, the depths of penetration will be quite different. Figure 24 can be used to quantify these trends). We select  $x = 2.5$  cm for the location at which we

want the two jets to arrive at the same time of  $t = 0.72$  ms. We again identify the tip of the gas jet with the center of its head vortex and use the correlation for 70%  $u_{CL, steady}$  (Equation 11), thus getting

$$(DRe_p^{0.053}) U_{inj} = 2.04 \text{ (cm}^2/\text{ms)} \quad (31)$$

Since we have one equation and four unknowns, there are many gas jets that satisfy the requirement. But if we want the gas to be injected in the same atmosphere as the spray we also select  $\rho_g = 0.0344 \text{ g/cm}^3$  and  $\mu_g = 210^{-4} \text{ g/cms}$ . We still have one more choice. We may impose that the mass flow rate of the two jets be equal

$$D^2 U_{inj} = 0.198 \text{ (cm}^3/\text{ms)} \quad (32)$$

No more constraints can be put on the gas jet but Equations 31 and 32 can be solved for its diameter and injection velocity:  $D=0.187\text{cm}$ ,  $U_{inj}=5.66\text{cm/ms}$ . Its Reynolds number turns out being  $1.8210^5$ . Figures 24, 25, and 26 could now be used to study the differences in the axial distributions of the two jets and how they change in time. Their radial distributions will be different, if for no other reason, because their angles are different. The angle of the spray is  $11.4^\circ$  and that of the turbulent gas jet about  $25^\circ$ . Thus, even though the mass flow rates are the same and axially the heads of the two jets penetrate at very similar rates around the 2.5 cm location (but at 4 cm the turbulence jet already arrives 15% later), radially the gas jet is thicker than the spray. But the angle of the spray changes with nozzle design and gas-liquid density ratio (Figure 2) and for appropriate conditions even the initial angles of the two jets could be similar.

#### CONCLUDING COMMENT

The main result of this work is the identification of the length, velocity, and time scales for the transient and steady state of incompressible laminar and turbulent jets and nonvaporizing and vaporizing sprays and of the steadying time functions for the three families of jets. The findings are summarized in Table 5. A few sample applications were then given including a discussion of similarities and differences of gas and spray jets and computations of jet tip penetration rates.

The information was obtained

through the numerical solution of model equations. The results were compared to measurements whenever possible. But the models are complex and the experimental information scant, particularly about transient jets. Thus a comment on the confidence that should be attached to the results is appropriate.

The model for incompressible laminar jets consists of the complete Navier-Stokes equations with laminar viscosity and includes no unknown, or even controversial, parameter. Thus we consider the given length, velocity, and time scales final. The steadying time functions depend on the velocity profile at the nozzle exit. The curve fits of Table 5 are for uniform velocity profiles. The curves were fitted to the results of many computations and small local inaccuracies are possible. However more extensive studies of the problem are expected to bring about only minor changes in the coefficients of the curve fits. For different exit velocity profiles, different steadying time functions exist but they will have to be determined with additional computations.

The model for incompressible turbulent jets includes the  $k-\epsilon$  submodel for turbulence diffusion that has only limited engineering validity. Nevertheless we consider the given length, velocity, and time scales quite accurate with the exception of the small exponent of  $Re_p$ , 0.053, that is likely to change somewhat as more information becomes available. Again the steadying time functions depend on the velocity profile at the nozzle exit, and, for turbulent jets, also on a variety of details of the experiment and measuring technique. The given curve fits are for uniform exit velocity profiles but their coefficients can be expected to change somewhat depending on the details of the specific application and as more information becomes available.

The model for thick sprays is the most recent and uncertain. So far it has predicted correctly difficult trends, and even magnitudes, but has undergone only limited tests. The proposed characteristic velocity scale is very likely to be the correct one. But the characteristic length,  $d_{eff}$ , must be considered a "theoretical" result to be tested further and possibly improved. The same applies to the spray steadying time functions.

Nevertheless, we expect our statements in the section on similarities and differences of laminar, turbulent, and spray jets to be correct. They are

based on the computed structures of the three jets that are both logical and realistic, as shown by comparisons with experimental data. In all, model uncertainties relate more to accuracy than to essential structural features.

#### NOMENCLATURE

$C_{DIS}$	Discharge coefficient of nozzle
$c_l$	Liquid specific heat
$c_{p_g}$	Gas specific heat at constant pressure
$c_{p_I}$	Inert species specific heat at constant pressure
$c_{p_v}$	Vapor species specific heat at constant pressure
$d_{eff}$	Effective orifice diameter
$D$	Nozzle orifice diameter
$D_t$	Turbulent eddy diffusivity
$E_{coal}$	Coalescence efficiency
$E_{12}$	Collision efficiency
$f$	Drop distribution function
$\underline{F}$	Drop acceleration (= $dv/dt$ )
$\underline{F}_a$	Aerodynamic drag on a drop
$G$	Turbulence generation expression, see Table 1
$h_g$	Gas enthalpy
$h_l$	Liquid enthalpy
$k$	Turbulence kinetic energy
$\lambda$	Turbulent eddy size
$L$	Length of calculation domain
$L$	Latent heat of vaporization



SYMBOL	DEFINITION	SYMBOL	DEFINITION
$Nu_g$	Gas phase Nusselt number	$u_{CL,0}$	Centerline axial velocity at jet exit plane
$Nu_l$	Liquid phase Nusselt number	$u_{CL, steady}$	Local, steady value of the centerline axial velocity
$p$	Pressure	$u_{CL,x}$	Centerline axial velocity at axial position $x$
$Pr$	Prandtl number	$U$	Jet exit velocity profile
$p_v$	Equilibrium vapor pressure	$\bar{U}$	Mean jet exit velocity
$P_{inj}$	Fuel injector upstream pressure	$U_e$	Coflow velocity
$P_{amb}$	Chamber gas pressure	$U_o$	Parcel injection velocity
$r$	Radial coordinate or drop radius	$U_{inj}$	Liquid injection velocity $= C_{Dis} \left[ \frac{2(P_{inj} - P_{amb})}{\rho_l} \right]^{1/2}$
$R$	Radius of calculation domain or drop radius change ( $= dr/dt$ )	$v$	Radial velocity component
$R$	Universal gas constant	$\underline{v}$	Drop velocity
$R_o$	Jet orifice radius	$W_I$	Inert species molecular weight
$Re_D$	Reynolds number based on the jet diameter and mean jet exit velocity $= \rho U \bar{D} / \mu_l$	$W_v$	Vapor species molecular weight
$S_i$	Source term of conservation equations	$We_i$	Jet Weber number $= \rho_g U_{inj}^2 D / \sigma_l$
$SMR_o$	Initial drop Sauter mean radius	$We$	Drop coalescence Weber number
$t$	Time	$x$	Coordinate in the direction of jet axis
$T_d$	Drop temperature	$\underline{x}$	Position in physical space
$\dot{T}_d$	Time rate of drop temperature change	$y$	Coordinate in the radial direction
$T_g$	Mean gas temperature	$Y_I$	Inert species mass fraction
$T_s$	Drop surface temperature	$Y_v$	Vapor species mass fraction
$T_{i, init}$	Temperature of injected liquid parcel	$Y_{vs}$	Drop surface vapor mass fraction
$u$	Axial component of velocity	$\theta$	Void fraction (mean gas volume fraction)
$\underline{u}_g$	Mean gas velocity	$\theta_o$	Gas volume fraction in the injection cell
$\underline{u}'_g$	Fluctuating component of gas velocity experienced by a drop	$\theta_{1/2}$	Spray half-angle
		$\mu_g$	Viscosity of gas

SYMBOL	DEFINITION
$\mu_l$	Viscosity of liquid
$\nu$	Kinematic viscosity or collision frequency
$\epsilon$	Rate of turbulent energy dissipation
$\delta$	Dirac delta function
$\lambda_g$	Gas heat conductivity
$\lambda_l$	Liquid heat conductivity
$\rho$	Density
$\rho_g$	Gas mass per unit gas volume
$\rho'_g$	Gas mass per unit mixture volume = $\theta \rho_g$
$\rho_l$	Liquid density
$c$	Transition probability function for collisions
$c_l$	Surface tension of liquid
$c_k$	Turbulent Prandtl number for $k$
$c_\epsilon$	Turbulent Prandtl number for $\epsilon$
$\tau$	Correlation time for fluctuating gas velocity along the path of a drop or turbulent stress tensor
$c$	General dependent variable of conservation equation
$z_p$	Effective injection pressure ( $P_{inj}$ - $P_{amb}$ )
$\Delta t$	Numerical time step
FRATE	Particle injection rate
<u>Subscript</u>	
$l$	Laminar or liquid
$o$	Jet exit plane
$t$	Turbulent
$in$	Initial value specified at jet exit plane
CL	Location on jet centerline
eff	Effective quantity
$r$	Reduced quantity

SYMBOL	DEFINITION
ref	Reference quantity
$s$	Averaged property over a drop's surface
<u>Superscript</u>	
-	Mean value
*	Dimensionless quantity

## ACKNOWLEDGEMENTS

Support for this work was provided by the Department of Energy, Contract EC-77-S-02-4192.A002, the Army Research Office DAAG29-78-G-0132, Volkswagenwerk, FIAT, General Motors, and Komatsu.

## REFERENCES

1. Kuo, T.W. and Bracco, F.V., "Computations of Drop Sizes in Pulsating Sprays and of Liquid-core Length in Vaporizing Sprays." SAE Congress, 1982.
2. Rizk, W., "Experimental Studies of the Mixing Processes and Flow Configurations in Two-Cycle Engine Scavenging," Proc. of I. Mech. E., Vol. 172, 1958, p. 417.
3. Reitz, R.D., "Atomization and Other Breakup Regimes of a Liquid Jet," Department of Mechanical and Aerospace Engineering, Princeton University, Ph.D. Thesis #1375-T, May 1978.
4. Hengrussamee, D., Ma, A.S.C., and Ong, K.S., "Numerical Integration Techniques for an Impulsively Starting Incompressible Jet," Numerical Methods in Fluids Dynamics, Proceedings of the International Conference, Univ. of Southampton, England, 1973, p. 121.
5. Witze, P.O., "The Impulsively Started Incompressible Turbulent Jet," SAND 80-8617, 1980.
6. Abramovich, S. and Solan, A., "The Initial Development of a Submerged Round Jet," J. Fluid Mech., Vol. 59, 1973, p. 791.
7. Kuo, T.W., "On the Scaling of Transient Laminar, Turbulent, and Spray Jets," Department of Mechanical and Aerospace Engineering, Princeton University, Ph.D. Thesis #1538-T, 1981.
8. Gosman, A.D., Ideriah, F.J.K., "Teach-3P, A General Computer Program for Two-Dimensional, Turbulent, Recirculating Flows," Department of

Mechanical Engineering, Imperial College, London, 1976.

9. duPless, M.P., Wang, R.L. and Tsang, S., "Development of a Submerged Round Laminar Jet from an Initially Parabolic Profile," *Trans. ASME, J. Dynam. Sys. Meas. and Control*, 95, 1973, p. 155.
10. Andrade, E.N. and Tsien, H.S., "The Velocity Distribution in a Liquid into Liquid Jet," *Proc. Phys. Soc.* 49, 1973, p. 95.
11. Pai, S.I. and Hsieh, T., "Numerical Solution of Laminar Jet Mixing with and without the Free Stream" *Appl. Scientific Research*, 27, 1972, p. 39.
12. Hatta, K. and Nozaki, T., "Two Dimensional and Axisymmetric Jet Flows with Finite Initial Cross Sections," *Bull. Japan Soc. Mech. Engrs.*, 16, 1975, p. 349.
13. Launder, B.E., Spalding, D.B., "The Numerical Computation of Turbulent Flows," *Comput. Method Appl. Mech. Eng.*, Vol. 3, 1974, p. 269.
14. Khalil, E.E., Spalding, D.B., Whitelaw, J.H., "The Calculation of Local Flow Properties in Two-Dimensional Furnace," *J. Heat Mass Transfer*, Vol. 18, 1975, p. 775.
15. Patankar, S.V., "Numerical Prediction of Three-Dimensional Flows," *Studies in Convection-Theory, Measurement and Application*, Launder, B.E. (editor), Academic Press, 1975.
16. Dedeoglu, N., "Scavenging Model Solves Problems in Gas Burning Engine," *SAE Transactions*, 710579, 1971, p. 1930.
17. Borman, G.L. and Johnson, J.H., "Unsteady Vaporization History and Trajectories of Fuel Drops Injected into Swirling Air," *SAE Paper 598C*, 1962.
18. Taylor, D.H. and Walsham, B.E., "Combustion Processes in a Medium Speed Diesel Engine," *Symposium on Diesel Engine Combustion*, *Proc. 1. Mech. E.*, London, Part 3, 1967, p. 1970.
19. O'Rourke, P.J. and Bracco, F.V., "Modeling of Drop Interactions in Thick Sprays and a Comparison with Experiments," *Stratified Charge Automotive Engines Conference*, The Institution of Mechanical Engineers, 1930.
20. Williams, F.A., "Progress in Spray-Combustion Analysis," *Eighth International Symposium on Combustion*, Williams and Wilkins Co., Baltimore, MD, 1962, p. 50.
21. O'Rourke, P.J., "Collective Drop Effects in Vaporizing Liquid Sprays,"

Department of Mechanical and Aerospace Engineering, Princeton University, Ph.D. Thesis #1532-T, August 1981.

22. Schlichting, H., "Boundary Layer Theory," 6th ed., McGraw-Hill, 1968.
23. Dukowicz, J.K., "A Particle-Fluid Numerical Model for Liquid Sprays," *J. Comp. Phys.*, Vol. 35, 1980, p. 229.
24. Bergwerk, W., "Flow Pattern in Diesel Nozzle Spray Holes," *Proceedings of the Inst. of Mech. Engineers*, Vol. 173, 1959, p. 655.
25. Reitz, R.D. and Bracco, F.V., "On the Dependence of Spray Angle and Other Spray Parameters on Nozzle Design and Operating Conditions," *SAE Paper 790494*, 1979.
26. Hiroyasu, H. and Kadota, T., "Fuel Droplet Size Distribution in Diesel Combustion Chamber," *SAE Paper 740715*, 1974.
27. Groeneweg, J.F., El-Wakil, M.M., Myers, P.S., and Uyehara, O.A., "The Role of Drop Velocity in Statistical Spray Description," *First International Conference on Liquid Atomization and Spray Systems*, Tokyo, 1978.
28. Witze, P.O., "A Generalized Theory for the Turbulent Mixing of Axially Symmetric Compressible Free Jets," *Fluid Mechanics of Mixing*, Joint Meeting of the Fluid Engineering Division and the Applied Mechanics Division, ASME, 1973.
29. Schweitzer, P.H., "Penetration of Oil Sprays," *Pennsylvania State College Bulletin No. 46*, 1937.
30. Lyshevskiy, A.S., "The Coefficient of Free Turbulence in a Jet of Atomized Liquid Fuel," *NASA TT-F351*, 1956.
31. Wakuri, Y., Fujii, M., Amitani, T., and Tsuneya, R., "Studies of the Penetration of a Fuel Spray in a Diesel Engine," *Bull. J.S.M.E.*, Vol. 3, 1960, p. 123.
32. Sitkei, G., "Kraftstoffaufbereitung und Verbrennung bei Diesel Motoren," *Springer-Verlag*, 1964.
33. Parks, M., Polonski, C., and Toye, R., "Penetration of Diesel Fuel Sprays in Gases," *SAE Paper 660747*, 1966.
34. Hakki Oz, I., "Calculation of Spray Penetration in Diesel Engines," *SAE Paper 690254*, 1969.
35. Taylor, D.H., and Walsham, B.E., "Combustion Process in a Medium Speed Diesel Engine," *Diesel Engine Combustion*, *Proc. Instn. Mech. Engrs.*,

Vol. 184, Part 3J, 1970, p. 67.

36. Dent, J.C., "A Basis for the Comparison of Various Experimental Methods for Studying Spray Penetration," SAE Transactions, Vol. 80, 1971.

37. Williams, T.J., "Parameters for Correlation of Penetration Results for Diesel Fuel Sprays," Combustion Engine Group, Proc. Instn. Mech. Engrs., Vol. 187, 1973, p. 771.

38. Chiu, W.S., Shahed, S.M., and Lyn, W.T., "A Transient Spray Mixing Model for Diesel Combustion," SAE Paper 760128, 1976.

39. Hiroyasu, H., Kadota, T., and Arai, M., "Supplementary Comments: Fuel Spray Characterization in Diesel Engines," Proc. of the Symp. on Combustion Modeling in Reciprocating Engines, GMR, Michigan, 1978.

This paper is subject to revision. Statements and opinions advanced in papers or discussion are the author's and are his responsibility, not SAE's; however, the paper has been edited by SAE for uniform styling and format. Discussion will be printed with the paper if it is published in SAE Transactions. For permission to publish this paper in full or in part, contact the SAE Publications Division.

Persons wishing to submit papers to be considered for presentation or publication through SAE should send the manuscript or a 300 word abstract of a proposed manuscript to: Secretary, Engineering Activity Board, SAE.

Printed in U.S.A.

APPENDIX G

COMPUTATIONS OF DROP SIZES  
IN PULSATING SPRAYS AND OF  
LIQUID CORE LENGTH IN VAPORIZING SPRAYS

T.-W. Kuo and F.V. Bracco

# SAE Technical Paper Series

820133

## Computations of Drop Sizes in Pulsating Sprays and of Liquid-Core Length in Vaporizing Sprays

**T.-W. Kuo and F. V. Bracco**

Dept. of Mechanical and Aerospace Engrg.  
Princeton Univ.  
Princeton, NJ

International Congress  
& Exposition  
Detroit, Michigan  
February 22-26, 1982

The appearance of the code at the bottom of the first page of this paper indicates SAE's consent that copies of the paper may be made for personal or internal use, or for the personal or internal use of specific clients. This consent is given on the condition, however, that the copier pay the stated per article copy fee through the Copyright Clearance Center, Inc., Operations Center, 21 Congress St., Salem, MA 01970 for copying beyond that permitted by Sections 107 or 108 of the U.S. Copyright Law. This consent does not extend to other kinds of copying such as copying for general distribution, for advertising or promotional purposes, for creating new collective works, or for resale.

Papers published prior to 1978 may also be copied at a per paper fee of \$2.50 under the above stated conditions.

SAE routinely stocks printed papers for a period of three years following date of publication. Direct your orders to SAE Order Department.

To obtain quantity reprint rates, permission to reprint a technical paper or permission to use copyrighted SAE publications in other works, contact the SAE Publications Division.



# Computations of Drop Sizes in Pulsating Sprays and of Liquid-Core Length in Vaporizing Sprays

T.-W. Kuo and F. V. Bracco

Dept. of Mechanical and Aerospace Engrg.  
Princeton Univ.  
Princeton, NJ

TWO STUDIES ARE REPORTED THAT ARE CONNECTED only in that the same model for thick spray was used in both and their conclusions may be significant for applications to direct-injection stratified-charge and Diesel engines.

The first study concerns the effect of pulsating injection on the penetration rate and the downstream drop size. Hiroyasu and Kadota (1)\* measured downstream drop sizes using various numbers of injection pulses about 3 ms in duration and reported an increase in the drop size with increasing number of pulses. We made

\*Numbers in parentheses designate References at end of paper.

computations for their injections and sought to understand the reason for the observed trend.

The second study regards the longstanding question of the presence or absence of liquid drops in the combustion chamber of Diesel engines and of direct-injection stratified-charge engines (today more popular under the name of ignition-assisted Diesel engines). Thus Lyn, Shahed and coworkers (2,3) have always treated the injected fuel as gaseous jets whereas the Wisconsin group (4,5) has concentrated on drop and spray effects. In spite of the apparent contradiction, according to our computations, both groups may in fact have been right.

## ABSTRACT

Computations are reported of transient axisymmetric pulsating and evaporating sprays that account also for drop collisions and coalescence. It is found that, for the same upstream and gas conditions, pulsating injections result in smaller drops than continuous injections. The difference is particularly marked at high gas densities and is due to the inhibition of collisions and coalesce of drops generated by the gas gap in between the pulses. However, the tip penetration rates are not markedly different for continuous and pulsating injections. For transient evaporating sprays it is found that all drops except the largest

evaporate within a well defined distance from the injector. Beyond this distance only vaporized liquid and entrained gas continue the penetration. For engine applications the length of the liquid core is found to be of the order of centimeters and sensitive to conditions. In particular it decreases with increasing injection pressure, gas temperature, and gas density. The sensitivity of the liquid core length to conditions may explain the different importance attached by different authors to the liquid phase in direct injection stratified-charge and Diesel engines.

Only small differences in conditions would separate the two limits.

The paper is organized as follows. The main features of the model used in the computations are summarized first. The description is of necessity concise, but some details are available in Reference 6 and considerable information in References 7 and 8. The results of the pulsating spray computations are discussed next in specific comparisons with the data of Hiroyasu and Kadota. They were for nonvaporizing sprays. In the next section, the results are reported of a

study in which gas conditions similar to those that may be found in Diesel engines were selected and a parametric study undertaken of the length of the liquid core and its sensitivity to various parameters.

#### THE MODEL

The equations of the model for the transient and steady state of nonevaporating and evaporating thick sprays are those of O'Rourke and Bracco (6). They are:

#### Spray Equation

$$\frac{\partial f}{\partial t} + \nabla_{\underline{x}} \cdot (f \underline{v}) + \nabla_{\underline{v}} \cdot (f \underline{v}) + \frac{\partial}{\partial r} (f R) + \frac{\partial}{\partial T_d} (f T_d) =$$

$$1/2 \iint f(\underline{x}, \underline{v}_1, r_1, T_{d1}, t) f(\underline{x}, \underline{v}_2, r_2, T_{d2}, t)$$

$$v(r_1 + r_2)^2 |v_1 - v_2| R_{12}(\underline{x}, \underline{v}_1, r_1, \underline{v}_2, r_2, t)$$

$$[\sigma(\underline{v}, r, T_d, \underline{v}_1, r_1, T_{d1}, \underline{v}_2, r_2, T_{d2}, \underline{x}, t)$$

$$- \delta(r - r_1) \delta(\underline{v} - \underline{v}_1) \delta(T_d - T_{d1})$$

$$- \delta(r - r_2) \delta(\underline{v} - \underline{v}_2) \delta(T_d - T_{d2})]$$

$$dr_1 d\underline{v}_1 dT_{d1} dr_2 d\underline{v}_2 dT_{d2} \quad (1)$$

#### Gas Phase Mass Equation

$$\frac{\partial \rho}{\partial t} + \nabla \cdot (\rho \underline{u}) = - \iiint 4\pi r^2 R \rho_L f dr d\underline{v} dT_d \quad (2)$$

#### Vapor Mass Equation

$$\frac{\partial \rho' Y_v}{\partial t} + \nabla \cdot (\rho' Y_v \underline{u}) =$$

$$- \iiint 4\pi r^2 R \rho_L f dr d\underline{v} dT_d + \nabla \cdot [\rho' D_t \nabla Y_v] \quad (3)$$

#### Gas Phase Momentum Equation

$$\frac{\partial \rho' \underline{u}}{\partial t} + \nabla \cdot (\rho' \underline{u} \underline{u}) + \nabla(p_g) =$$

$$- \iiint [4\pi r^2 R \underline{v} + \frac{4}{3} \pi r^3 \underline{f}] \rho_L f dr d\underline{v} dT_d + \nabla \cdot \underline{\tau}_t \quad (4)$$

$$\text{where } \underline{\tau}_t = \rho' D_t [\nabla \underline{u} + \nabla \underline{u}^T - \frac{2}{3} \nabla \cdot \underline{u} \underline{I}]$$

#### Gas Phase Energy Equation

$$\frac{\partial \rho' h}{\partial t} + \nabla \cdot (\rho' h \underline{u}) = 0 \left( \frac{\partial p}{\partial t} + \underline{u} \cdot \nabla p_g \right)$$

$$- \iiint f \rho_L [4\pi r^2 R (h_g(T_d) + \frac{1}{2} (\underline{v} - \underline{u})^2)$$

$$+ \frac{4}{3} \pi r^3 (F_A (\underline{v} - \underline{u}) + c_L T_d)] dr d\underline{v} dT_d$$

$$+ \underline{\tau}_t : \nabla \underline{u} + \nabla \cdot [\rho' c_p D_t \nabla T_g] \quad (5)$$

#### Equations Determining Exchange Rates

$$- \rho_L R = \frac{\lambda_L}{c_{p_g}} \cdot \frac{Nu_g Y_{v_g} - Y_v}{2r (1 - Y_{v_g})} \quad (6a)$$

$$- \rho_L R = \frac{\lambda_L}{c_{p_g}} \frac{Nu_L}{2r} \left\{ \frac{c_{p_g}}{h(T_g)} \left[ (T_g - T_s) - \frac{Nu_L \lambda_L}{Nu_g \lambda_g} (T_s - T_d) \right] \right\} \quad (6b)$$

$$\frac{\frac{Y_{v_g}}{Y_v} + \frac{Y_{L_g}}{Y_L}}{\frac{Y_{v_g}}{Y_v} + \frac{Y_{L_g}}{Y_L}} = \frac{p_v(T_g)}{p_g} \quad (6c)$$

$$\dot{T}_d = \frac{3}{2} \frac{\lambda_d}{\rho_d c_d r^2} \kappa_{d1} (T_g - T_d) + 3(R/r) (T_g - T_d) \quad (6d)$$

$$\underline{F} = \frac{3}{8} \frac{\rho_g}{\rho_d} \frac{|u_g + u'_g - v|}{r} (u_g + u'_g - v) c_D$$

$$-\frac{1}{\rho_d} \nabla p_g = \underline{F}_a - \frac{1}{\rho_d} \nabla p_g \quad (6e)$$

Equations of State

$$p_g = \rho_g R T_g \left( \frac{Y_v}{W_v} + \frac{Y_I}{W_I} \right) \quad (7a)$$

$$h_g = (c_{p_v} Y_v + c_{p_I} Y_I) T_g = c_{p_g} T_g \quad (7b)$$

$$h_d(T_d) = c_{p_v} T_d - L(T_d) \quad (7c)$$

$$L(T_d) = L_{ref} + (c_{p_v} - c_{p_l})(T_d - T_{ref}) \quad (7d)$$

Equation 1 is the traditional spray equation (9) plus two new terms that account for the heating of drops and for drop collisions and coalescence. The term  $\partial(f\dot{T}_d)/\partial T_d$  was tested for the first time in the present study and accounts for the effects of unsteady drop heating and a distribution of drop temperatures. The integral on the right hand side accounts for the effects of drop collisions. The collision efficiency  $E_{12}$ , which has been demonstrated by O'Rourke and Bracco to have essentially a value of 1 in the present application, modifies the following collision frequency between drops having velocities, sizes and temperatures in the implied range:

$$f(\underline{x}, \underline{v}_1, r_1, T_{d1}, t) f(\underline{x}, \underline{v}_2, r_2, T_{d2}, t) \\ \pi(r_1 + r_2)^2 |\underline{v}_1 - \underline{v}_2| \\ d\underline{v}_1 dr_1 dT_{d1} d\underline{v}_2 dr_2 dT_{d2}$$

The portion of the integrand within the brackets gives the sources (given by the transition probability function,  $\sigma$ ) and the sinks (given by the delta functions,  $\delta$ ) of drops of velocity  $\underline{v}$ , radius  $r$ , and temperature  $T_d$ , due to collisions between drops with subscript 1 properties and those with subscript 2

properties. The transition probability function gives the outcome of a collision and has a complicated mathematical expression (7). Physically, it determines whether the outcome of a collision is coalescence or separation. The criterion for drop separation after collision is that the rotational energy of the coalesced drop pair exceeds the surface energy required to reform the original drops from the coalesced pair. For the coalescence efficiency,  $E_{coal}$ , which is the probability of coalescence given that collision has occurred, O'Rourke and Bracco give the expression

$$E_{coal} = \min(2.4 f^* \left(\frac{r_2}{r_1}\right) \frac{1}{We}, 1.0) \quad (8)$$

$$\text{where } We = \frac{\rho_l |\underline{v}_1 - \underline{v}_2|^2 r_1}{\sigma_l}, \quad r_1 \leq r_2$$

and  $\sigma_l$  is the surface tension coefficient. The function  $f^*$

$$f^* \left(\frac{r_2}{r_1}\right) = \left(\frac{r_2}{r_1}\right)^3 - 2.4 \left(\frac{r_2}{r_1}\right)^2 + 2.7 \left(\frac{r_2}{r_1}\right) \quad (9)$$

has the value of 1.3 for  $r_2/r_1 = 1$  and 3.8 for  $r_2/r_1 = 2$ , and behaves as  $(r_2/r_1)^3$  when  $r_2/r_1$  approaches infinity. The process of drop re-separation (called grazing collision by O'Rourke and Bracco) is important. Without it, that is if all collisions are assumed to result in coalescences, unphysically large drops result (7).

In the gas phase mass, momentum and energy conservation equations, the integrals on the right-hand sides represent the exchange functions. They are the sum over all drops at point  $\underline{x}$  and time  $t$  of the rate of mass, momentum, and energy exchanges between each drop and the gas; thus they involve the rate of drop radius change  $R$ , velocity change  $\underline{F}$ , and temperature change  $\dot{T}_d$ .

The rate of drop radius change  $R$  is found by solving equations (6a)-(6c) simultaneously for the unknown drop surface temperature  $T_g$ , surface vapor mass fraction  $Y_{v_g}$ , and  $R$ . After  $R$  and  $T_g$  are found, the rate of drop temperature change  $\dot{T}_d$  is obtained from (6d). The drop acceleration  $\underline{F}$ , given by equation (6e), has two contributions: one due to aerodynamic

drag  $F_a$  and the other due to the mean pressure gradient which has been shown to be important in some applications by O'Rourke (7). In Equations (6a)-(6e), there are three unknown functions; the drag coefficient  $C_D$ , and the gas and liquid phase Nusselt numbers,  $Nu_g$  and  $Nu_L$ , respectively. After a detailed survey of experimental and theoretical studies of fluidized beds, heat transfer in regular arrays of spheres, and packed beds, O'Rourke proposed the following correlations to account for the effect of the gas volume fraction,  $\theta$ ,

$$C_D(\theta, Re) = \frac{24}{Re} \left( \theta^{-2.65} + \frac{Re^{2/3}}{6} \theta^{-1.78} \right) \quad (10)$$

$$Nu_g = \left[ 2\theta^{-1.75} + 0.6 \left( \frac{Re}{6} \right)^{1/2} Pr^{1/3} \right] \frac{\ln(1+B)}{B} \quad (11)$$

$$\text{where } B = \frac{Y_v - Y_{v,s}}{1 - Y_{v,s}} \text{ is the transfer number.}$$

Equations (10) and (11) were used in the present non-evaporating and evaporating studies with the  $Nu_L = 1$  and  $Pr = 0.7$ .

The effect of turbulence on the gas phase are accounted for by the terms involving  $D_t$  in Eq. (3)-(5), where  $D_t$  is the turbulent diffusivity, and was assumed to be equal to that of turbulent gas jets and related to the kinematic momentum (10)

$$D_t = 0.0161 \left( \frac{\pi D^2}{4} U_{inj}^2 \right)^{1/2} \quad (12)$$

The turbulence effects on the drops are calculated by adding to the mean gas velocity,  $u_g$ , a fluctuating component,  $u'_g$ , when computing the aerodynamic drag force  $F_a$  and the gas phase Nusselt number  $Nu_g$ .  $u'_g$  is chosen randomly from an isotropic Gaussian distribution with mean square deviation  $2/3k$ , where  $k$  is the turbulence kinetic energy and is assumed to be a fixed fraction ( $C = 0.20$ ) of the local mean flow kinetic energy, as is the case, approximately, in the downstream part of steady gaseous jets

$$k = C \frac{3}{2} u_g^2 \quad (13)$$

For each drop, after a turbulent correlation time  $\tau_t$ , a new value of  $u'_g$  is chosen. Dukowicz (11) took this correlation time to be constant. O'Rourke (7) took  $\tau_t$  to be the residence time of a drop in a turbulent eddy of size  $\ell$  found from

$$D_t = C_\ell k^{1/2} \ell \quad (14)$$

with the optimized constant  $C_\ell = 0.045$ .  $\tau_t$  is then given by

$$\ell = \int_t^{t+\tau_t} |v(t') - u_g(t')| dt' \quad (15)$$

where  $u_g(t')$  is the mean gas velocity at the drop position at time  $t'$ .

A detailed derivation and discussion of the equations of the thick-spray model is given in Reference 7.

The axisymmetric transient motion of a liquid spray is computed from the beginning of the thick spray regime to a downstream region where the spray is very thin. The computational mesh used is shown in Fig. 1. For all the cases studied, the cells were smallest near the nozzle exit, where  $\Delta r = 0.05$  cm and  $\Delta x = 0.1$  cm. Away from the nozzle exit, the size of the cells increased in both the axial and radial direction with corresponding expansion factors of 4% and 7%. A total of 44 cells in the axial direction and 26 cells in the radial direction were used, giving the computational domain a length of 9.5 cm and width of 3.2 cm.

The top and right boundaries were treated as open boundaries, the left boundary as a solid wall and drops and gas injected from the cell of the left boundary next to the axis of symmetry. The condition on the top boundary allows for free entrainment from the surroundings. The pressure at the top and right boundary were assumed to be uniform and equal to the ambient value to simulate the free spray conditions.

All the computations were initiated at that axial location of the spray where the initial gas volume fraction,  $\theta_0$ , is approximately 0.9. Gas and liquid were injected with equal axial velocity  $U_0$ , computed by using conservation of momentum, that is somewhat lower than the liquid injection velocity,  $U_{inj}$ , in turn calculated with a discharge coefficient,  $C_{D1s}$ , estimated from the

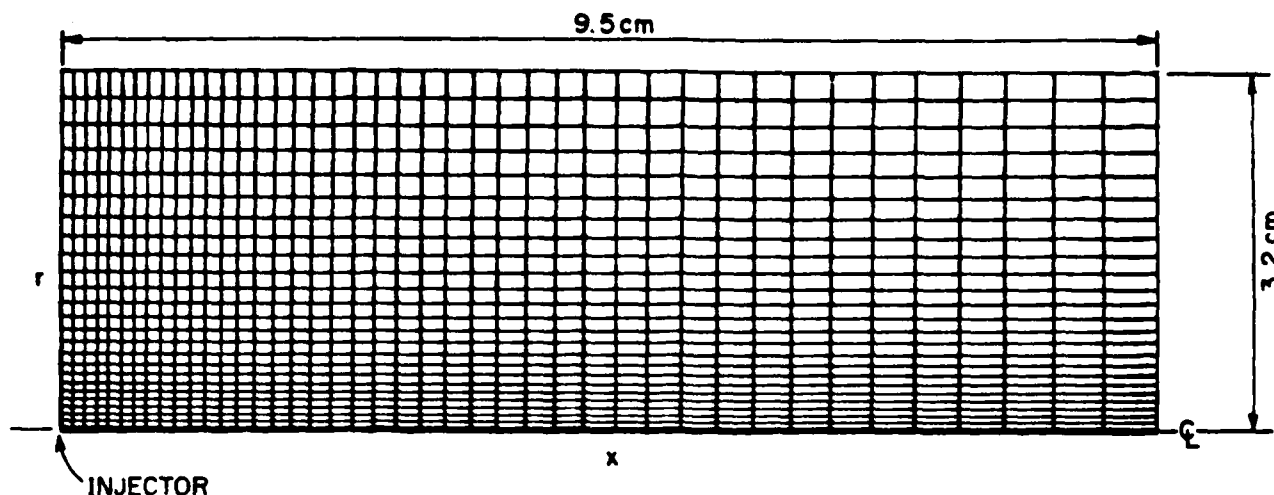


Fig. 1 - Computation domain

experimental data of Bergwerk (12). The procedure to compute  $U_0$  was explained by O'Rourke and Bracco (6). The initial spray angle and mean size of the drops was computed using correlations proposed by Reitz and Bracco (13) for the atomization process. They were able to show that under the condition of

$(\rho_l/\rho_g)(Re_l/We_l)^2 \gg 1$ , the measured initial spray half angle,  $\theta_i$ , is correlated well by

$$\tan \theta_i = \frac{1}{C_\theta} [4\pi(\sigma_l/\rho_l)^{1/2} \frac{\sqrt{3}}{6}] \quad (16)$$

where the proportionality constant,  $C_\theta$ , depends on the geometry of the nozzle. For example, for straight round holes,  $C_\theta$  increases when the length-to-diameter ratio of the nozzle increases. Reitz and Bracco argued that the corresponding initial mean drop size should be correlated by

$$SMR_0 = B[4\pi(\sigma_l/\rho_l)^{1/2} U_{inj}^2 \frac{3}{2}] \quad (17)$$

where the constant  $B$  is independent of the nozzle geometry and of order one, but no experimental verification of Equation 17 has yet been provided. Note that in this expression, the initial mean drop size  $SMR_0$  is predicted to decrease when the chamber gas density increases. However the computed downstream mean drop size is found to increase with increasing gas density due to collisions and recombination (6) and in agreement with the measurements of Hiroyasu and Kadota (1).

The computer code LDEF(Lagrangian Drop-Eulerian Fluid)

developed by O'Rourke (7) was employed for the present study with some modifications. This code incorporates the basic methodology of the stochastic parcel method of Dukowicz (11) as well as additional features added by O'Rourke to improve its accuracy and extend its applicability. Typical examples are: compressibility effects were included by a modified form of the ICE technique, the momenta equations were cast in conservation form, and the swirl velocity equations were added for the liquid and gas. Use of the ICE method obviates the need to observe the Courant sound speed restriction on the size of the computational time step. Detailed description of the iteration procedure used in the code and the momentum exchange calculation are given in Reference 7.

The modifications we have made to O'Rourke's code for the present study include: 1) a numerically more efficient grazing collision calculation procedure; 2) a new implicit iteration scheme to compute the time advanced liquid parcel temperature for evaporating sprays; 3) gravitational acceleration in the computation of the liquid parcel velocity; 4) and algorithm for the evaluation of the drop velocity distribution function and the axial distribution of mean drop size. More information on these modifications and other spray computations can be found in Reference 8.

In Figure 2 drop parcels and gas velocity plots of a typical computation are seen at three times during the transient. In Figure 3 typical gas temperature and fuel vapor contours inside the jet are shown for a vaporizing spray. In general,

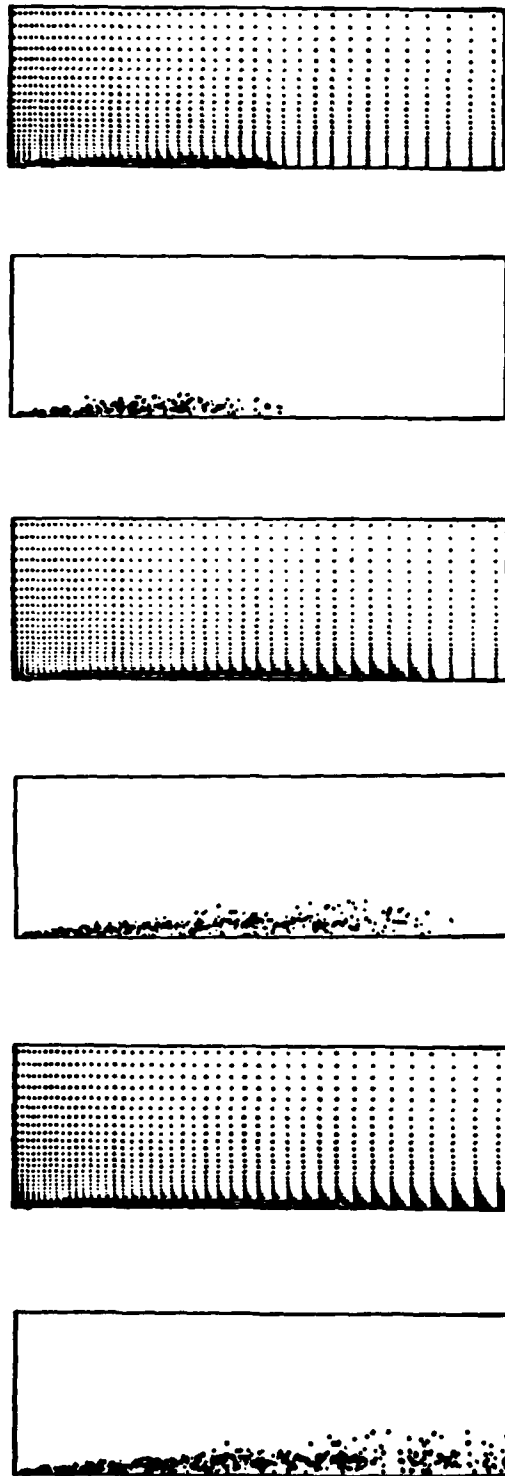


Fig. 2 - Some typical results of a computation: drop parcel and gas velocity maps

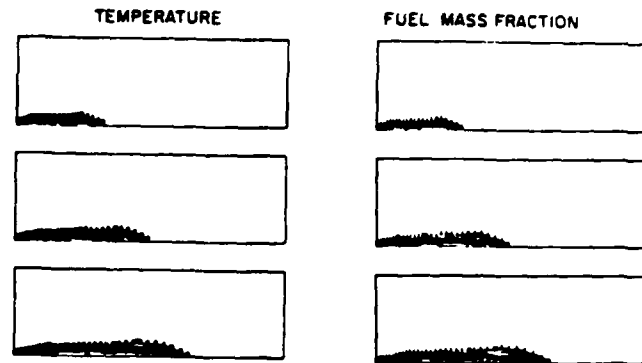


Fig. 3 - Typical computed gas temperature and vaporized fuel mass fraction inside a vaporizing spray

any function of the dependent variables can be evaluated, plotted, and studied.

#### PULSATING SPRAY COMPUTATIONS

In Figure 4 computed tip penetration rates are compared with those measured by Hiroyasu and Kadota at the three different gas (nitrogen) pressures of 1.1, 3.0, and 5.0 MPa. They used Diesel-type fuel and injection system and a single straight-hole nozzle 300  $\mu\text{m}$  in diameter and 6.67 in length-to-diameter ratio. Since their experiment was at room temperature the gas density also changed. The computed results are of Cases #1, 2, 3 of Table 1 where more information is given about the conditions of the various cases. In the computations the tip of the spray was identified with the location at which the instantaneous, axial, center-line velocity reaches 70% of its steady state value. It corresponds roughly to the center of the head vortex. The reason for this choice is explained in Reference 8. All computations were made with the same model constants.

For each case, the tip penetration result of Fig. 4 is the ensemble average of five different computations each with different random number sequences. The agreement is seen to be good. The computed and measured downstream drop size distribution functions and corresponding Sauter mean radii for the three cases are shown in Fig. 5, in the coordinates of the incremental volume fraction,  $1/V_T dV(r)/dr$ , versus drop radius,  $r$ .

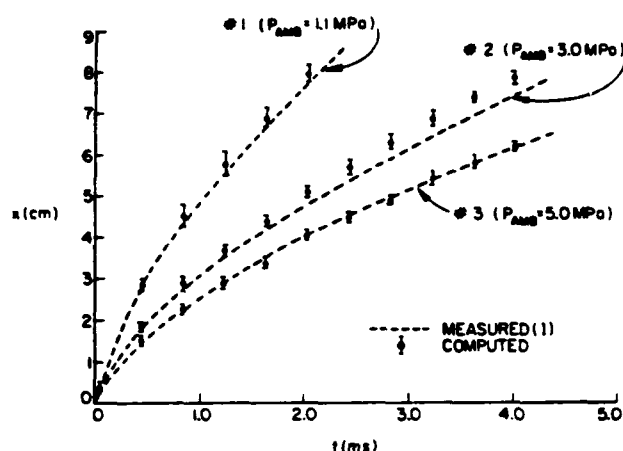


Fig. 4 - Tip penetration rates, computed with continuous injection, compared with those measured by Hiroyasu and Kadota (1)

It is observed that the agreement is not good for the high ambient pressure (5.0 MPa) in which the computations predict larger drops than measured. However, on one trend the computed and measured downstream drop size do agree: when the chamber pressure increases, the downstream Sauter mean radius also increases.

This is in spite of the fact that in the computations when the gas density increases the size of the injected drops decreases (See Table 1), since the injected drops are considered the outcome of the liquid jet atomization process and their maximum angle and mean radius are computed with Equations

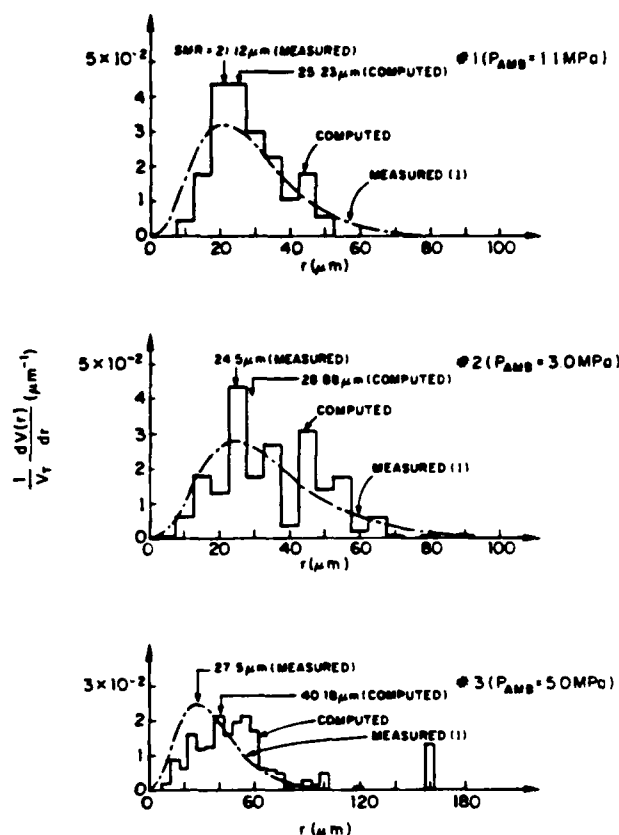


Fig. 5 - Downstream drop size distributions, computed with continuous injection, compared with those measured by Hiroyasu and Kadota (1)

Table 1 - Input Parameters of Computations

CASE #	P <sub>inj</sub> MPa	P <sub>amb</sub> MPa	C <sub>DIS</sub>	U <sub>inj</sub> cm/ms	U <sub>o</sub> cm/ms	θ <sub>o</sub>	SMR <sub>o</sub> μm	θ <sub>1/2</sub> Rad	l/d	D <sub>t</sub> cm <sup>2</sup> /ms	P <sub>RATE</sub> ms <sup>-1</sup>	δt μs	D cm	T <sub>g</sub> K	ρ <sub>g</sub> g/cm <sup>3</sup>	T <sub>l</sub> K	ρ <sub>l</sub> g/cm <sup>3</sup>
1	9.9	1.1	0.7	10.2	8.92	0.9	3	.0785	6.67	.0043	900	0.5	0.03	300	.0126	300	0.84
2	9.9	3.0	0.7	9.03	6.91	0.88	1.5	.0993	6.67	.0039	900	0.5	0.03	300	.0344	300	0.84
3	9.9	5.0	0.8	8.64	5.92	0.87	1.2	.1220	6.67	.0037	900	0.5	0.03	300	.0577	300	0.84

	CR	BTDC deg	C <sub>DIS</sub>	U <sub>inj</sub> cm/ms	Δp psi	l/d	SMR <sub>o</sub> μm	θ <sub>1/2</sub> Rad	γ	ρ <sub>init</sub> g/cm <sup>3</sup>	T <sub>init</sub> K	P <sub>init</sub> atm	D cm	T <sub>g</sub> K	ρ <sub>g</sub> g/cm <sup>3</sup>	T <sub>l</sub> K	ρ <sub>l</sub> g/cm <sup>3</sup>	T <sub>l,b</sub> K
4	20	30	.65	16.2	4000	4.0	1.8	.0698	1.4	.0012	360	1.0	0.02	860	.0077	300	0.84	500
5	20	30	.65	14.4	3000	4.0	2.5	.0698	1.4	.0012	360	1.0	0.02	860	.0077	300	0.84	500
6	20	30	.65	14.4	3000	4.0	1.6	.0924	1.4	.0014	360	1.5	0.02	860	.0131	300	0.84	500
7	19.2	20	.65	16.2	4000	4.0	0.9	.1045	1.4	.0013	300	1.1	0.02	700	.0164	300	0.84	500
8	19.2	20	.65	16.2	4000	4.0	0.9	.1045	1.4	.0013	300	1.1	0.02	550	.0164	300	0.84	500
9	20	20	.65	14.4	3000	4.0	1.6	.0900	1.4	.0012	360	1.0	0.02	994	.0125	300	0.84	500

16 and 17. But the initial drops collide and recombine within the spray as they move downstream. The collision frequency increases with drop number density and relative velocity and the coalescence efficiency increases with decreasing drop size and relative velocity. When the gas density increases, the initial drop number density increases and the drop size decreases, both resulting in higher collision frequencies and recombination rates. The decrease in drop relative velocity reduces the collision frequency (as  $\Delta v$ ) but increases the coalescence efficiency more markedly (as  $(\Delta v)^2$ , see Equation 8). Thus the net effect of increasing the gas density is a strong increase in the coalesce of drops. Coalesce occurs mostly near the injector and tapers off rapidly downstream as the spray fans out. In Figure 6, the Sauter mean radius of the cross-section drops is shown versus the distance from the injector for the three sprays after they have reached their respective steady states within the first 9 cm from the injector. The initial rapid growth and subsequent leveling off of the mean radius is evidenced.

To understand the possible cause of the disagreement between predicted and measured drop sizes at high gas density, the computational method used to determine the size distribution of Fig. 5 needs to be explained. After the spray tip has penetrated out of the outflow boundary of the computational domain, the calculation is continued until the spray reaches its steady configuration at that boundary. (The real time of this transient is different for

different ambient pressures as shown in Table 2 in the column of steadying time.) Then we sample the drops and compute its size distribution at the axial location  $x = 7.6$  cm downstream of the injector orifice and over the volume bound by the two planes  $x = 7.4$  cm and  $x = 7.8$  cm by averaging over a time interval. The duration of the interval is determined by the condition of no further significant changes in the computed distribution, and varies from case to case, as also shown in Table 2 in the column of sampling time. The distributions thus obtained correspond also to those that would be measured by drop collection techniques if the gathering of drops occurs far downstream and is continued over a time that is much longer than the transient start up and shut down times of the injections.

While inquiring as to the possible reasons for the disagreement in the computed and measured distributions for the high pressure case, we first made sure that the computed results were insensitive to the various parameters of the numerical solution. We varied independently the numerical time step,  $\Delta t$ , the parcel injection rate, and the coalescence efficiency  $E_{\text{coal}}$  as shown in Table 3 and studied their effect on the drop size distribution function at selected cells (8). All the other input parameters were kept the same (Case #3, Table 1). It was observed that increasing the time resolution and the parcel injection rate had little effect on the results. The effect of varying coalescence efficiency slightly was not marked, in part due to the stochastic technique used, and even though the total elimination of grazing collision has been demonstrated by O'Rourke and Bracco to result in unphysically large drops. Finally, that the spatial resolution is adequate had already been demonstrated (6,7).

Thus it was concluded that numerical errors were acceptably small and could not be responsible for the discrepancy.

Next, we re-examined the experimental method used by Hiroyasu and Kadota and found that they had employed Diesel type pulsating injections with an injection duration of the order of 3 ms for the cases with which we compared (but the exact duration was not spelled out in all cases). Since such period is of the same order as the computed steadying time at the 7.6 cm downstream section, and since Hiroyasu and Kadota used a drop collection technique, we

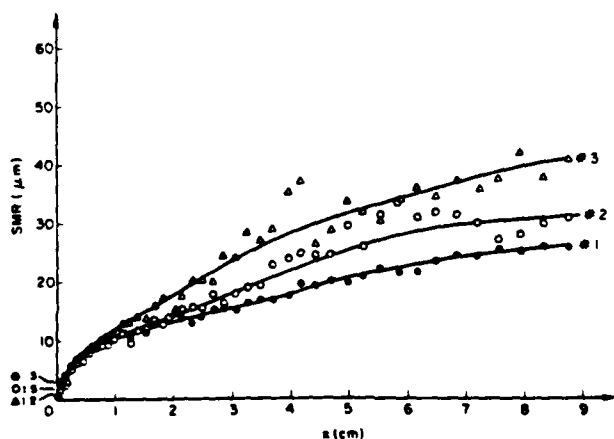


Fig. 6 - Computed Sauter mean radius of the drops in the cross-section of three sprays (Cases #1, 2, 3 of Table 1) after reaching steady state



Table 2 - Parameters of Study of Continuous vs Pulsating Injections

Case #	$P_{amb}$ (MPa)	Hiroyasu & Kadota's [1] Injection Duration (ms)	CONTINUOUS INJECTION		PULSATING INJECTION	
			Steadying Time (ms)	Sampling Time (ms)	Computation Injection Duration (ms)	Duration of Computation After End of Injection (ms)
1	1.1	~3.0	2.6	3.0	3.0	4.0
2	3.0	3.0 to 4.0	5.2	6.1	3.0	4.0
					4.0	4.0
3	5.0	3.0 to 4.0	7.6	6.1	3.0	4.0
					4.0	4.0

Table 3 - Parameter of Sensitivity Study

Case #	$t$ (s)	Particle Injection Rate ( $ms^{-1}$ )	Coefficient of $E_{coal}$
3	0.5	900	2.4
3A	0.5	1800	2.4
3B	0.5	1800	2.16
3C	0.2	1800	2.4
3D	0.5	3600	2.4

decided that our sampling technique may be inappropriate for the comparison. So, in a second set of calculations, we computed the injection for the same duration of the experiment. Then we continued the computation for an additional 4 ms for all cases, simulating the flight of the drops away from each other and toward the collection pan in the experiment, and finally we counted all drops that had flowed out of the computational domain through the outflow boundary, if any, and those that still remained inside the domain.

The drop distribution functions computed with 3 ms injections are presented in Figure 7. Several important differences with respect to the results for the continuous injection are noticed in comparing Figure 7 with Figure 5. For all three gas pressures (actually the gas density is the important parameter), the drop distributions from short injections shift toward the smaller drop sizes. The shift is progressively larger as the gas density increases. The computed distributions are now in much better agreement with the measured ones at all gas densities. The difference with respect to the con-

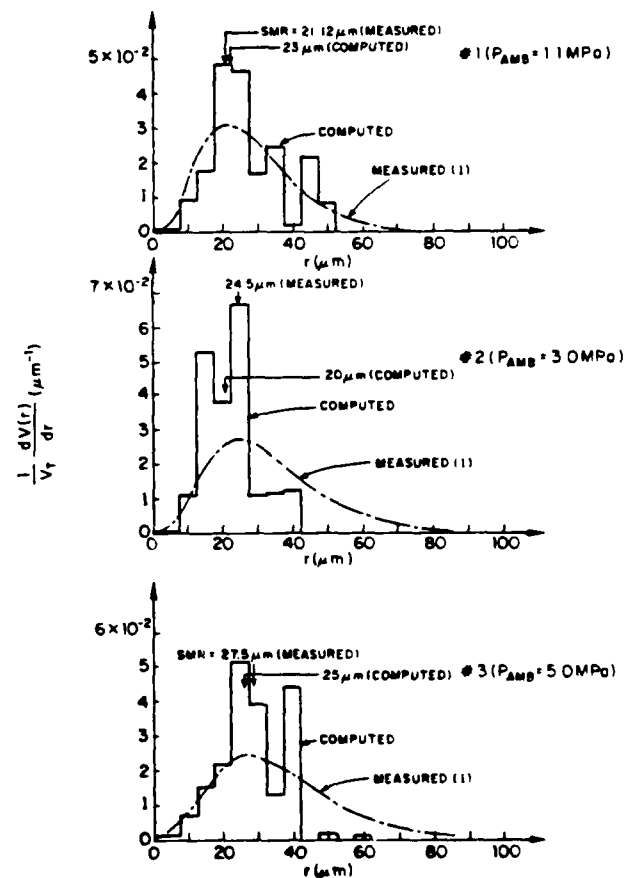


Fig. 7 - Downstream drop size distributions, computed with 3 ms injections, compared with those measured by Hiroyasu and Kadota (1)

tinuous injection is particularly marked at the highest gas density where the short injection computation does not yield anymore very large drops and the computed SMR is reduced from 40.18 to 25.55  $\mu\text{m}$  versus 27.5  $\mu\text{m}$  of the experiment. In a third set of computations we used an injection duration of 4 ms, instead of 3 ms, and the computed distributions shifted back toward larger drops (see Figure 8) but not nearly all the way to the distributions of the continuous injection. Also interesting is that the computed tip penetration rates changed very little with injection duration. In particular, in the second study, for the two high ambient pressure cases (#2 and #3), at the moment the injection is cut off, the tips have penetrated only about two-third and one-half of the computational domain respectively, and yet their subsequent penetrations followed very closely the curves of the continuous injection even after the end of injection. If nothing else, the above findings demonstrate again (6) that the tip penetration is not sensitive to the variation of upstream injection conditions whereas the downstream mean drop size and, most of all, the size distribution are.

The above results are the net outcome of the interaction of several controlling processes, as clearly evidenced by the complexity of the equations, and attributing them to a few parameters implies oversimplifications and inaccuracy. Nevertheless it is clear from the computations that some parameters are more important than others. The main effect is droplet coalescence.

The high velocity drops in a short pulse coming into a quiescent gas with initially divergent trajectories (the initial spray angle) rapidly move away from each other and slow down while transferring their momentum to the gas. The rapid decrease of the drop number density and relative velocity brings about a decrease in collision and coalescence rates.

But the initial momentum of the parcel of drops is large due to their high density and initial velocity and the speed imparted to the entrained gas is also large and tending to the drop velocity. A second pulse of drops that is injected into the already moving gas, slows down less markedly and in fact catches up with the first parcel producing collisions and coalesce above those that would have been experi-

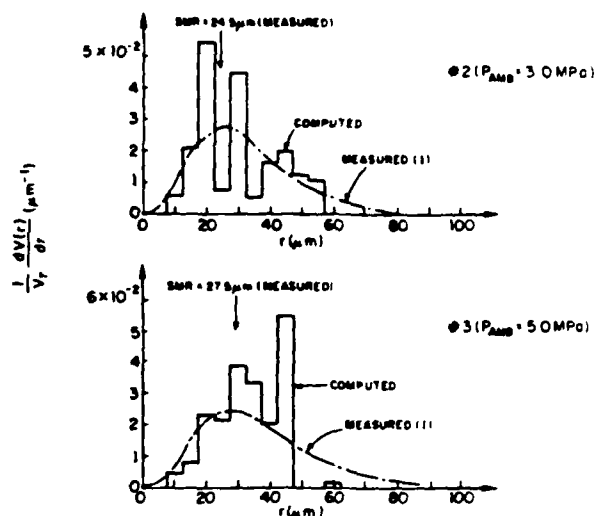


Fig. 8 - Downstream drop size distributions, computed with 4 ms injections, compared with those measured by Hiroyasu and Kadota (1)

enced by each of the parcels separately. Since the axial speed of the entrained gas is largest along the axis, the drops of later pulses move faster along the axis and catch up with drops of earlier pulses first. As pulses follow each other more and more closely, the continuous injection limit is reached in which drops along the axis of the jet penetrate all the way to the back of the head vortex and add to it the new momentum that propels it. Accordingly, pulsating a spray allows drops to move apart from each other and leads to smaller drop relative velocity thus reducing collision frequency and coalescence, and ultimately giving smaller drops downstream.

Hiroyasu and Kadota (1) measured this trend and had suggested the correct reason: "the Sauter mean diameter increases with an increase in the number of injections; this is pronounced at high pressure. It may be mainly due to the coalescence of successive sprays. The probability for the coalescence increases with an increase in ambient gas pressure."

As explained earlier, coalescence increases markedly with increasing gas density so that the difference between continuous and pulsating sprays is also more noticeable at higher gas densities.

However, the reasons for the predicted tip penetration rate to be essentially the same for pulsating and continuous injections remain unclear. Since the average momentum flux of a

pulsating spray is smaller than that of the corresponding continuous spray, the predicted rate of momentum transfer from the spray to the surrounding gas must also be smaller for pulsating jets. But a more detailed study of this specific aspect is necessary to isolate the mechanism of this predicted scaling.

#### LIQUID CORE LENGTH

Earlier computations of spray in Diesel-type environments (14) showed that the drops vaporize completely within a certain distance from the nozzle exit. Since the injected drops have different radii, move at different velocities within the spray, are exposed to different gas temperatures and vaporized fuel concentrations, and actively collide and coalesce, one cannot readily identify a typical drop and a typical vaporization time. Nevertheless, it is convenient to schematize the process and state that in the trajectory of the typical drop of the spray a maximum penetration is reached that corresponds to its vaporization time. Beyond this penetration, only the larger drops, vaporized fuel, and entrained air exist and the steady liquid injection at the actual nozzle plane becomes equivalent to a gaseous injection at the maximum penetration plain, as far as the subsequent development of the jet is concerned.

We called the maximum penetration of the liquid the liquid core length and illustrated the process in the sketch of Figure 9.

We also noticed that the computed liquid core length was of the order of a few centimeters, that is, similar to

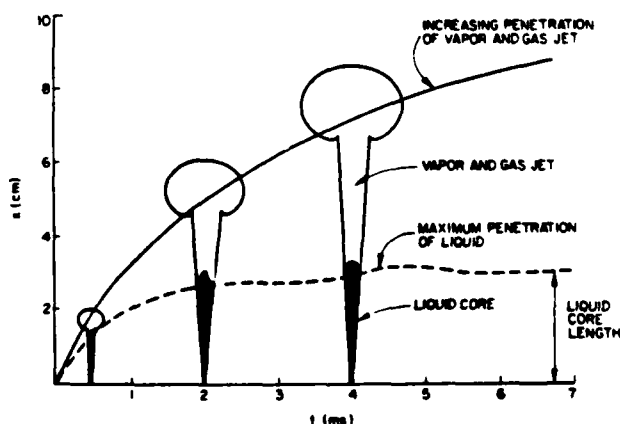


Fig. 9 - Sketch of penetrations of gas and drop tips and liquid core length

the radius of many direct injection stratified-charge and Diesel engines. Had the computed liquid core length been of the order of tens of centimeters, we would have concluded that, even considering possible inaccuracies of the model, sprays were likely to be present in all such engines. Had the computed length been of the order of a few millimeters we would have concluded that sprays are not likely to be present in such engines and the gas jet representation is correct. But the closeness of the computed liquid core length to the typical cylinder radius led us to the conclusion that, in such engines in some situations one may observe mostly sprays and in others mostly gas jets. This conclusion would be strengthened if it could be shown that the computed liquid core length is sensitive to the differences in the spray parameters of different engines (on the other hand, insensitivity would lead to the conclusion that the same condition, whatever that may be, should be observed in all engines). Thus we undertook the sensitivity study reported in this section. The parameters varied were injection velocity, chamber gas density, chamber gas temperature, and injection timing (Cases 4-9 of Table 1).

EFFECT OF INJECTION VELOCITY - shown in Figure 10 is the computed tip penetration vs time of Case #4 which corresponds to the injection of Diesel fuel at 30° BTDC into the compressed air of an engine with compression ratio of 20. On the left are the fuel vapor mass fraction contours, and on the right are the corresponding parcel location plots at subsequent times. The solid line was obtained by identifying the tip in terms of the 20% steady total mixture (gas, vapor, and liquid) momentum (8). It follows closely the fuel vapor mass fraction contours and shows continuously increasing penetration of the gasified fuel as the steady injection of liquid fuel persists. The dashed line was obtained by tracking the tip of total drop surface and mass (8). It indicates that very few drops penetrate past about 7.3 cm from the injector even though steady injection of liquid continues. The corresponding results of Case #5, which has a lower liquid injection velocity, are given in Figure 11. Decreasing  $\Delta p$ , the penetration of the gas jet decreases but the length of the liquid core increases slightly. The smaller momentum of the jet results in

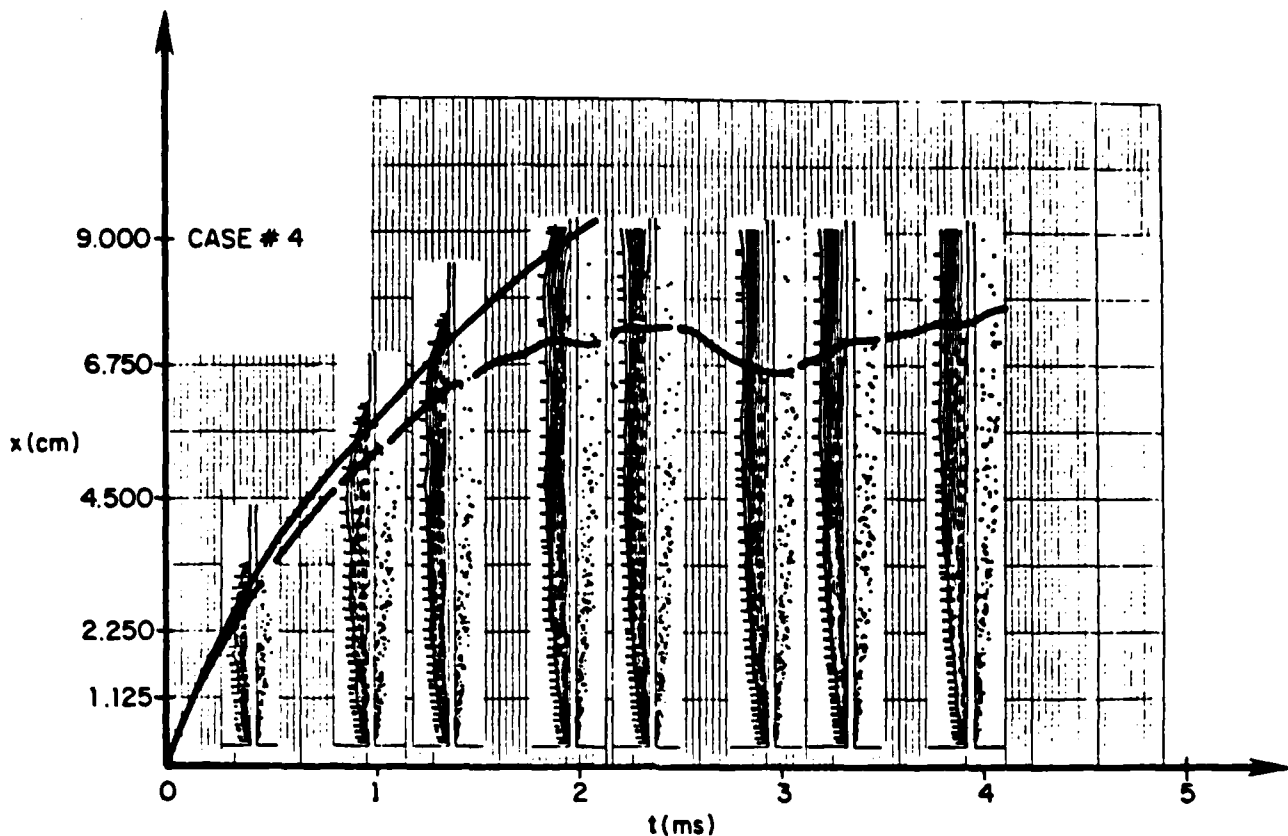


Fig. 10 - Gas tip penetration and liquid core length of Case #4 of Table 1

slower gas tip penetration but the lower injection velocity results in larger initial drops (Equation 17 and Table 1), longer vaporization time, and longer liquid core.

**EFFECT OF GAS DENSITY** - Cases #5 and 6 differ only on account of the chamber gas density as shown in Table 1. Shown in Figure 12 are the computed penetration rates of Case #6. Increasing the gas density, both the penetration rate of the gas jet and the length of the liquid core decrease. This is mostly due to the higher density of the entrained gas decreasing the penetration due to conservation of momentum. But the decrease in the liquid core length is particularly large due at least in part to smaller drops having been formed by atomization and vaporizing faster (Equation 17 and Table 1).

**EFFECT OF GAS TEMPERATURE** - Cases #7 and 8 differ only on account of their gas temperature. Shown in Figure 13 is the computed tip penetration vs time

results of Case #7 which corresponds to the injection of Diesel fuel at 20° BTDC into the compressed air of an engine with compression ratio of 19.2. In Figure 14 are the results of Case #8 which has lower gas temperature than Case #7. It is observed that increasing the gas temperature, both the penetration rate of the gas jet and the length of the liquid core decrease. This is mostly due to higher chamber gas temperature resulting in higher drop evaporation rate and smaller conservation of the momentum by the jet.

**EFFECT OF INJECTION TIMING** - Finally, a combination of gas temperature and density changes are considered. Shown in Figure 15 are the results of Case #9 which corresponds to the injection of Diesel fuel at 20° BTDC into the compressed air of an engine with compression ratio of 20, whereas Case #5 shown previously corresponds to injection at 30° BTDC. Since Case #9 has both higher gas temperature and higher gas density, it results in

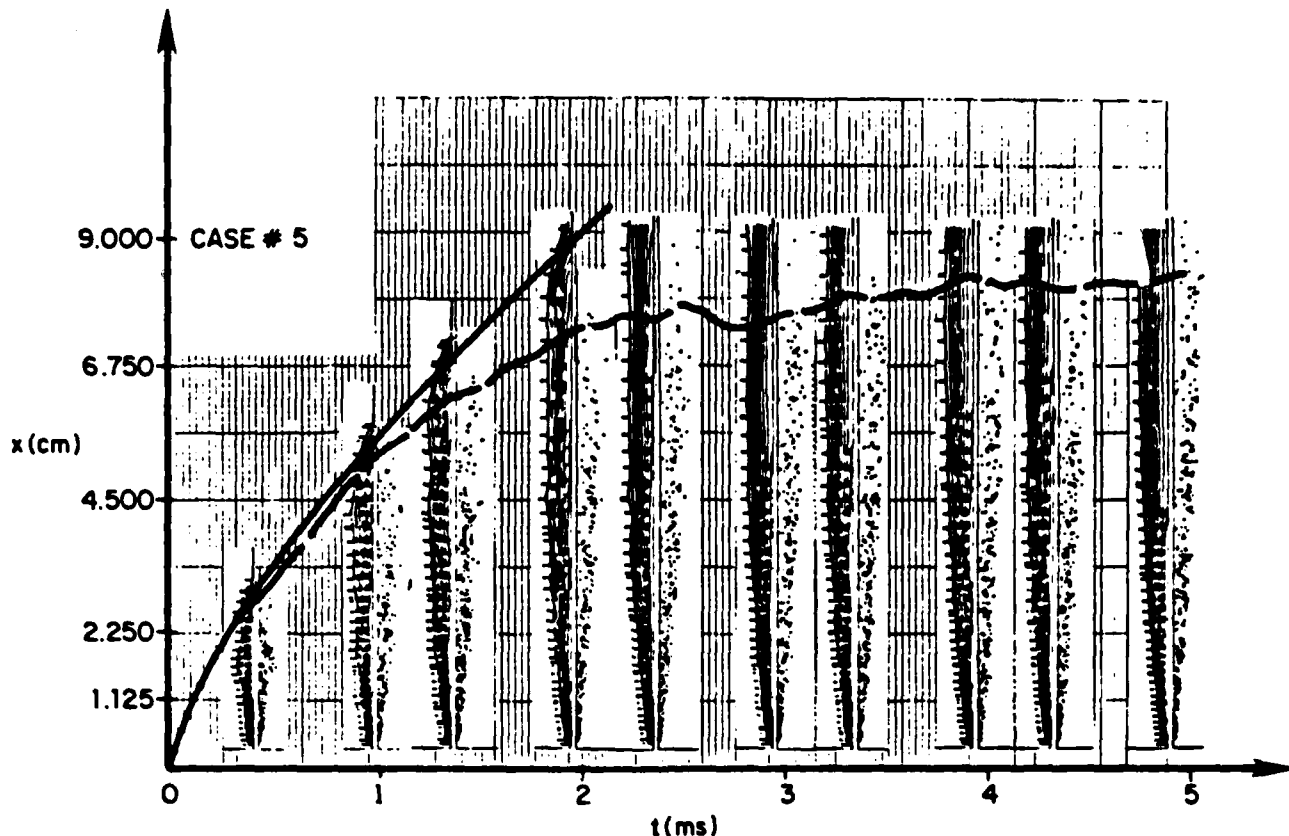


Fig. 11 - Gas tip penetration and liquid core length of Case #5 of Table 1. Injection pressure lower than in Case #4

smaller penetration and shorter liquid core as expected from the previous two comparisons. It is significant that retarding the injection by  $10^\circ$  results in a predicted 40% reduction of the liquid core length.

The model used in the computations is very recent and has undergone only limited testing. Thus it is unlikely that the predicted liquid core length is very accurate. However, its magnitude and its sensitivity to injection and chamber conditions is likely to be correct. Thus it is possible that under certain engine design and operation conditions, the length of the

liquid core is of the order of the chamber radius and drops are observed and drop vaporization is controlling, whereas under other not-too-dissimilar conditions, the length of the liquid core becomes very small and only gaseous jets are detected and mixing is controlling. This may explain why in the field of Diesel combustion, some have held the view that vaporization is fast and fuel jets can be considered as gaseous jets, while others have held the opposite view that the development of sprays and the vaporization of drops are controlling.

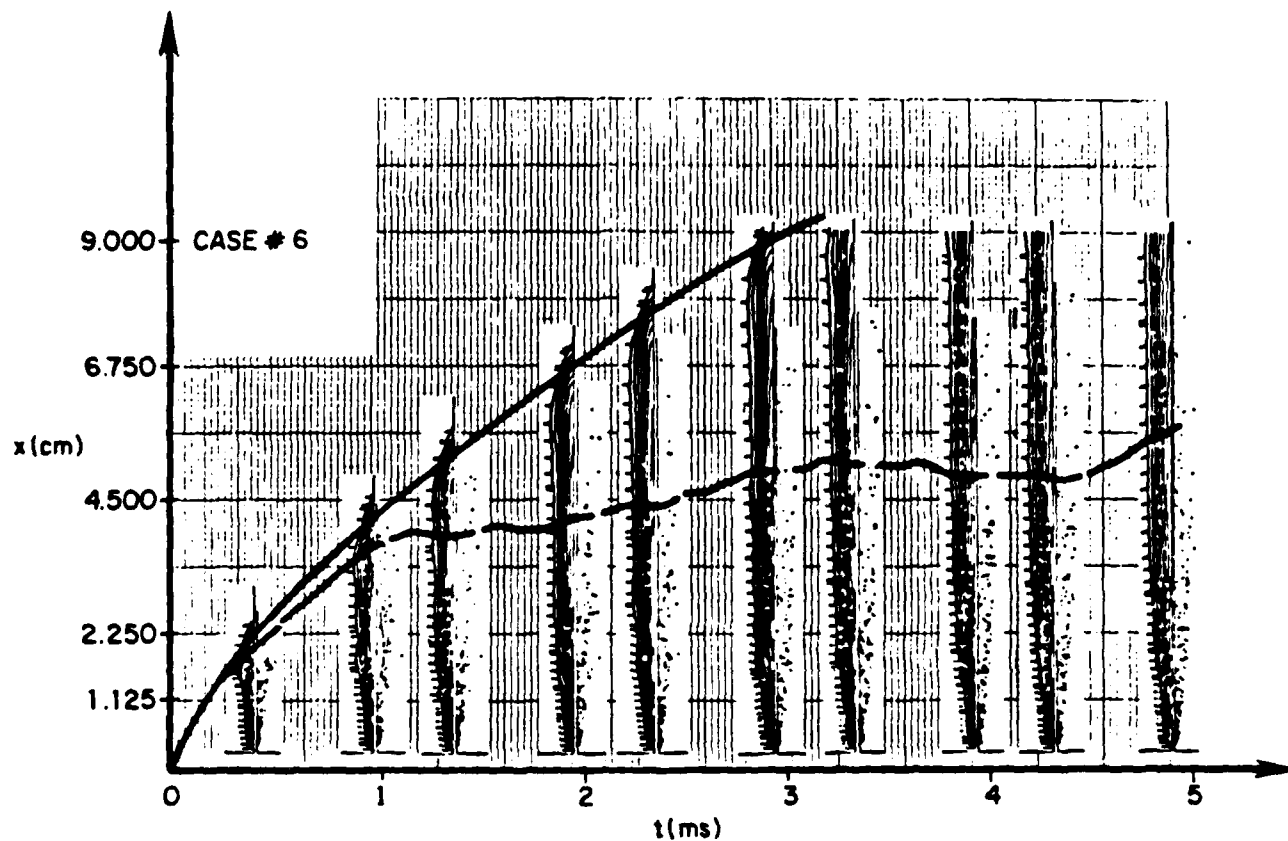


Fig. 12 - Gas tip penetration and liquid core length of Case #6 of Table 1. Gas density higher than in Case #5

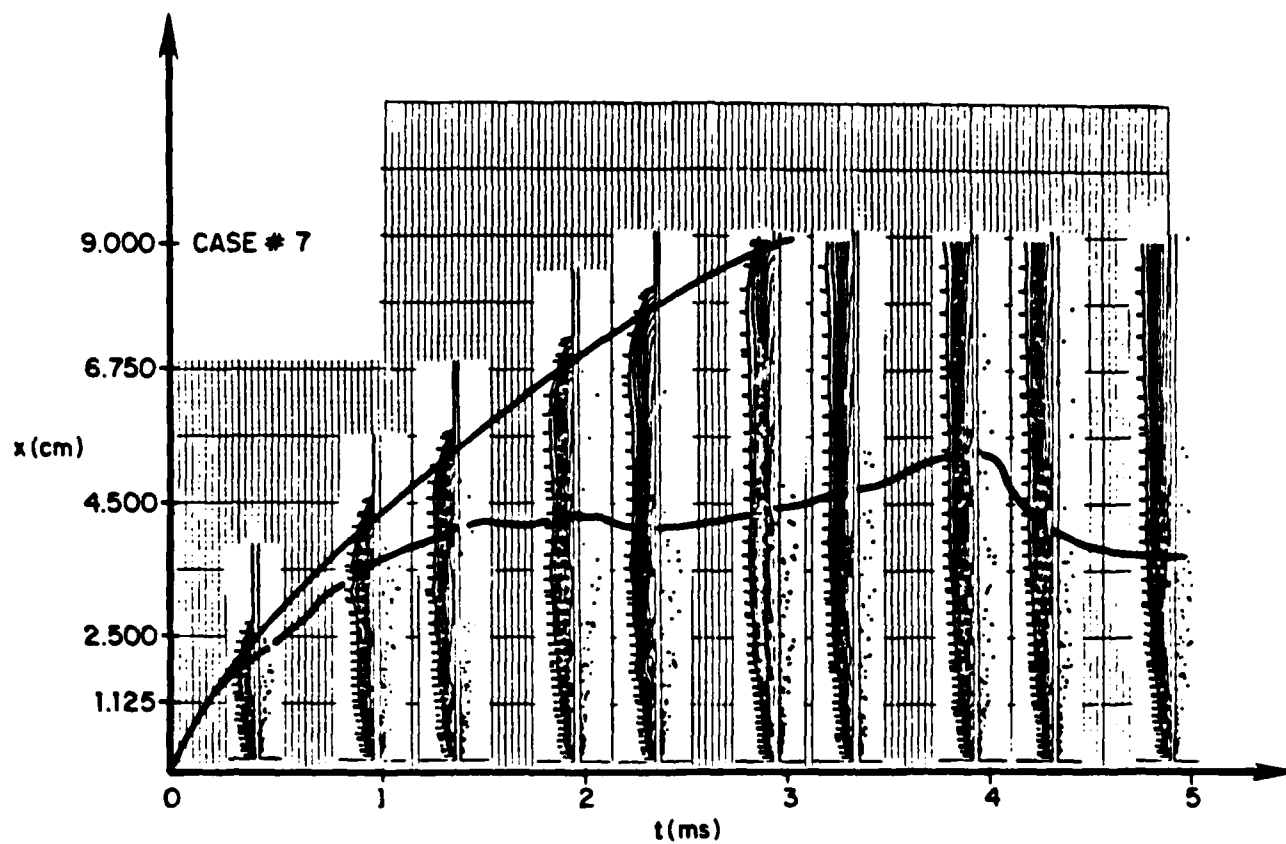


Fig. 13 - Gas tip penetration and liquid core length of Case #7 of Table 1

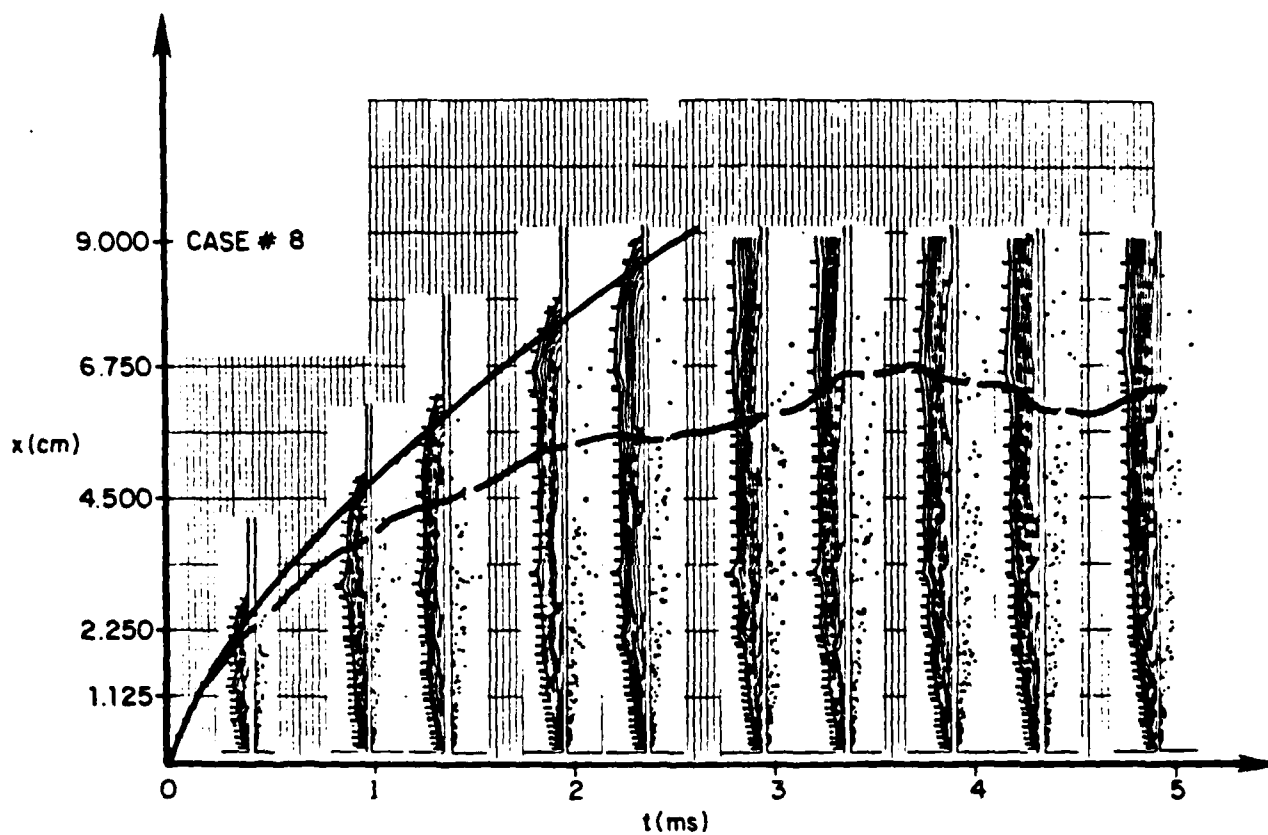


Fig. 14 - Gas tip penetration and liquid core length of Case #8 of Table 1. Gas temperature lower than Case #7



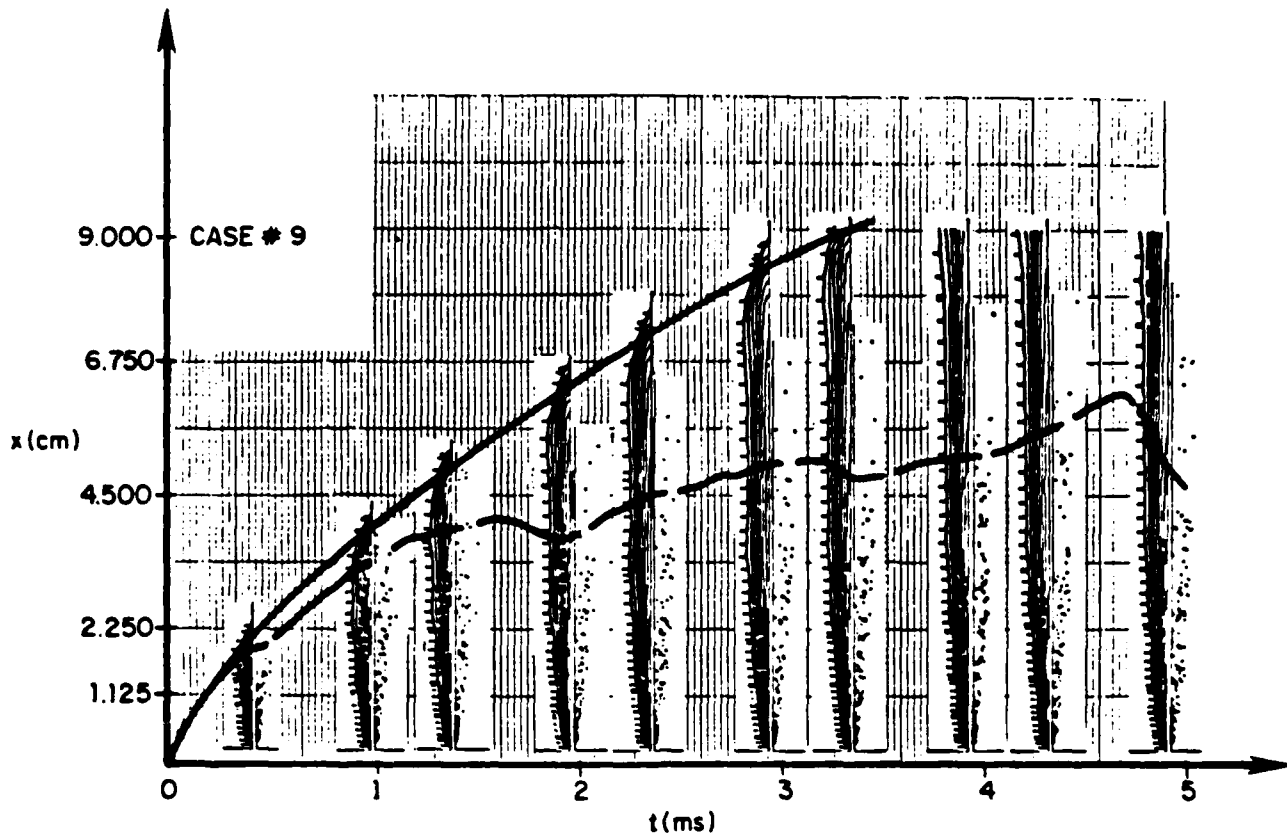


Fig. 15 - Gas tip penetration and liquid core length of Case #9 of Table 1. Gas density and temperature higher than in Case #5

## CONCLUSIONS

**PULSATING INJECTIONS** - Computations with a recently developed model for thick sprays have shown that for the same upstream and gas conditions, pulsating injections result in smaller drops than continuous injections. This is due to the inhibition of collisions and coalescence of drops. The gap in between the pulses allow the drops to move apart, thus reducing the collisions and coalescence frequencies. Since collisions and coalescence are more frequent at high gas densities, the effect is more noticeable under such conditions. However, tip penetration rates are not markedly different for continuous and pulsating injections. These trends in drop sizes and penetration rates may be pertinent to the problem of achieving control of the fuel distribution within combustion chambers.

**LIQUID CORE LENGTH** - Computations with the same model have also shown that the liquid core of sprays from single-hole straight nozzle, under the conditions of direct-injection stratified-charge and Diesel engines, achieves a maximum length beyond which only the largest of drops, vaporized fuel and entrained air propagate. The liquid core length decreases with increasing gas temperature (due primarily to faster vaporization), injection pressure (due primarily to smaller initial drops), and, most of all, with increasing gas density (due primarily to the higher inertia of the entrained gas and to smaller initial drops). For Diesel-type environments, the liquid core length is of the order of centimeters and sensitive to the liquid and gas conditions. This may explain why in some Diesel engines, and under certain conditions, sprays have been observed (and even used to impinge on

walls) whereas in other engines and conditions primarily gaseous jets have been found.

# NOMENCLATURE

$C_{DIS}$	Discharge coefficient of nozzle
$c_l$	Liquid specific heat
$c_{p_g}$	Gas specific heat at constant pressure
$c_{p_I}$	Inert species specific heat at constant pressure
$c_{p_v}$	Vapor species specific heat at constant pressure
CR	Compression ratio
$d_{eff}$	Effective orifice diameter
D	Nozzle orifice diameter
$D_t$	Turbulent eddy diffusivity
$E_{coal}$	Coalescence efficiency
$E_{12}$	Collision efficiency
$f$	Drop distribution function
$\underline{F}$	Drop acceleration (= $\underline{dv}/dt$ )
$\underline{F}_a$	Aerodynamic drag on a drop
$h_g$	Gas enthalpy
$h_l$	Liquid enthalpy
k	Turbulence kinetic energy
$l$	Turbulent eddy size, nozzle length
L	Length of calculation domain
$L$	Latent heat of vaporization

# SYMBOL DEFINITION

$Nu_g$	Gas phase Nusselt number
$Nu_l$	Liquid phase Nusselt number

P	Pressure
$Pr$	Prandtl number
$P_v$	Equilibrium vapor pressure
$P_{init}$	Pressure at beginning of compression
$P_{inj}$	Fuel injector upstream pressure
$P_{amb}$	Chamber gas pressure
r	Radial coordinate or drop radius
R	Radius of calculation domain or drop radius change (= $dr/dt$ )
R	Universal gas constant
$Re$	Reynolds number
$SMR_0$	Initial drop Sauter mean radius
t	Time
$T_{init}$	Temperature at beginning of compression
$T_d$	Drop temperature
$\dot{T}_d$	Time rate of drop temperature change
$T_g$	Mean gas temperature

# SYMBOL DEFINITION

$T_s$	Drop surface temperature
$T_l$	Temperature of injected liquid parcel
$T_{l,b}$	Boiling temperature of liquid
$\underline{u}_g$	Mean gas velocity
$\underline{u}'_g$	Fluctuating component of gas velocity experienced by a drop
$U_0$	Parcel injection velocity

$U_{inj}$	Liquid injection velocity $= C_{Dis} \left[ \frac{2(P_{inj} - P_{amb})}{\rho_l} \right]^{1/2}$	$\rho_g$	Gas mass per unit gas volume
$v$	Drop velocity	$\rho'_g$	Gas mass per unit mixture volume = $\theta \rho_g$
$W_I$	Inert species molecular weight	$\rho_l$	Liquid density
$W_v$	Vapor species molecular weight	SYMBOL	DEFINITION
$We_j$	Jet Weber number $= \rho_g U_{inj}^2 D / \sigma_l$	$\sigma$	Transition probability function for collisions
$We$	Drop coalescence Weber number	$\sigma_l$	Surface tension of liquid
$x$	Coordinate in the direction of jet axis	$\tau$	Correlation time for fluctuating gas velocity along the path of a drop or turbulent stress tensor
$\underline{x}$	Position in physical space	$\Delta p$	Effective injection pressure ( $P_{inj} - P_{amb}$ )
$y$	Coordinate in the radial direction	$\delta t$	Numerical time step
$Y_I$	Inert species mass fraction	PRATE	Particle injection rate
SYMBOL	DEFINITION	<u>Subscript</u>	
$Y_v$	Vapor species mass fraction	$l$	Laminar or liquid
$Y_{vs}$	Drop surface vapor mass fraction	$o$	Jet exit plane
$\gamma$	Ratio of specific heats	$t$	Turbulent
$\theta$	Void fraction (mean gas volume fraction)	$in$	Initial value specified at jet exit plane
$\theta_o$	Gas volume fraction in the injection cell	$CL$	Location on jet centerline
$\theta_{\frac{1}{2}}$	Spray half-angle	$eff$	Effective quantity
$\mu_g$	Viscosity of gas	$s$	Averaged property over a drop's surface
$\mu_l$	Viscosity of liquid	<u>Superscript</u>	
$\nu$	Kinematic viscosity or collision frequency	$-$	Mean value
$\delta$	Dirac delta function	$*$	Dimensionless quantity
$\lambda_g$	Gas heat conductivity	ACKNOWLEDGEMENTS	
$\lambda_l$	Liquid heat conductivity		Support for this work was provided by the Department of Energy, Contract EC-77-S-02-4192.A002, The Army Research Office DAAG29-78-G-0132 Volkswagenwerk, FIAT, General Motors, and Komatsu.
$\rho$	Density		
$\rho_{init}$	Density at beginning of compression		

## REFERENCES

1. Hiroyasu, H. and Kadota, T., "Fuel Droplet Size Distribution in Diesel Combustion Chamber," SAE Paper 740715, 1974.
2. Adler, D. and Lyn, W.T., "The Evaporation and Mixing of a Liquid Fuel Spray in a Diesel Air Swirl", Symposium on Diesel Engine Combustion, Institution of Mechanical Engineers, 1970.
3. Chiu, W.S., Shahed, S.M., and Lyn, W.T., "A Transient Spray Mixing Model for Diesel Combustion," SAE Paper 760128, 1976.
4. Borman, G.L. and Johnson, J.H., "Unsteady Vaporization History and Trajectories of Fuel Drops Injected into Swirling Air," SAE Paper 598C, 1962.
5. Shipinski, J.H., Myers, P.S., and Ueyehara, O.A., "A Spray Droplet Model for Diesel Combustion," Symposium on Diesel Engine Combustion, Institution of Mechanical Engineers, 1970.
6. O'Rourke, P.J. and Bracco, F.V., "Modeling of Drop Interactions in Thick Sprays and a Comparison with Experiments," Stratified Charge Automotive Engines Conference, The Institution of Mechanical Engineers, 1980.
7. O'Rourke, P.J., "Collective Drop Effects in Vaporizing Liquid Sprays," Department of Mechanical and Aerospace Engineering, Princeton University, Ph.D. Thesis #1532-T, August 1981.
8. Kuo, T.-W., "On The Scaling of Transient Laminar, Turbulent, and Spray Jets," Department of Mechanical and Aerospace Engineering, Princeton University, Ph.D. Thesis #1538-T, December 1981.
9. Williams, F.A., "Progress in Spray-Combustion Analysis," Eighth International Symposium on Combustion, Williams and Wilkins Co., Baltimore, MD, 50-69, 1962.
10. Schlichting, H., "Boundary Layer Theory," 6th ed., McGraw-Hill, 1968.
11. Dukowicz, J.K., "A Particle-Fluid Numerical Model for Liquid Sprays," J. Comp. Phys., Vol. 35, 1980, pp. 229-253.
12. Bergwerk, W., "Flow Pattern in Diesel Nozzle Spray Holes," Proceedings of the Inst. of Mech. Engineers, Vol. 173, 1959, pp. 655-660.
13. Reitz, R.D. and Bracco, F.V., "On The Dependence of Spray Angle and Other Spray Parameters on Nozzle Design and Operating Conditions," SAE Paper 790494, 1979.
14. Kuo, T.-W. and F.V. Bracco, "Further Computations of Thick Sprays," 13th DISC Meeting, Los Alamos National Laboratory, New Mexico, March, 1981.

This paper is subject to revision. Statements and opinions advanced in papers or discussion are the author's and are his responsibility, not SAE's; however, the paper has been edited by SAE for uniform styling and format. Discussion will be printed with the paper if it is published in SAE Transactions. For permission to publish this paper in full or in part, contact the SAE Publications Division.

Persons wishing to submit papers to be considered for presentation or publication through SAE should send the manuscript or a 300 word abstract of a proposed manuscript to: Secretary, Engineering Activity Board, SAE.

Printed in U.S.A.

APPENDIX H

ON THE SCALING OF  
IMPULSIVELY STARTED  
THICK SPRAYS

T.-W. Kuo and F.V. Bracco

ON THE SCALING OF IMPULSIVELY  
STARTED THICK SPRAYS

T.-W. Kuo and F. V. Bracco

Department of Mechanical and Aerospace Engineering  
Princeton University  
Princeton, NJ 08544

March 1981

Submitted for Publication to the  
Journal of Fluids Engineering

## ABSTRACT

A scaling law for transient and steady, non evaporating and evaporating, sprays is reported. It is deduced through parametric studies with a set of coupled two-dimensional unsteady conservation equations for gas and liquid. The equations are solved numerically with a deterministic Eulerian scheme for the gas and a stochastic Lagrangian scheme for the drops. Thick sprays effects, such as drop collisions, followed by either coalescence or re-separation, and the influence of gas volume fraction on the rates of exchange of mass, momentum, and energy between drops and gas, are included.

It is found that the characteristic velocity is the injection velocity; the characteristic length is a function of nozzle diameter, nozzle geometry, liquid and gas densities, and drop transfer number; and the characteristic time is the ratio of the two. Defining the instantaneous position of the spray tip as the location at which 70% of the steady state centerline velocity is first reached, a unique function is determined for its penetration rate. The function is shown to compare favorably with classical experimental and theoretical tip penetration rate equations. It is also found that the 70% steady velocity is reached within the head vortex so that a transient spray, practically, is a steady spray except within its head vortex.



## INTRODUCTION

In Diesel and stratified-charge engines, liquid fuel is introduced into hot compressed air at high velocity often through small, cylindrical passages. Typically, the nozzle diameter is 100-300  $\mu\text{m}$ , the length-to-diameter ratio 4 to 8, and the injection velocity is of the order of  $10^4$  cm/s. Under such conditions, fine sprays are observed to form at the nozzle exit and, subsequently, to penetrate the gas and to vaporize. The process that leads to the formation of the very small drops very near the nozzle exit has been called atomization. In the atomization regime both drop diameter and jet intact length are of the order of a few microns.

Even though sprays in the atomization regime have received considerable attention, many important details of their structure are still poorly understood.

It would appear that the initial breakup of the outer part of the cylindrical liquid jet into fine drops near the injector is due to aerodynamic interactions between the liquid surface and the surrounding gas that force the selective and rapid growth of surface perturbations in turn initiated within the nozzle [1,2].

However, the inner structure of the jet in the immediate vicinity of the nozzle exit is now known and not likely to consist of clearly demarked drops surrounded by minute amounts of gas, but rather of mingled and rapidly changing liquid and gas continua. This has been called the churning flow regime [3,4] and could extend some ten nozzle diameters downstream of the nozzle for typical spray angles of  $10^\circ$ . At that distance, on the average over the spray cross section, the volume occupied by the liquid is 10% of the volume of the jet and the distance between the surfaces of neighboring drops about equal to their diameter. Due to their small separation, drops are likely to influence directly each other's rates of transfer of mass, momentum, and energy with the gas. Also collisions and coalescence can be expected. This is the thick spray regime [3,5]. Further downstream, in the thin spray regime [3,5], the interdrop distance becomes much larger than the drop diameter, drops interact with each other only indirectly, and the spray should behave as a gas jet.

In this paper, the transient and steady state scaling of thick sprays is studied but under the idealized conditions of impulsively started, constant velocity injections in infinite, initially quiescent, compressed air. Vaporization is allowed but not combustion.

The study was conducted with a model for thick sprays that is of recent development but has given satisfactory results in comparisons with several sets of experimental data. The coupled conservation equations for gas and liquid are solved numerically with a deterministic Eulerian scheme for the gas and a stochastic Lagrangian scheme for the drops. The intricate computational technique was devised by Dukowicz [6] and further developed by O'Rourke and Bracco [3,4]. Dukowicz did not consider evaporating sprays, collisions and coalescence, and the effect of the gas volume fraction on drop drag.

O'Rourke and Bracco extended Dukowicz's approach to account for thick spray effects. From the fields of fluidized and packed beds, heat transfer in regular arrays of spheres, and cloud physics they derived expressions for the influence of gas volume fraction on the rates of exchange of mass, momentum, and energy between the drops and the gas and for drops collisions, whether followed by coalescence or simply altered trajectories. In their preliminary applications, they reached the conclusions that: a) drop collisions and coalescence are important in thick sprays and account for the difference between the relatively large drops measured downstream of non-vaporizing sprays, and the relatively small drops formed upstream by the jet atomization process; b) contrary to intuition, gas volume fraction effects on drop drag are not very significant; and c) drop sizes are more sensitive to the details of the structure of the spray than tip penetration rates.

In the following sections, first a brief description of the model is given including some typical results and some comparisons with measurements. Then the question of the definition of the spray tip is considered. Finally the scaling studies are reported and the specific application to the penetration rate of fuel sprays is discussed.

## THE MODEL

The equations of the model for the transient and steady state of nonevaporating and evaporating thick sprays are those of O'Rourke and Bracco [3]. They are:

## Spray Equation

$$\begin{aligned} \frac{\partial f}{\partial t} + \nabla \cdot (f \underline{v}) + \nabla_{\underline{v}} \cdot (f \underline{F}) + \frac{\partial}{\partial r} (f R) + \frac{\partial}{\partial T_d} (f \dot{T}_d) = \\ = \frac{1}{2} \iint f(\underline{x}, \underline{v}_1, r_1, T_{d_1}, t) f(\underline{x}, \underline{v}_2, r_2, T_{d_2}, t) \pi(r_1 + r_2)^2 \\ |\underline{v}_1 - \underline{v}_2| E_{12}(\underline{x}, \underline{v}_1, r_1, \underline{v}_2, r_2, t) \{ \sigma(\underline{v}, r, T_d, \underline{v}_1, r_1, T_{d_1}, \\ \underline{v}_2, r_2, T_{d_2}, \underline{x}, t) - \delta(r - r_1) \delta(\underline{v} - \underline{v}_1) \delta(T_d - T_{d_1}) \\ - \delta(r - r_2) \delta(\underline{v} - \underline{v}_2) \delta(T_d - T_{d_2}) \} dr_1 d\underline{v}_1 dT_{d_1} dr_2 d\underline{v}_2 dT_{d_2} \end{aligned} \quad (1)$$

## Gas Mass Equation

$$\frac{\partial \hat{\rho}_g}{\partial t} + \nabla \cdot (\hat{\rho}_g \underline{u}_g) = - \iiint 4\pi r^2 R \rho_\ell f dr d\underline{v} dT_d \quad (2)$$

## Vapor Mass Equation

$$\frac{\partial \hat{\rho}_g^Y}{\partial t} + \nabla \cdot (\hat{\rho}_g^Y \underline{u}_g) = \nabla \cdot (\hat{\rho}_g^Y \underline{D}_T \nabla Y_v) - \iiint 4\pi r^2 R \rho_\ell f dr d\underline{v} dT_d \quad (3)$$

## Gas Momentum Equation

$$\begin{aligned} \frac{\partial \hat{\rho}_g \underline{u}_g}{\partial t} + \nabla \cdot (\hat{\rho}_g \underline{u}_g \underline{u}_g) + \nabla p = \nabla \cdot \underline{I}_t - \iiint [4\pi r^2 R \underline{v} \\ + \frac{4}{3} \pi r^3 \underline{F}] \rho_\ell f dr d\underline{v} dT_d \end{aligned} \quad (4)$$

where  $\underline{I}_t = \hat{\rho}_g D_t [\nabla \underline{u}_g + \nabla \underline{u}_g^T - \frac{2}{3} \nabla \cdot \underline{u}_g \underline{I}]$

### Gas Energy Equation

$$\begin{aligned} \frac{\partial \hat{\rho}_g h_g}{\partial t} + \nabla \cdot (\hat{\rho}_g h_g \underline{u}_g) = & \theta \left( \frac{\partial p}{\partial t} + \underline{u}_g \cdot \nabla p \right) + \nabla \cdot [\rho_g c_{p_g} D_t \nabla T_g] \\ & - \iiint f \rho_l \left\{ 4\pi r^2 R [h_l(T_d) + \frac{1}{2} (\underline{v} - \underline{u}_g)^2] \right. \\ & \left. + \frac{4}{3} \pi r^3 [\underline{F}_a \cdot (\underline{u}_g + \underline{u}'_g - \underline{v}) + c_l \dot{T}_d] \right\} dr d\underline{v} dT_d + \underline{I}_t : \nabla \underline{u}_g \end{aligned} \quad (5)$$

### Equations Determining Exchange Rates

$$a) \quad -\rho_l R = \frac{\lambda_g}{c_{p_g}} \frac{Nu_g}{2r} \frac{Y_{v_s} - Y_v}{1 - Y_{v_s}} \quad (6a)$$

$$b) \quad -\rho_l R = \frac{\lambda_g}{c_{p_g}} \frac{Nu_g}{2r} \left\{ \frac{c_{p_g}}{L(T_s)} [(T_g - T_s) - \frac{Nu_l \lambda_l}{Nu_g \lambda_g} (T_s - T_d)] \right\} \quad (6b)$$

$$c) \quad \frac{\frac{Y_{v_s}}{W_v}}{\frac{Y_{v_s}}{W_v} + \frac{Y_{I_s}}{W_I}} = \frac{p_v(T_s)}{p} \quad (6c)$$

$$d) \quad \dot{T}_d = \frac{3}{2} \frac{\lambda_l}{\rho_l c_l r^2} Nu_l (T_s - T_d) + 3 \frac{R}{r} (T_s - T_d) \quad (6d)$$

$$e) \quad \underline{F} = \underline{F}_a - \frac{1}{\rho_l} \nabla p + \underline{G} \quad (6e)$$

where  $\underline{F}_a = \frac{3}{8} \frac{\rho_g}{\rho_l} \frac{|\underline{u}_g + \underline{u}'_g - \underline{v}|}{r} (\underline{u}_g + \underline{u}'_g - \underline{v}) C_D$

### Equations of State

$$a) \quad p = \rho_g R T_g \left( \frac{Y_v}{W_v} + \frac{Y_I}{W_I} \right) \quad (7a)$$

$$b) \quad h_g = (c_{p_v} Y_v + c_{p_I} Y_I) T_g = c_{p_g} T_g \quad (7b)$$

$$c) \quad h_l(T_d) = c_{p_v} T_d - L(T_d) \quad (7c)$$

$$d) \quad L(T_d) = L(T_{ref}) + (c_{p_v} - c_l) (T_d - T_{ref}) \quad (7d)$$

Equation 1 is Williams' spray equation [7] plus two new terms that account for unsteady drop heating and a distribution of drop temperatures ( $\partial(f\dot{T}_d)/\partial T_d$ ) and for drop collisions and coalescence (the integral on the right hand side). The collision efficiency  $E_{12}$ , which is close to 1 in the present application, modifies the collision frequency (i.e.  $f(\underline{x}, \underline{v}_1, r_1, T_{d1}, t) f(\underline{x}, \underline{v}_2, r_2, T_{d2}, t) \pi(r_1 + r_2)^2 |\underline{v}_1 - \underline{v}_2| d\underline{v}_1 dr_1 dT_{d1} d\underline{v}_2 dr_2 dT_{d2}$ ). Between drops with subscript 1 properties and those with subscript 2 properties. The portion of the integrand within the brackets gives the sources (given by the transition probability function,  $\sigma$ ) and the sinks (given by the delta functions,  $\delta$ ) of drops of velocity  $\underline{v}$ , radius  $r$ , and temperature  $T_d$ , due to collisions between drops with subscript 1 properties and those with subscript 2 properties. The transition probability function determines whether the outcome of a collision is coalescence or separation. Its mathematical expression is complicated [4]. The criterion for drop separation after collision is that the rotational energy of the coalesced drop pair exceeds the surface energy required to reform the original drops from the coalesced pair. For the resulting coalescence efficiency,  $E_c$ , which is the probability of coalescence given that collision has occurred, O'Rourke and Bracco give the expression

$$E_c = \min(2.4f^* \left(\frac{r_2}{r_1}\right) \frac{1}{We}, 1.0) \quad (8)$$

$$\text{where } We = \frac{\rho_l |\underline{v}_1 - \underline{v}_2|^2 r_1}{\sigma_l}, \quad r_1 \leq r_2$$

and  $\sigma_l$  is the surface tension coefficient and the function  $f^*$  is of order one when  $r_2/r_1$  is of order one:

$$f^*\left(\frac{r_2}{r_1}\right) = \left(\frac{r_2}{r_1}\right)^3 - 2.4\left(\frac{r_2}{r_1}\right)^2 + 2.7\left(\frac{r_2}{r_1}\right) \quad (9)$$

In the present application, most of the colliding drops have radii of similar magnitudes so that the Weber number in equation (8) is important, the coalescence efficiency is generally  $<1.0$ , and drop re-separation (called grazing collision by O'Rourke and Bracco) is important.

In the gas phase mass, momentum and energy conservation equations, the integrals on the right-hand sides represent the exchange functions. They are the sum over all drops at point  $x$  and time  $t$  of the rate of mass, momentum, and energy exchanges between each drop and the gas; thus they involve the rate of drop radius change  $R$ , velocity change  $\underline{F}$ , and temperature change  $\dot{T}_d$ .

The rate of drop radius change  $R$  is found by solving equations (6a)-(6c) simultaneously for the unknown drop surface temperature  $T_s$ , surface vapor mass fraction  $Y_v$ , and  $R$ . After  $R$  and  $T_s$  are found, the rate of drop temperature change  $\dot{T}_d$  is obtained from (6d). The drop acceleration  $\underline{F}$ , given by equation (6e), has a contribution due to aerodynamic drag  $\underline{F}_a$  and one other due to the mean pressure gradient which has been shown to be important in some applications [4]. In equations (6a)-(6e), there are three unknown functions; the drag coefficient  $C_D$ , and the gas and liquid phase Nusselt numbers,  $Nu_g$  and  $Nu_l$ , respectively. After a detailed survey of experimental and theoretical studies of fluidized beds, heat transfer in regular arrays of spheres, and packed beds, O'Rourke and Bracco proposed the following correlations to account for the effect of the gas volume fraction,  $\theta$ ,

$$C_D(\theta, Re_d) = \frac{24}{Re_d} (\theta^{-2.65} + \frac{Re_d^{2/3}}{6} \theta^{-1.78}) \quad (10)$$

$$Nu_g = [2\theta^{-1.75} + 0.6(\frac{Re_d}{\theta})^{1/2} Pr^{1/3}] \frac{\ln(1+B_d)}{B_d} \quad (11)$$

where  $B_d = (Y_{v_s} - Y_v)/(1 - Y_{v_s})$  is the drop transfer number.

In the present studies we set  $Pr = 0.7$  and  $Nu_l = 1$ .

The effect of turbulence on the gas phase is accounted for by the terms involving  $D_t$  in equations (3)-(5), where  $D_t$  is the turbulent diffusivity, and was assumed to be equal to that of turbulent gas jets and related to the kinematic momentum [8]

$$D_t = 0.0161 \left( \frac{\pi D^2}{4} u_{inj}^2 \right)^{1/2} \quad (12)$$

The turbulence effects on the drops are calculated by adding to the mean gas velocity,  $\underline{u}_g$ , a fluctuating component,  $\underline{u}'_g$ , when computing the aerodynamic drag force  $\underline{F}_a$  and the gas phase Nusselt number  $Nu_g$ .  $\underline{u}'_g$  is chosen randomly from an isotropic Gaussian distribution with mean square deviation  $2/3k$ , where  $k$  is the turbulence kinetic energy and is assumed to be a fixed fraction ( $C = 0.20$ ) of the local mean flow kinetic energy, as is the case, approximately, in the downstream part of steady incompressible jets

$$k = C \frac{3}{2} \underline{u}_g^2 \quad (13)$$

For each drop, after a turbulent correlation time  $\tau_t$ , a new value of  $\underline{u}'_g$  is chosen. Dukowicz [6] took this correlation time to be constant. O'Rourke and Bracco [3] took  $\tau_t$  to be the residence time of a drop in a turbulent eddy of size  $l$  found from ( $C_l = 0.045$ )

$$D_t = C_l k^{1/2} l \quad (14)$$

and  $\tau_t$  is then given by

$$l = \int_t^{t+\tau_t} |\underline{v}(t') - \underline{u}_g(t')| dt' \quad (15)$$

where  $\underline{u}_g(t')$  is the mean gas velocity at the drop position at time  $t'$ .

A detailed derivation and discussion of the equations of the thick-spray model is given in Reference 4.

All the computations were initiated at that axial location of the spray where the initial gas volume fraction,  $\theta_0$ , is approximately 0.9. Gas and liquid were injected with equal axial velocity  $U_0$ , computed by using conservation of momentum, that is somewhat lower than the liquid injection velocity,  $U_{inj}$ , in turn calculated with a discharge coefficient,  $C_{DIS}$ , estimated

from the experimental data of Bergwerk [9]. The procedure to compute  $U_0$  was explained by O'Rourke and Bracco [3].

The initial spray angle and mean size of the drops was computed using correlations proposed by Reitz and Bracco [1] for the atomization process. They were able to show that under the condition of  $(\rho_l/\rho_g)(Re_l/We_l)^2 \gg 1$ , the measured initial spray half angle,  $\theta_{1/2}$ , is correlated well by

$$\tan \theta_{1/2} = \frac{1}{C_\theta} [4\pi(\rho_g/\rho_l)^{1/2} \frac{\sqrt{3}}{6}] \quad (16)$$

where the proportionality constant,  $C_\theta$ , depends on the geometry of the nozzle. For example, for straight round holes,  $C_\theta$  increases when the length-to-diameter ratio of the nozzle increases. Reitz and Bracco argued that the corresponding initial mean drop size should be correlated by

$$SMR_0 = B[4\pi(\sigma_l/\rho_g U_{inj}^2)^{3/2}] \quad (17)$$

where the constant  $B$  is independent of the nozzle geometry and of order one. Note that in equation (17) the initial mean drop size  $SMR_0$  is predicted to decrease when the chamber gas density increases. However the computed downstream mean drop size is found to increase with increasing gas density due to collisions and recombination [3,10] and in agreement with the measurements of Hiroyasu and Kadota [11].

The computer code LDEF (Lagrangian Drop, Eulerian Fluid) developed by O'Rourke [4] was employed with some modifications. This code incorporates the methodology of the stochastic parcel method of Dukowicz [6] in which the two-dimensional unsteady Eulerian equations for the gas and the Lagrangian equations for non-vaporizing drops are solved fully coupled. Most significant was Dukowicz's stochastic treatment of the drops. O'Rourke improved the accuracy and extended the applicability of the method by: allowing for drop vaporization; including compressibility effects (by a modified ICE technique that removes the Courant sound speed limitation on the time step); casting the momenta equations in conservation form; and adding the third momenta equations for the tangential motion of gas and drops. But the



most significant contribution of O'Rourke was to account for the first time for direct drops interactions such as collisions, coalescence, and the effects of the gas volume fractions on the exchange rates of mass, momentum and energy between the gas and the drops.

We extended O'Rourke's program by including: a numerically more efficient grazing collision calculation procedure; a new implicit iteration scheme to compute the time advanced liquid parcel temperature for evaporating sprays; gravitational acceleration in the computation of the liquid parcel velocity; and an algorithm for the evaluation of the drop velocity distribution function and the axial distribution of mean drop size.

In the computational mesh, the cells were smaller near the nozzle exit where  $\Delta r = 0.05 \text{ cm}$  and  $\Delta x = 0.1 \text{ cm}$ . Away from the nozzle exit, the size of the cells increase in both the axial and radial direction with corresponding expansion factors of 4% and 7%. A total of 44 cells in the axial direction and 26 cells in the radial direction were used, giving the computational domain a length of 9.5 cm and width of 3.2 cm.

The top and right boundaries were treated as open boundaries, the left boundary as a solid wall and drops and gas injected from the cell of the left boundary next to the axis of symmetry. The condition on the top boundary allows for free entrainment from the surroundings. The pressure at the top and right boundary were assumed to be uniform and equal to the ambient value to simulate a spray in a semi-infinite gas.

The accuracy of the numerical solution of the equations is checked indirectly by reducing spatial and temporal increments and increasing the particle injection rate until the results become acceptably insensitive to them [4,10]. The accuracy of the model is checked by comparisons with measured data. Thus O'Rourke and Bracco [3,4] compared computed tip penetration rate and the downstream drop size distribution with those measured by Hiroyasu and Kadota [11] in one Diesel-type injection

and drop size and velocity distributions with those measured by Groeneweg et al [12] at several locations within a spray from a swirl atomizer.

We made additional comparisons [10] with more of the data of Hiroyasu and Kadota (Cases #1, 2, and 3 of Table 1). In Fig. 1a, computed and measured tip penetration rates are given for different gas pressures (and densities since the experiments were at room temperature) of 1.1, 3.0, and 5.0 MPa. The agreement is seen to be good. The computed and measured downstream drop size distributions (and corresponding Sauter mean radii) for the three cases are shown in Fig. 2 in the coordinates of incremental volume fraction,  $(1/V_T)dV(r)/dr$ , versus drop radius  $r$ . It is observed that both computed Sauter mean radii and computed distributions compare favorably with the measured ones. All computations were made with the same model and model constants.

Shown in Fig. 1b is the computed typical structure of an impulsively started vaporizing spray. Even though steady injection persists, the tip of the liquid core reaches a maximum penetration past which only the largest of drops propagate. However the tip of the gas jet, which is made up of vaporized liquid and entrained ambient gas continues its propagation. As far as the gas jet is concerned, the liquid injection is equivalent to a gas injection at the end of the liquid core length. Other typical results are given in Fig. 3 where drop parcels and gas velocity plots for a non-vaporizing spray (Case #1 of Table 1) and gas temperature and vapor contours inside a vaporizing spray (Case #4 of Table 1) are shown at three times during their respective transients. In general, any function of the dependent variables can be computed, plotted, and studied.

Further information on the model, the method of solution, comparisons with measured data, and computed structure of thick sprays can be found in References 3 and 6 and all details in References 4 and 10.

### DEFINITION OF SPRAY TIP

The few parcels of drops leading the spray seen in Figure 3a represent few large drops that have conserved their initial momentum better than most of the drops. They are unlikely to be picked up by most measuring techniques and to be identified with the experimentally determined position of the spray tip. In fact, the definition of the tip position is a function of the experimental technique used to measure it. Thus, for example, if a flash of back light is used, the greatest contrast will be noted where the total surface of the drops undergoes a sudden increase. The problem of defining the tip is even more complex for evaporating sprays since drops no longer exist past an appropriate downstream station but a gas jet continues its propagation.

Accordingly, the following quantities were explored for possible use in the definition of the tip: a) The maximum axial distance from the injector of any liquid parcel - This was the definition used by O'Rourke and Bracco; b) The axial distribution of the centerline velocity - This is the quantity often used in incompressible jet studies; c) The axial distribution of total mixture momentum; d) The axial distribution of total number of drops; e) The axial distribution of total drop surface - This is likely to be the quantity measured by photographic techniques based on the scattering of light; f) The axial distribution of total drop volume.

Figs. 4a<sub>1</sub> - 4a<sub>5</sub> give the axial distribution of the total mixture momentum of Case #1 at  $t = 1.2$  ms. The five curves are from five computations of the same case but with different random number sequences. Fig. 4a<sub>6</sub> gives the ensemble average of the five computations. Since the drop model is stochastic, the same

case is computed several times with different random number sequences and the results are averaged thus obtaining average values and standard deviations (the "error" bars of Fig. 1a) in complete parallel with common experimental procedures. The mean value of the plateau in Fig. 4a<sub>6</sub> is the flowrate of momentum of the injection, which remains constant on any cross section of the steady jet, and the local deviations from it decrease with increasing number of computations. As shown in Fig. 4a<sub>6</sub>, the transition to steady state occurs very rapidly and fractions of steady state values can be selected to identify the position of the tip of the spray at any given time. Figs. 4b<sub>1</sub>, 4b<sub>2</sub>, and 4b<sub>3</sub> show the instantaneous axial distribution of, respectively, total axial momentum, total drop surface, and total drop volume from one computation of the same Case #1 (non-vaporizing spray) at  $t = 1.2$  ms. The three functions are seen to increase rapidly at about the same location thus identifying similar positions for the tip at  $t = 1.2$  ms.

We concluded that definitions c), e), and f) yield similar locations for the tip of non-vaporizing sprays. For vaporizing sprays, definitions e) and f) show that the spray penetrates only up to a certain depth, called the liquid core length in Fig. 1b, whereas definition c) tracks the continuously increasing penetration of the head vortex. Beyond the liquid core length, the head vortex is made up of vaporized liquid and entrained gas. The liquid core length roughly corresponds to the vaporization time of the average drop.

More precisely, from figures similar to Fig. 4, at each axial position, one can determine the time when any specific fraction of the steady state value of any quantity is first reached. We call such a  $t$ -vs- $x$  plot the steadying time curve for that fraction of that quantity. If a specific fraction of a specific quantity is selected to represent the tip of the spray, the corresponding steadying time curve becomes the familiar tip penetration curve. However there is no fundamental reason to select any fraction of any quantity to represent the tip. In fact, the

selection should be made corresponding to the needs of the given application or measuring technique.

It was also found that the steadying time curves based on 70%  $u_{CL,steady}$  and on 20% steady momentum coincide throughout the propagation of the spray. That is, the two thresholds are always reached at the same time at all axial locations. The same occurs for the 99.9%  $u_{CL,steady}$  and 85% steady momentum. Moreover, 70% of the steady state centerline velocity is first reached within the head vortex. Thus, practically, in an impulsively started transient spray, the transition to steady state occurs mostly within the head vortex and the stem is always in steady state. Incompressible laminar and turbulent jets were found to exhibit the same properties [10,13].

Later in the next section we will use the classical 70%  $u_{CL,steady}$  definition for the tip. It identifies the trajectory of a point within the head vortex for both non-vaporizing and vaporizing sprays. When drops are present, on the centerline the velocity of the gas and the average velocity of the drops are found to be very nearly equal.

## SCALING

In looking for the scaling law of transient, impulsively started sprays, at each axial location, we plotted the steadying time curves for selected quantities and for each spray. Then we looked for characteristic time and length scales that, for each selected quantity, would bring together the steadying time curves for all sprays. The selected quantities (and their steady state fractions) were the center line axial velocity (70% and 99.9%) and the total axial momentum (20%, 85%, and 99.9%). In general, one universal steadying time curve is obtained for each selected quantity and steady state fraction. But the characteristic time and length scales are the same for all quantities and fractions.

In the search for the characteristic length and time scales of sprays we were guided by our findings for incompressible laminar [10] and turbulent [10,13] jets. There the characteristic velocity was always the injection velocity so that the characteristic time became determined as soon as the characteristic length was identified. The characteristic length turned out being  $D Re_D$  for laminar jets and  $D Re_D^{0.053}$  for turbulent jets but both can be written as  $D/\tan\theta_{\frac{1}{2}}$  since for laminar jets  $\tan\theta_{\frac{1}{2}} \sim Re_D^{-1}$  and for turbulent jets  $\tan\theta_{\frac{1}{2}} \sim Re_D^{-a}$  ( $a \approx 0.053$ ). Thus, formally, both jets have the same length and time scales ( $D/\tan\theta_{\frac{1}{2}}$ ;  $D/U_{inj} \tan\theta_{\frac{1}{2}}$ ) and nozzle diameter, injection velocity, and initial jet angle are the important quantities for scaling. We extended this information to sprays as described below.

1. Effect of orifice diameter (same nozzle geometry). Using case #1 as reference (Table 1), in case #9 only the orifice diameter was halved corresponding to changing the nozzle size but not its geometry. Figure 5 shows steadying time curves based on 70% of  $u_{CL,steady}$ . It can be seen that the spray penetrates less rapidly when  $D$  is halved. Decreasing the diameter reduces

the jet momentum, that goes as  $D^2$ , more than the loss of momentum to the surrounding fluid, that may be expected to be related to the jet surface and to go as  $D$ , and a smaller penetration rate results. In analogy to laminar and turbulent incompressible jets, the orifice diameter and the injection velocity were tried as possible length and velocity scales and found successful in correlating the effect of orifice diameter as shown in Fig. 5.

2. Effect of injection velocity. The above finding also suggested that if the injection velocity is changed,  $D$  and  $D/U_{inj}$  may still be the appropriate scales. This was confirmed by cases #10 and #1 that differ only in injection velocity.

3. Effect of nozzle geometry (same orifice diameter). In the atomization regime, by changing the nozzle geometry the initial angle of the spray can be varied and, the larger is the angle, the smaller the penetration rate because of the enhanced entrainment. Cases #11, 12, 13 differ from cases #1, 2, 3 respectively only in the initial injection angle (Table 1). Again, recalling that for laminar and turbulent incompressible jets effective nozzle diameters could be defined that included the jet angle, the same approach was tried for sprays. Indeed, the injection velocity and  $D/(\tan \theta_1)^{0.25}$ , as characteristic effective length, were found to be adequate to scale the effect of nozzle geometry.

4. Effect of gas density. In the atomization regime, increasing the gas density changes both the initial angle of the spray, as  $(\rho_g/\rho_l)^{1/2}$  from equation (16), and the initial size of the drops, as  $\rho_l/\rho_g$  from equation (17). It also increases the drop collision and recombination rates, equations (1) and (8), ultimately leading to larger drops [10]. The larger spray angle and gas inertia in turn lead to smaller penetration rates but the larger drop size has the opposite effect. The computations show that on balance the larger the gas density the smaller the penetration rate. This suggested that the effect of gas density may be accounted for by considering an effective orifice diameter

that decreases as the gas density increases. Modification of the nozzle diameter by the factor  $\rho_g^{-1}$  led to a good correlation for cases differing mostly in gas density (cases #1, 2, and 3, and also cases #11, 12, and 13).

5. Effect of liquid density. Although the liquid density does not vary much for practical liquids, it can be expected to have an effect opposite to that of the gas density and the ratio of the two is the simplest dimensionless parameters that may account for both. In case #15 the liquid density is 40% smaller than in case #2 ( $\rho_g/\rho_l$  changes the same amount from case #2 to case #3 but on account of different gas densities) and the two cases scale with  $\rho_l$  as expected.

6. Effect of gas temperature. When the gas temperature is raised, the vaporization rate increases and the tip penetration rate decreases. The trend is the same as that given by a decreasing orifice diameter. Thus an effective diameter could possibly exist to scale gas temperature effects. Since the vaporization rate depends on the transfer number ( $B_T = C_p (T_g - T_{l,initial})/L$ , where  $L$  is at  $T_{l,initial}$ ), an effective diameter of the form  $D(1+B_T)^a$  was tried and, with  $a = -0.45$ , was found adequate to bring together the steadying time curves of cases #1, 5, and 6 that differ only in gas temperature.

7. Effect of multiple changes. Since the equations of the model are highly nonlinear, there is no a priori reason to expect that the same correlations are sufficient when many parameters are changed simultaneously. However they worked well for cases #1, 2, 3, 11, 12, and 13 that, in various combinations, differ simultaneously in three ( $U_{inj}, \theta_k, \rho_g$ ) of the six parameters, in cases #1 and 4 that differ in four parameters ( $U_{inj}, \theta_k, T_g, \rho_g$ ) and in cases #1 and 8 that differ in five parameters ( $U_{inj}, \theta_k, D, T_g, \rho_g$ ).

8. Length and time scales. Summarizing the above findings, the characteristic length, velocity, and time scales for the axial properties of transient (and steady) impulsively started sprays in the atomization regime are:



Characteristic Length

$$d_{\text{eff}} = D(\tan\theta_k)^{-0.25} (\rho_l/\rho_g)(1+B_T)^{-0.45}$$

Characteristic Velocity

$$U_{\text{inj}}$$

Characteristic Time

$$d_{\text{eff}}/U_{\text{inj}}$$

(18)

Typical steadying time curves are given in Figure 6. As previously explained, each curve gives the time necessary for the selected variable first to reach the specified fraction of its steady state value at any given axial location. The curves are valid for all sprays. Differences among sprays are accounted for by the characteristic scales given by equation (18).

9. Tip Penetration Rate. If the tip of the spray is assumed to be at the location at which 70% of the steady state centerline velocity is first reached, then the 70%  $u_{\text{CL,steady}}$  curve of Figure 6 gives the position of the tip versus time. A suitable fit for this curve is

$$x^* = 0.656 t^{*0.662} \quad 0.6 < x^* < 7.0 \quad (19)$$

When  $U_{\text{inj}}$  and the expression for  $d_{\text{eff}}$  from equation (18) are replaced in the above equation and terms are regrouped so as to isolate the various parameters, exponents of the parameters are derived that can be compared with the exponents of tip penetration correlations proposed by other authors and obtained through theoretical considerations or curve fits of experimental data. The comparison is made in Table 2 which is an extended version of one presented by Hay and Jones [14]. It can be seen that the proposed exponents are in general agreement with those already in the literature.

Actually, the seemingly small differences among the various exponents of Table 2 are significant, in our opinion. The exponent 0.662 for the time dependence from equation (19) is adequate only within the indicated range of dimensionless distances. Near the

injector the exponent tends to 1.0, i.e.,  $x \propto U_{inj} t$  and convection is controlling. Sufficiently downstream the exponent should tend to 0.5, as for turbulent incompressible jets, but our field of integration extended only to 9.5 cm. Thus a single exponent for the time dependence of the tip position masks the physics of the problem and leads to inaccuracies. As mentioned earlier, different experimental techniques give different instantaneous positions for the tip depending on the quantity to which they are sensitive. If we had used a quantity other than the 70%  $u_{CL, steady}$  we would have arrived at a different exponent. The duration of the injection, the steadiness of the back pressure and the design of the nozzle influence the tip penetration rate but are not always properly documented in experimental studies. Thus it is not always obvious for which experiments the exponents of the various quantities of Table 2 should be the same and for which experiments the exponents, or even the quantities, should be different. Finally the scaling quantities themselves are uniquely determined by experiments or computations only if the proper parameters are varied over adequately broad ranges. Thus within the narrow range of our computations,  $(T_g/T)^{-0.5}$  was found to correlate temperature effects at constant density as well as  $(1 + B_T)^{-0.45}$  because within the computed range the two coefficients happen to give very similar values. This is not a drawback when correlations are used within the ranges for which they were obtained but is confusing when the controlling physics is sought.

#### CONCLUDING COMMENTS

Our main results about impulsively started thick sprays are: the evidence that non-vaporizing and vaporizing thick sprays scale up in time and space and that the transition to steady state occurs mostly in the head vortex; the identification of the injection velocity as the characteristic velocity; the suggestion that the characteristic length is a function of nozzle diameter, nozzle geometry, liquid and gas densities and drop transfer number; the warning that the tip position is a vaguely defined quantity which

is a function also of the measuring technique; the evidence that the spray penetration length is initially proportional to time and then progressively slows down until it becomes proportional to the square root of time far downstream in the thin spray regime.

The above conclusions were reached through numerical solutions of a recently developed complex model. So far the model has predicted correctly difficult trends and even magnitudes but it has undergone only limited tests, some aspects of the process are still poorly understood, and well characterized experimental data are still scant. We believe that the main consequence of new and better knowledge will be the improvement of the expression for  $d_{eff}$ , not the change of the above stated general conclusions.

#### ACKNOWLEDGEMENTS

Support for this work was provided by the Department of Energy, Contract EC-77-S-02-4192.A002, The Army Research Office DAAG29-78-G-0132, Volkswagenwerk, FIAT, General Motors, and Komatsu. Some of the results were presented at the 13th and 14th DISC Meetings in March and October 1981.

## NOMENCLATURE

$B_d$	drop transfer number
$B_T$	spray transfer number
$C_D$	drop drag coefficient
$C_{DIS}$	discharge coefficient of nozzle
$c_l$	liquid specific heat
$c_{p_g}$	gas specific heat
$c_{p_I}$	gaseous inert specific heat
$c_{p_v}$	vapor specific heat
$d_{eff}$	effective orifice diameter
$D$	nozzle orifice diameter
$D_t$	turbulent eddy diffusivity
$E_c$	coalescence efficiency
$E_{12}$	collision efficiency
$f$	drop distribution function
$\underline{F}$	drop acceleration
$\underline{F}_a$	aerodynamic drag on a drop
$\underline{G}$	gravitation acceleration
$h_g$	gas enthalpy
$h_l$	liquid enthalpy
$\underline{I}$	unit tensor
$k$	turbulence kinetic energy
$l$	turbulent eddy size, nozzle length
$L$	length of calculation domain
$L$	latent heat of vaporization
$Nu_g$	gas phase Nusselt number
$Nu_l$	liquid phase Nusselt number
$p$	gas pressure
$Pr$	drop Prandtl number = $c_{p_I} \mu_g / \lambda_g$
$p_v$	equilibrium vapor pressure
$p_{inj}$	fuel injector upstream pressure
$P_{rate}$	particle injection rate
$r$	radial coordinate or drop radius

$R$	radius of calculation domain or time rate of change of drop radius
$R$	universal gas constant
$Re_d$	drop Reynolds number = $\frac{2\rho_g  \underline{u}_g + \underline{u}'_g - \underline{v}  r}{\mu_g}$
$Re_D$	incompressible jet Reynolds number = $\rho U_{inj} D / \mu$
$Re_\ell$	liquid jet Reynolds number = $\frac{\rho_\ell U_{inj} D}{\mu_\ell}$
$SMR_o$	initial drop Sauter mean radius
$t$	time
$T_d$	drop temperature
$\dot{T}_d$	time rate of change of drop temperature
$T_g$	gas temperature
$T_s$	drop surface temperature
$T_\ell$	drop temperature at injection
$T_{ref}$	reference temperature
$u_{CL, steady}$	center line steady state value of the gas axial velocity
$\underline{u}_g$	mean gas velocity
$\underline{u}'_g$	fluctuating component of gas velocity experienced by a drop
$U_o$	parcel injection velocity
$U_{inj}$	liquid injection velocity = $C_{DIS} \left[ \frac{2(p_{inj} - p)}{\rho_\ell} \right]^{1/2}$
$\underline{v}$	drop velocity
$W_I$	inert species molecular weight
$W_v$	vapor species molecular weight
$We_\ell$	liquid jet Weber number = $\rho_g U_{inj}^2 D / \sigma_\ell$
$We$	drop coalescence Weber number
$x$	coordinate in the direction of jet axis
$\underline{x}$	position in physical space
$Y_I$	inert gas mass fraction
$Y_{I,s}$	drop surface inert mass fraction
$Y_v$	vapor mass fraction
$Y_{v,s}$	drop surface vapor mass fraction
$\delta$	Dirac delta function
$\delta t$	numerical time step

$\Delta p$	effective injection pressure ( $P_{inj} - P$ )
$\theta$	void fraction (gas volume fraction)
$\theta_o$	gas volume fraction in the injection cell
$\theta_{\frac{1}{2}}$	initial spray half-angle
$\lambda_g$	gas heat conductivity
$\lambda_l$	liquid heat conductivity
$\mu_g$	viscosity of gas
$\mu_l$	viscosity of liquid
$\nu$	collision frequency
$\rho_g$	gas mass per unit gas volume
$\beta_g$	gas mass per unit mixture volume = $\theta\rho_g$
$\rho_l$	liquid density
$\sigma$	transition probability function for collisions
$\sigma_l$	surface tension of liquid
$\tau_t$	correlation time for fluctuating gas velocity along the path of a drop
$\underline{I}_t$	turbulent stress tensor

## REFERENCES

- 1 Reitz, R.D. and Bracco, F.V., "On the Dependence of Spray Angle and Other Spray Parameters on Nozzle Design and Operating Conditions," SAE Paper 790494, 1979.
- 2 Reitz, R.D. and Bracco, F.V., "Ultra-High-Speed Filming of Atomizing Jets," Physics of Fluids, Vol. 22, 1979, p. 1054.
- 3 O'Rourke, P.J. and Bracco, F.V., "Modeling of Drop Interactions in Thick Sprays and a Comparison with Experiments," Stratified Charge Automotive Engines Conference, The Institution of Mechanical Engineers, Publication 085298-469, 1980.
- 4 O'Rourke, P.J., "Collective Drop Effects in Vaporizing Liquid Sprays," Department of Mechanical and Aerospace Engineering, Princeton University, Ph.D. Thesis #1532-T, August 1981.
- 5 Bracco, F.V., "Introducing a New Generation of More Detailed and Informative Combustion Models," SAE Transactions, Vol. 84, 1975, p. 3317.
- 6 Dukowicz, J.K., "A Particle-Fluid Numerical Model for Liquid Sprays," J. Comp. Phys., Vol. 35, 1980, p. 229.
- 7 Williams, F.A., "Progress in Spray-Combustion Analysis," Eighth International Symposium on Combustion, Williams and Wilkins Co., Baltimore, MD, 1962.
- 8 Schlichting, H., "Boundary Layer Theory," 6th ed., McGraw-Hill, 1968.
- 9 Bergwerk, W., "Flow Pattern in Diesel Nozzle Spray Holes," Proceedings of the Inst. of Mech. Engineers, Vol. 173, 1959, p. 655.
- 10 Kuo, T.-W., "On the Scaling of Transient Laminar, Turbulent, and Spray Jets," Department of Mechanical and Aerospace Engineering, Princeton University, Ph.D. Thesis #1538-T, December 1981.
- 11 Hiroyasu, H. and Kadota, T., "Fuel Droplet Size Distribution in Diesel Combustion Chamber," SAE Paper 740715, 1974.
- 12 Groeneweg, J.F., El-Wakil, M.M., Myers, P.S. and Uyehara, O.A., "The Role of Drop Velocity in Statistical Spray Description," First International Conference on Liquid Atomization and Spray Systems, Tokyo, 1978.
- 13 Kuo, T.-W. and Bracco, F.V., "On the Scaling of Impulsively Started Incompressible Turbulent Round Jets," To appear in the Journal of Fluids Engineering.

- 14 Hay, N. and Jones, P.L., "Comparison of the Various Correlations for Spray Penetration," SAE Paper 720776, 1972.
- 15 Schweitzer, P.H., "Penetration of Oil Sprays," Pennsylvania State College Bulletin No. 46, 1937.
- 16 Lyshevskiy, A.S., "The Coefficient of Free Turbulence in a Jet of Atomized Liquid Fuel," NASA TT-F351, 1956.
- 17 Wakuri, Y., Fujii, M., Amitani, T. and Tsuneya, R., "Studies of the Penetration of a Fuel Spray in a Diesel Engine," Bull. J.S.M.E., Vol. 3, 1960, p. 123.
- 18 Sitkei, G., "Kraftstoffaufbereitung und Verbrennung bei Diesel Motoren," Springer-Verlag, 1964.
- 19 Parks, M., Polonski, C. and Toye, R., "Penetration of Diesel Fuel Sprays in Gases," SAE Paper 660747, 1966.
- 20 Hakki Oz, I., "Calculation of Spray Penetration in Diesel Engines," SAE Paper 690254, 1969.
- 21 Taylor, D.H. and Walsham, B.E., "Combustion Process in a Medium Speed Diesel Engine," Diesel Engine Combustion, Proc., Instn. Mech. Engrs., Vol. 184, Part 3J, 1970, p. 67.
- 22 Dent, J.C., "A Basis for the Comparison of Various Experimental Methods for Studying Spray Penetration," SAE Transactions, Vol. 80, 1971.
- 23 Williams, T.J., "Parameters for Correlation of Penetration Results for Diesel Fuel Sprays," Combustion Engine Group, Proc. Instn. Mech. Engrs., Vol. 187, 1973, p. 771.
- 24 Chiu, W.S., Shahed, S.M. and Lyn, W.T., "A Transient Spray Mixing Model for Diesel Combustion," SAE Paper 760128, 1976.
- 25 Hiroyasu, H., Kadota, T. and Arai, M., "Supplementary Comments: Fuel Spray Characterization in Diesel Engines," Proc. of the Symp. on Combustion Modeling in Reciprocating Engines, Plenum Press, 1980.



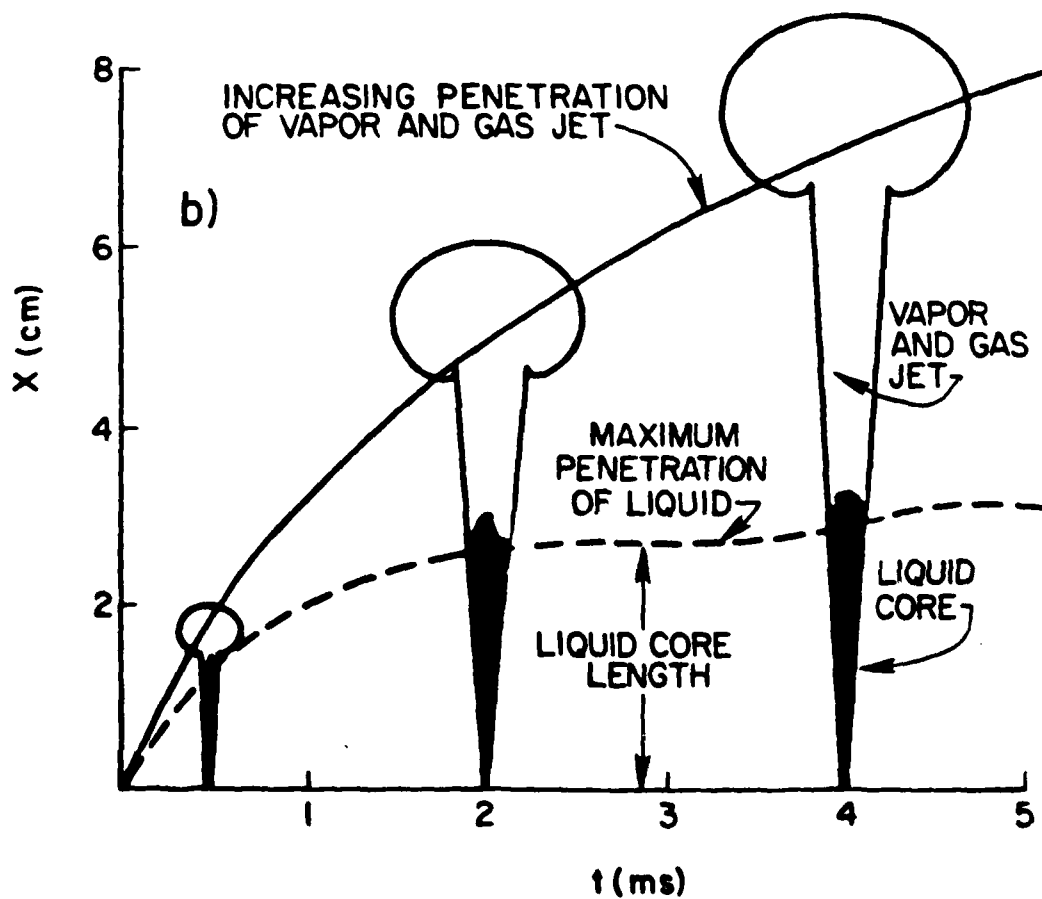
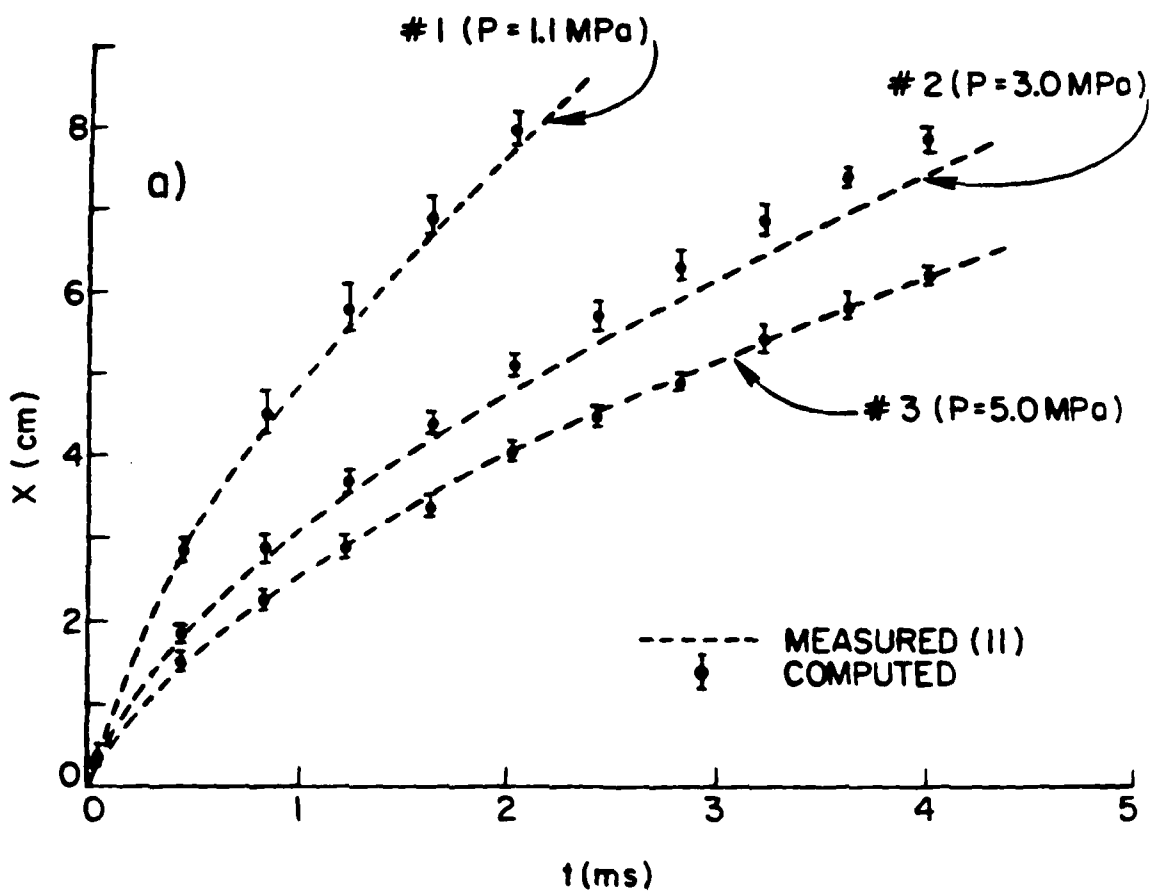
$P_{inj}$ MPa	$P$ MPa	$C_{DIS}$	$U_{inj}$ cm/ms	$U_o$ cm/ms	$\theta_o$	$SR_o$ $\mu m$	$\theta_y$ Rad	$\frac{l}{D}$	$D_t$ $cm^2/ms$	$P_{RATE}$ $ms^{-1}$	$\Delta t$ $\mu s$	$D$ $cm$	$T_g$ $K$	$\rho_g$ $g/cm^3$	$T_i$ $K$	$\rho_i$ $g/cm^3$
9.9	1.1	0.7	10.2	8.92	0.9	3	.0785	6.67	.0043	900	0.5	0.03	300	.0126	300	0.84
9.9	3.0	0.7	9.03	6.91	0.88	1.5	.0993	6.67	.0039	900	0.5	0.03	300	.0344	300	0.84
9.9	5.0	0.8	8.64	5.92	0.87	1.2	.1220	6.67	.0037	900	0.5	0.03	300	.0577	300	0.84
12.9	6.0	0.7	9.03	6.91	0.88	1.5	.0993	6.67	.0039	900	0.5	0.03	600	.0344	300	0.84
10.45	1.65	0.7	10.2	8.92	0.9	3	.0785	6.67	.0043	900	0.5	0.03	450	.0126	300	0.84
11.0	2.2	0.7	10.2	8.92	0.9	3	.0785	6.67	.0043	900	0.5	0.03	600	.0126	300	0.84
11.0	2.2	0.7	10.2	8.92	0.9	3	.0785	6.67	.0043	900	0.5	0.03	600	.0126	300	0.84 thin spray
34.0	3.4	0.65	16.2	13.13	0.923	0.9	.1047	4.0	.0046	900	0.5	0.02	700	.0164	300	0.84
9.9	1.1	0.7	10.2	7.073	0.968	3	.0785	6.67	.0022	900	0.5	0.015	300	.0126	300	0.84 D effect
0 18.7	1.1	0.7	14.43	12.74	0.9	1.5	.0785	6.67	.0062	900	0.5	0.03	300	.0126	300	0.84 $U_{inj}$ effect
1 9.9	1.1	0.7	10.2	8.92	0.9	3	.1312	6.67	.0043	900	0.5	0.03	300	.0126	300	0.84 $\theta_i$ effect
2 9.9	3.0	0.7	9.03	6.91	0.88	1.5	.1745	6.67	.0039	900	0.5	0.03	300	.0344	300	0.84 "
3 9.9	5.0	0.8	8.64	5.92	0.87	1.2	.2182	6.67	.0037	900	0.5	0.03	300	.0577	300	0.84 "
4 13.8	5.0	0.7	10.2	7.0	0.873	0.6	.1220	6.67	.0043	900	0.5	0.03	300	.0577	300	0.84 $\rho$ effect
5 9.9	3.0	0.7	11.71	7.51	0.86	0.9	.1220	6.67	.005	900	0.5	0.03	300	.0344	300	0.50 $\rho_i$ effect

Table 1. Input parameters of the spray computations

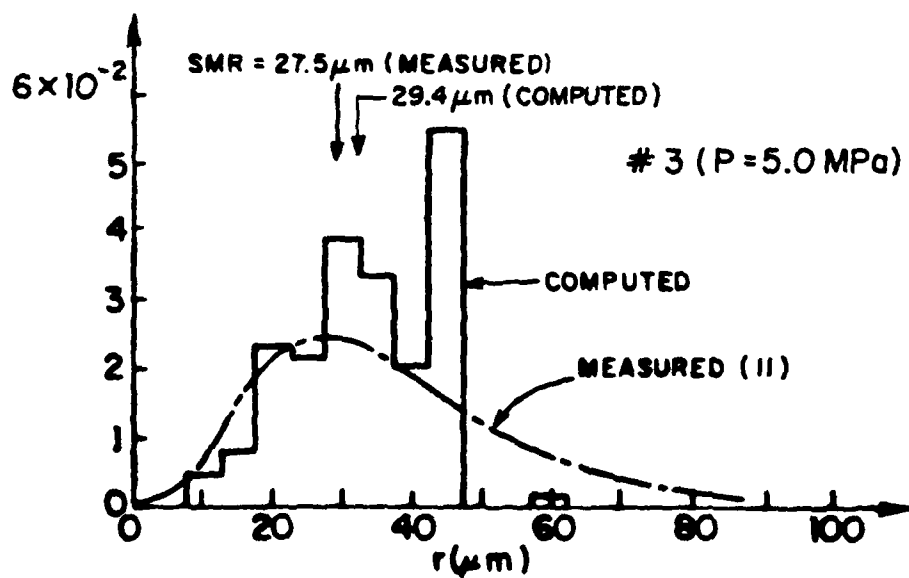
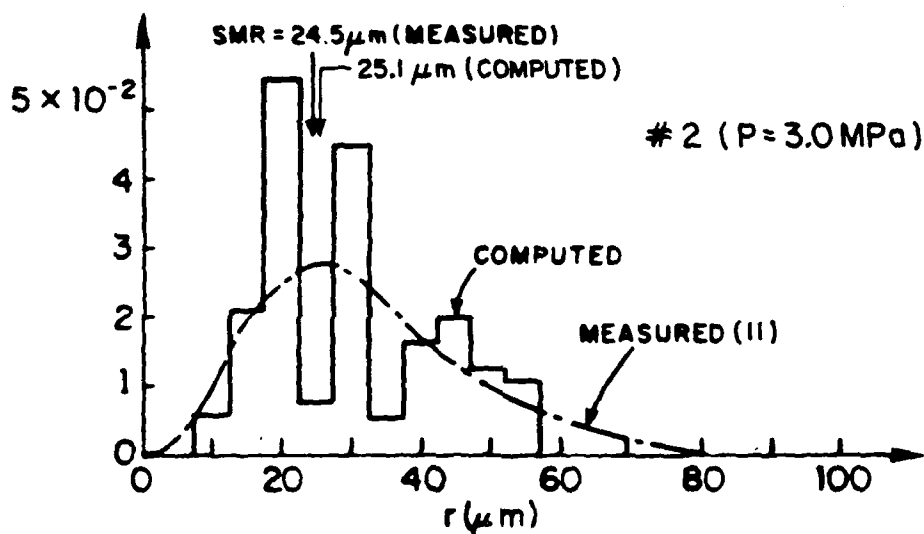
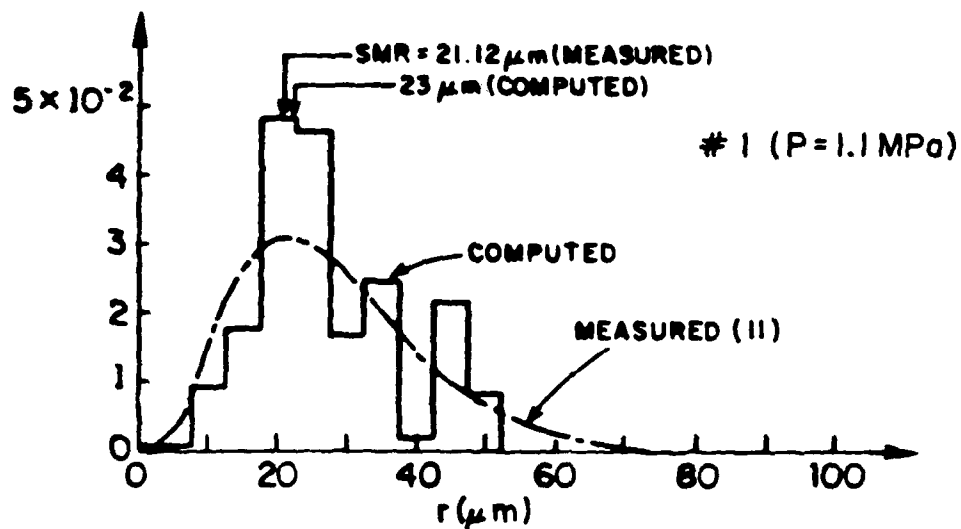
PROPOSER OF CORRELATION	POWER OF PARAMETER										
	$\Delta p$	D	$\rho_g$	$T_g$	t	$r_f$	$v_c$	$r_g$	Tan $\theta$	Remarks	
SCHWEITZER (15)	0.2936	0.4127	-0.4127	—	0.5873	—	—	—	—	exp.	
LYSEVSKIY (16)	0.3	0.4	-0.5	—	0.5	0.4	0.3	—	—	theor.	
MAKURI, ET AL (17)	0.25	0.5	-0.25	—	0.5	—	—	—	-0.5	theor.	
SITKEI (18)	0.39	0.82	-0.35	—	0.48	-0.04	-0.3	—	—	theor.	
PARKS, ET AL (19)	0.3	0.4	-0.4	0.6	0.6	—	—	—	—	exp.	
JANKI OZ (20)	—	—	—	—	0.5	—	—	—	—	theor.	
TAYLOR, ET AL (21)	0.32	0.18	-0.32	—	0.64	—	—	0.18	—	exp.	
DEB (22)	0.25	0.5	-0.25	-0.25	0.5	—	—	—	—	theor.	
WILLIAMS (23)	0.25	0.5	-0.25	—	0.5	—	—	—	—	theor.	
CHIU, ET AL (24)	0.25	0.5	-0.35	—	0.6	0.4	—	—	—	exp.	
HIROYASU, ET AL (25)	0.25	0.5	-1	—	0.5	—	—	—	—	$t > t_{break}^*$	
	0.5	—	—	—	1	-0.05	—	—	—	$t < t_{break}^*$	
PRESENT STUDY	0.331	0.338	-0.338	-0.152	0.662	0.0	—	—	-0.085	$x^* > 0.6$	
	0.5	—	—	—	1	-0.05	—	—	—	$x^* < 0.6$	

$$*t_{break} = 28.65 \rho_t D / (\rho_g \Delta p)^{1/2}$$

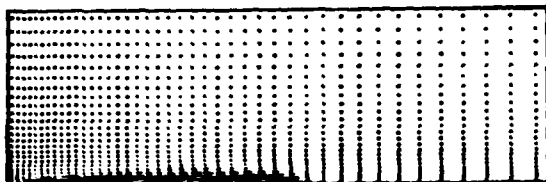
Table 2. Powers of the independent parameters of the tip penetration function



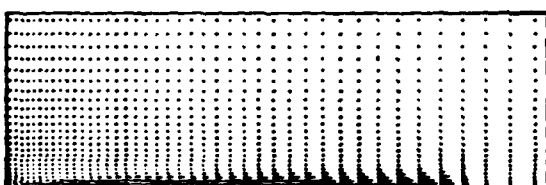
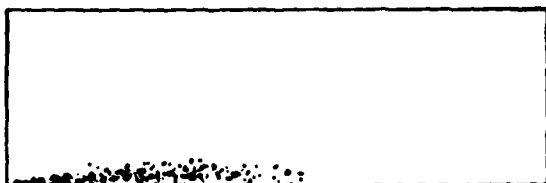
$$\frac{1}{V_T} \frac{dV(r)}{dr} (\mu\text{m}^{-1})$$



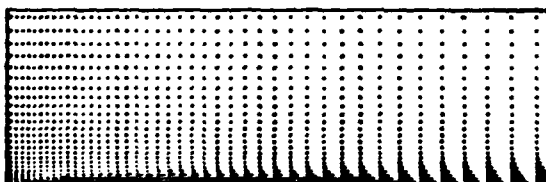
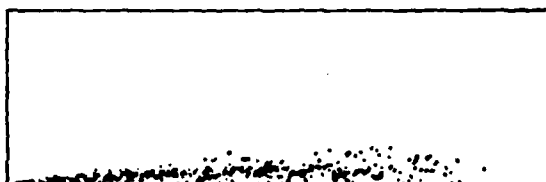
# VELOCITY AND DROP PARCELS



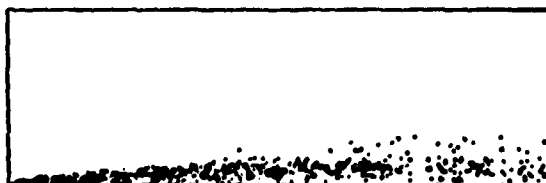
$t = 1 \text{ ms}$



$t = 2 \text{ ms}$



$t = 3 \text{ ms}$



a)

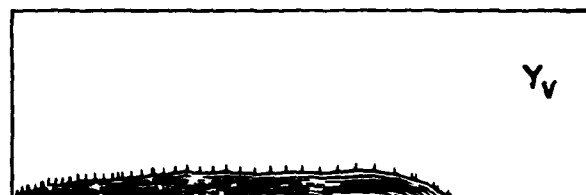
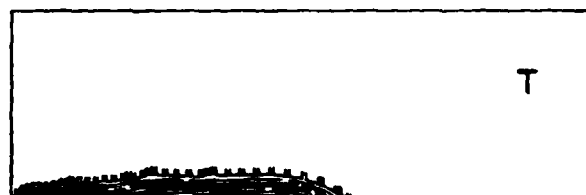
# VAPOR MASS FRACTION AND GAS TEMPERATURE



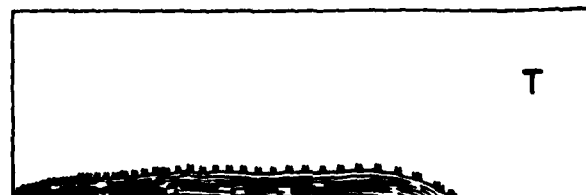
$t = 1.2 \text{ ms}$



$t = 2.4 \text{ ms}$



$t = 3.6 \text{ ms}$



b)

FIGURE 1

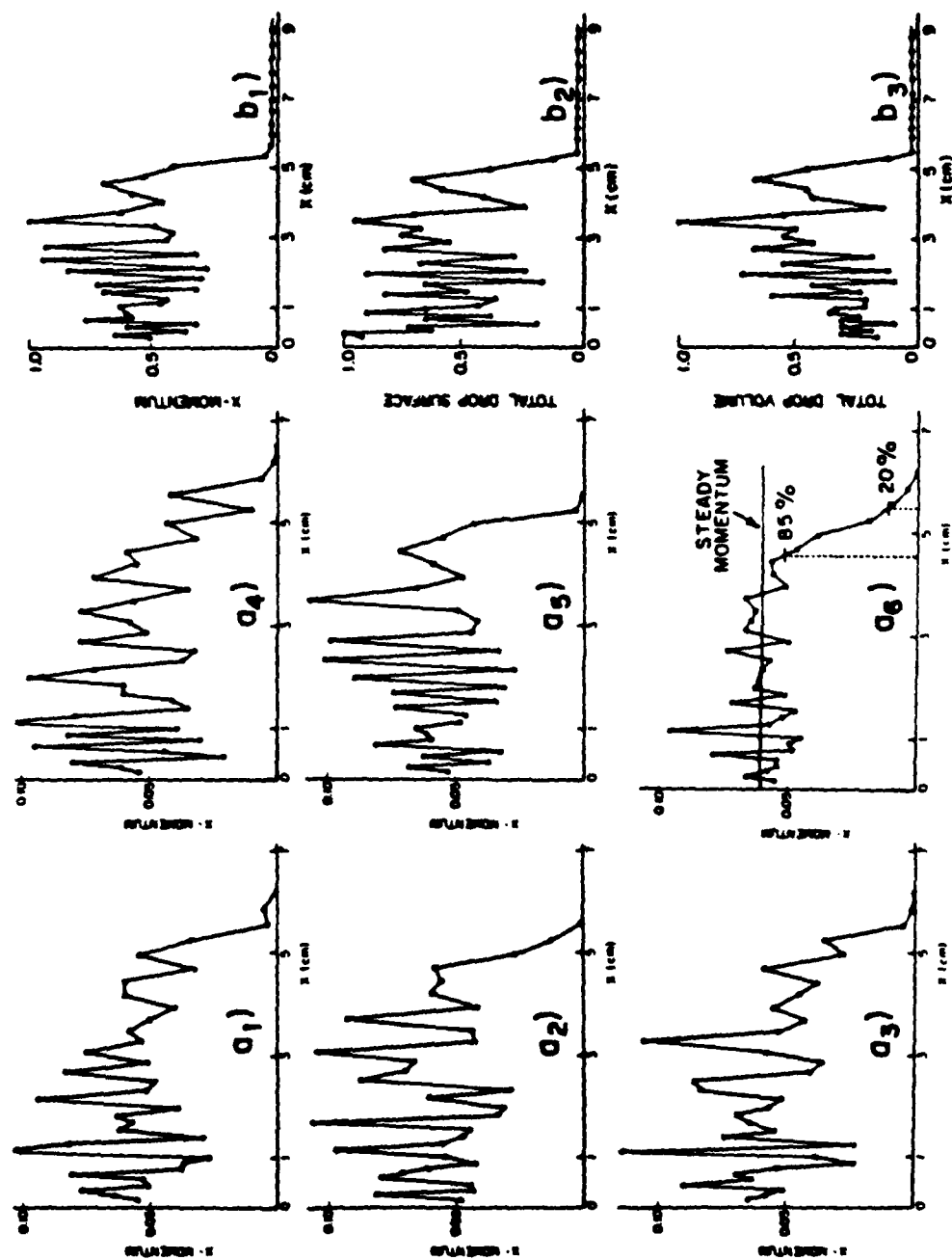


FIG 4

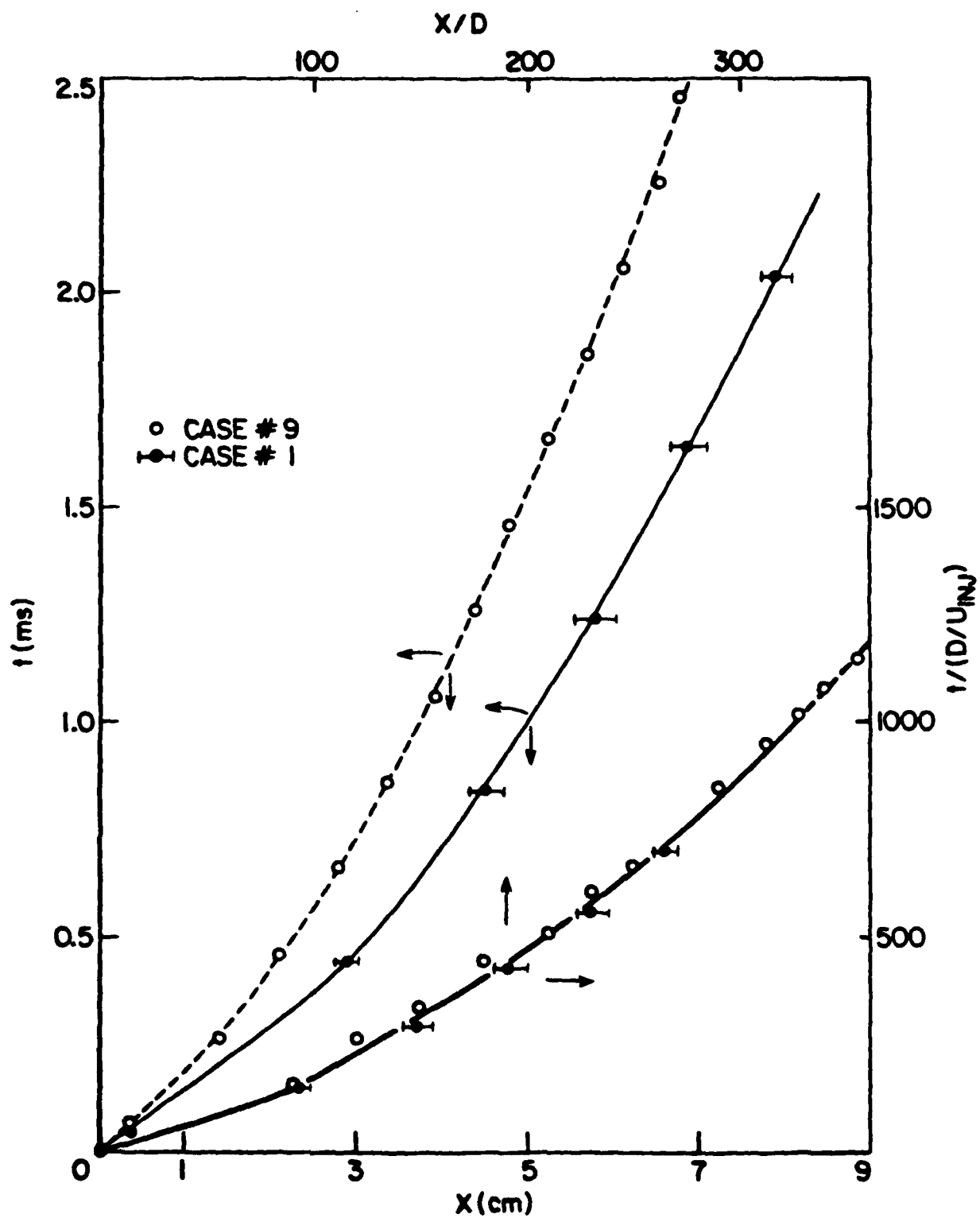


FIG 5

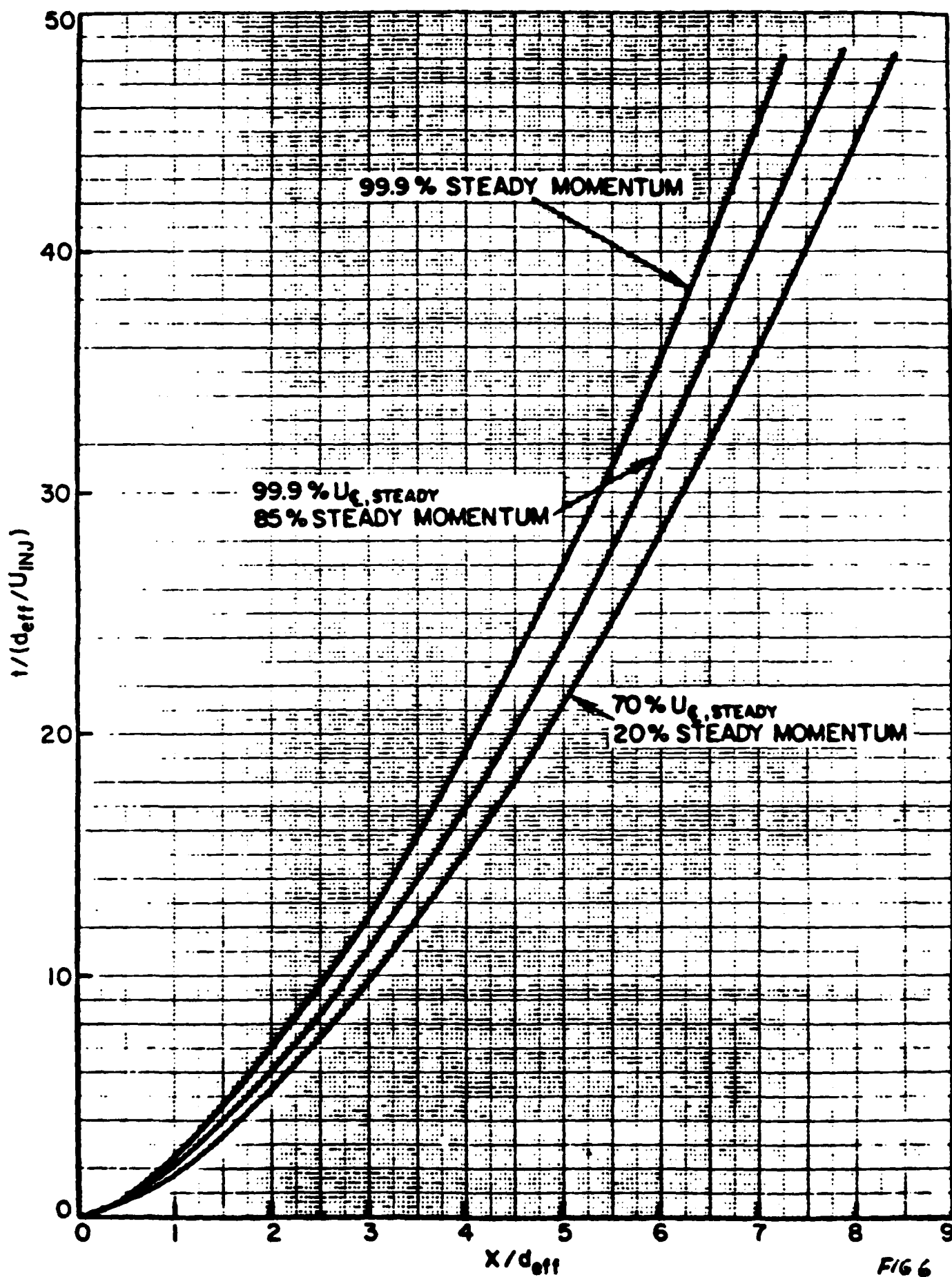


FIG 6



## FIGURE CAPTIONS

- Fig. 1 Computed tip penetration rates: a) for three non-vaporizing sprays, compared with measurements [11]; b) for a vaporizing spray, emphasizing gas tip and liquid core length.
- Fig. 2 Computed and measured [11] downstream drop size distributions at three ambient pressures.
- Fig. 3 Typical computed transient spray structure: a) drop parcels and gas velocity for a non-evaporating spray (Case #1 of Table 1); b) gas temperature and vapour contours for a vaporizing spray (Case #4 of Table 1).
- Fig. 4 Axial distributions (Case #1 of Table 1) of: a) axial momentum at  $t = 1.2$  ms in five computations and their ensemble average ( $a_c$ ); b) axial momentum ( $b_1$ ), total drop surface ( $b_2$ ), and total drop volume ( $b_3$ ) in one computation.
- Fig. 5 Effect of orifice diameter. Dimensional and dimensionless steadying time curves for Cases #1 and 9 based on the 70%  $u_{CL, steady}$  definition.
- Fig. 6 Steadying time curves for non-vaporizing and vaporizing sprays based on 70% and 99.9% of the steady state centerline velocity and 20%, 85%, and 99.9% of the steady state axial momentum.

